Universitat Autònoma de Barcelona

IRIDIUM OXIDE-CARBON HYBRID MATERIALS AS ELECTRODES FOR NEURAL SYSTEMS. ELECTROCHEMICAL SYNTHESIS AND CHARACTERIZATION

Nina Magali Carretero González

Tesis Doctoral

Programa de Doctorado en Ciencia de Materiales

Directora: Prof. Nieves Casañ Pastor

Tutor: Dr. Jaume Casabó i Gispert

DEPARTAMENTO DE QUÍMICA

FACULTAD DE CIENCIAS

2014

CSIC

ICMAB

Institut de Ciència de Materials de Barcelona (ICMAB)
Consejo Superior de Investigaciones Científicas (CSIC)
Campus de la UAB
08193 Bellaterra (Barcelona)

Universitat Autònoma de Barcelona
Facultat de Ciències
Departament de Química
08193 Bellaterra (Barcelona)

Nieves Casañ Pastor,

Profesora de Investigación del CSIC en el

Institut de Ciència de Materials de Barcelona (CSIC)

Certifica:

Que **Nina Magali Carretero González**, licenciada en Química, ha realizado bajo su dirección el trabajo que lleva por título "Iridium Oxide-Carbon Hybrid Materials as Electrodes for Neural Systems. Electrochemical Synthesis and Characterization", el cual se presenta en esta memoria para optar al grado de Doctora por la Universitat Autònoma de Barcelona.

Y para que así conste, firma el presente certificado.

Bellaterra, Abril de 2014

A mi gran familia, en especial a mi padre.

“Research is to see what everybody else has seen, and to think what nobody else has thought”

“Investigar es ver lo que todo el mundo ha visto, y pensar lo que nadie más ha pensado”

(Albert Szent-Györgi)

ACKNOWLEDGMENTS

La realización de este trabajo no hubiera sido posible sin el apoyo de mucha gente que ha estado a mi lado (aún separados por algunos kilómetros) aportándome su conocimiento y sus ánimos, tanto en el terreno profesional como en el personal.

En primer lugar, me gustaría agradecer a mi familia, mis padres y hermanos, Virginia y Manuel. Y también a mi pequeño-gran sobrino, Darío. Gracias por aportarme la fuerza en momentos difíciles y por siempre estar ahí. Especial mención también a todos mis tíos y primos, que me hacen sentir orgullosa de pertenecer a la familia que tengo. Y por supuesto, a mi primo Adrián, por abrirme la puerta grande del ICMAB y permitirme conocerle mejor en estos años por Barcelona…. ¡Eres un primazzo con mayúsculas!

A mi directora de tesis, Nieves Casañ, por darme la oportunidad de empezar mi carrera científica y haber confiado en mí desde el principio.

A los miembros de mi Tribunal, por haber aceptado la invitación de formar parte en esta tesis.

A los integrantes del Equipo Bio. Ana Mi y Javi, con vosotros aprendí a moverme por el laboratorio y lo que empezó con disoluciones y potenciostatos terminó en una bonita amistad. Los buenos momentos que hemos pasado juntos hará que me sea muy difícil volver a encontrar compañeros de trabajo como vosotros. A Estela por ser un apoyo constante en el desarrollo de mi trabajo, ayudándome tanto en el laboratorio, como de psicoanalista a veces. A la parte más Bio, Mateu y Cristina del IibB, por la realización de los experimentos neuronales en mis muestras y por ser tan pacientes a la hora de resolver dudas celulares.

Al grupo de química del estado sólido en general, por acogerme y mostrar siempre amabilidad. En particular a Gerard por suministrarme las primeras muestras de nanotubos y grafeno para mis híbridos… ¡no se que hubiera sido de mi tesis sin ti! A Judit Oró, por su paciencia en la búsqueda de "bosques de nanotubos" y su eterna sonrisa.

Al personal de administración y servicios del ICMAB, por su trabajo y eficiencia. En especial, a Vicente y a Trini, por su implicación en la causa.

Y por supuesto, a mis niñas OnFire: Laura, Stefania, Nerea, Ana López, Jessica, Ángela, Marixa, Jullieth y Nerea. Habéis sido mi familia aquí y no tendría páginas en esta tesis para escribir todos los momentos buenos que he vivido con vosotras, y todo lo que os echaré de menos cuando acabe "yonosedonde". También a mis niñas del Nanotubes-Team, por haber aceptado con tanta ilusión ser mis esclavas y suministrarme sus materiales tan alegremente. A mis compis de despacho y a los que pasaron por aquí: Francesc, Belencita, Álex, Ashley y especial mención a Zacaria y Sebastien, vuestra estancia aquí, ha sido uno de los momentos mejores del ICMAB.

A Pablo García, por su ayuda con las medidas de rayos X y la posterior interpretación.

A Andrés, por su paciencia en las medidas de AFM y a Markos, por su posterior explicación de los resultados y por ser tan buena gente.

A Mónica Roldán y Elena Bailo, por su ayuda con las medidas de Confocal y Raman-Confocal, respectivamente.

A Vanesa y Mara, por sus indicaciones en el tema de supercapacitores.

A Toñi del Departamento de Química, por su implicación y ser tan atenta.

A la gente del ICMAB y alrededores, que aún no siendo parte de mi grupo de trabajo me ha aportado tanto, ya sea en lo profesional o en lo personal,

Marc, Roque, David Pesquera, Dieguito, Maria Milla, Jaque, Rául, Marta, Cristina, Regina, Jessi (sexy-mami), Muling, Elisa, Simo, Rouco, Cavallaro, RoberTito... y tantos otros con los que he compartido algo de ciencia y muchas risas.

A mis compañeros de Máster con los que tantos buenos momentos he compartido, MiMajo, CésaL, James, EsteL y Nuria. ¡Vamos, que lo conseguimos!

A mis andaluces en Barcelona, que le ponen un poquito de sur a estas tierras: Manu, Manolo, Juanjo, Pablo Caballero, Santi y en especial a mi Sari, sin ella no se que hubiera sido de mi vida aquí… ¡eres un sol querida amiga!

A mis amigos de toda la vida, que desde la distancia me mandan sus energías: Elisa, Mariana, José, Silvio, Merce, Rocío Félix y tantos otros… ¡ya mismo lo celebramos juntos!

A mis compañeros de piso durante estos años, por todos esos momentos que hemos compartido: Otto, Sara, Gustavo y Fabrizio. Especial agradecimiento a mi Fabri, no solo por cocinarme bastante a menudo, sino también por ayudarme con la portada. He sido muy afortunada de vivir con vosotros.

Y por último, y no menos importante a Apolo. Por tu paciencia, tu cariño y por compartir tantas cosas conmigo. Tengo mucha suerte, la verdad.

Me gustaría destacar que este trabajo ha sido posible gracias a la financiación recibida por el Consejo Superior de Investigaciones Científicas y su programa de Junta para la Ampliación de Estudios (JAE-predoc) y de los proyectos del Ministerio de Educación y Ciencia (MAT2011-24363, MAT2008-06643-C02-01), del CSIC (PIF06-021), de la Comisión Europea Programa FP6-2004-NEST STREP (Contrato 028473) y del proyecto de la Marató de TV3 de 2011 (Ref 110131).

ABSTRACT

The development of neural interfaces requires new electroactive and biocompatible materials, capable to apply electric fields without secondary effects, as large impedances at the interface or radical formation, which can cause damage in the tissues and the degradation of the electrode functionality. Currently, different types of electroactive materials are available for application as electrodes in the neural system: gold, platinum, glassy carbon, Pt-Ir, TiN or IrOx, among others, being the last, the one with superior performance. Properties such as high electrochemical efficiencies, good bio-stability and significant biocompatibility, have turned out IrOx into one of the most promising material for neural recording and stimulation electrodes. However, new technological breakthroughs have generated a demand of novel materials, with enhanced properties and which also minimize the drawbacks found in the actual ones, as low stability under electrochemical conditions, small values for charge capacity or the inherent rigidity of these oxides, which involves low compatibility with soft tissues. These improvements required may be achieved by hybrid materials, which join different properties from both counterparts. In this sense, IrOx-CNTs hybrids have been electrochemically prepared with enhanced properties provided by the carbon nanotubes (CNTs). The chemical composition at the surface is very similar to that for IrOx, but the incorporation of carbon nanotubes makes the surface rougher, increasing the available interface area of the material. These properties, joined with the conductivity provided by the CNTs, yield very high values for charge storage capacity in electrochemical measurements. Also, the stability of the resulting coatings is improved in comparison with bare IrOx. The IrOx-CNTs biocompatibility tests have shown high cellular survival and neuron functionality, similar to those values obtained for bare IrOx or borosilicate (used for reference), which validates these new materials as promising neural electrodes.

IrOx hybrids with graphite and graphene also have been prepared. In both coatings, the presence of carbon particles has been demonstrated, although the confirmation of single graphene sheets instead of few-layered graphene needs more experimental studies. The electrochemical properties of these IrOx-graphene and IrOx-graphite hybrids are similar than those obtained for IrOx-CNTs electrodes, with high values of charge storage capacity. However, the stability during consecutive cycling for the graphite-hybrid is poor and the coating is finally delaminated. These results are presumably due to heterogeneous structure in graphite-hybrids, in which the big carbon particles are not completely embedded in the IrOx matrix. Also, IrOx hybrids with N-doped graphene have been prepared, showing promising properties and very high values for charge storage capacity and stability, even when compared with non-doped IrOx-graphene coatings. The enhanced conductivity of these materials can be related with the presence of nitrogen, which induces the increase of the defects in the graphene sheets. The biocompatibility of these graphitic hybrid materials is under study.

Polymeric tri-hibrids, IrOx-PEDOT-CNTs, have been also electrochemically synthesized. The use of a polymeric matrix is an effort to confer more flexibility to the future electrode, which is desirable for soft tissue applications. However, the first results show that the polymer may encapsulate the CNTs and the IrOx particles, minimizing the electrochemical properties of these species. As a consequence, the electrochemical performance of the hybrid material is similar to those obtained for other polymers, as PEDOT-PSS. The biocompatibility tests for these polymeric hybrids have shown low neuronal viability in these substrates; however, co-cultures (astrocytes-neurons) have been proposed as a novel method to improve biocompatibility in these types of materials.

The materials obtained in all cases, are well adehered coatings, which leads to an feasible future use as electrodes or cells substrates.

RESUMEN

El desarrollo de interfaces neuronales requiere el uso de nuevos materiales electroactivos y biocompatibles, capaces de aplicar campos eléctricos sin causar efectos secundarios, como gran impedancia en la interfase o formación de radicales, que pueden dañar los tejidos o la degradar la funcionalidad del electrodo. A día de hoy, hay disponibles diferentes tipos de materiales electroactivos para aplicaciones como electrodos en el sistema nervioso: oro, platino, carbón, Pt-Ir o IrOx entre otros, siendo el último el que ha mostrado superiores resultados. Las buenas propiedades observadas en eficiencia electroquímica, estabilidad en condiciones biológicas y biocompatibilidad, han hecho del IrOx el material más prometedor como electrodo para estimulación y registro de señales neuronales. Sin embargo, los avances tecnológicos han generado una demanda de nuevos materiales con mejor propiedades y que consigan minimizar los inconvenientes encontrados en los actuales, como bajos valores de capacidad de carga o la rigidez inherente de este tipo de óxidos, ya que presenta poca compatibilidad con los tejidos blandos. Estas mejoras se pueden conseguir con el uso de materiales híbridos, que unan las diferentes propiedades de los componentes. En este sentido, se han preparado electroquímicamente híbridos IrOx-CNTs, con propiedades mejoradas tras la adicción de nanotubos de carbono. La composición química de estos híbridos es muy parecida a la obtenida en muestras de IrOx, aunque la incorporación de nanotubos de carbono hace la superficie más rugosa, aumentando de esta manera el área superficial del material. Estas propiedades, junto con la conductividad proporcionada por los nanotubos de carbono, tienen como consecuencia elevados valores de capacidad de carga durante las medidas electroquímicas. También, la estabilidad de las capas resultantes ha mejorado en comparación con las muestras de IrOx. Las pruebas de biocompatibilidad realizadas a las muestras IrOx-CNTs han mostrado una alta supervivencia y

funcionalidad neural, parecida a la obtenida con IrOx o borosilicato (usado como referencia). Estos datos, validan este tipo de nuevos materiales como prometedores electrodos neurales.

También se han preparado híbridos de IrOx y grafito y grafeno. En ambas capas, se ha demostrado la presencia de partículas de carbón, aunque la presencia de capas de grafeno de única lámina no ha podido ser confirmada, y serán necesarios más experimentos. Las propiedades electroquímicas de estos híbridos, IrOx-grafito e IrOx-grafeno, son similares a las previamente obtenidas para IrOx-CNTs, pero con mayores valores de capacidad de carga. Sin embargo, la estabilidad tras un ciclado continuo es pobre para el híbrido de grafito, y finalmente la capa se despega. Estos resultados son debidos, presuntamente, a la estructura heterogénea de los híbridos de grafito, en la cual, grandes partículas de carbón no están completamente introducidas en la matriz del IrOx. Híbridos de IrOx con grafeno dopado con nitrógeno se han preparado también, mostrando propiedades prometedoras y altos valores de capacidad de carga y estabilidad, incluso comparados con los resultados obtenidos para los híbridos con grafeno sin dopar. El aumento de la conductividad en estos materiales se puede deber a la presencia de nitrógeno, que induce el aumento de defectos en las láminas de grafeno. La biocompatibilidad de estos materiales híbridos grafíticos está siendo estudiada.

Tri-híbridos poliméricos también han sido sintetizados electroquímicamente, IrOx-PEDOT-CNTs. El uso de una matríz polimérica, ofrece más flexibilidad al futuro electrodo, lo que es deseable para aplicaciones en tejidos blandos. Sin embargo, en los primeros resultados obtenidos parece que el polímero puede encapsular los nanotubos de carbono y las partículas de IrOx, minimizando sus propiedades electroquímicas. Como consecuencia, la conducta electroquímica del material híbrido es muy similar a la obtenida en otros polímeros, como PEDOT-PSS. Las pruebas de biocompatibilidad para estos híbridos poliméricos

han mostrado una baja viabilidad neuronal, aunque un nuevo modelo de co-cultivos (astrocitos-neuronas) se ha propuesto como método para mejorar la biocompatibilidad en este tipo de materiales.

Los materiales obtenidos en todos los casos, son capas bien adheridas, lo que permite su futuro uso como electrodos o substratos de crecimiento neuronal.

CONTENTS

Chapter 1

Introduction

This chapter gathers a brief introduction of the fundamental basis of the work carried out in this thesis.

In the first part the main objectives of the project are exposed.

Next, a historical reference of the use of electrical fields in the neural system is introduced, with a short explanation about the morphology of neurons and the bioelectricity. Also, the different possible techniques using bioelectrodes are enumerated.

The third part deals with the different types of electrodes and protocols during electrochemical measurements, pointing out some important parameters, crucial for the good electrical behavior required in biological environments.

In the next section, hydrous iridium oxide (IrOx), the base material for the novel hybrids shown is described, mentioning the principal characteristics of the material, and the importance of the synthetic method. Also, the aim to pursue hybrids synthesis: the improvement expected in properties such stability or conductivity with the incorporation to the oxide structure of carbonaceous species or/and conducting polymers.

Finally, the specific objectives are exposed.

1.1 Main Objective

The aim of the work presented in this thesis is the development of new materials with enhanced properties to be used as electrodes for neural growth and stimulation. A possible electric field approach to stimulate neural growth, requires electroactive and biocompatible materials as electrodes, which could promote cell migration and neural dendrites polarization, therefore, creating the possibility to generate new connections between cells and even to repair possible tissue damage (for example, in the spinal cord after an accident). For functional stimulation, similar characteristics are sought for the material in terms of stability and biocompatibility. However, the application of electric fields (EFs) in this case pursues to reach the rate and intensity of the proper neural electrical signals, preventing cellular or tissue damage.

Considering these two possible applications, new hybrids based on the well known electrodeposited iridium oxide (EIROF or IrOx) have been developed and characterized. The aim of hybrids preparation is to improve the stability of the IrOx material, enhancing the electronic conductivity and the electrochemical properties of the future bioelectrode. With this objective, single walled carbon nanotubes (SWCNTs) were incorporated in the iridium oxide structure, with a considerable improvement in the material properties. The same electrochemical synthetic method also yielded outstanding results with the incorporation of other carbonaceous species within the oxide matrix, as graphite and graphene. The properties and bio-applications of these IrOx-graphite and IrOx-graphene hybrids, are currently under study, with promising results.

The second type of hybrid synthesized in this work is in fact, a tri-hybrid, a material consisting of a conducting polymer, IrOx and SWCNTs. The insertion of IrOx particles and carbon nanotubes (CNTs) as dopants within the polymer structure is expected to improve the final properties of the resulting hybrid material, by combining those of the counterparts: the proven biocompatibility and high electrochemical performance of IrOx, the stability and high conductivity of CNTs, and the versatility and intrinsic flexibility of the polymer, which is more appropriate for soft tissue implantation.

1.2 Electric Fields and Neural Behavior

The use of electric current as therapy for some diseases has been known for long time. Some Egyptian references in hieroglyphics from the 3rd millennium BC express the use of the potent Nile catfish in causing fishermen to "release the troupes" when they felt its strong current, using these animals later to relieve particular symptoms. Another example is a Roman text from 47 AD which suggests that multiple ailments (e.g. gout) could be treated by using the shocks from this type of fish [1]. The use of electrical currents has advanced considerable since then, mainly in areas related with the nervous system, with important contributions of Galvani or Volta, among others. Nowadays, electrodes inducing electrical fields in the neural tissue have numerous applications. The main three types are listed below. This work has been particularly focused in the first two ones.

- *Stimulation*. The injection of rapid pulses (simulating neuronal action potentials) to the neural tissue promotes cell response. Safe reversible charge injection electrodes and charge-balanced pulses are necessary to maintain the electrodes in a range of safe potential, preventing irreversible reduction or oxidation side reactions, which can cause tissue damage.

- *Growth and modulating*. The implementation of a steady electrical current within the extracellular media in peripheral nerves, promotes processes as division, migration and even repair of damaged tissue, showing the relevance of chemical, physical and electrical gradients in the cell behavior. Physiologically stable electrodes with low impedance are been tested, in order to maintain the current during large periods of time, without degradation or temperature increase. In addition, materials must permit the adhesion and cell proliferation.

- *Recording*. Low impedance electrodes are used for recording the action potentials of single neurons, allowing the transduction of neural expression signals.

1.2.1 Neural System and Bioelectricity

Before a detailed explanation of the different applications exposed above, it is necessary to briefly describe the biological system under study. The nervous system tissue is composed by two main cells: nerve cells (neurons) and glial cells (astrocytes are the main sub-type of glial cells). In vertebrates, there is 10 to 50 times more glia than neurons in the central nervous system (CNS). The main function developed by glial cells is to support neurons, providing the brain structure, among others as production of myelin or synapse regulation [2]. However, in this work we focus our studies principally in neurons, which are typically defined by four regions: the cell body, the dendrites, the axon, and the nucleus (Figure 1.1).

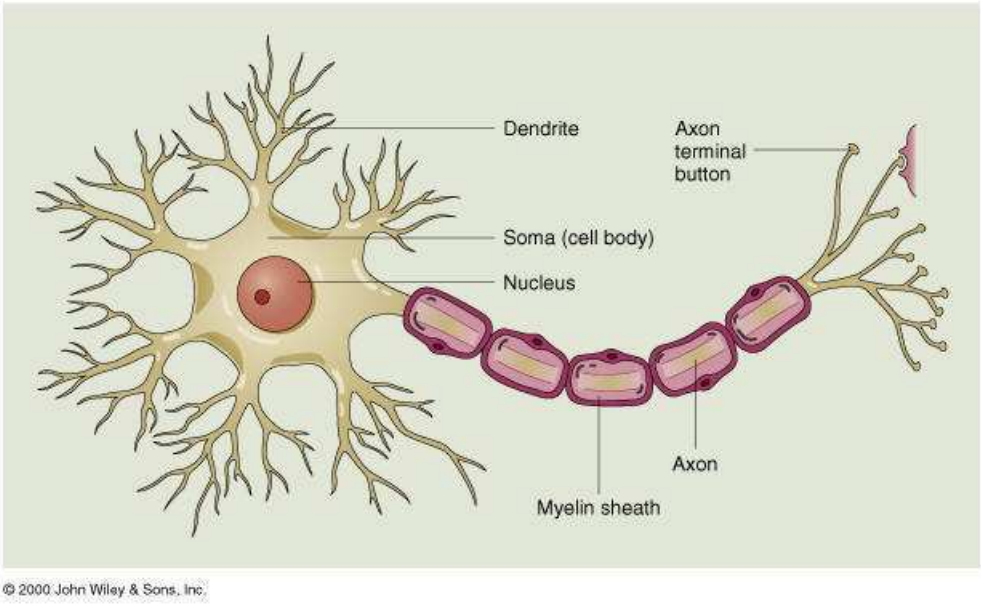

Figure 1.1. Schematic image of a neuron, composed mainly by the cell body (soma), the nucleus, the dendrites and the axon. (Figure of 2000 John Wiley and Sons, Inc.)

All of these regions have a distinct role in the generation of signals and communication between nerve cells. The cell body is the metabolic center of the neuron and contains the nucleus, where the genes are stored. The dendrites are the main apparatus for receiving incoming signals from other nerve cells, and the axon is

the main conducting unit for carrying electrical signals to other neurons. Near its end, the tubular axon divides into fine branches that form communication sites with other neurons. The point at which two neurons communicate is known as a synapse.

Santiago Ramón y Cajal was the first who showed that nervous tissue is not continuous but a network of discrete cells. In the course of his work, Ramón y Cajal developed some of the key concepts and much of the early evidence for the *Neuron Doctrine*—the principle that individual neurons are the elementary signaling elements of the nervous system [3,4].

Signals used by neurons are determined in part by the electrical properties of the cell membrane. At rest, all cells maintain a difference in the electrical potential through both sides of the membrane, known as resting membrane potential (in a typical mammalian neuron the electrical potential difference is about -65 mV [5,6]). The difference in electrical potential when the cell is at rest results from two factors: (1) the unequal distribution of electrically charged ions, in particular Na^+ and K^+ ions, and the negatively charged amino acids and proteins on either side of the cell membrane, and (2) the selective permeability of the membrane to mainly one of these ions, K^+, due to the selective ion channels. When the cell is at rest, there are many open K^+ channels and these ions tend to migrate from the inside outward powered by the potassium concentration gradient, leaving behind a cloud of unneutralized negative charge. Therefore, net charge inside the membrane is more negative than outside [7,8].

In excitable cells, such as nerve cells, the membrane potential can be significantly and quickly altered (becoming zero or even reversed), resulting in a signaling mechanism. When the membrane potential is reduced (depolarization), it becomes much more permeable to Na^+ than to K^+ thus, an influx of positively charged Na^+ ions tends to neutralize the negative charge inside the cell, resulting in an even greater reduction in membrane potential, which is called depolarization. The voltage change produced in one part of the axon, triggers the opening of channels in the next section of the axon, inducing an action potential, which is conducted down the cell's axon terminal. Hence, an action potential can be defined as a rapid and self-regenerating voltage

change, localized across the cell membrane, and which constitutes the electric signals used by the brain to receive, analyze, and convey information. Typically, an action potential lasts about one millisecond after which, the membrane returns to its resting state, with its normal separation of charges and higher permeability to K^+ than to Na^+.

The result of the action potential is the release of neurotransmitters (as glutamate, dopamine, γ-aminobutyric acid (GABA), nitric oxide, etc…) which can diffuse across the synaptic gap and bind to specific receptors in the membrane of the receiving neuron, executing the transmission of the signal (Figure 1.2).

Artificial neuron depolarization can be achieved by changing the K^+ concentration in the extracellular matrix (ECM) [2] in order to study the neurotransmitter release of the neuronal functionality.

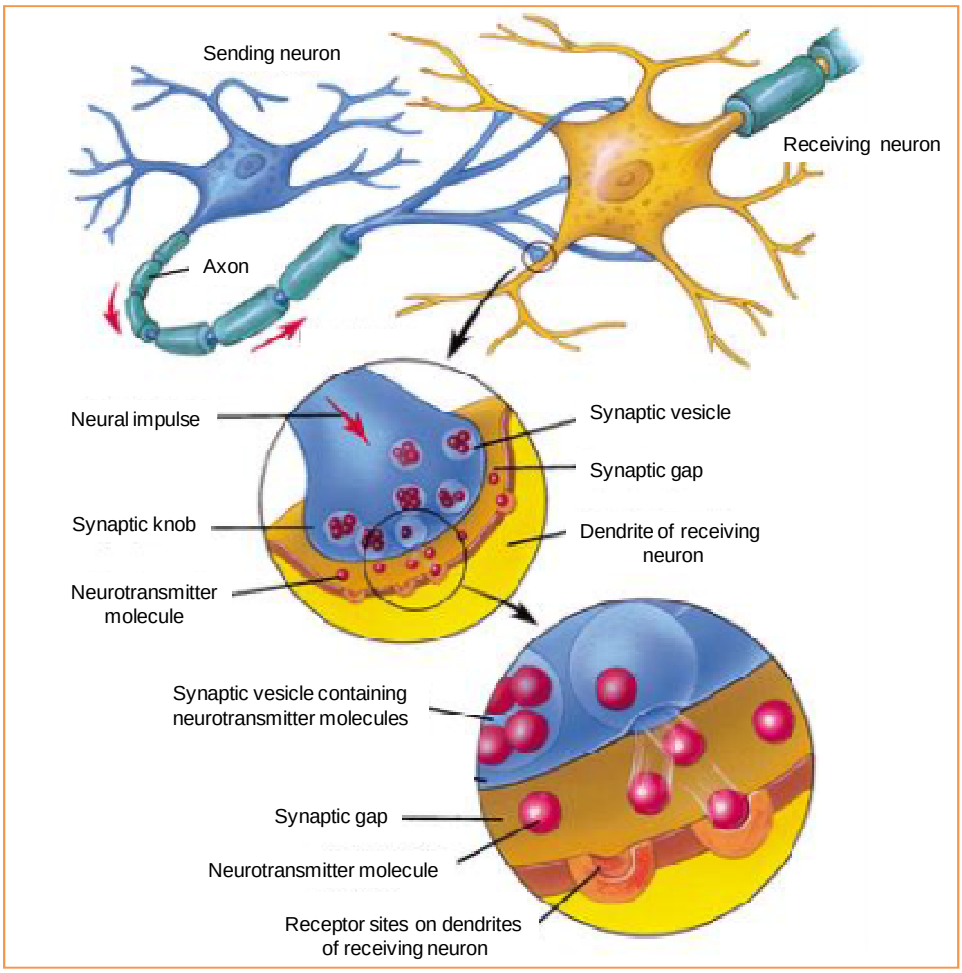

Figure 1.2. Schematic image of two neurons during synapse.

1.2.2 Stimulation Applications

The interest for devices used to electrically stimulate the central nervous system started more than a century ago, when in 1870, Fritsch and Hitzig demonstrated that cerebral cortex regions related with the voluntary movement, could be electrically stimulated in dogs [9]. Four years later, Bartholow found that similar stimulation could be also done in humans [10,11]. Nowadays, therapies based on this type of stimulation have received great interest, and numerous applications have been developed for diseases as epilepsy, depression or Parkinson among others [12-16].

Neural external depolarization can be achieved modulating the potassium concentration in the ECM, as mentioned above, or by induced ionic current flows produced by two or more electrodes in contact with nervous tissue. In both cases, ionic gradients can be transferred to the cell membrane due to passive (capacitive and resistive) membrane properties, as well as trough active ion channels. Therefore, by using electrodes it is possible to modify cells environment and to induce neuron response, which is the main aim of functional stimulation electrodes.

1.2.3 Growth and Modulation Applications

The existence of steady (direct current; DC) electrical signals within the extracellular spaces of plants, animals and humans has been known for centuries. However, bioelectricity has not received much attention by the scientific community, and just few potential uses of this phenomenon to modulate processes at cell scale have been reported, in contrast with the high number of stimulation protocols described. Nevertheless, crucial behaviors such as cell division, migration and differentiation take place within an extracellular milieu, in which standing voltage gradients persist for several hours, or even days [17]. The first experiments showing the relation between electrical control and cell physiological modulation was carried out by Galvani in the second half of 18^{th} century [18,19]. He achieved the induction of muscular movement in frog legs by applying an electric current directly on the peripheral nerves. With these experiments he also demonstrated the existence of an

endogenous electric field, the denominated “injury potential”. The injury potential is defined as a steady, long-lasting DC voltage gradient induced within the extracellular and intracellular spaces by current flowing, into and around an injured nerve [20]. It has been reported the hypothesis that this injury potential might impede regeneration and thus, the application of a DC EF to offset and reverse the polarity of this injury potential, would promote regeneration [21,22]. This statement is the basis of new research directions on this field, whose objectives are spinal-cord repair or neuronal migration, among others.

For example, these induced EFs in the neural environment can provoke the dendritic migration towards a particular direction. In the brain, axons and dendrites are guided by extracellular membrane molecules of other cells, which are recognized by membrane receptors of the own neuron [23]. This guidance is determinant for future synapse junctions, and it is important to induce new cellular connections after an injury. However, the influence of membrane guidance molecules to redirect dendrites is not observed after a lesion or *in vitro* experiments, as cells are dispersed and the contact is minimized. Having no possibility of artificial molecule immobilization, new techniques of guidance are necessary. In this sense, McCaig et al. have presented a work where Xenopus spinal cells from frogs are excited by an external electric field, as observed in Figure 1.3 [20,24]. He observed that neurons in absence of electric fields, point their dendrites randomly, having a circular dispersion (Fig 1.3.C). However, neurons exposed to a defined DC current during the growing step have a preferentially dendrite orientation to the cathode. Even, it can be observed how one growth cone crosses another neurite to migrate towards the cathode (Fig 1.3.E). Figure 1.3.F shows neurite paths curving dramatically towards the cathode, and in general, neurites extending faster cathodally than anodally. Also, the same work indicates that growth rates can be modulated by EF polarity thus, a voltage switching might promote growth in both directions. However, growth cones are attracted to or repelled by a cathode, depending on the nerve cell type, the substrate, and whether the process is axonal or dendritic.

Even though the results for mammalian cells could be different, this experiment clearly demonstrates that electric stimulation can be a very good candidate to modulate cell behavior.

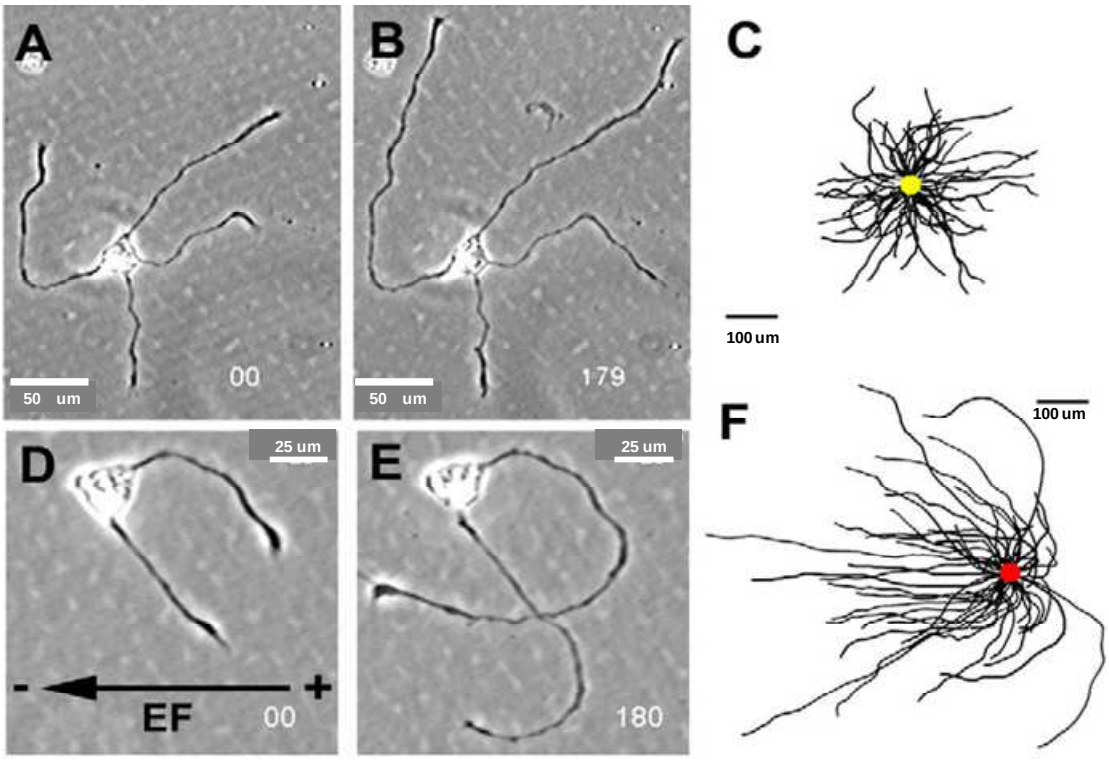

Figure 1.3. Time-elapsed experiment showing Xenopus spinal neurons grown in vitro, exposed to physiological EFs. Time (min) is shown in the lower right corner. A) and B) First and last frames from time-lapse sequences of growing neurons in the absence of EFs. C) Composite drawing, in which the cell bodies (yellow dot in centre) of several neurons have been superimposed to show the path of neurites outgrowth over 5 hours (no EF). D) and E) show the same neuron under the influence of a 150 mV/mm electric field (symbolize as a vector in the Figure D) at the beginning and after 3 hours of stimulation. F) Composite diagram for cells exposed to a 150 mV/mm EF for 5 hours. [From Reference 24]

1.2.4 Recording Applications

Recording applications are based on the endogenous extracellular potential, or action potential, which might be recorded as a signal that identifies the firing of a single neuron. Action potentials are recorded with microelectrodes implanted in close

proximity to the target neuron, and such neural recordings are the basis for design of prostheses that could provide cognitive control of external devices, to aid patients with paralysis [25,26]. Other recent application for this type of recording electrodes is the determination of the neuronal output of implanted stimulation electrodes [27].

1.3 Electrochemical Features of Neural Electrodes

The ideal material to be used as neural electrode has to accomplish mainly two characteristics. First, the material has to be biocompatible, to avoid damage in the adjacent tissue or inmuno response after the implant (as fibrosis, which provokes an increase in the electrode impedance). And secondly, the mechanism of charge injection once implanted has to be reversible, easily controlled and do not produce dangerous species during its use [28].

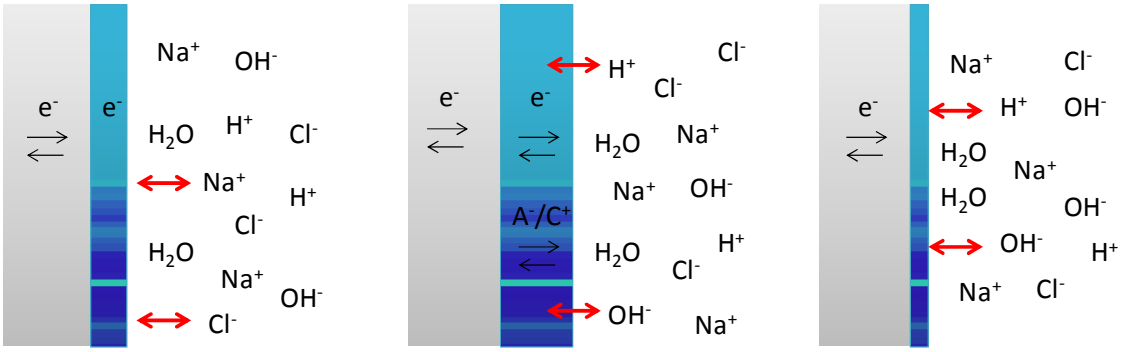

Figure 1.4 Examples of the different mechanisms for charge injection. A) Capacitive, B) three dimensional faradaic (pseudocapacitive), and C) faradaic (Pt) [From reference 29].

Charge injection at the electrode-electrolyte interface can be produced by two primary mechanisms. One is a non-faradaic reaction (capacitive) where no electrons are transferred in the interface and only a redistribution of charged chemical species

in the electrolyte occurs (electrical double layer). The second mechanism is a faradaic reaction, with electron transfers, resulting in reduction or oxidation of the chemical species in the interface. The mechanisms described are presented in the Figure 1.4.

During electrical stimulation of excitable tissue, like brain, it is desirable the development of materials with large reversible charge storage capacity (CSC), which is defined as the total amount of charge that may be stored reversibly, including storage in double layer capacitance, pseudocapacitance or any reversible faradaic reaction. The reversibility of CSC depends on the material selected for the electrode, the size and shape, the electrolyte composition and the electrical stimulation waveform used. Hence, these parameters would have to be optimized in order to get best electrochemical performance.

Capacitive charge injection mechanism can be considered as the best option for neural electrodes since no chemical species are created or consumed during stimulation pulses. However, the double layer charge per unit area at the interface material-electrolyte is small, and sufficient charge injection is only possible for porous coatings or high dielectric constant electrodes, which are a limitation in the use of this type of capacitive materials. An example of this type of materials is titanium nitride (TiN), which operates by charging and discharging the double-layer at the material-electrolyte interface. The TiN main advantages are the high biocompatibility and the wide safe potential limits (where irreversible reactions do not occur) however, its charge injection capacity is low when compared with other materials, as IrOx [30].

Emerging prostheses and therapies involving neural stimulation and recording electrodes frequently require charge-injection and impedance levels beyond the capabilities of noble metals [31]. High levels of charge are achieved using faradaic electrodes. However, the finite rate of faradaic reactions and the changes produced in the electrolyte can yield to irreversible reactions and radicals formation, which must be controlled. Among the most used faradaic charge injection materials are platinum (sometimes considered only capacitive) and iridium oxide.

In IrOx coatings, charge is injected from the electrode to the electrolyte by faradaic reduction and oxidation processes, which involves the iridium self-redox reaction between Ir (IV) and Ir (III) shown in Reaction 1.1. The product obtained in the electrochemical reaction remains bound to the electrode surface thus, the reactant may be easily recovered when current is reversed, avoiding the necessity of diffusion of electrochemically active molecules to the electrode surface. This type of behavior is known as pseudocapacity. Usually, to compensate the net charge in the material, ionic intercalation from the solution occurs in a reversible way, which presumably, does not affect the stability of the electrode. Therefore, pseudocapacity works as an electrochemical capacitor, preventing dissipative processes and enhancing the charge storage capacity [1].

$$2IrO_2 + 2H^+ + 2e^- \leftrightarrows Ir_2O_3 + H_2O \quad \textit{Reversible reduction of } IrO_2 \quad \text{(Reaction 1.1)}$$

Significantly, for IrOx it has been demonstrated that different preparation methods can influence the final charge storage capacity. For example, maximum values of 194 mC/cm^2 can be obtained for sputtered metallic iridium and subsequent oxidation to IrOx [32] in comparison with lower values of 25 mC/cm^2 for IrOx electrochemically synthesized presented by Cogan et al. [33]. However, not only CSC values change with the synthesis method, but other important electrode properties like thickness, porosity, hydration or even oxidation state of the metal, can be modified [34].

1.4 Electrochemically Synthesized Iridium Oxide (IrOx)

The extended use of iridium oxide as neural electrode is mainly due to the reproducible biocompatible behavior, the high electrochemical performance and the bio-stability shown in chronic stimulation, in comparison with other materials [35]. However, not only bio-applications have been described in literature, and other applications such as electrochromic displays [36,37], sensitive material in pH-sensors [38-40], catalyst [41-46] and supercapacitor devices [47] have been reported. All of them are based on the outstanding electrical, optical and electrochemical properties

that this material exhibits, as low resistivity at room temperature, considerable electrical conductivity due to the iridium mixed valence state, and high stability in acidic and basic solutions.

Depending on the synthesis method, different properties can be achieved, as previously mentioned. The abbreviations used to name the different types of IrOx correspond with the synthesis method: anodic or activated (AIROF), sputtered (SIROF), thermal (TIROF) and electrodeposited (EIROF) iridium oxide films.

In this work, electrochemically synthesized IrOx has been used as starting material for the new hybrids described. The advantages observed with this method of synthesis are numerous. First, the feasibility of thin film deposition in any specific surface or geometry (as the only substrate requirement is to be conductive), facilitates the preparation of microelectrodes, used in deep brain stimulation (DBS). Secondly, the formation of homogeneous and well adhered coatings is achieved, as well as an easy control of its thickness, by modulation of electrodeposition charge. Finally, the resulting hydrated and porous structure of the coatings is optimal to obtain high values of charge storage capacity.

1.5 Hybrids Based on IrOx

The stability of the neural electrodes in physiological fluids, especially in a chronic use, is critical for the success of an implantable electrode for bio-applications. In fact, poor adhesion to underlying substrates and delamination under *in vivo* experiments have been reported as the main problems observed for this type of electrodes, since these inconveniences may cause tissue damage and aggravate inflammatory responses [48,49].

Another typical problem for neural electrodes is tissue damage caused by *in situ* implantation. This surgical trauma caused by electrode implantation, can be minimized by using microelectrodes, although impedance increases as decreasing in size, which is not desirable in recording or stimulation applications. Thus, the

possibility to modulate and optimize the electrode size, depending on the application, is an important issue to consider in practical uses.

The stimulation waveform used during charge injection is also an important parameter to minimize electrode or tissue damage. This topic will not be treated deeply in this thesis, but it is worth mentioning the necessity of electrochemical reversibility in most of the stimulation protocols: all processes occurring at the electrode after the application of a current pulse have to be reversed by a second current pulse of opposite polarity in many instances. For this reason, it is important the use of materials with large CSC and reversible charge injection capacity (Q_{inj}), defined as the total amount of charge per unit of area which may be injected in the electrolyte without damaging the electrodes [29].

In principle, IrOx fulfills all these requirements, not only because of its biocompatibility or the possibility to coat microelectrodes, but for the good electrochemical properties as electrode. However, the observed mechanical stability for IrOx after long-term cycling is not reproducible, as reported in literature [48,49]. Physical properties as density, roughness or thickness, can be optimized to increase the stability**,** and for example, it has been demonstrated that thinner films are more resistant. However, reducing the thickness, the CSC also decreases.

The aim to achieve new materials with improved mechanical and electrochemical (CSC and Q_{inj}) properties is the basis of the proposed hybrid synthesis based on IrOx.

1.5.1 Carbon Nanotubes (CNTs) and Other Carbon Species

Since in 1952 Radushkevich and Lukyanovich published the first images of carbon tubes of 50 nm of diameter [50], numerous attempts to synthesize and characterize these carbonaceous materials have been carried out. However, the official preparation of CNTs is attributed to Iijima, who in 1991 presented his results in Nature Letters [51]. Due to its exceptional characteristics, CNTs have been extensively used by researchers in fields such as chemistry, physics, materials science and electrical engineering. In bio-applications, carbon nanotubes have emerged as an

alternative to the usual TiN, Pt, IrOx or alloys for neural electrodes, as the high electrochemical surface area, inherent to the nanotube structure, gives rise to a large double-layer charge capacity. On the other hand, the addition of a small amount of conductive CNTs to an insulating matrix, results in nanocomposites with highly enhanced electrical conductivity [52]. The critical content of CNTs that characterizes a drastic increase in conductivity is commonly termed as the electrical percolation threshold. For carbon nanotubes, this percolation threshold is lower than the observed for other common conductive fillers as carbon black [53,54]. These outstanding mechanical, thermal and conductive properties have been decisive to study the CNTs incorporation in the iridium oxide matrix.

Multi-walled carbon nanotubes (MWCNTs) are normally used in initial tests due to easier availability. However, single-walled CNTs (SWCNTs) present higher curvatures and small diameters and therefore, are predicted to produce larger strength, better suiting for composites, as the hybrids studied.

Many examples of bio-related applications of carbon nanotubes are reported in literature [55], and particularly as neural electrodes [56,57]. The use of CNTs and derivatives, has achieved results as the promotion of neuron differentiation [58], the stimulation of neurite outgrowth [59], the improvement of neural performance [60] and recording [56], the boost of neural electrical signal [61], and as substrates for neural growth [62-64].

Despite all bio-applications, the toxicity of CNTs has not been well contrasted [65] and biocompatibility has been highly questioned, mainly for two considerations: due to the size, since nanotubes are capable to get into the cytoplasm, causing several damages and the final death of the cells [66] and due to the metal impurities that the synthesis method involves, which can reach cytotoxic levels [67,68]. This last issue has been minimized in the last years, improving the synthesis and purification techniques [69]. On the other hand, apoptosis due to CNTs incorporation to the cell´s interior is completely avoided in the IrOx-CNTs hybrid presented in this work, as IrOx coats the CNTs, which in turn, form a very stable scaffold for the oxide.

For these reasons, the combination of both materials is expected to yield self-standing electrodes that can be used in biological electrostimulation, recording or as electroactive support for cell development [56].

However, these types of materials are not only used in bio-applications, and other oxide-CNTs nanocomposites have been reported in the literature, mainly as electrodes for supercapacitors, or in order to improve mechanical properties in ceramic materials [70]. For example, hydrous manganese oxide-carbon nanotubes nanocomposites have been obtained for electrochemical capacitators, showing a considerably enhanced capacitance in comparison with bare manganese oxide [71]. This improvement is correlated with the reduction of electronic resistivity and the increase of the electrode porosity. Also mechanical properties, as stiffness, can be improved with the addition of carbon nanotubes to zirconium oxide [72]. In parallel with our work, IrOx-MWCNTs nanocomposites have also been synthesized by Chen et al. using chemical vapor deposition (CVD) or sputtering. The aim was obtaining suitable electrodes for supercapacitors, with increased specific capacitance and reduced resistance, in comparison with bare IrO_2 or pristine MWCNTs [73,74]. A considerable improvement of the oxide properties after the CNTs incorporation has been achieved in all of the examples shown above, indicating the good perspectives for these hybrids materials.

In this thesis, a biocompatible IrOx-CNTs hybrid has been electrochemically synthesized, to future application as neural electrodes. But also, the synthesis of IrOx hybrids with other carbonaceous species, as graphite and graphene, has been performed. IrOx-graphite and IrOx-graphene hybrids are expected to have similar biocompatibility as observed with CNTs, due to the likeness of their chemical composition [75-77]. The exceptional electric and electrochemical properties of these carbon species have been also widely reported [78,79], and stand out the promising results in the synthesis of IrOx-graphite and IrOx-graphene hybrids.

In particular, numerous applications for graphene have been reported in different fields as sensing, energy storage, microelectronic or bioapplications, among others [80], due to the outstanding mechanical, electrical and chemical properties, as well as

the easily functionalization of the surface, which would modulate the future device performance. For example, N-doping of carbonaceous species has been demonstrated to improve electric conductivity and/or biocompatibility [81].

1.5.2 PEDOT and SWCNTs

Conducting polymers have been presented as a possible alternative for IrOx and Pt stimulation electrodes. Advantages over metal electrodes include modulated biocompatibility, regulation of charge injection by modifying the dopant, lower electrode impedance in some cases, and the fact that inherent polymer flexibility makes it a good candidate for soft tissue implantation. In addition, the possibility of chemical surface modification with physiologically active species has been a goal for the promotion of these materials. Polypyrrol (Ppy), polythiophene and their derivatives, as poly(ethylenedioxythiophene) (PEDOT), have been widely used as electrodes due to the high biocompatibility and the easy electrochemical polymerization onto neural probes from aqueous solutions [82-85]. Even, direct electropolimerization of PEDOT around living neural cells has been achieved, with high cellular survival [86]. However, the limitation of conductive-polymer coatings used as neural electrodes has been the irreproducible results and the unsatisfactory long-term stability in chronic electrical stimulation. This reduced performance of polymeric electrodes is due to cracks formation and delamination of thicker films, as it has been reported [87,88].

The doping of PEDOT is necessary for the polymer synthesis, and this anionic dopant will be relevant for final electronic conductivity and charge injection properties. Most of the studies to date employ surfactants like poly(styrene sulphonate) (PSS) as dopant, which is incorporated within the polymer structure during the electrochemical process, forming a charge transfer complex that results in the oxidation of the monomer, leading to an increase of the electronic conductivity of the polymer. However, other authors as well as the results obtained in our group, agree that these surfactants increase the toxicity in cell cultures, and neural development is only achieved with growth factors [89,90].

Composites of polymer-CNTs have been reported in literature, and most of them with the aim of obtaining low-weight nanocomposites of extraordinary mechanical, electrical, thermal and multifunctional properties [91-93]. Even PEDOT-CNTs or polypyrrol-CNTs (PPY-CNTs) materials have been previously proposed as chronic neural stimulation electrodes, showing good results in stability and *in vitro* cell survival, demonstrating the promising properties of this type of composites [94,95].

In this thesis, PEDOT has been considered as the most suitable conducting polymer due to its ordered and well-defined chemical structure, which offers a steady conduction and stability. With the aim to improve electrochemical performance, long-term stability of PEDOT coatings during chronic electrical stimulation, and possible damages in the electrodes due to the cracks formation [88], polymer has been doped with carbon nanotubes and IrOx particles. The simple electrochemical synthesis, allows obtaining hybrid thin films, with good adherence and stability. In our research group, nanocomposite particles of conducting polymer-IrOx hybrid have been reported [96]. The chemical oxidation used for that synthesis, yielded to IrOx particles encapsulated by the polymer, but the impossibility shown to obtaining self-standing coatings, reduces possible application as electrodes.

1.6 Specific Objectives

- Study of the alkaline pre-deposition solutions of $IrCl_3$ with and without oxalate, and the electrochemical synthesis procedure to better understand the solid formation mechanism and the final composition and properties of the starting material of the new hybrids, the IrOx.

- Electrochemical synthesis, optimization and fully characterization of IrOx-CNTs hybrids obtained.

- Synthesis of IrOx hybrids with other types of carbonaceous species: graphite, graphene and N-doped graphene.

- Synthesis of IrOx-PEDOT-CNTs, optimization and complete characterization of the new polymeric hybrid.

- Electrochemical evaluation of the different coatings to determine the feasibility as electrodes in physiological conditions.

- Evaluation of the biocompatibility and the toxicity of the novel hybrid materials, studying the cell growth and development onto them, as well as the neuronal functionality and response to external stimulus.

1.7 References

-[1] Arle J.E. and Shils J. L. Essential Neuromodulation. Elsevier Inc. (1st edition). 2011.

-[2] Kandel E.R., Schwartz J.H. and Jessell T.M. Principles of Neural Science. McGrawhill (4th edition). 2000.

-[3] Llinás R.R. The contribution of Santiago Ramón y Cajal to functional neuroscience. *Nat. Rev. Neurosci*. **4**, 77-80. 2003.

-[4] Ramon y Cajal S. Recollections of my life. MIT Press. (1st edition). 1989.

-[5] Stuart G., Spruston N., Häusser M., et al. Action potential initiation and backpropagation in neurons of the mammalian CNS. *Trends Neurosci*. **20**, 125–131. 1997.

-[6] Llinás R. R. The intrinsic electrophysiological properties of mammalian neurons: Insights into central nervous system function. *Science.* **242**, 1654-1664. 1988.

-[7] Lodish H., Berk A., Kaiser C.A., et al. Molecular Cell Biology. W. H. Freeman (7th edition). 2012.

-[8] Nelson D.L. and Cox M.M. Lehninger Principles of Biochemistry. W. H. Freeman (4th edition). 2004.

-[9] Gross C.G. The discovery of motor cortex and its background. *Journal of the History of the Neurosciences*. **16**, 320–331. 2007.

-[10] Bartholow, R. Experimental investigations into the functions of the human brain. *Am. J. Med . Sci*. **67**, 305-313. 1874.

-[11] Harris L.J. and Almerigi J.B. Probing the human brain with stimulating electrodes: The story of Roberts Bartholow's (1874) experiment on Mary Rafferty. *Brain and Cognition*. **70**, 92–115. 2009.

-[12] Li Y. and Mogul D.J. Electrical control of epileptic seizures. *J. Clin. Neurophysiol.* **24**, No.2, 197–204. 2007.

-[13] Perlmutter J.S. and Mink J.W. Deep brain stimulation. *Annu. Rev. Neurosci.* **29**, 229–257. 2006.

-[14] Jezernik S., Craggs M., Rijkhoff N.J., et al. Electrical stimulation for the treatment of bladder dysfunction: current status and future possibilities. *Neurol. Res.* **24**, No.5, 413–430. 2002.

-[15]. Hoffer J.A., Stein R.B., Durfee W.K., et al. Neural signals for command control and feedback in functional neuromuscular stimulation: a review. *J. Rehabil. Res. Dev.* **33**, No.2, 145–157. 1996.

-[16] Limousin P., Krack P., Benabid A.L. et al. Electrical stimulation of the subthalamic nucleus in advanced Parkinson's disease. *The New England Journal of Medicine.* **339,** No.16, 1105-1111. 1998.

-[17] Levin M. Large-scale biophysics: ion flows and regeneration. *Trends in Cell Biol.* **17**, No.6, 261-270. 2007.

-[180] Piccolino M. Luigi Galvani and animal electricity: two centuries after the foundation of electrophysiology. *Trends Neurosci*. **20**, No.10, 443–448. 1997.

-[19] Geddes L.A. and Hoff H.E. The discovery of bioelectricity and current electricity, The Galvani-Volta controversy. *IEEE Spectrum*. **8**, No.12. 1971.

-[20] McCaig C.D., Rajnicek A.M, Zhao M. et al. Controlling cell behavior electrically: current views and future potential. *Physiol. Rev.* **85,** 943–978. 2005.

-[21] Borgens R.B., Roederer E. and Cohen M.J. Enhanced spinal cord regeneration in lamprey by applied electric fields. *Science*. **213**, 611-617. 1981.

-[22] Shapiro S.,Borgens R., Nelson P., et al. Oscillating field stimulation for complete spinal cord injury in humans: a Phase 1 trial. *J. Neurosurg. Spine*. **2,** 3–10. 2005.

-[23] Kim S. and Chiba A. Dendritic guidance. *Trends Neurosci*. **27**, No.4, 1947-202. 2004.

-[24] McCaig C.D., Song B. and Rajnicek A.M. Electrical dimensions in cell science. *J. Cell Sci.* **122**, 4267-4276. 2009.

-[25] Lebedev M.A. and Nicolelis M.A. Brain-machine interfaces: past, present and future. *Trends in Neurosci*. **29**, No.9, 536-546. 2006.

-[26] Donoghue J.P. Connecting cortex to machine: recent advantages in brain interfaces. *Nat. Neurosci*. **5**, 1085-1088. 2002.

-[27] McCreery D., Lossinsky A., Liu X., et al. Microelectrode array for chronic deep-brain microstimulation and recording. *IEEE Trans. Biomed. Eng*. **53**, No.4. 726-737. 2006.

-[28] Beebe X. and Rose T.L. Charge injection limits of activated iridium oxide electrodes with 0.2 ms pulses in bicarbonate buffered saline. *IEEE Trans. Biomed. Eng*. **35**, No.6. 1988.

-[29] Cogan S.F. Neural stimulation and recording electrodes. *Annu. Rev. Biomed. Eng.* **10**, 275-309. 2008.

-[30] Weiland J.D., Anderson D.J. and Humayun M.S. *In vitro* electrical properties for iridium oxide versus titanium nitride stimulating electrodes. *IEEE Trans. Biomed. Eng*. **49**, No.12, 1574-1579. 2002

-[31] Cogan S.F., Plante T.D. and Ehrlich J. Sputtered iridium oxide films (SIROFs) for low-impedance neural stimulation and recording electrodes. *Conf. Proc. IEEE Eng. Med. Biol. Soc*. **6**, 4153-4156. 2004.

-[32] Cogan S.F., Ehrlich J., Rizzo J.F., et al. Sputtered iridium oxide for neural stimulation electrodes. *J. Biomed. Mater. Res. B Appl. Biomater*. **89**, No.2, 353-61. 2009.

-[33] Meyer R.D., Cogan S.F., Rauh R.D., et al. Electrodeposited iridium oxide for neural stimulation and recording electrodes. *IEEE Trans. Neural. Syst. Rehabil. Eng*. **9**, No.1, 2-11. 2001.

-[34] Belova I.D., Varlamova T.V., Sevostyanov M.A., et al. The composition, structure and electronic properties of thermally prepared iridium dioxide films. *Mater. Chem. Phys*. **20**, 39-64. 1988.

-[35] Agnew W.F., Yuen T.G.H., Bullara L.A., et al. Histopathologic evaluation of prolonged intracortical electrical stimulation. *Exp. Neurol*. **92**, 162-185. 1986.

-[36] Patil P.S., Mujawar S.H., Inamdar A.I., et al. Effect of film thickness on electrochromic activity of spray deposited iridium oxide thin films. *Mater. Chem. Phys*. **99**, 309–313. 2006.

-[37] Nishio K., Watanabe Y. and Tsuchiya. Preparation and properties of electrochromic iridium oxide thin film by sol-gel process. *Thin Solid Films*. **350**, 96-100. 1999.

-[38] Marzouk S.A.M. Improved electrodeposited iridium oxide pH sensor fabricated on etched titanium substrates. *Anal. Chem*. **75**, 1258-1266. 2003.

-[39] Olthuis W., Van Kerkhof J.C. and Bergveld P. Preparation of iridium oxide and its application in sensor-actuator systems. *Sens. Actuators B*. **4**, 151-156. 1991.

-[40] Elsen H.A., Monson C.F. and Majda M. Effects of electrodeposition conditions and protocol on the properties of iridium oxide pH sensor electrodes. *J. Electrochem. Soc*. **156**, No.1, F1-F6. 2009.

-[41] Gottesfeld S. and Srinivasan S. Electrochemical and optical studies of thick oxide layers on iridium and their electrocatalytic activities for the oxygen evolution reaction. *J. Electroanal. Chem*. **86**, 89-104. 1978.

-[42] Zhao Y., Hernandez-Pagan E.A., Mallouk T.E., et al. A high yield synthesis of ligand-free iridium oxide nanoparticles with high electrocatalytic activity. *J. Phys. Chem. Lett*. **2**, 402–406. 2011.

-[43] Yagi M., Tomita E. and Kuwabara T. Remarkably high activity of electrodeposited IrO_2 film for electrocatalytic water oxidation*. J. Electroanal. Chem*. **579**, 83–88. 2005.

-[44] Harriman A., Nahor G.S., Neta P., et al. Iridium oxide hydrosols as catalysts for the decay of zinc porphyrin radical cations in water*. J. Chem. Soc., Faraday Trans. 1*. **84**, No.8, 2821-2829. 1988.

-[45] Nakagawa T., Beasley C.A. and Murray R.W. Efficient electro-oxidation of water near its reversible potential by a esoporous IrOx nanoparticle film*. J. Phys. Chem. C.* **113**, 12958-12961. 2009.

-[46] Yagi M., Tomita E., Nagai K., et al. Self-assembly of active IrO_2 colloid catalyst on an ITO electrode for efficient electrochemical water oxidation. *J. Phys. Chem. B*. **109**, 21489-21491. 2005.

-[47] Liu D.Q., Yu S.H., Joo S.K., et al. Electrochemical performance of iridium oxide thin film for supercapacitor prepared by radio frequency magnetron sputtering method. *ECS Trans*. **16**, No.1, 103-109. 2008.

-[48] Cogan S.F., Guzelian A.A., McCreery D.B., et al. Over-pulsing degrades activated iridium oxide films used for intracortical neural stimulation. *J. Neurosci. Methods*. **137**, 141–150. 2004.

-[49] Negi S., Bhandari R., Solzbacher F., et al. Neural electrode degradation from continuous electrical stimulation: Comparison of sputtered and activated iridium oxide. *J. Neurosci. Methods*. **186**, 8–17. 2010.

-[50] Radushkevich L.V. and Lukyanovich V.M. O strukture ugleroda, obrazujucegosja pri termiceskom razlozenii okisi ugleroda na zeleznom kontakte. *Zurn Fisic Chim*. **26**, 88-95. 1952.

-[51] Ijima S. Helical microtubules of graphitic carbon. *Nature*. **354**, 56-58. 1991.

-[52] Seo M-K., Lee J-R. and Park S-J. Crystallization kinetics and interfacial behaviors of polypropylene composites reinforced with multi-walled carbon nanotubes. *Mater. Sci. Eng. A*. **404**, 79-84. 2005.

-[53] Li J., Ma P.C., Kim J.K., et al. Correlations between percolation threshold, dispersion state, and aspect ratio of carbon nanotubes. *Adv. Funct. Mater*. **17**, 3207–3215. 2007.

-[54] Zeng X., Xu X., Zhao Y., et al. Characteristics of the electrical percolation in carbon nanotubes/polymer nanocomposites. *J. Phys. Chem. C.* 115, No.44, 21685–21690. 2011.

-[55] Lu F., Gu L., Sun Y-P., et al. Advances in bioapplications of carbon nanotubes. *Adv. Mater*. **21**, 139–152. 2009.

-[56] Keefer E.W., Botterman B.R., Gross G.W., et al. Carbon nanotube coating improves neuronal recordings. *Nat. Nanotechnol*. **3**, 434-439. 2008.

-[57] Wang K., Fishman H.A., Harris J.S., et al. Neural Stimulation with a Carbon Nanotube Microelectrode Array. *Nano Lett*. **6**, No.9, 2043-2048. 2006.

-[58] Chao T-I., Xiang S., Lu J., et al. Carbon nanotubes promote neuron differentiation from human embryonic stem cells. *Biochem. Biophys. Res. Commun*. **384**, No.4, 426-30. 2009.

-[59] Matsumoto K., Sato C., Shimizu N., et al. Stimulation of neuronal neurite outgrowth using functionalized carbon nanotubes. *Nanotechnology*. **21**, 1-8. 2010.

-[60] Cellot G., Cilia E., Ballerini L., et al. Carbon nanotubes might improve neuronal performance by favouring electrical shortcuts. *Nat. Nanotechnol*. **4**, 126-133. 2009.

-[61] Lovat V., Pantarotto D., Ballerini L., et al. Carbon Nanotube Substrates Boost Neuronal Electrical Signaling. *Nano Lett*. **5**, No.6, 1107-1110. 2005.

-[62] Mattson M.P., Haddon R.C. and Rao A.M. Molecular functionalization of carbon nanotubes and use as substrates for neuronal growth. *J. Mol. Neurosci*. **14**, 175-182. 2000.

-[63] Hu H., Ni Y., Parpura V., et al. Polyethyleneimine Functionalized Single-Walled Carbon Nanotubes as a Substrate for Neuronal Growth. *J. Phys. Chem. B*. **109**, No.10, 4285-4289. 2005.

-[64] Hu H., Ni Y., Parpura V., et al. Chemically functionalized carbon nanotubes as substrates for neuronal growth. *Nano Lett*. **4**, No.3, 507–511. 2004.

-[65] Smart S.K., Cassady A.L., Martin D.J., et al. The biocompatibility of carbon nanotubes. *Carbon*. **44**, 1034–1047. 2006.

-[66] Porter A.E., Gass M., Welland M., et al. Direct imaging of single-walled carbon nanotubes in cells. *Nat. Nanotechnol*. **2**, 713-717. 2007.

-[67] Lacerda L., Bianco A., Kostarelos K., et al. Carbon nanotubes as nanomedicines: From toxicology to pharmacology. *Adv. Drug Delivery Rev*. **58**, 1460–1470. 2006.

-[68] Patiolla A., Knighten B. and Tchounwou P. Multi-walled carbon nanotubes induce cytotoxicity, genotoxicity and apoptosis in normal human dermal fibroblast cells. *Ethn. Dis*. **20**, 65-72. 2010.

-[69] Tobias G., Shao L., Green, M.L.H., et al. Purification and Opening of Carbon Nanotubes Using Steam. *J. Phys. Chem. B*. **110**, 22318-22322. 2006.

-[70] Zhang W-D., Xu B. and Jiang L-C. Functional hybrid material based on carbon nanotubes and metal oxides. *J. Mater. Chem*. **20**, 6383-6391. 2010.

-[71] Zhou Y.K., He B.L., Li H.L., et al. Hydrous manganese oxide/carbon nanotube composite electrodes for electrochemical capacitors. *J. Solid State Electrochem*. **8**, 482-487. 2004.

-[72] Lupo F., Kamalakaran R., Rühle M., et al. Microstructural investigations on zirconium oxide–carbon nanotube composites synthesized by hydrothermal crystallization. *Carbon*. **42**, 1995–1999. 2004.

-[73] Chen Y-M., Cai J-H., Tsai D.S., et al. Preparation and characterization of iridium dioxide-carbon nanotube nanocomposite for supercapacitors. *Nanotechnology*. **22**, 115706 (7pp). 2011.

-[74] Chen Y-M., Cai J-H., Tiong K-K., et al. A nanostructured electrode of IrOx foil on the carbon nanotubes for supercapacitors. *Nanotechnology*. **22**, 355708 (7pp). 2011.

-[75] Kenner G.H., Williams W.S., Lovell J.E. et al. Two-year biocompatibility study of ORNL graphite. *J. Biomed. Mater. Res. Symposium*. **6**, 67-72. 1975.

-[76] Pinto A.M., Gonçalves I. and Magalhaes F.D. Graphene-based materials biocompatibility: A review. *Colloids Surf. B*. **111**, 188– 202. 2013.

-[77] Wang K., Ruan J., Cui D., et al. Biocompatibility of graphene oxide. *Nanoscale Res. Lett.* **6**, No.8, 1-8. 2011.

-[78] Castro-Neto A.H., Guinea F., Geim A.K., et al. The electronic properties of graphene. *Rev. Mod. Phys*. **8**1, No.1, 109-162. 2009.

-[79] Primak W. and Fuchs L.H. Electrical conductivities of natural graphite crystals. *Phys. Rev*. **95**, No.1, 22-30. 1954.

-[80] Geim A.K. and Novoselov K.S. The rise of graphene. *Nat. Mat*. **6**, 183-191. 2007.

-[81] Carrero-Sánchez J.C., Elías A.L., Terrones M., et al. Biocompatibility and toxicological studies of carbon nanotubes doped with nitrogen. *Nano Lett*. **6**, No.8, 1609-1616. 2006.

-[82] Xiao Y., Cui X., Martin D.C., et al. Electrochemical polymerization of poly(hydroxymethylated-3,4-ethylenedioxythiophene) (PEDOT-MeOH) on multichannel neural probes. *Sens. Actuators B*. **99**, 437–443. 2004.

-[83] Abidian M.R., Ludwig K.A., Kipke D.R., et al. Interfacing Conducting polymer nanotubes with the central nervous system: chronic neural recording using poly(3,4-ethylenedioxythiophene) nanotubes. *Adv. Mater*. **21**, 3764–3770. 2009.

-[84] Cui X., Hetke J.K., Martin D.C., et al. Electrochemical deposition and characterization of conducting polymer polypyrrole/PSS on multichannel neural probes. *Sens. Actuators A*. **93**, 8-18. 2001.

-[85] Cui X. and Martin D.C. Electrochemical deposition and characterization of poly(3,4-ethylenedioxythiophene) on neural microelectrode arrays. *Sens. Actuators B*. **89**, 92-102. 2003.

-[86] Richardson-Burns S.M., Hendricks J.L., Martin D.C., et al. Polymerization of the conducting polymer poly(3,4-ethylenedioxythiophene) (PEDOT) around living neural cells. *Biomaterials*. **28,** No.8, 1539–1552. 2007.

-[87] Jan E., Hendricks J.L., Kotov N.A., et al. Layered carbon nanotube-polyelectrolyte electrodes outperform traditional neural interface materials. *Nano Lett*., **9**, No.12, 4012-4018. 2009.

-[88] Cui X.T. and Zhou D.D. Poly(3,4-ethylenedioxythiophene) for chronic neural stimulation. *IEEE Trans. Neural Syst. Rehabil. Eng.* **15**, No.4, 502-508. 2007.

-[89] Collazos-Castro J.E., Polo J.L., García-Rama C. et al. Bioelectrochemical control of neural cell development on conducting polymers. *Biomaterials*. **31**, No.35, 9244-9255. 2010.

-[90] Moral-Vico J. Materiales electroactivos poliméricos e híbridos como sustrato de crecimiento neuronal. Ph.D Thesis, Universidad Autónoma de Barcelona, Spain. 2012.

-[91] Bhandari S., Deepa M., Kant R., et al. Poly(3,4-ethylenedioxythiophene)-multiwalled carbon nanotube composite films: structure-directed amplified electrochromic response and improved redox activity. *J. Phys. Chem. B*. **113**, 9416–9428. 2009.

-[92] Byrne M.T. and Gun'ko Y.K. Recent advances in research on carbon nanotube-polymer composites. *Adv. Mater*. **22**, 1672–1688. 2010.

-[93] Zou J., Tran B., Zhai L., et al. Transparent carbon nanotube/poly(3,4-ethylenedioxythiophene) composite electrical conductors. *Soft Mater*. **7**, No.4, 355–365. 2009.

-[94] Luo X., Weaver C.L., Cui X.T, et al. Highly stable carbon nanotube doped poly(3,4-ethylenedioxythiophene) for chronic neural stimulation. *Biomaterials*. **32**, 5551-5557. 2011.

-[95] Lu, Y., Li, T. Duan Y.Y., et al. Electrodeposited polypyrrole/carbon nanotubes composite films electrodes for neural interfaces. *Biomaterials*. **31**, 5169-5181. 2010.

-[96] Moral-Vico J., Sánchez-Redondo S., Casañ-Pastor N., et al. Nanocomposites of iridium oxide and conducting polymers as electroactive phase in biological media. *Acta Biomater*. **10**, 2177-2186. 2014.

Chapter 2

Materials and Methods

In this second chapter the different experimental techniques used during the development of this thesis are introduced.

First, a brief explanation of the synthesis methods and the corresponding equipment used for all the samples preparation are enumerated.

Secondly, a description of the characterization techniques is presented. The main objective of these techniques is to study the formation of the coatings and the final properties; analyzing the chemical composition, the microstructure and the physical properties, as well as the conductivity or the electrochemical performance.

Finally, the biological-related experiments are exposed. Mainly, studies of development and viability of cellular cultures, biocompatibility of the materials and functionality of the grown neurons onto the substrates.

2.1 Pre-deposition Solutions Preparation

The synthesis of materials as electrodeposited coatings entails the previous preparation of a pre-deposition solution. For IrOx-based solutions, the preparation procedure requires aging during at least 4 days due to the slow hydrolysis observed. Once prepared, these solutions are stable during few months. Polymeric pre-deposition solutions are also described.

2.1.1 IrOx With and Without Oxalate Using K_2CO_3

The preparation of IrOx pre-deposition solutions has been done following the protocol reported by Cruz et al. [1], a modification of that first reported by Petit et al. [2]. A solution 4 mM of iridium (III) chloride ($IrCl_3 \cdot xH_2O$, Sigma-Aldrich, 206245 reg) in 50 mL of milliQ water is prepared. Then, oxalic acid ($H_2C_2O_4 \cdot 2H_2O$, Sigma-Aldrich, 99%) is added up to a concentration of 20 mM and finally, the addition of potassium carbonate (K_2CO_3, Pro-bys, 99%) up to 0.1 M is necessary to adjust the pH to 10. The solution prepared under these conditions, is aged during 4 days at 37ºC in an incubator and then kept in refrigeration until use. To prepare the non-oxalate pre-deposition solution, the steps are the same but without addition of oxalic acid.

2.1.1.1 IrOx With and Without Oxalate Prepared in Na_2CO_3 Buffer

IrOx with and without oxalate pre-deposition solutions in Na^+ media were prepared following the protocol described above, but using 0.1 M of Na_2CO_3 (Panreac, 99%) instead of potassium carbonate.

2.1.1.2 IrOx With and Without Oxalate Prepared in KOH Buffer

IrOx with and without oxalate pre-deposition solutions were prepared following the protocol described for IrOx, but using 0.01 M KOH (LabKem, 85%) instead of potassium carbonate.

2.1.2 IrOx-CNTs

IrOx-CNTs pre-deposition solutions were prepared sonicating 5.5 mg/mL of functionalized single-walled carbon nanotubes (SWCNTs-COOH, <90%, D 1-2 n, L 5-30 µm; Nanostructured & Amorphous Materials, Inc.) in 10 mL of milliQ water during 30 minutes. The certificate of analysis declares a COOH content of 2.59-2.87% thus, the final concentration of COOH groups is ~0.33 mM). Once the CNTs suspension was stable and totally black, $IrCl_3 \cdot xH_2O$ (Sigma-Aldrich, 206245 reg) was added until a final concentration of 8 mM and sonicated for 30 minutes. Finally the pH is adjusted to 10 with K_2CO_3 (Pro-bys, 99%) and the resulting solution is aged in an incubator during 7 days at 37ºC. After aging, the solution was kept at 4ºC until use.

2.1.3 IrOx-PEDOT-CNTs (IPC)

In order to prepare IrOx-PEDOT-CNTs pre-deposition solutions, 3,4-Ethylenedioxythiophene (EDOT, Sigma-Aldrich, 97%) is added to the IrOx-CNTs pre-deposition solution (10 mL), with final concentration of 0.03 M. To assist the electro-synthesis of PEDOT it is necessary to neutralize the media, so oxalic acid (Sigma-Aldrich, 99%) is added to achieve pH 8.

2.1.3.1 PEDOT-Ref. This sample has been synthesized as blank to compare compositional differences with IPC coatings. The pre-deposition solution is prepared by adding 0.03 M EDOT (Sigma-Aldrich, 97%), 0.01 M of K_2CO_3 (Pro-bys, 99%) and $H_2C_2O_4 \cdot 2H_2O$ (Sigma-Aldrich, 99%) until pH 8.

2.1.4. PEDOT-PSS. Pre-deposition solutions for PEDOT-PSS synthesis have been prepared following the protocol described by Moral [3]. A solution 0.12 M of poly(sodium-4-styrenesulfonate), (PSS, Sigma-Aldrich, M_w ~ 70000) and 0.03 M EDOT (Sigma-Aldrich, 97%) in 60 mL of milliQ water was stirred during 1 hour, just prior deposition.

2.1.5 IrOx-Graphite

To prepare the IrOx-Graphite pre-deposition solutions, the same procedure to that used in IrOx-CNTs preparation was followed, but adding 5.5 mg/mL of graphite-COOH instead of functionalized carbon nanotubes.

The first step was to oxidize kish graphite coarse powder (100 mesh, 0.15 mm) provided by Nanomagnetics Ltd, following the method described in the article of G. Tobias et al. [4] by treating the graphite with nitric acid (HNO_3, Fisher Chemical, 65%). Around 200 mg of graphite was added to a round-bottomed flask with 100 mL of 3 M HNO_3 and refluxed at 130ºC during 45 hours in order to ensure the mild oxidation. Then, the mixture was filtered with a 0.2 μm Millipore polycarbonate membrane and rinsed with distilled water until pH=7. The black powder is then dried in air. Quantification of functional groups was performed by X-Ray Photoelectron Spectroscopy (XPS) on pre- and after-treated graphite, yielding an atomic relation O/C around 0.08.

2.1.6 IrOx-Graphene and IrOx-(graphene-N)

Pre-deposition solutions for the synthesis of IrOx-graphene and IrOx-(graphene-N) hybrid coatings have been prepared starting from the carbon precursors prepared by the ICMAB group of *Carbon Nanomaterials and Inorganic Nanostructures.* Graphene oxide (GO) was prepared by Hummers method [5], and was characterized by termogravimetric analysis (TGA) showing around 20 wt (%) of functionalized groups. N-doped graphene was obtained by ammonolysis of the previously prepared GO. Nitrogen content was also studied by TGA and the results show a 20 wt (%) of functionalization (including nitrogen and oxygen species). Pre-deposition solution was prepared following the same protocol used in IrOx-CNTs preparation, but adding 5.5 mg/mL of graphene precursor instead of CNTs-COOH.

Along the thesis, the term “graphene” will be used despite the uncertainty on graphitic and graphene proportion.

2.2 Electrochemical Synthesis

All the samples described in this thesis have been synthesized by electrochemical deposition. Electrodeposition is a synthesis method used to deposit in the surface of an electrode a conductive material, from a pre-deposition solution containing the reduced/oxidized precursor, or other species that will get involved in secondary electrode reactions. The method is very versatile and the modulation of intensity or potential improves the control of the final thickness, homogeneity and microstructure of the coatings. Also, electrochemical methods have significant advantages, as high sensibility and selectivity, the chance to operate in ambient conditions and the possibility of coating any geometry or size, since the only requirement is to have a conductive substrate.

2.2.1 Potentiodynamic Deposition

The potentiodynamic deposition is a technique where repetitive pulsed or triangular potential signals cause the potential of the working electrode to sweep back and forth between designated values (switching potentials). For dynamic potential voltammetries, which are equivalent to triangular potential waves, the current at the working electrode may be measured during the potential scan. The potential provides the driving force for reactions at the working electrode, while the current is proportional to the rate of these reactions. Representative curves for the iridium oxide (IrOx) electrodeposition are shown in Figure 2.1.

In potentiodynamic depositions used in this thesis, the solution was not stirred so, the system current was limited by the diffusion of the reactants to the electrode surface. This can be observed in the I vs E voltammograms (Figure 2.1B): when the potential is increased until a voltage value large enough for a redox reaction, the current increases until a maximum value but then decreases for the depletion of the reactive specie near the surface, yielding a characteristic wave. If the process is reversible, an identical cathodic wave will appear in the reduction direction.

However, usually secondary reactions or the structural reorganization of the solid synthesized made the process irreversible.

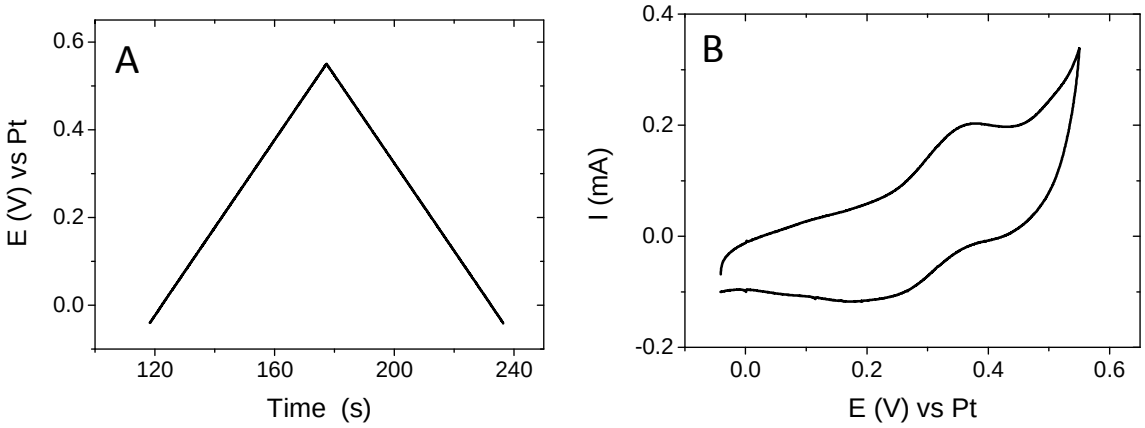

Figure 2.1. Potentiodynamic deposition of IrOx coatings. A) Triangular potential excitation sweep and B) Voltammogram (intensity vs potential curve).

Iridium oxide anodic electrodeposition was firstly presented by Petit et al. [286] using a constant current technique, which are generally utilized when a unique crystallization process exists, and other chemical reactions do not interfere. However, previous works in our research group demonstrated that potentiodynamic synthesis methods lead to a more homogeneous film microstructure, with better adhesion to Pt-coated substrates [6].

A schematic representation of the electrochemical cell used for the electrodeposition is shown in Figure 2.2. A glass recipient is filled with the aqueous pre-deposition solution and three electrodes are immersed. The counter-electrode is a rectangular platinum foil and the pseudo-reference electrode is a platinum wire (both from Goodfellow, 99%). The use of a conventional reference electrode (like Ag/AgCl) as reference instead a Pt wire, has been dismissed for technical aspects. However, the use of platinum as pseudo-reference electrode has been reported under particular conditions, yielding similar potentials that Ag/AgCl reference ones [7]. The working electrode, in which the sample is deposited, is a transparent soda-lime glass slide

(76x25 mm^2 AFORA) covered with 5 nm of titanium (as adhesion film) and 12 nm of platinum. For all the hybrid coatings, the size of the substrate and the counter-electrode used was smaller, around 38x12 mm^2. The Ti-Pt deposition was carried out by vacuum thermal evaporation in the Optical laboratory of the *Universidad Autónoma de Barcelona*. The thickness of the metallic layers was controlled by a sensing quartz microbalance. To increase crystallinity, the homogeneity and the electrical conductivity of metals, substrates were heated 4 hours at 450ºC before their use as electrodes.

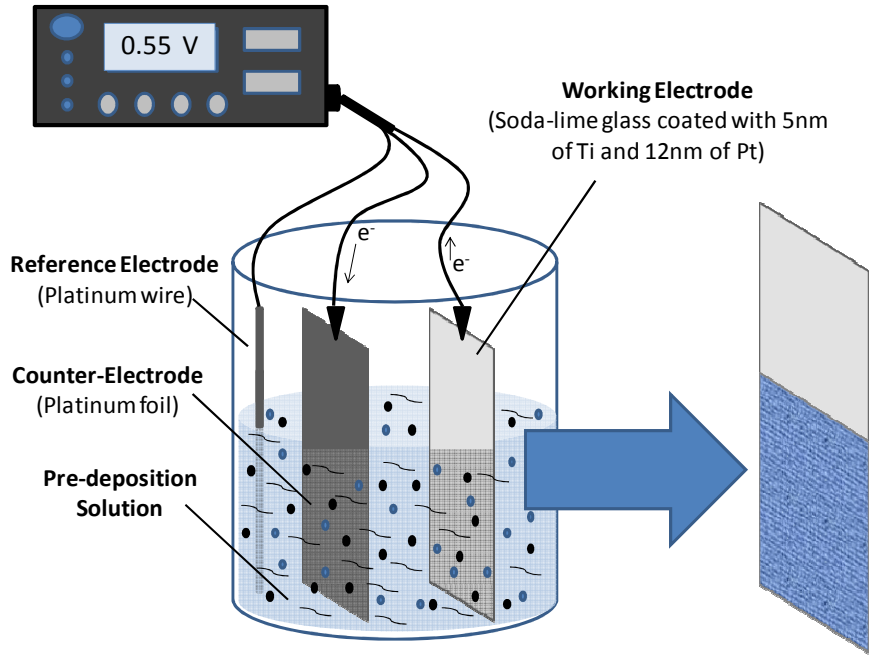

Figure 2.2. Representation of the three-electrode system used during IrOx CV synthesis.

The final appearance of the substrate is a translucent slide, which allows the synthesis of semi-transparent coatings on it. Transparency has been searched to easily control cell cultures onto it. To ensure maximum reproducibility and electric field homogeneity, working and counter electrodes have the same dimensions and the separation between them in the cell is kept constant at 1 cm, by Teflon holders.

The equipment used for electrochemically deposition of the coatings was a VMP3 potentiostat/galvanostat from Biologics Science Instruments.

Electrodeposition of the coatings was performed using different parameters depending on the coating, as shown in Table 2.1. Switching potentials were optimized depending on the different mobility of the species in solution or their redox potentials. The number of cycles used during the synthesis determines the final thickness of the coating and has been modified from 5 to 50. After the synthesis, the coatings were washed with distilled water and dried in air until further use.

Coating	Scan Rate (mV/s)	Switching Potentials (V)	Cycles
IrOx	10	OPC – 0.55	50
IrOx-CNTs	5	OPC – 0.70	25-50
IPC	5	OPC – 0.90	5-50
PEDOT-Ref	10	OPC – 0.90	5-25
PEDOT-PSS	10	OPC – 0.90	5-25
IrOx-graphite	5	OPC – 0.70	25
IrOx-graphene	5	OPC – 0.85	20-25
IrOx-(graphene-N)	5	OPC – 0.85	25-50

Table 2.1. Electrochemical parameters used in the potentiodynamic synthesis of different coatings. (OPC is open circuit potential or rest potential, ~0.0 V).

2.2.2 Potentiostatic Electrodeposition

Some of the polymeric samples synthesized in this work have been prepared by constant potential deposition using the same potentiostat previously described. As mentioned above, potentiodynamic methods yield more homogeneous IrOx coatings,

but for some polymers, constant potential methods have demonstrated very good results. In electrochemical potentiostatic methods, a constant potential is fixed and the intensity is recorded versus the time. This fixed potential prevents over-oxidation and possible side reactions that can take place at other potentials. The synthesis is finished when the required charge is reached.

This method was used to deposit some polymeric samples in order to compare possible differences with the coatings synthesized by potentiodynamic processes. The same pre-deposition solutions previously described in Section 2.1 are used to synthesize IPC, PEDOT-Ref and PEDOT-PSS coatings, using a constant potential of 0.9 V, and reaching final charges from 0.07 to 0.8 C/cm^2.

Also, by constant potential methods PEDOT-CNTs and PEDOT-IrOx coatings have been prepared, to compare electrochemical properties with IPC and PEDOT-PSS samples.

PEDOT-CNTs coatings were prepared based in the previously reported work of Luo et al. [8]. 3 mg/mL of CNTs-COOH (<90%, D 1-2 n, L 5-30 µm; Nanostructured & Amorphous Materials, Inc.) were dispersed by sonication 30 minutes in 10 mL of milliQ water and EDOT (Sigma-Aldrich, 97%) is added up to 0.02 M, and stirred during 1 hour. Then, coatings are electrodeposited at a constant potential of 0.9 V, up to a total charge of 90 mC/cm^2.

PEDOT-IrOx coatings were prepared starting from the pre-deposition solution of IrOx (described in the Section 2.1.1) and adding 0.03 M of EDOT (Sigma-Aldrich, 97%). The resultant solution is stirred for 1 hour and the pH is adjusted to 8 with $H_2C_2O_4$ (Sigma-Aldrich, 99%). Then, the potentiostatic deposition is performed at 0.9 V, up to a total charge of 90 mC/cm^2.

2.3 Characterization Techniques

2.3.1 Electrochemical Quartz Crystal Microbalance (EQCM)

EQCM was used to calculate the final mass deposited after electro-synthesis at different cycles, to study the mass variations taking place in the first steps of the

deposition (in order to elucidate the synthesis mechanism) and to study the ionic intercalation when the final electrodeposited material is used as electrode.

A Seiko Eg&G PAR EQCM instrument was coupled with the potentiostat/galvanostat VMP3 BIOLOGIC. The three-electrode electrochemical system was similar to that used in the synthesis but in this case, the working electrode is the 0.196 cm^2 Pt-coated quartz AT-cut crystal (QA-A9M-PT-50, BIOLOGIC). The electrochemical parameters were modulated for each experiment, and more details are exposed in the results chapters.

EQCM technique provides an easy way to study the relevant surface reactions or effects, such as species transport, adsorption kinetics and film growth [9]. The basis is a quartz resonator that in this case is coated by Pt and used as working electrode for deposition. The quartz crystal is resonating in a particular frequency (9 MHz for AT-cut crystals), which changes as the mass in the surface is modified. The relationship between the mass change (Δm) and the change in resonant frequency (Δf) can then be calculated by the Sauerbrey equation (Equation 2.1):

$$\frac{\Delta m}{\Delta f} = \frac{-A\sqrt{\mu_q \rho_q}}{2 f_0^2} \qquad \text{(Equation 2.1)}$$

Where:

μ_q = Shear modulus of the quartz crystal ($2.947 \cdot 10^{11}$ $g \cdot cm^{-2} \cdot Hz^{-1}$)

ρ_q = Density of the quartz crystal (2.648 $g \cdot cm^{-3}$)

F_0 = Initial resonant frequency (Hz)

A = Piezoelectrically active crystal area (For BIOLOGIC resonators is 0.196 cm^2)

This simplified Sauerbrey's equation can only be applied to systems in which the following conditions are achieved: the deposited mass must be rigid and distributed evenly, and the frequency change $\Delta f/f < 0.02$ [10].

In liquid applications, the resonant frequency depends also on the viscosity and density of the liquid. However, it has been confirmed that Equation 2.1 is still valid if these liquid properties do not change during the EQCM experiment [11].

The mass of the electrodeposited solid can also be calculated by the Faraday's law of electrolysis, which states that the quantity of electricity passed through the system (coulombs) is directly proportional to the amount of chemical reaction (equivalents) which takes place at an electrode (Equation 2.2).

$$Q = \int_0^t i \cdot dt = (F)(equivalents) = F \cdot \frac{m}{M} n \xrightarrow{\text{i = cte}} i \cdot t = F \cdot \frac{m}{M} n \quad \text{(Equation 2.2)}$$

Where *m* is the total mass deposited (g), *M* the molecular weight of the deposited specie (g/mol), *n* the exchanged electrons in the reaction, *F* the Faraday number (96485 C/eq), *i* the intensity (A) and *t* the time of the electrodeposition (s).

Therefore, a combination of data from EQCM and charge may yield the number of electrons per mol of deposited species, or the molecular weight of intercalated species.

2.3.2 Grazing Incidence X-Ray Diffraction (GIXRD)

X-Ray Diffraction was used to identify the crystal structure of coatings as prepared and after thermal treatment. GIXRD measurements were carried out to study in detail thin films, to achieve a significant amount of material exposed, preventing substrate contributions. Powder diffraction patterns were obtained by placing the sample at fixed grazing angles while the 2θ is scanned. By changing the incidence angle the X-ray penetration depth into the samples can be changed: at higher angle, higher penetration.

Some IrOx and IrOx-CNTs coatings were synthesized onto quartz Pt-coated slides and subject to a 4h thermal treatment at 500ºC in air (with a temperature ramp of 200ºC/h). The resulting coatings were studied by X-ray grazing incidence diffraction at

the CIN2-ICN (Centre d'Investigació en Nanociència I Nanotecnologia- Institut Catalá de Nanociència y Nanotecnología) using a Diffractometer Panalytical X´Pert Pro MRD (Material Research Diffractometer) with a grazing angle incidence of 0.5°, radiation Cu Kα (λ= 1.5406 Å) and a measuring 2θ interval between 5-72°.

IPC coatings with the same thermal treatment described above were measured in the *Centres Científics I Tecnologics (CCiT) of University of Barcelona*. The measurements were carried out at 0.1°, 0.4°, and 1.0° incidence angles on a Siemens D500 Diffractometer equipped with parallel beam attachment in the diffracted beam and using 0.05° step in data acquisition and using the Cu Kα (λ= 1.5418 Å) radiation.

2.3.3 X-Ray Photoelectron Spectroscopy (XPS)

XPS or ESCA (Electron Spectroscopy for Chemical Analysis) is a superficial characterization method which provides chemical information (can detect concentrations above 0.1%) with a broad type of samples.

XPS analysis can provide qualitative and quantitative information of all the elements present in the surface, except Hydrogen and Helium, in the first 3-10 nanometers of the sample. This limited penetration is due to the emitted electrons in the inner layers once excited by X-rays, which cannot escape from the solid and reach the detector. This feature makes this technique very sensitive to superficial changes.

The basis of the XPS is the photoelectric effect: photons can interact with an electron in an atomic orbital, transferring its energy to the electron and provoking the electron's emission. The kinetic energy of the emitted electrons is linearly proportional to the frequency of the exciting photons, and the relation is given by the Einstein equation (Equation 2.3).

$$E_B = h\nu - KE \qquad \text{(Equation 2.3)}$$

Where E_B is the binding energy of the electron in the atom, hv the energy of the X-Ray source and KE the kinetic energy of the emitted electron detected in the analyzer of the spectrometer.

Binding energy is dependent of each particular element, and it can change depending on its direct bonding to other atoms, as the electronic distribution is modified. Therefore, the determination of elements and its molecular environment are possible with this technique.

Samples synthesized in this thesis were analyzed at the CCiT (Centres Científics i Tecnològics) of the *Universitat de Barcelona*. The equipment used was a PHI 5500 Multitechnique System (from Physical Electronics) with a monochromatic X-Ray source (Aluminium Kα: 1486.6 eV energy and 350 W) placed perpendicular to the analyzer axis and calibrated using the $3d_{5/2}$ line of Ag with a full width at half maximum (FWHM) of 0.8 eV. All the measurements were made in an ultra high vacuum (UHV) chamber pressure between $5 \cdot 10^{-9}$ and $2 \cdot 10^{-8}$ Torr. The protocol used, previously optimized, was the same for all the samples. The analyzed area was a circle, 0.8 mm in diameter, and the selected resolution for the spectra was 187.5 eV Pass Energy and 0.8 eV/step for general survey spectra, and 11.75eV Pass Energy and 0.05 eV/step for depth profile spectra of each element. When necessary, a low energy electron flood gun (less than 10 eV) was used to discharge the surface.

Spectra from many of the samples have been charge-corrected by referencing all peaks to the adventitious C 1s spectral component (C-C, C-H) at binding energy set to 284.8 eV. The quantification of the survey spectra and the deconvolution of the depth profile spectrum of each element were carried out with *Multipack Data Analysis* software, using generally Gaussian-Lorentzian line shapes and Shirley background correction.

2.3.4 3D Confocal Microscopy

In order to study the surface morphology and roughness, a Leica DCM 3D microscope was used. This microscope has a dual core technology that combines confocal and

interferometry techniques for high speed and resolution measurements down to 0.1 nm.

The measurements were done at the *Serveis de Microscopia* of Universitat Autònoma de Barcelona, using 100x and 50x lenses and ambient conditions of temperature and pressure. The data acquisition was triple for each sample and the area captured was 128x95 μm^2. The data was subsequently processed with the *MountainsMap Premium* software. To analyze in detail the surface, filters are used to separate the roughness and the waviness of the data obtained. The standard filter used is the Gaussian as specified in ISO 11562. However, due to the large roughness of the samples, a non-linear version of the Gaussian filter was used, which is "robust" against sharp peaks and valleys. Robust Gaussian filter has been described in ISO TS 16610-31. To calculate the roughness of the samples the 3D parameter S_q, was used instead of profile (2D) parameters, to achieve a more representative value for the entire surface. S_q is a general and widely used parameter, described as:

$$S_q = \sqrt{\frac{1}{A}\iint_A z^2\,(x,y)dxdy} \qquad \text{(Equation 2.4)}$$

Where A is the number of points per profile and z the height of the point (x,y). The value computes the standard deviation for the amplitudes observed at the surface.

2.3.5 Atomic Force Microscopy (AFM)

AFM in dynamic mode was performed at ICMAB-CSIC, with a Pico Plus Molecular Imaging microscope, using 10 nm size silicon tips. The cantilever strength used was approximately 40 N/m and the resonance frequency 170 kHz. 5 images in different areas of the sample were taken in order to subsequently analyze the roughness and grain size with the *MountainsMap Premium* software. The roughness value (RMS) was calculated with Equation 2.4, the same used to calculate roughness with confocal microscopy.

2.3.6 Scanning Electron Microscopy (SEM)

The microstructure and the thickness of the samples were studied by Scanning Electron Microscopy (SEM), at the *Institut de Ciencia de Materiales de Barcelona* (ICMAB-CSIC), using QUANTA FEI 200 FEG-ESEM microscope. Secondary electrons were detected using a voltage of 5-30kV and high vacuum conditions were used in most of the cases. Specific technical conditions are presented for each of the images taken in the results section.

The thickness of the thin films was evaluated placing the transversal fractured substrate in parallel with the electron beam.

Energy-dispersive X-ray spectroscopy (EDX) was used for the elemental analysis of some coatings. The technique is based in the analysis of the emitted X-Rays when an atom is irradiated with an electron beam. The fundamental principle is that each element has a unique atomic structure and as consequence, a unique set of peaks on its X-ray spectrum is obtained. A semi-quantitative measurement is also possible, but for samples synthesized in this thesis, usually thin, the elements present in the substrate (soda-lime glass) are detected and the data obtained is not representative of the material under study.

The possible surface alterations after sterilization and cell cultures were also studied by SEM. IrOx, IrOx-CNTs and IPC coatings with 5 DIV neural cells were treated with gluraraldehyde to immobilize the cells and kept in phosphate buffer solution (PBS) until SEM measurements. SEM images were taken in high vacuum conditions, at a voltage of 5 kV. Low voltage was optimized for high detail of the surface components, without cell damaging.

2.3.7 Transmission Electron Microscopy (TEM) and High Resolution TEM

In TEM measurements, a beam of electrons is transmitted through an ultra-thin sample, interacting with the specimen as it passes through. An image is formed from the interaction, and is magnified and focused onto an imaging device, usually with a

proper camera. Images give us information about the size, the morphology and the microstructure of the sample under study.

In this thesis, two different microscopes have been used. First a 120 KV JEOL 1210 at the *Institut de Ciencia de Materials de Barcelona* (ICMAB-CSIC). The specimen holder was a double tilt (Tilt X=±60°, Tilt Y=± 30°) GATAN 646 and the camera an ORIUS 831 SC 600, GATAN. The second one is a JEM-2011 at the UAB *Serveis de Microscòpia*. In this case, the holder was a JEOL of double inclination and the camera a CCD 895 USC 4000, GATAN.

For such analyses, samples were removed from the substrate, suspended in ethanol (Panreac, 96%) and then deposited on a copper grid covered with a polymer film.

2.3.8 Attenuated Total Reflectance (ATR)

Infrared measurements of the samples were carried out at the *Ciencia de Materiales de Barcelona* (ICMAB-CSIC), in Attenuated Total Reflectance (ATR) mode, using a Perkin Elmer HART with a 60° ZeSe flat plate accessory. Some samples were measured as prepared directly placing the substrate, while others were removed from the substrate and disks, of approximate 2 mm of thickness, were prepared with anhydrous KBr (Sigma-Aldrich).

2.3.9 Micro-Raman and Confocal-Raman Microscopy

Micro-Raman was performed in samples at room temperature without previous preparation, utilizing a Jobin-Yvon LabRam HR 800 spectrophotometer, coupled to an optical microscope Olympus BXFM, in back-scattering geometry. Signals were detected by a charge coupled device (CCD) camera cooled at -70ºC. Spectra were taken with the 532 nm excitation line and the diffraction grating was 600 lines/mm. Laser power over the samples was 0.5-4 mW and the microscope lens were 50x and 100x.

Raman spectra and ultra-fast high resolution 3D chemical imaging were recorded with a WITec Confocal Raman Microscope (WITec alpha300 R, Ulm, Germany). This instrument was described in detail before [12,13]. The spectroscopic detector was an electron multiplying-CCD . The excitation line was 531.85 nm and diffraction grating 600 lines/mm. To obtain the images, the scan used was 100 points per line, 100 lines per image and a total area scanned of 9.5 μm^2. The scan width was 10 µm and the scan speed 5 s/line.

In Confocal Raman Imaging the complete Raman spectrum is acquired at each image pixel and the final image is calculated by isolating spectral characteristics as height, width or the most common peak position from these Raman spectra. The experimental values of peak positions used to determine the species present in the samples were 1544.2 - 1614.6 cm^{-1} for CNTs and 527.1 - 565.59 cm^{-1} for IrOx.

2.3.10 Contact Angle

The hydrophilicity of the samples was measured by contact angle measurements. The contact angle is defined as the angle formed between a drop of liquid and the surface of a substrate, as shown in Figure 2.3. The measurement was done with a Pocket Goniometer PG2 model at room temperature, with micro-drops of milliQ water.

The contact angle is related with the wettability (hydrophility in case of water) of the sample, and a bigger angle (θ as defined in Figure 2.3) means a more hydrophobic surface. Hydrophobicity may be defined as $\theta > 90^o$.

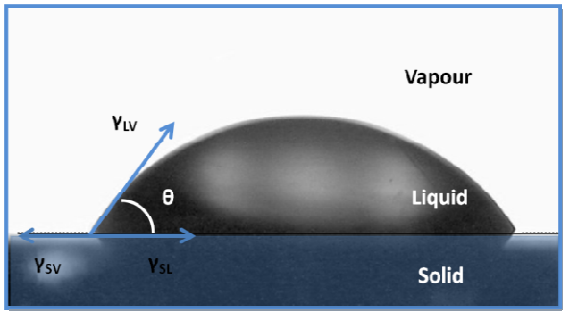

Fig 2.3. Representation of a drop in the surface, indicating the corresponding contact angle.

2.3.11. Dynamic Light Scattering (DLS)

DLS measurements were performed with a Zetasizer Nano ZS (from Malvern Instruments, Ltd. UK), equipped with a He/ne 633 nm laser. Both IrOx solutions, with and without oxalate, were previously filtered with a 0.2 μm Millipore polycarbonate membrane. Measurements were done in automatic mode, in which the equipment made the necessary runs depending on the size fluctuations.

2.3.12 Electrochemical Characterization

Electrochemical behavior of the coatings was studied by cyclic voltammetry (CV) with the same potentiostat and system described in the section 2.2.1. The area of the samples exposed to the electrolyte was in all cases 1 cm^2 and the separation between working and counter electrodes was 1 cm. The electrolyte was pH-7.4 phosphate buffered solution, PBS (in mM: 137 NaCl, 2.7 KCl, 10 Na_2HPO_4, 1.8 KH_2PO_4, all from Sigma-Aldrich) although in specific cases 1M KOH (LabKem, 85%) was used. The different electrochemical parameters were optimized depending on the sample, and are specified in the corresponding chapters.

Cathodal charge storage capacity (CSC_c) was determined from the time integral of the cathodic current during a potential sweep, within the safe potential limits, divided by the sweep rate and the area of the electrode [14]. For IrOx and IrOx-hybrids these potential limits were -0.6 V to 0.8 V vs Pt, whereas for PEDOT-based coatings was -0.6 V to 0.6 V vs Pt. The sweep rate was modulated from 10 to 50 mV/s, although most of the measurements were done at 10mV/s. Stability tests were carried out to monitor the variation of the CSC_c values throughout 1000 cycles.

Specific capacitance (C_g) was calculated by the equation 2.5.

$$C_g = \frac{\int I\, dV}{m\Delta V S} \qquad \text{(Equation 2.5)}$$

Where C_g is the specific capacitance (F/g), $\int I\,dV$ is the integrated area enclosed in the cathodic CV curve (mA·V), *m* the mass of the active material (g), ΔV the scanned potential range (V) and *S* the scan rate (mV/s).

Mass of the studied IrOx-CNTs coatings, was calculated from EQCM results.

2.4. Bio-Experiments. Preparation and Viability of Cell Cultures

All the experiments performed with cells, were done by the group of *Neuroquímica y Neurofarmacología* in the *Instituto de Investigaciones Biomédicas de Barcelona* (IibB), by Matheu Lichstentein and the supervision of Cristina Suñol.

2.4.1 Preparation of Materials for Neuronal Culture

IrOx, IrOx-CNTs and IPC coatings, have been tested as substrates for neural growth and development. For this purpose, the samples were cut in 1x1 cm^2 pieces and sterilized by two hour-immersion in milliQ water at 60 ºC in 12-well plate (Nunc). Borosilicate cover-slips were used as control material and were sterilized in autoclave. Afterwards, all materials were washed with 1 mL sterile water in the laminar flux cabin, transferred carefully with forceps to a new sterile 12-well plate and incubated for 1 hour with aqueous poly-L-lysine (PLL) 45 µg/mL at 37ºC. Finally, the PLL-coated films were washed again with sterile water to remove excess of PLL.

2.4.2 Neuronal Cultures

Primary cultures of cortical neurons were prepared from the cerebral cortex of 16 day-old NMRI mice embryos (Charles River, Iffa Credo, Saint Germain-sur-l'Arbreste, France). Cortices were dissected in PBS (pH=7.4) under a magnifier glass and meninges were carefully removed. Isolated tissue was then minced with a razor blade and dissociated for 10 min at 37ºC in KREBS buffer supplemented with $MgSO_4$, albumin, trypsin and DNAase (all from Sigma-Aldrich), followed by trituration with Pasteur pipettes. The resulting cell suspension was seeded at a density of 115000

cells/cm^2 in previously prepared 12-well plate with sterile materials (1 mL per well). Cells were plated in Dulbecco's Modified Eagle's medium:Nutrient mixture F12 (DMEM:F12) with 10% FBS (Fetal Bovine Serum) and after two hours, the medium was changed to Neurobasal supplemented with 2 mM L-glutamine (from Sigma), B27 (which is a serum-free supplement to give optimal growth to neurons), and Penicillin-Streptomycin (all from Invitrogen). The day after plating cells, a mixture of 5 µM 5-fluroro-2'-deoxyuridine and 20 µM uridine was added to the media. In some cases, other anti-mitotic agent was used, 10 µM cytosine arabinoside (AraC). The replacement of the plating medium with serum-free Neurobasal, and the presence of uridine/deoxyuridine were intended to prevent the proliferation of non-neuronal cells. In these conditions, as about 99% of the cells were neurons. We only detected a small percentage of astroglia, about 0.5% of the cells were positive for Glial Fibrillary Acidic Protein (GFAP, 1:1000, Sigma G-3893) staining. Cultures were maintained in an incubator at 37ºC in humidified atmosphere with 5% CO_2 up to five days *in vitro* (DIV) when cell survival was quantified.

2.4.3 Immunocytochemistry and Cell Quantification

After 5 DIV, Neurobasal was removed from the culture wells, and neurons were fixed with 4% Paraformaldehyde (PFA) at room temperature for 10 min. After washing with PBS, cells were permeabilized with PBS containing 0.15% Triton X-100 (Sigma-Aldrich) for 15 min, and blocked with 1% bovine serum albumin (BSA) for 1 hour to prevent unspecific binding. Primary antibody against Tau (1:1000, whole antiserum produced in rabbit, Sigma T-6402), which is a specific component of neuronal cytoskeleton, was diluted in PBS-BSA 0.1% and incubated overnight on cells. On the following day, and after three washes with PBS, Alexa-488 anti-rabbit (1:1000, Molecular Probes, A11008) was used as secondary antibody to enable green fluorescence visualization. Bis-benzimide (Sigma, 5µM diluted in PBS for 5 minutes) was used for nuclear staining and identification of living cells. Photographs were taken using a Leica DMI 4000B fluorescence microscope. Fluorescent images of both nuclear and Tau staining were combined and used for quantification of healthy neurons on materials. Six radial

fields (450x616 μm^2) were systematically photographed in each sample and cell count was extrapolated to the total surface area.

For the detection of neurotransmitter receptors the immunocytochemistry protocol was slightly modified. For GABA (γ-aminobutyric acid) receptor, the permeabilization step was omitted as the antibody recognizes an extracellular epitope on the N-terminal of the $GABA_A$ receptor α1 subunit (1:200, rabbit polyclonal IgG, Abcam ab33299). For NMDA (N-methyl-D-aspartate) receptor detection (1:50, goat polyclonal Santa Cruz sc-1467), cells were processed according to a previously described protocol in Briz et al. [15]. Briefly, after PFA fixation, cells were incubated with -20ºC methanol for 10 min, followed by a 5 min incubation with 0.03% Triton X-100 in PBS. Subsequently, for both receptors, cells were incubated overnight at 4ºC with corresponding primary antibodies diluted in PBS-BSA 0.1%. Fluorescent detection was performed using Alexa-488 anti-goat (1:1000, Molecular Probes, A11055) for NMDA and Alexa-488 anti-rabbit (1:1000, Molecular Probes, A11008) for GABA receptors, respectively.

2.4.4 Neurotransmitters Release

Cells growing on borosilicate coverslips or materials were transferred to a new 12-well plate filled with 0.4 mL/well Hank's Balanced Salt Solution with HEPES (HBSS; in mM: 137 NaCl, 5.4 KCl, 1.3 $CaCl_2$, 0.5 $MgCl_2$, 0.4 $MgSO_4$, 0.3 Na_2HPO_4, 0.4 KH_2PO_4, 4.2 $NaHCO_3$, 8 HEPES, 5.5 glucose adjusted at pH 7.4) pre-warmed at 37ºC and incubated for 10 min. After this, cells were sequentially incubated for 2 minutes each time with low K^+ HBSS (5 mM K^+) and with high K^+ (90 mM K^+) depolarizing solution. The latest was prepared by increasing the concentration of KCl to 90 mM and decreasing NaCl to 42 mM in the HBSS solution to maintain osmolarity. At the end of each exposure, HBSS solution from each well was collected in an eppendorf tube and stored at -20ºC until amino acid analysis by high performance liquid chromatography (HPLC).

2.4.5 Glutamate and GABA Analysis

Glutamate and GABA content in the HBSS exposure buffer was determined by high performance liquid chromatography-fluorimetric analysis (Waters 2475, Cerdanyola, Spain). 100 µL of solution were derivatized with 15 µL of o-pthaldialdehyde and 100 µL of that mixture were injected for reverse-phase separation on a C18 column (Tracer Nucleosil C18 5-µm particle size, 10 × 0.4 cm; Teknokroma, Spain) and fluorescence detection at 360/450 nm [16]. For both neurotransmitter detection the mobile phase consisted of two components: solution A, made up of 0.05 M NaH_2PO_4 adjusted at pH 5.4 with 85 % H_3PO4 and 28 % methanol, and solution B made up of methanol/water (80:20). The mobile phase was used at a flow rate of 0.8 mL/min with a Waters 600 quaternary pump. Under these conditions retention times for glutamate and GABA were 2.2 min and 11.6 min, respectively. Neurotransmitter content was calculated using an external standard method with glutamate and GABA as standards.

2.4.6 Co-Cultures on IPC

With the purpose of performing biocompatibility tests in a closer situation to *in vivo* conditions, some experiments were done using a co-culture of astrocytes and neurons. It is well known, that a bidirectional communication at several levels exist between these two cellular types with important functional implication [17]. Therefore, we consider that the co-culture of neurons on a monolayer of confluent astrocytes represents a relevant and appropriate model to study the biocompatibility of our new electrodes. For this purpose, astrocytes first and subsequently neurons were grown in IPC samples as substrates, and borosilicate coverslips to compare. The sterilizing treatment of IPC and borosilicate samples, has been the same as the previously mentioned for neuron cultures (section 3.1).

2.4.6.1 Astroglial Cultures

Embrionary primary astrocytes were obtained following the same method as for primary neurons, with the exception that they were first grown in flasks to enable their differentiation and then transferred onto the materials tested. After the dissection (see section 3.2) the cell suspension was seeded at a density of 230000 cells/cm^2 in DMEM:F12 supplemented with 10% FBS, 0,1% Penicillin-Streptomycin and 0,1 % Fungizone (complete DMEM:F12), in untreated (no Poly-Lysine, to prevent the adhesion on neurons) T-75 Flasks (Corning). Media changes were performed every 3-4 days with complete DMEM:F12 until reaching confluence at 14-16 days. When astrocytes formed a confluent monolayer, and in order to prevent the proliferation of contaminant microglial and remove the loosely attached cells, 10 µM cytosine-arabinoside was added, and the flasks were shaken overnight at 200 rpm at 37ºC .

The following day, the media was removed from the flasks, cells were rinsed with 12 mL PBS, and were incubated during 5min at 37ºC with 3 mL 0.25% Trypsin- 1mM EDTA (Ethylenediaminetetraacetic acid) to detach them from the flasks. Trypsin was stopped by adding 9 mL of complete DMEM:F12. The cell suspension was then collected in 50 mL Falcon tubes and centrifuged at 1000 rpm for 5 min. The resulting pellet was re-suspended in fresh complete DMEM:F12 at density of 115000 cells/cm^2 and seeded into 12-well plate, containing the material samples or control borosilicate coverslips. Again, media changes were performed every 3-4 days during 15 days.

2.4.6.2 Co-Culture Model

Once astrocytes grown on material samples became confluent (around 7-8 days after seeding) they were cultured for an additional week to enable possible detrimental or beneficial effects of growing on the different material samples to appear.

Around 15 days after seeding, neurons (obtained as described in the section 3.2) were seeded on top of astrocytes. For that, media was removed from the 12-well plates and 1 mL of a freshly obtained primary suspension in complete DMEM:F12

containing 115000 cells/cm^2 was added to each well. After two hours, the medium was changed to Neurobasal supplemented with 2 mM L-glutamine (from Sigma), B27, and Penicillin-Streptomycin. The following day, 10 µM AraC was added to the media to halt cell proliferation. After 7 days, cells were fixed with 4% PFA and processed for immunocytochemistry experiments and subsequent cell counting.

2.5. References

-[1] Cruz A. M., Abad LL., Casañ-Pastor N. et al. Iridium oxohydroxide, a significant member in the family of iridium oxides. Stoichiometry, characterization, and implications in bioelectrodes. *J. Phys. Chem. C*. **116**, 5155−5168. 2012.

-[2] Petit M. A. and Plichon V. Anodic electrodeposition of iridium oxide films. *J. Electroanal. Chem*. **444**, 247-252. 1998.

-[3] Moral-Vico J. Materiales electroactivos poliméricos e híbridos como sustrato de crecimiento neuronal. Ph.D Thesis, Universidad Autónoma de Barcelona, Spain. 2012.

-[4] Tobías G., Shao L., Greeb M.L.H. Enhanced sidewall functionalization of single-wall carbon nanotubes using nitric acid. *J. Nanosci. Nanotechnol*. **9**, 6072-6077.2009.

-[5] Hummers W.S. and Offeman R.E. Preparation of graphitic oxide. *J. Am. Chem. Soc.* **80**, No.6, 1339–1339. 195.

-[6] Cruz A.M. Obtención y caracterización de materiales electroactivos para soporte de crecimiento neuronal. Ph.D Thesis, Universidad Autónoma de Barcelona, Spain. 2010.

-[7] Kasem K.K and Jones S. Platinum as a reference electrode in electrochemical measurements. *Platinum Metals Rev.* **52**, No.2, 100–106. 2008.

-[8] Luo X., Weaver C.L., Cui X.T, et al. Highly stable carbon nanotube doped poly(3,4-ethylenedioxythiophene) for chronic neural stimulation. *Biomaterials*. **32**, 5551-5557. 2011.

-[9] Lori J.A. and Hanawa T. Characterization of adsorption of glycine on gold and titanium electrodes using electrochemical quartz crystal microbalance. *Corros. Sci*. **43**, 2111-2120. 2001.

-[10] Srivastava A.K. and Sakthivel P. Quartz-crystal microbalance study for characterizing atomic oxygen in plasma ash tools. *J. Vac. Sci. Technol. A*. **19**, No.1, 97-100. 2001.

-[11] Bruckenstein S. and Shay M. Experimental aspects of use of the quartz crystal microbalance in solution. *Electrochim. Acta*. **30**, No.10, 1295-1300. 1985.

-[12] Schmidt U., Vargas F., Hollricher O., et al. Confocal Raman AFM – A powerful tool for the nondestructive characterization of heterogeneous materials. *NSTI-Nanotech*. **4**, 48-51. 2007.

-[13] Dieing T., Hollricher O. and Toporski J. Confocal Raman Microscopy. Ed. Springer. (1st Edition). 2010.

-[14] Cogan S.F. Neural stimulation and recording electrodes. *Annu. Rev. Biomed. Eng*. **10**, 275-309. 2008.

-[15] Briz V., Galofre M, and Suñol C. Reduction of glutamatergic neurotransmission by prolonged exposure to dieldrin involves NMDA receptor internalization and metabotropic glutamate receptor 5 downregulation. *Toxicol. Sci*. **113**, No.1, 138-149. 2010.

-[16] López-Gil X., Artigas F., and Adell A. Role of different monoamine receptors controlling MK-801-induced release of serotonin and glutamate in the medial prefrontal cortex: relevance for antipsychotic action. *Int. J. Neuropsychopharmacol*. **12**, No.4, 487-499. 2009.

-[17] Jones E.V., Cook D., and Murai K.K A neuron-astrocyte co-culture system to investigate astrocytes-secreted factors in mouse neuronal development. *Methods Mol. Biol*. **814**, 341-352. 2012.

Chapter 3

Electrodeposited IrOx Thin Films

This chapter gathers a brief introduction of the pre-deposition solutions and IrOx films which are the basis of the new hybrids synthesized. Preparations with and without oxalic acid has been tested in order to appreciate possible differences between the two solutions.

A complete ultraviolet-visible spectroscopy study has been done in order to identify the species involved in the pre-deposition solution and the evolution during the preparation and the aging process.

Also, electrochemical quartz microbalance was used in order to determine fundamental aspects of the electrochemical deposition mechanism and to quantify the final mass deposited in the coatings.

After the synthesis, a complete characterization of the coatings was done, to analyze the surface chemical composition, the structure and the microstructure, using different techniques as DRX, micro-Raman, ATR, SEM or XPS among others.

Finally, the electrochemical properties were evaluated by CVs in different conditions.

3.1 IrOx Thin Films. Routes of Synthesis With and Without Oxalate.

The challenge for neural interface materials is to design bio-electrodes capable to modulate the function of nervous tissue or individual neurons, causing minimal inflammation and avoiding cellular death. Currently, different types of conductive materials are available for application as electrodes in the neural system: gold, platinum, iridium oxide, titanium nitride or glassy carbon, are some of them. Comparing these materials, and despite the high cost and the low terrestrial abundance of iridium, hydrated IrOx has demonstrated superior performance, showing the lowest polarization losses during charge injection and the highest electrical efficiencies. In addition, its good biocompatibility and its high charge injection capacity, with no significant tissue damage, are the main reasons for the increasing use of IrOx as material for recording and stimulation electrodes [1-6]**.** As example, the charge injection limit (Q_{inj}) for TiN is 0.87 mC/cm^2 whereas for iridium oxide is 4 mC/cm^2 [7]. Thus, the latter uses less voltage to transfer the same amount of charge, in response to a biphasic current pulse. The electrochemical performance and biocompatibility enhancement is mainly consequence of the faradaic charge-injection properties of IrOx, instead of the capacitive character of other materials as TiN [8]. During an electrical stimulation pulse within safe potential limits, IrOx can undergo reversible redox changes itself, with the corresponding intercalation processes, procuring a high charge capacity and preventing side reactions. This redox-intercalation capability prevents electrode alteration/degradation or tissue damage by possible irreversible reactions [9].

Iridium oxides can be classified into two categories: hydrous and anhydrous.

Anhydrous oxides are normally crystalline and the usual syntheses are melt oxidation [10], sol-gel combined with thermal treatments [11] and pyrolysis [12], among others. Crystalline IrO_2 has the same structure rutile than TiO_2 (Figure 3.1), with a symmetry space group of $P4_2/mnm$. In this structure, iridium atoms are surrounded by a nearly octahedral array of six oxygen atoms. Another structures hollandite-type (AMO_2) have also been described for IrO_2 when considerable amounts of potassium

are present in the structure (K_xIrO_2). This type of structure, as previously reported [13], consists of infinite rutile chains sharing the edges and the corners of their MO_6 octahedra, forming large square tunnels where A cations are located.

Hydrous oxides are usually prepared by methods such as sol-gel [14,15], electro-deposition [16-18], activation or anodic growth [19,20] and sputtering [1,21-23]. Hydrated films are normally amorphous, due to the high water content in the oxide structure. The porosity and the open structure allow an increased ionic and, not only iridium sites on the surface, but those in the interior of the film are accessible for electrochemical reactions, leading to a large electrochemically active area. Therefore, although hydrous IrOx coatings can be crystallized by thermal treatments [24], low crystallinity and high water content may be the reason of the increased electrode capacity in electrochemical processes, and even of the biocompatibility.

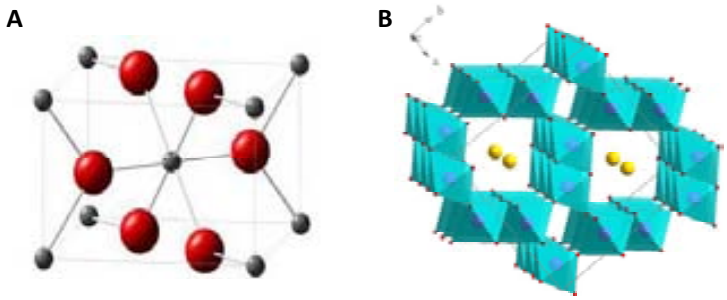

Figure 3.1. A) Rutile structure of the crystalline IrO_2: Iridium atoms in red and oxygen atoms in grey. B) Hollandite structure of $BaRu_6O_{12}$ (image from Penn State website)

In order to fabricate neural electrodes, electrochemical synthesis presents several advantages when compared with other methods, as the possibility to cover electrodes of any geometry (IrOx obtained by sol-gel procedure is powder), the reduced cost of the preparation, not needing expensive metallic iridium substrates (used in AIROF synthesis) or the possibility to only coat the conducting parts of the electrode (in contrast with SIROF synthesis, in which all the surface exposed is coated), allowing the development of ultra-microelectrodes of any size [25].

The synthesis of electrodeposited iridium oxide starts from an iridium salt solution, which normally has to be aged to form the precursor, which finally is oxidized in the electrode surface to yield IrOx. This initial solution (pre-deposition solution), the aging process and the mechanism involved in the oxide formation, have been previously described in the literature. However, its complexity results in incomplete or contradictory data. For this reason, a study in detail of all the steps has been done, in order to understand the future hybrid coatings formation and properties.

Two types of pre-deposition solutions can be found in literature: with and without complexing ligands, usually oxalate. The most commonly used protocol and the basis of the films presented in this work, is the solution prepared with oxalic acid presented by Yamanaka in 1989 [17] and later modified by Petit and Plichon in 1998 [16]. However, other solutions based in sulfates have been previously reported by Yoshino [26] and more recently even solutions without any complexation agents, just based on iridium (III) or (IV) hexachlorides, which are supposed to form water/hydroxyl complexes before electrodeposition, have been presented by Baur and Spaine [25]. The color changes produced in the solution during thermal treatment or aging, and the necessity of high pH values (around 10) to get the stabilized solutions are common aspects for all the processes, except for Yoshino, the only one who starts from an acidic solution.

Both, Yamanaka and Petit pre-deposition solutions use oxalic acid during the synthesis process, which presumably complexes the iridium cation, after a previous hydrolysis of the Ir-Cl bonds in alkaline conditions. In that scheme, the electrochemical deposition is proposed to be the result of an iridium oxide insolubilization near the anode, after the destructive oxidation of oxalate ligands to yield CO_2 [16]. However, some experimental evidences question the existence of these iridium-oxalate complexes and the synthesis mechanism. In first place, the direct synthesis to obtain tris(oxalato)iridate (III or IV) is achieved after heating at 130ºC during 11 hours [27], which does not correspond with the mild conditions used in Petit et al. methodology. Secondly, UV-visible spectra of the pre-deposition solutions do not show bands corresponding with iridium-oxalate bonds. Neither, the

electrochemical formation of CO_2 has been demonstrated in alkaline media and, to date, only Kruszyna and coworkers have observed some evidences of CO_2 formation in acidic medium [27]. However, the best evidence of no oxalate (or other ligands) required for IrOx formation is that, under the same conditions, a very similar IrOx solution and coating are obtained, in absence of any complexing agent.

In general terms, most of the different electrochemical methodologies described in the literature, starting from solutions with or without ligands, from Ir(III) or Ir(IV) salts, even the oxidation of metallic iridium to obtain AIROF, give rise to very similar coatings: blue-colored and with equal electrochemical performance. This feature indicates the likely possibility for all the pre-deposition solutions containing the same precursors: a mixture of iridium (III) and in higher concentration iridium (IV) aquo or/and hydroxyl complexes. This change in iridium oxidation state from (III) to (IV) in alkaline media has been previously reported [28,29]. Also, the tendency of these iridium species to form bridged intermediates in solution, as the ones shown in Figure 3.2 [30-32], yields to the possibility of formation of dimers, trimers, different-size oligomers or even IrO_x colloidal nanoparticles, as some works have proposed [14,18].

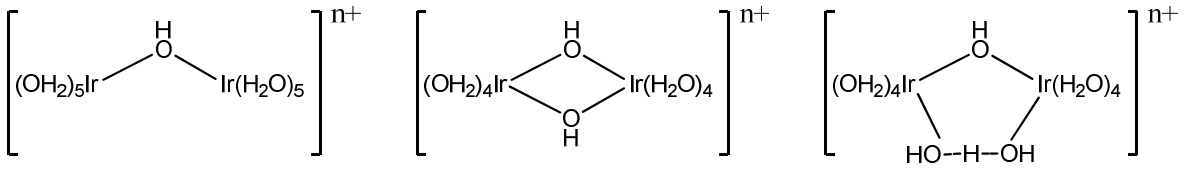

Figure 3.2. Some dimers bridged species for iridium (III) and (IV) in solution [30].

In this work, two pre-deposition solutions, with and without oxalate, have been prepared, studied and used to electrochemically deposit IrOx films, which in turn, have been characterized in order to observe possible differences between them.

3.2 Pre-Deposition Solution Preparation

Preparation of IrOx with and without oxalate films has been performed using the same protocol, described in the Materials and Methods chapter. Both procedures start from a solution with same concentrations or iridium salt and potassium carbonate, but one does not contain oxalic acid. Once prepared, solutions are aged at 37ºC during 4 days. Resulting solutions are very stable and can be kept at 4ºC several months. Only an important decrease in the pH yields to precipitation, as also reported by others authors [14,33].

The color evolution of the pre-deposition solutions during the aging steps can be observed in Figure 3.3. It is possible to appreciate the changes from green to deep blue-violet, according with a coordination change of the metallic center, a change in the oxidation state of the iridium (III), becoming mostly Ir(IV) or/and the formation of polynuclear species.

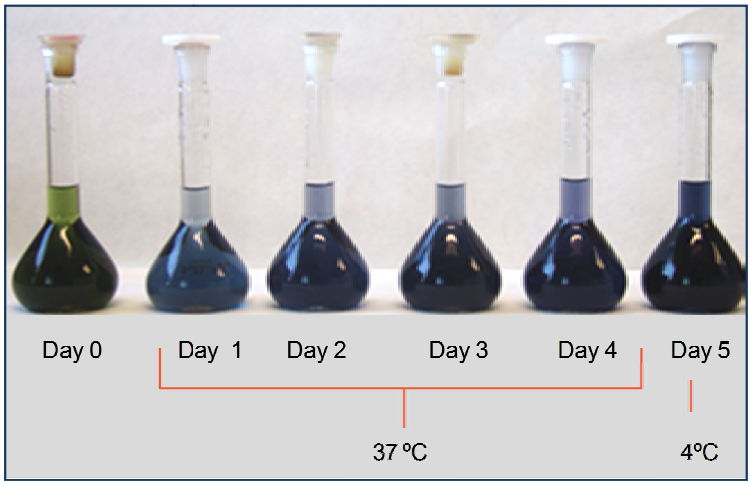

Figure 3.3. Evolution of the IrOx pre-deposition solution (with oxalate) during the aging step. The evolution of solutions without oxalate shows very similar aspect.

A study of ultraviolet-visible (UV-vis) spectroscopy has been done with the aim to elucidate possible chemical changes during the alkaline and aging steps. Figure 3.4 shows the results obtained from the initial $IrCl_3$ aqueous solution, until 4 days of incubation, for solutions with (A) and without (B) oxalate.

The UV-vis spectra obtained for the evolution of both solutions are very similar, with no extra bands or at least not clearly appreciated. Neither the characteristic band of metal-carboxylate is observed, usually around 360 nm [34]. These results suggest that no iridium-oxalate complex is formed or, considering the existence of such complex, the concentration is negligible. Also, the blue color observed, does not agree with the formation of tris-oxalato complexes, since $[Ir(C_2O_4)_3]^{3-}$ is yellow and the oxidized specie $[Ir(C_2O_4)_3]^{2-}$ reddish-orange [35].

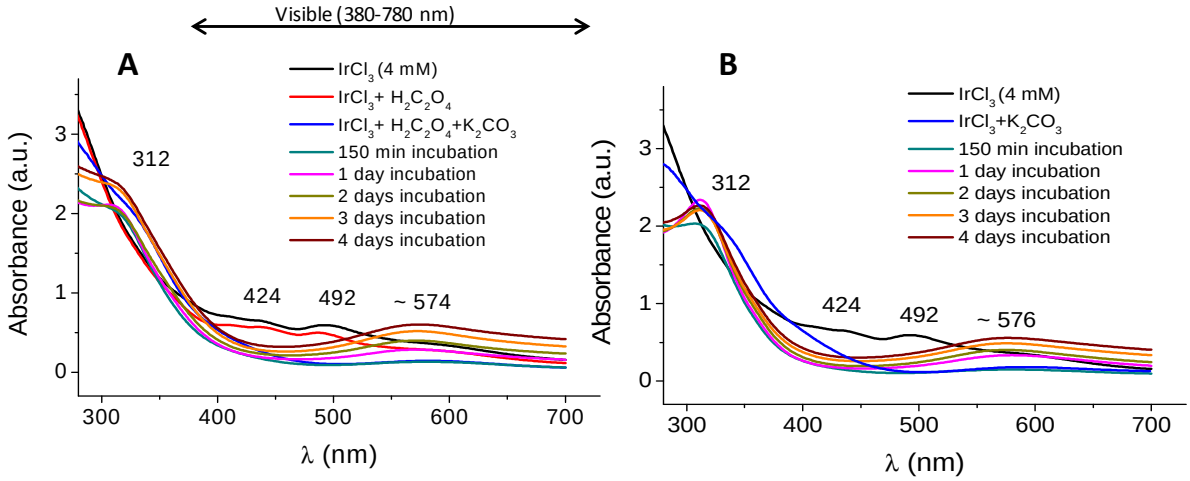

Figure 3.4. Evolution of Iridium chloride alkaline solution. Preparation and aging steps for pre-deposition solutions, with (A) and without oxalate (B).

Both solutions show two defined bands at ~492nm and ~424 nm when $IrCl_3$ is dissolved. This set of bands corresponds with the bond Ir-Cl, as previously reported for $IrCl_3$ and even K_2IrCl_6 iridium compounds in solution [14,36]. Also, similar bands are observed for chloride complexes with different cations, as rhodium [37].

Metal-Cl_n complexes are generally unstable in aqueous solutions, giving a fast release of chloride and the formation of aquo-complexes. However, in $IrCl_3$ solutions, chloride is not released until the pH is increased, as shown in Figure 3.4. The stability of iridium (III) chloro-complexes in water has been previously demonstrated by Bestaoui and Prouzet [15], who connect this inertia with the stable low spin d^6 electronic configuration of iridium (III) complexes [38,39]. They observed, using X-ray

absorption spectroscopy (XAS) experiments, the absence of chlorine release until a huge excess of base added and also, how this alkalinization yields to oxo-chloroiridate oligomers before complete hydrolysis of the chloro-aquo iridium complexes. XAS results showed the presence of only one-third of water molecules in the ligands (Cl/O ratio equal to 0.33), whereas considering monomers in an octahedral environment, this ratio would have been 1. On the other hand, a hypothetical total hydrolysis of the chloride in neutral media, would have lead to the formation of yellow species $Ir(H_2O)_6^{3+}$, the most inert aquo-complex known to date [40] and thus, further reactions would have been improbable.

Once the oxalic acid is added, no substantial changes are observed in the spectrum. However, when the pH increases after the K_2CO_3 addition, the bands at 492 nm and 424 nm disappear, and a new one at 312 nm starts to increase with aging time. This absorption band around 312 nm indicates the hydrolysis of Ir-Cl bonds and the formation of new Ir-OH bonds [41-43]. At this point, the color of the solution is dark green, corresponding with the hydrated complex $IrCl_3 \cdot H_2O$ [44,45] but during aging, the color changes gradually to deep blue-violet. This color change is correlated with the rise of a broad absorption band at 574-576 nm, which is attributed to the condensation of $Ir(OH)_6^{n-}$ complexes to yield polynuclear (Ir-O-Ir) mixed valence species. This condensation releases protons to the media, and in fact, a decrease in pH has been observed during such aging step if carbonate is not added in excess to the pre-deposition solution.

Some authors have demonstrated the existence IrO_x colloidal nanoparticles related with this UV-vis band, showing that at low concentration of iridium chloride precursor (lower than 0.15 mM), the peak at ~575 nm is not longer observed [14,18,46]. In addition, bulk Ir (IV) oxides also show this band, supporting the formation of condensed species with close proximity of iridium atoms, as the band is related with the charge transfer process present in mixed valence polynuclear species [47]. In literature this peak can appear shifted in a range of 570-580 nm, because is highly pH dependent: as the solution becomes more alkaline, the absorption band decreases in intensity and shifts to shorter wavelengths [43].

However, the remaining high absorbance band at 312 nm (Ir-OH bond) indicates that not only IrO_x colloidal nanoparticles conform the solution, but is possible a mixture with the iridium hydrolyzed, $Ir(OH)_6^{n-}$ at observed by Zhao et al. [14] in similar iridium solutions. Even the formation of not only $Ir(OH)_6^{2-}$ or IrO_x colloids but species of intermediate size as Ir(IV)-Ir(III) oxo-hydroxo dimers or bigger oligomers may be considered, due to the ability of these iridium species to condense [29-31,41,48].

The proposed UV-vis band assignation also agrees with the spectrochemical series of ligands: $Cl^- < OH^- < C_2O_4^{=} \sim H_2O$. Based on the Crystal Field Theory, the smallest energy splitting in a possible iridium complex, would be observed with the Cl^- ligand, yielding a larger wavenumber in the UV-vis spectrum in comparison with OH^- , H_2O or $C_2O_4^{=}$ ligands. Thus, a possible iridium complex with any of these others ligands would give a band between the UV zone and 424 nm (Ir-Cl band), as observed for Ir-OH band at 312 nm. Therefore, the band at 571-576 nm (Figure 3.4) cannot be related with any of these ligands, supporting the idea of an intervalence charge transfer (IVCT) band.

The oxidation state of the iridium precursor has also been considered. Initially, the synthesis starts from Ir(III) chloride, but in literature, similar preparations using Ir(IV) precursors yield similar IrOx coatings [16]. The reason is that dissolved oxygen easily oxidizes Ir(III) to Ir(IV) in alkaline media [28,32], or even in acidic media by heating [49]. In previous X-ray absorption fine structure (EXAFS) experiments done in our group, results showed the same oxidation state (3.5) for the iridium in both commercial $IrCl_3$ and $IrCl_4$ reactants [6]. The intermediate valence obtained demonstrates the feasibility of redox transitions between (III) and (IV) iridium states, even in atmospheric conditions. However, in order to determine possible differences in Uv-vis results, the same spectroscopic study has been done starting from $IrCl_4$ in comparison with $IrCl_3$ (Figure 3.5).

The spectra shown in Figure 3.5A are very similar for the two iridium (III) and (IV) chlorides, with the characteristic bands for Ir-Cl bonds at 424 nm and 492 nm. After the pH increase by the addition of K_2CO_3 and 3 days aging, the spectra in Figure 3.5B show the same bands for the three different solutions ($IrCl_3$ with and without oxalate and $IrCl_4$): the peak at 312 nm related with the Ir-OH bond, and the extinction of Ir-Cl

bands, which indicates the complete hydrolysis of iridium-chloride bonds, as well as the corresponding peak at 573 nm, assigned to the formation of IrOx oligomer/colloidal nanoparticles. Hence, no relevant differences in UV-vis results are observed. In addition, electrodeposition of the $IrCl_4$ pre-deposition solution yields blue coatings similar to those obtained starting from $IrCl_3$ solutions.

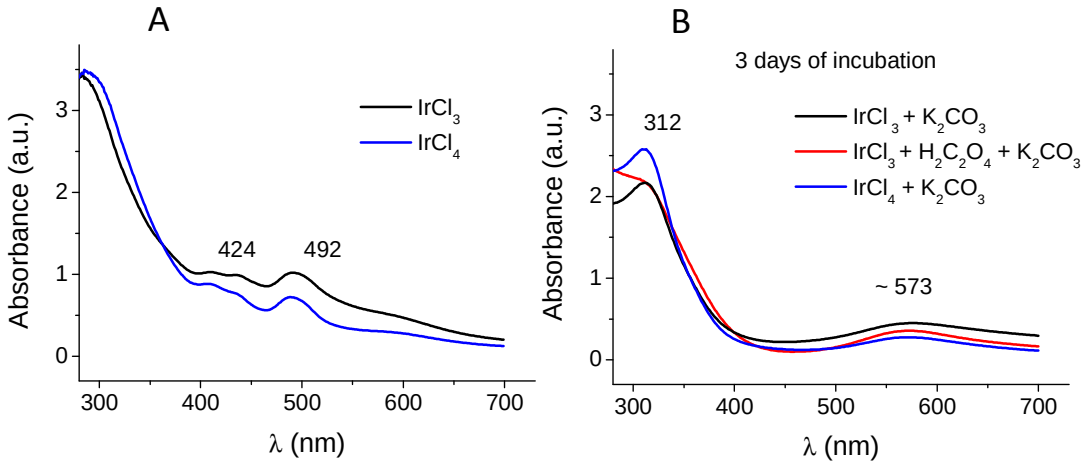

Figure 3.5. Evolution of iridium(III) and (IV) chloride solutions, A) fresh aqueous solutions of $IrCl_3$ and $IrCl_4$ and B) after the addition of potassium carbonate (and oxalate in one case) and 3 days of aging at 37ºC.

The presence of nanoparticles in the pre-deposition solution has been demonstrated in order to support the idea of oligomers/colloids formation instead of iridium-oxalate complexes, which are perfectly soluble. Previously filtered pre-deposition solutions were subject to DLS (Dynamic Light Scattering) and the results show the presence of colloidal nanoparticles in both preparations. For IrOx solution prepared with oxalate, small particles are observed with a medium hydrodynamic diameter of 18 nm. However, for the IrOx without oxalate solutions, the aggregates obtained are considerably larger and the polydispersion more pronounced (Figure 3.6). These results show how oxalate stabilizes the nanoparticles, enhancing the dispersion in the media and partially preventing the aggregation, which is more relevant in the non-oxalate solutions.

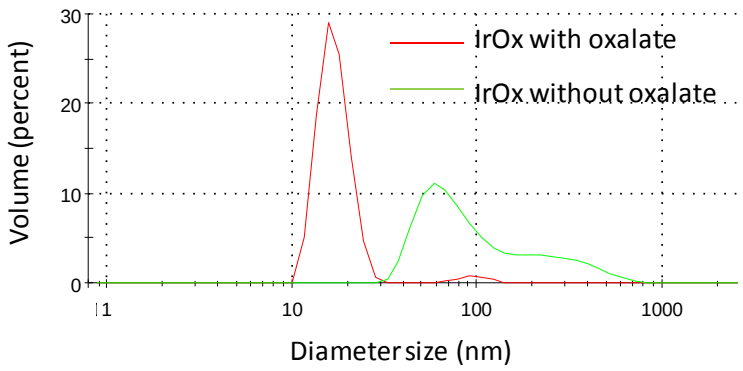

Figure 3.6. DLS results showing the hydrodynamic size distribution by volume of the nanoparticles present in solutions with and without oxalate.

Also TEM images of solutions with and without oxalate show the presence of nanoparticles with diameters in the range 1-3 nm (Figure 3.7). The larger diameter value obtained in DLS measurements is a result of the hydrodynamic diameter, which includes the hydration sphere around the nanoparticles, thus is always larger. Also, the tendency to nanoparticles aggregation is manifested in the non-oxalate solutions.

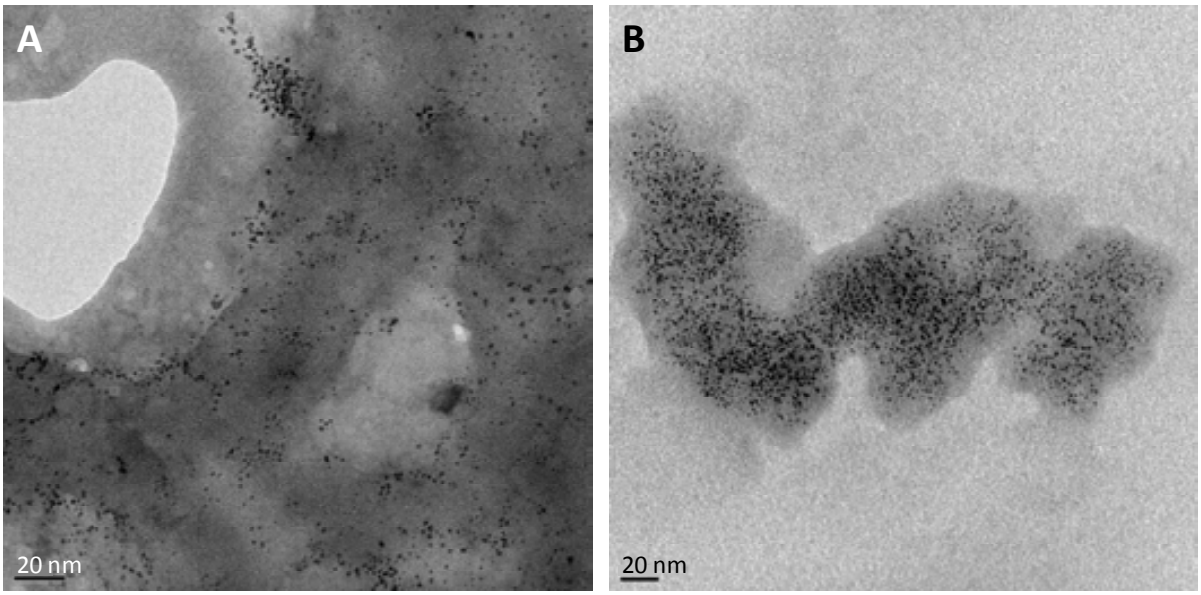

Figure 3.7. TEM images of nanoparticles observed in the previously filtered pre-deposition solutions. A) with oxalate and B) without oxalate.

$IrCl_3$ with and without oxalate alkaline solutions do not show significant differences other than the larger aggregation of iridium precursors in non-oxalate solutions. These results, confirm the absence of any type of iridium-oxalate complex, and the formation of condensed polynuclear $(IrOx)_n$ O-bridged species of variable extension: dimers, oligomers and colloidal nanoparticles (as demonstrated by DLS and TEM), negatively charged and with mixed valence properties as reflected in the broad UV-Vis IVCT band at 570-580 nm [50,51]. In this sense, polynuclear metal-oxo species with similar structure to the proposed for the iridium precursors have been previously reported, as molybdenum, tungsten or ruthenium polyoxometalates [52,53] or the manganese water-oxidizing complex (WOC), which acts as cofactor bound to polypeptides in photosynthetic systems [54,55].

3.3 Electrochemical Synthesis of IrOx Coatings

The electrochemical dynamic deposition of IrO_x depends mainly on three parameters: the upper and lower potential limits, the sweep rate and the number of cycles. In our experiments, IrOx coatings were synthesized by potential sweeps from open circuit potential (OPC) ~0.0V to a voltage of 0.55V vs Pt, at scan rate of 10 mV/s and for 50 cycles, as explained in the Chapter 2. This potential sweep method was used instead of a deposition in potentiostatic/galvanostatic mode, in order to obtain smoother, more homogeneous and better adhered films, as demonstrated by A. M. Cruz in literature [6], in comparison with constant current methods, which yields easily scratched and poorly adhered coatings [56].

The shape of the curves registered during the synthesis is very similar for both solutions, with and without oxalate, as seen in Figure 3.8. However, the intensity reached was larger for the non-oxalate coating synthesis, under the same conditions. The total charge provided to the system was around 45-55 mC/cm^2 for non-oxalate, whereas for the solution with oxalate, this value was 25-35 mC/cm^2. As result, the non-oxalate coating is expected to be thicker, as more charge has passed through the system and more active species have reacted. Thus, a type of hindering is observed in

the deposition of coatings from solutions containing oxalate, suggesting that the stabilization of the iridium precursors by this ligand has a negative effect in the IrOx electrochemical formation.

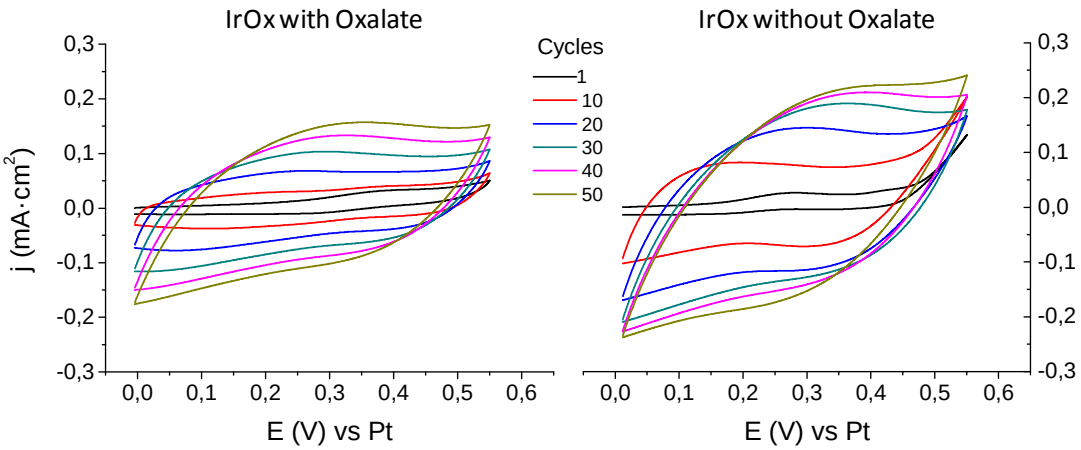

Figure 3.8. Voltammetries corresponding with the synthesis of IrOx coatings, with and without oxalate. Scan rate of 10 mV/s, 50 cycles. For clarity, only one in ten cycles is shown.

The final appearance of the coatings obtained is very similar. Films are well adhered to the substrate, presenting a semitransparent blue color just lightly deeper, or even green-like for the sample without oxalate, which may be related with the larger thickness (Figure 3.9).

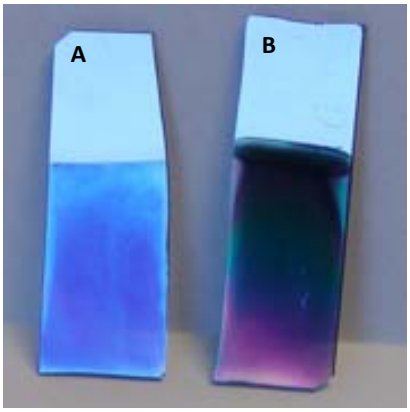

Figure 3.9. Aspect of the 50-cycle IrOx coatings as prepared. A) With oxalate and B) without oxalate.

3.3.1 Synthesis Study by Electrochemical Quartz Crystal Microbalance

EQCM provides an easy way to study the relevant surface situations, such as species transport, adsorption kinetics and film growth [57]. In this work, it was used to determine the mass deposited during the synthesis and the processes occurring in the electrode surface during the first steps of synthesis.

Dynamic electrodeposition of IrOx coatings were performed under the usual conditions, but using a Pt-coated resonant quartz crystal (Q-crystal) as working electrode. Current flow (j) versus potential curves obtained for IrOx with oxalate electrodeposition at room temperature, are shown in Figure 3.10. The similarity of the curves corresponding to the deposition onto the Q-crystal when compared with the normal substrate (Figure 3.8) indicates the validity of this method for a reproducible synthesis study.

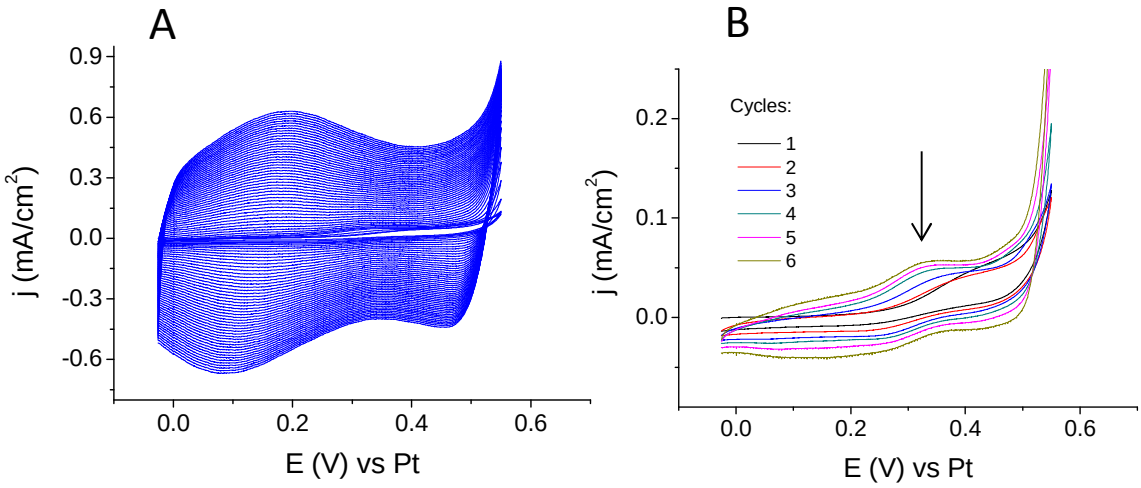

Figure 3.10. Curves j vs E obtained in the dynamic electrochemical synthesis of IrOx with oxalate. A) 50 cycles, B) the first six cycles of the synthesis.

Quantitative EQCM data can also be extracted, but some experimental aspects can modify these results. In first place, the deposited film must have a rigid enough character, to avoid any alterations of the visco-elastic properties of the crystal resonance, particularly when the film is thick [58]. In second place, the equilibrium

conditions have to be respected in order to obtain reliable data, which usually imply slow scan rates and complete redox processes. For example, during the IrOx synthesis (Figure 3.10), the potential is reverted before the peak at 0.55 V finishes thus, the mass recorded, especially at high sweep rates, can be altered for this non-balanced, abrupt change. For these reasons, the quantitative mass data obtained can be subject to deviations. However, in our experiments, results were very reproducible, indicating the validity of the IrOx synthesis for these types of studies.

Figure 3.10A shows the complete IrOx film synthesis on the Pt-coated quartz electrode. Three peaks are observed: two in the anodic sweep at 0.19 V and 0.55 V and one in the cathodic sweep, around 0.09 V. The peak at 0.55 V is not complete, but the process occurring at this potential is the responsible for IrOx deposition. The set of peaks at 0.19 V (anodic) and 0.09 V (cathodic) have been very discussed in literature, and several interpretations exist: minor transitions between Ir (III) and (IV) [266], OH^- interactions [59] or the transition between Ir (IV)/(V) [33,60-63]. After the analysis of the results obtained, we agree with the hypothesis that these set of peaks may correspond with the redox couple Ir^{IV}/Ir^{V}, and it will be discussed properly.

Figure 3.10B shows the first six cycles registered for IrOx (with oxalate) synthesis. The voltammetries obtained, show the suggested Ir^{IV}/Ir^{V} redox couple oxidation and reduction peaks at 0.32 V (anodic) and 0.18 V (cathodic), respectively. Comparing the curves shown in Figure 3.10 A and B, is possible to observe a successive shift towards less positive potentials for this set of peaks as the number of cycles increases, which suggests that the reactions involved are favored in the solid formed on the surface. Changes produced in the deposited IrOx with the successive cycles (as modification of the coordination sphere geometry, for example) can make the coating more easily oxidizable or, this shift can be consequence of pH changes.

Even a relevant shift from 0.4 V to 0.32 V is observed between the second and third cycle, which is suggested to be consequence of the IrOx solid deposited during cycle 2 (Figure 3.11A), since the substrate changes from Pt to the oxide itself. However, as

the interface electrode-electrolyte has changed with the IrOx deposition, this shift is more convenient to be considered as the formation of a new peak, the corresponding oxidation of the deposited IrOx coating instead the iridium in solution. This interpretation does not imply the absence of the former peak (at 0.4 V), which can be overlapped.

Figure 3.11 left axis shows the mass increase respect to the previous cycle versus elapsed time, and on the right axis, the potential reached in each point versus time. The results show a complex mechanism, as no linear mass increase is obtained, but rather successive fluctuations. The mass increase responsible for the coating growth is produced at 0.55 V, but also secondary mass fluctuations are observed: a less pronounced mass increase once the potential is inverted (0.18 V, cathodic sweep, marked as * in Fig. 3.11), and a mass decrease at the beginning of a new cycle (0.36 V, anodic sweep, marked as ** in Fig. 3.11).

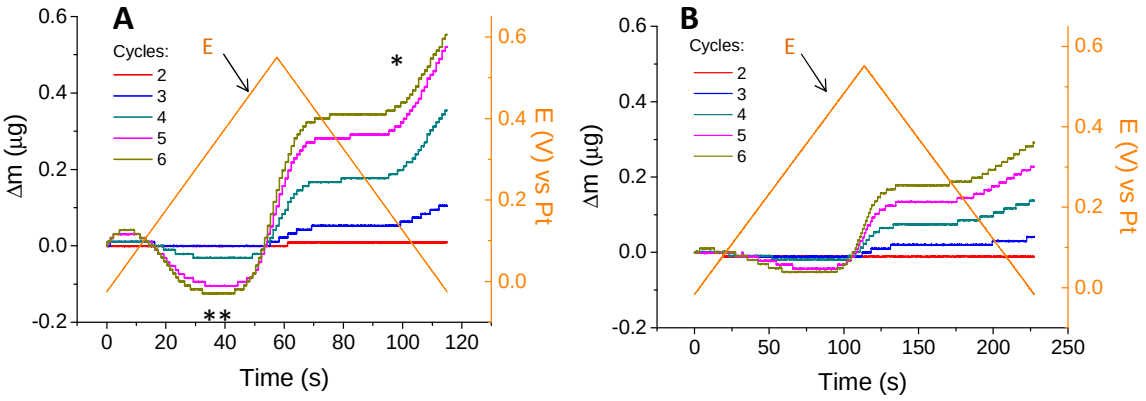

Figure 3.11. EQCM data. Mass (left) and potential (right) changes versus elapsed time, for the first cycles of the synthesis of IrOx with oxalate coatings. A) Normal synthesis at 10 mV/s and B) Slow rate of 5 mV/s. In both figures, the first cycle is not presented because is very unclear, due to the non-equilibrium situation in the electrode at the beginning of the process.

Synthesis under the same conditions but at half sweep rate (5 mV/s), has been performed (Figure 3.11B) in order to compare possible differences with synthesis at higher scan rate. The electrochemical synthesis performed at 5 mV/s yields to a lower

mass deposited in each cycle, compared with synthesis performed at higher scan rates, although the curve shapes are very similar. The final mass of the coating was 13.1 μg, also lower than that obtained depositing at higher scan rates. If we assume the flocculation of IrOx as consequence of a pH decrease localized in the surface of the electrode, lower rates of potential sweep may allow more effective H^+ diffusion to the solution. Consequently, pH is not as dramatically decreased as occurs when the sweep rate is higher, yielding a smaller deposition. Also, secondary mass fluctuations decreased (* and **), but these can be related with the lower mass available for redox reactions.

CV curves obtained in the synthesis of IrOx without oxalate are very similar to those obtained in the oxalate-containing coatings (Figure 3.12A).

The intensity curve of the electrochemical deposition can be very useful for the study of the processes occurring at the surface of the electrode, since the peaks reflect redox reactions. Hence, together with the corresponding mass changes, information of the reactions responsible for the mass fluctuations can be obtained. Figure 3.12B shows the comparison of CV curves (cycle 4) for IrOx coatings with and without oxalate. It is possible to observe how the flat parts of the mass curves correspond with the intensity peaks numbered 1a and 1b. Initially, the mass decrease (at intensity 1a) was interpreted as the oxalate oxidation to yield CO_2 [6]. However, the observation of this phenomenon also in coatings synthesized without oxalate led to raise another hypothesis.

For non-oxalate coatings, the intensity of peak 1a is larger and the related mass decrease smaller than in the synthesis with oxalate presence. This observation indicates that mass decrease and peak 1a intensity are not linearly related. In fact, a study in detail of the mass curves shows that the mass decrease starts at lower potentials, far from the maximum of intensity peak 1a. This observation suggests that a mass decreasing, not related with the intensity peak 1a, is already taking place, probably, the deintercalation of cations since the electrode becomes more positive. Therefore, the reaction corresponding with the intensity peak 1a (an oxidation), may

inject negative species from the solution with simultaneous cation deintercalation, resulting at some point an equilibrated mass change, as the flat part of the curve indicates. Although the intensity peak involves a faradaic reaction, the mass compensation also can be influenced by the migration of negative species to the electrode as it becomes more positive.

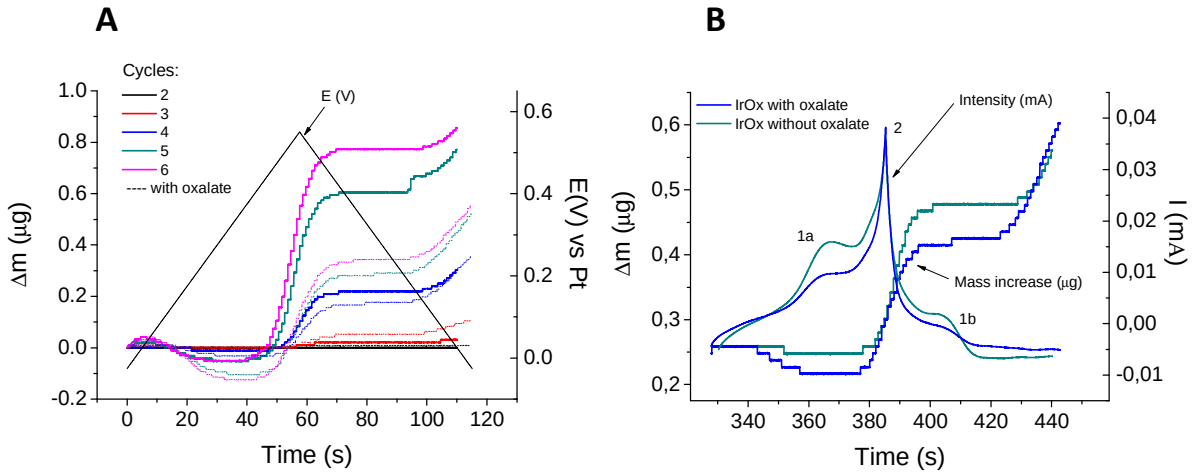

Figure 3.12. Comparison of EQCM data registered during deposition of coatings from solutions with and without oxalate. A) Mass and potential changes versus elapsed time, for the first synthesis cycles. B) Mass increase and intensity recorded for cycle 4 versus time.

Mass changes related with the intensity peak 1b show the opposite tendency. Initially, the mass tends to increase, presumably to maintain electroneutrality incorporating cations once the potential is reverted towards less positive. However, at the maximum intensity, when the faradaic reaction occurs, species are released from the coating, balancing the mass increase, and hence the net mass change is zero.

Despite of the complex mechanism shown, and the probability of simultaneous insertion and release of species, a possible reaction has been proposed. The suggested reaction consists in the deposited IrO_x oxidation to higher states. Starting from mainly Ir^{4+} (favored in alkaline media), the oxidation is proposed to yield species with higher oxidation state.

Simplifying $(IrOx)_n$ polynuclear species to IrO_2 or $Ir(OH)_4$), oxidation reactions between Ir (IV) and Ir (V) are suggested (Reactions 3.1), although other oxidation states cannot be discarded.

$$2IrO_2 + 2OH^- \leftrightarrow Ir_2O_5 + H_2O + 2e^- \quad \text{(Reaction 3.1a)}$$

$$Ir(OH)_4 + OH^- \leftrightarrow Ir(OH)_5 + e^- \quad \text{(Reaction 3.1b)}$$

The oxidation mechanism suggested for iridium in Reaction 3.1a, involves a condensation of the hydroxyl groups with the Ir, yielding an iridium (V) oxide. As the incorporation of hydroxyls is necessary, the resulting balance is a mass injection, which compensates the release of cations observed at the beginning of the each cycle. The reduction reaction therefore, would involve the release of OH^-, which agrees with the experimental data obtained. However, although the oxidation mechanism proposed involves a Ir (V) intermediate, which is oxidized and reduced during clycing, posterior analysis of the synthesized coating does not show any evidence of this high oxidation state, being the valence found for the iridium 3.5 [6].

As mentioned above, the gradually loss of weight observed at the beginning of the first cycles is related with the deintercalation of cationic species, mainly potassium (as is the one in major concentration) as consequence of the increase of positive charge upon oxidation. We have tried to use Faraday's law in this gradually decrease of mass to evaluate the molecular weight of the specie releasing the coating, but the value obtained resulted very high. This result indicates that the cation release is not in concordance with the number of electrons: one electron removed from the electrode does not involve the release of one K^+ ion. But also, the non-equilibrium conditions and the mixed intercalation processes occurring during the dynamic synthesis do not allow the molecular determination.

The abrupt intensity peak at 0.55 V (peak 2 in Figure 3.12B) coincides with the principal reaction responsible for iridium oxide deposition. Starting from a simple electrophoretic idea, the positive potential in the electrode facilitates the migration of the negatively charged hydrated iridium precursors through the electrode surface [403]. Once in contact, according with the mechanism proposed by Nakagawa et al. [33] electro-flocculation occurs. He suggested that, in basic media, the oxidation of water to form oxygen is favored in presence of IrOx, and the potential needed (usually around 1.2 V) decreases, and even at 0.55 V some activity is detected [64,65].

In basic conditions, we can assume that hydroxyls groups bonded to iridium centers or absorbed in the coating in close proximity, are the species involved in the oxygen formation. Protons released by this H_2O/OH^- oxidation decrease the local pH at the electrode surface and, the hydroxyl capping layer (complexing or stabilizing the IrOx nanoparticles/oligomers) partly neutralizes, yielding the deposition. The flocculation and precipitation of black hydrated IrOx is well observed when the pH of a normal solution is decreased until pH=7, corroborating this hypothesis.

Another feature supporting this idea is the fact that iridium oxide is a powerful water oxidation catalyst to O_2 [33,62-67] and, as can be observed in Figure 3.10B, since the cycle 3 when significant oxide has been deposited, the intensity reached for the peak at 0.55 V is higher compared with the preceding value. Therefore, the redox OH^-/H_2O oxidation reaction is favored when more IrOx is deposited, as predicted. The oxygen formation has not been proven in our lab, but Nakagawa obtained very high conversions with a similar IrOx as catalyst, and other authors have shown similar curves at high pH values, corresponding with the oxygen evolution [64,65]. On the other hand, oxygen evolved on a metal electrode can react with the metal itself to form an oxide thus, the potential at which O_2 is macroscopically observed at the electrode does not correspond with the potential at which the reaction starts [68]. Consequently, it is not necessary the entire conversion of hydroxyl/water to O_2 to occur, and considering the oxidations as a radicalary reaction, only the first steps may be taking place at low potentials. These oxygen radicals formed would improve the

oxide synthesis instead of the complete oxygen evolution. A proposed radical reaction, starting from a supposed iridium octahedral complex, $Ir(OH)_6^{n+}$, can be:

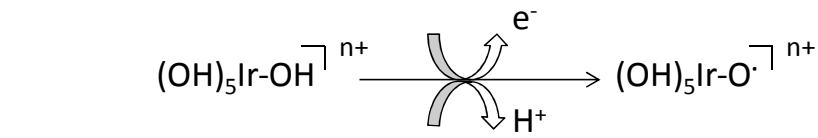

(1)

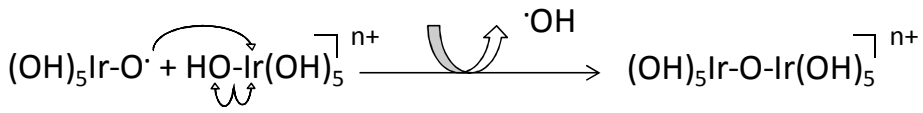

(2)

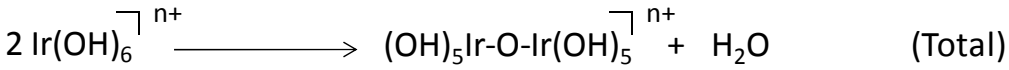

(Total)

The net reaction is a condensation and does not involve any iridium redox reaction but however, it can be initiated by the hydroxyl oxidation and loss of an electron. The first step can explain why this type of iridium oxide is a very good catalyst to obtain O_2: if the loss of an electron and the creation of a hydroxyl radical ($^{\cdot}OH$) is favored, the highly reactivity of this $^{\cdot}OH$ compared to OH^-, can improve further reactions until the O_2 formation. This theory is has not been proved, but is proposed as possible mechanism, similar to the one used when heterogeneous catalysts are involved.

This hypothesis also agrees with results found by Kötz et al. [69]. In their experiments, probe beam deflection (PBD) was used to determinate whether ions are released from the hydrous oxide film into the electrolyte or injected into the film from the bulk electrolyte, by comparison of the concentration in the electrode surface. They demonstrated that in alkaline media, during oxidation (at potentials near 0.7 V) the electrolyte concentration in the interface decreases and therefore, anions (OH^-) are consumed.

The behavior described above evolves with time, as more materials is deposited. Figure 3.13 represents the intensity, the potential and the mass increase versus elapsed time for the different cycles during a complete synthesis (50 cycles), to have a general vision of the process. The main wave at 0.55 V increases in intensity with the number of cycles, until it reaches a constant value, around cycle 10 (Figure

3.13A). On the other hand, the mass increase (related with this peak) for each cycle is maintained almost constant from the same cycle, as can be seen in Figure 3.13B. These features support the hypothesis of condensation proposed: initially, the material condenses only from the solution in contact with the electrode, but when some IrOx is deposited, the condensation and the water oxidation can come from deposited IrOx itself, increasing the intensity until saturation, which involves a constant surface available.

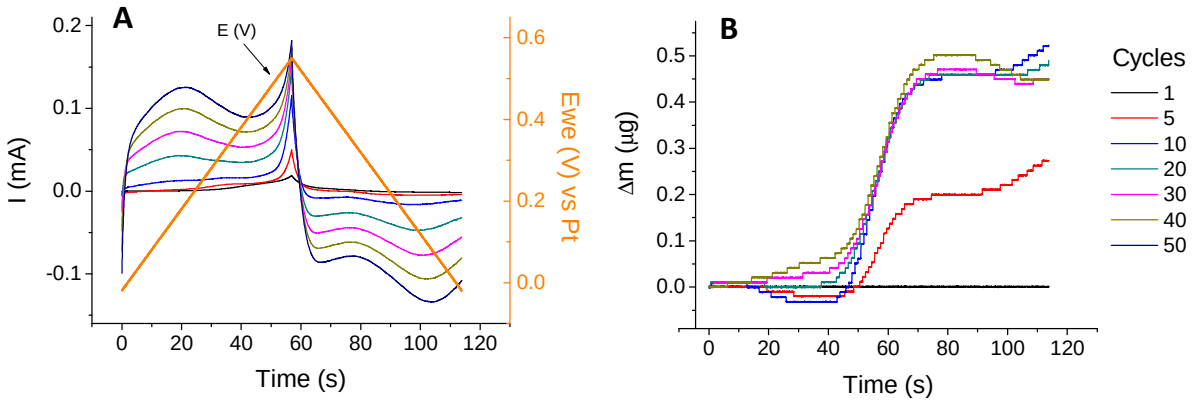

Figure 3.13. EQCM data for IrOx with oxalate: A) Intensity and the potential versus elapsed time and B) mass increase versus the elapsed time, for the entire synthesis. Only one in ten cycles is shown for clarity.

Figure 3.13 also shows how the intensity peaks 1a and 1b (numerated in Figure 3.12B) increase with the successive number of cycles, according with the suggested redox reactions involving the Ir^{4+}/Ir^{5+} couple: intensity would increase proportionally with time, as thicker coatings have more material to be oxidized or reduced. However, Figure 3.13B shows that the mass changes related with these intensity peaks (1a and 1b) revert the tendency observed in the first cycles. Cycle 20 shows a mass increase instead of the loss weight observed in the first cycles (and vice versa for reduction). Thus, according with the Reaction 3.1, as the coating becomes thicker, OH^- groups can be easily intercalated or deintercalated in/to the material, but the mobility of neutral water molecules and K^+ is hindered giving a net result of mass

increase, corresponding with intensity peak 1a, or mass decrease, corresponding with intensity peak 1b.

Figure 3.14 is shows the comparison between mass changes versus cycle number for the synthesis of both coatings. As expected, mass is increasing with the charge provided to the system, in an almost linear tendency. This linearity is indicative that coatings behave as semi-rigid films, which grows homogeneously. However, at the beginning of the synthesis the mass deposition is slower, as the slope of the line indicates, suggesting that IrOx can be easily synthesized on the oxide surface than in platinum substrate.

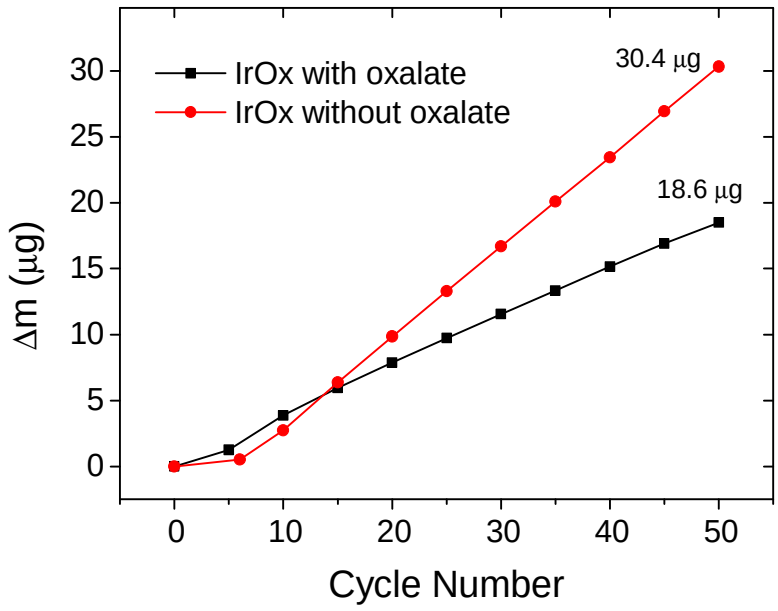

Figure 3.14. EQCM data for the mass increase versus the number of cycles for the synthesis of both IrOx coatings, with and without oxalate.

The total final mass of the coatings is 30.4 µg and 18.6 µg for the non-oxalate and oxalate-containing films respectively, which corresponds with a mass ratio of 1.6 times larger for non-oxalate coatings, under the same conditions of synthesis. As seen in the electrochemical synthesis section, the charge provided to the system during the deposition of non-oxalate coatings is almost 1.8 times higher than the

obtained for the deposition of IrOx with oxalate coatings. The close coincidence between the two values (charge and mass) indicates the linearity observed for these two parameters, which suggest that no side reactions other than water oxidation are involved. Hence, the differences observed in final mass deposited between the two solutions have to be correlated with an impediment during the synthesis process, presumably by a higher stabilization of the polynuclear iridium precursor by oxalate anions, which act as growth-inhibiting substance.

In order to better understand the synthesis mechanism and the mass fluctuations produced by ionic migration, the same protocol has been used to prepare IrOx with and without oxalate coatings but with Na_2CO_3 instead of potassium carbonate. Mass and intensity versus time curves are very similar to those obtained in the regular synthesis with K_2CO_3 however, the total mass deposited was lower, around 24 μg and 11.3 μg for coatings without and with oxalate, respectively, being the mass ratio without/with oxalate of 2.1, slightly larger than that obtained for potassium carbonate synthesis (1.6). This fact indicates that the stabilization attributed to the oxalate anions, enhances when sodium instead of potassium is present in the solution. The lower mass deposited for coatings with sodium, can be explained due to an enhanced stabilization of the iridium precursors in solution when sodium is present, or, considering that Na^+ is smaller than K^+, is more easily released from the coating during the synthesis, yielding to a lower sodium quantity in the film compared with the potassium content in the coating with K_2CO_3. In this sense, a posterior XPS analysis will be very useful.

Figure 3.15 shows the first steps in the synthesis of IrOx without oxalate prepared with Na_2CO_3 buffer. The mass deposited in each cycle is lower, and the mass fluctuations at 0.36 V (anodic) and 0.18 V (cathodic) less pronounced (Figure 3.15A) than those obtained in the synthesis with K_2CO_3. Therefore, the coating is growing slower, and a slight mass loss (related with the intensity peak 1a) is only observed from cycle 10, indicating the necessity of thicker coatings to observe mass fluctuations related with Na migration. Figure 3.15B shows how the intensity reached

during electro-flocculation is lower than those obtained for K_2CO_3 buffered solutions, indicating the influence of the cation used for the synthesis.

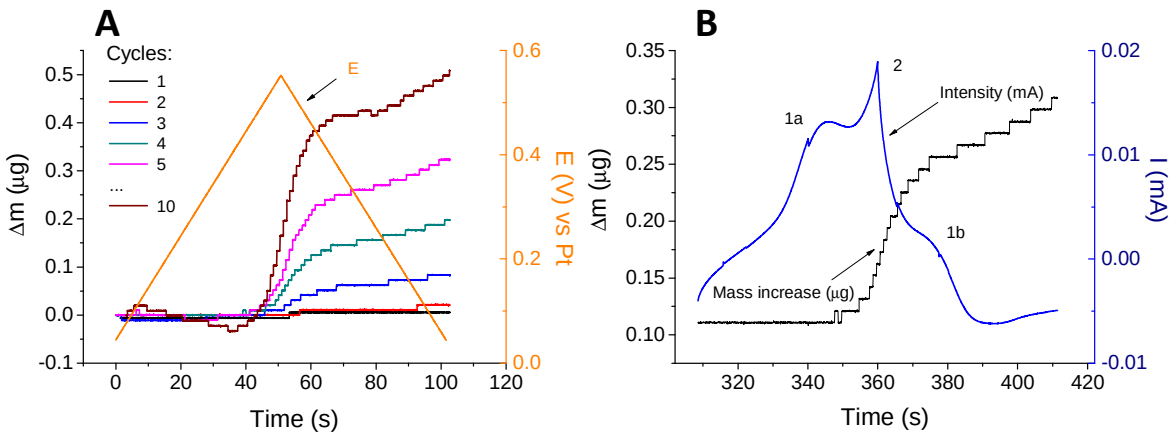

Figure 3.15. EQCM results showing the first cycles obtained for the synthesis of IrOx coating without oxalate and with Na_2CO_3 instead of K_2CO_3. A) Mass and potential changes versus elapsed time for the first cycles and B) mass and intensity changes versus time for cycle 4.

After the analysis of the EQCM results, a complex mechanism of deposition is suggested: an initial oxidation of water/hydroxyl groups coordinated to the iridium, followed by a proton release and dehydration, with the consequent formation of oxy- or hydroxy- bridges. This condensation results in a loss of the polymeric network structure and the condensed insoluble oxide resultant, with oxygen bridges between iridium centers, deposits onto the electrode surface. This proposed mechanism agrees with the results obtained in UV-vis and EQCM experiments, and explains the highly hydrated and porous final oxide structure, in addition to the large and reproducible K^+ content. These conclusions coincide in some aspects with previous works published by Elsen [56] and Steegstra [70]. Finally, the stabilization of the polynuclear iridium precursors produced by oxalate anions has been demonstrated and, although the mechanism has not been envisaged, it has been shown how this stabilization influences the electrochemical deposition.

3.4 Characterization Techniques

The characterization of both IrOx samples was carried out with the purpose of finding remarkable differences between them. For example, evidences of the existence of oxalate in the coatings, or structural changes due to the presence of the oxalate in the pre-deposition solution, as well as possible changes in the electrochemical behavior. Also, basic characterization aspects for subsequent comparison with the hybrids prepared and characterized in the chapters 4 and 5.

3.4.1 Grazing Incidence X-Ray Diffraction

The main characterization technique to know about the chemical structure of the coatings is X-Ray Diffraction (XRD). However, for these types of electrochemically synthesized oxides, the structure is more like a non-crystalline oxohydroxide, highly hydrated [71,72], as shown XRD patterns for as prepared samples.

Grazing incidence X-Ray measurements of the as prepared and annealed coatings have resulted in data shown in Figure 3.16. The necessity of grazing incident angle is due to the thin nature of the coatings. With this technique, small angles are representative of the most superficial phases, whereas large angles are representative of the total sample. Thus, to obtain an optimal pattern representative of the IrOx thin film, angles of 0.5^{o} have been used.

The pattern for the heated (and hence, crystallized) coating is coincident with that published for the structure of monoclinically distorted hollandite, with formula K_xIrO_2 (space group I2/m) [13]. The structure for this oxide may be described as built up from IrO_6 octahedra, sharing edges and corners, around holes occupied by potassium ions, as can be seen in Figure 3.17, where the structure scheme is shown. In absence of potassium, the diffractogram is considerably altered, showing the importance of its presence and quantity in the conformation of the final structure. The monoclinic distortion has been presumably attributed by Bestaoui et al. [13] to the existence of sites occupied for iridium atoms with different oxidation states, as the measured Ir-O distances were between that found for Ir(III) and Ir(IV). Similar iridium valence has

been obtained from quantification of XPS results, and also, the blue color of the coatings (related with the IVCT band observed in UV-vis) demonstrates this mixed valence in IrOx coatings.

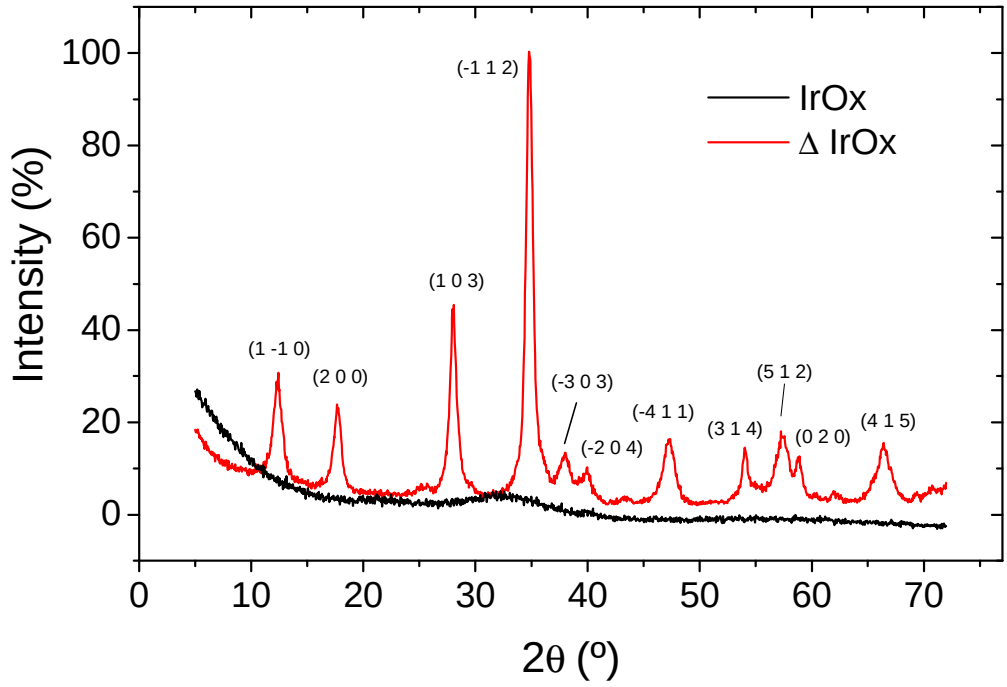

Figure 3.16. GIXRD pattern obtained for IrOx (with oxalate) coatings as prepared and after a 4h-thermal treatment at 500ºC in air. The most intense peaks are indexed corresponding with the previously published structure for K_xIrO_2 hollandite-type.

This structure differs from the obtained for IrO_2 synthesized by other methods, as the thermal procedure which usually yields rutile-type structure [73]. Also, previous experiments in our laboratory using different annealing methods, yield to rutile-type IrOx coatings, usual structure observed in other transition metal dioxides as TiO_2, RuO_2 or OsO_2. Therefore, the thermal treatment conditions used in the crystallization process is an important factor and different conditions induce rutile-type structure or the intermediate hollandite, with bigger channels to allow potassium incorporation and mobility. Both structures are clearly related, and a thermal process involving the formation and sublimation of KO_2, can yield to the transformation of holladyte-type K_xIrO_2 to rutile-type IrO_2.

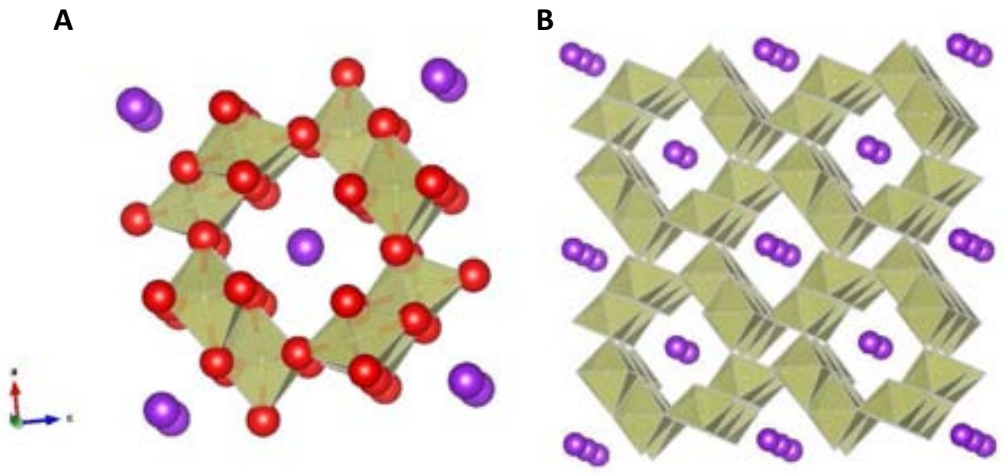

Figure 3.17. 3D images of the hollandite-type structure of $K_{0.25}IrO_2$, calculated by VESTA program and with data obtained from [13]. A) Unit cell and B) some unit cells to appreciate the ionic channels, where potassium ions (violet) are located.

3.4.2 X-Ray Photoelectron Spectroscopy

XPS was used to determine the elements present on the surface and the superficial atomic stoichiometry of the coatings. IrOx with and without oxalate samples, have been analyzed and the resulting general spectra are shown in Figure 3.18.

In XPS measurements, a general survey gives an idea of the elements present in the surface and a quantitative relation between them can be done, as the area of each peak is proportional to its concentration in the surface (Table 3.1). The analysis of the spectrum has been done using the Multipack software.

Analyzing the results obtained, both IrOx materials have very similar surface composition, showing iridium, oxygen, carbon and potassium. The high and reproducible concentration of potassium atoms is a demonstration of the cationic retention during the synthesis, initially to maintain the net charge of the oligomers/nanoparticles and that during the formation process are retained in the porous structure. Previously to this work, it had been demonstrated in our

laboratory, that when coatings are soaked in distilled water, potassium is released presumably by ionic exchange H^+/K^+ [6], which reinforces the idea of a very porous structure.

The unexpected high concentration of carbon in the surface is mainly due to the adventitious carbon (C_{ad}) present in the atmosphere, and adsorbed in the IrOx surface as an impurity, which also may alter the oxygen surface concentration. Iridium and potassium concentration is not modified by these impurities, so the relation K/Ir is an indicative of the similarity of the coatings. In this case, the K/Ir relation is 1.78 and 1.85 for coatings with and without oxalate, respectively.

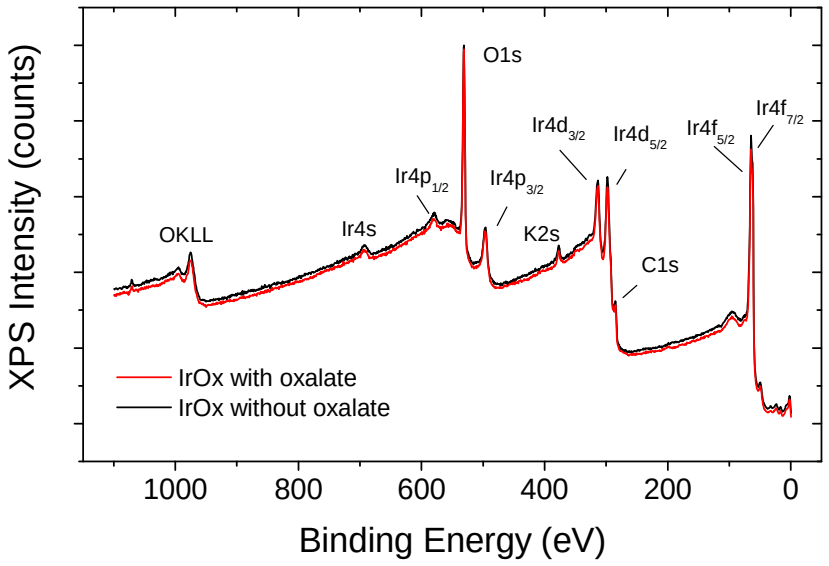

Figure 3.18. Comparison between XPS spectra for samples of IrOx with and without oxalate, prepared under the same electrochemical conditions.

Samples	C1s (at.%)	O1s (at.%)	Ir4f (at.%)	K2p (at.%)	O/Ir	K/Ir
IrOx with oxalate	15.7	47.6	13.2	23.5	3.6	1.78
IrOx without oxalate	14.8	47.0	13.4	24.8	3.5	1.85

Table 3.1. Quantification (atomic %) for IrOx with and without oxalate coatings, obtained from the data of the XPS survey spectra.

The binding energy (BE) of each peak is directly related with the chemical environment of the corresponding atom. Consequently, a study in detail of the spectra can be done for some particular elements, making a Gaussian-Lorentzian deconvolution of the main peaks and separating the different contributions.

The Ir4f analysis show an asymmetric peak-shape at BE locations of major and minor Ir $4f_{7/2}$ and $4f_{5/2}$ peaks around 62.0 eV and 64.9 eV respectively (Figure 3.19). These data coincide with the results in literature [74]. The BE value gives information about the oxidation state of the metal, but in the case of iridium, it can only differentiate between the metallic form (oxidation state 0) and oxidized species [75]. Therefore, as main conclusion, we do not detect presence of metallic iridium in our coatings. The asymmetric peak shape is normal for conductive samples, such as metals or graphite, due to a distribution of unfilled one-electron levels [76].

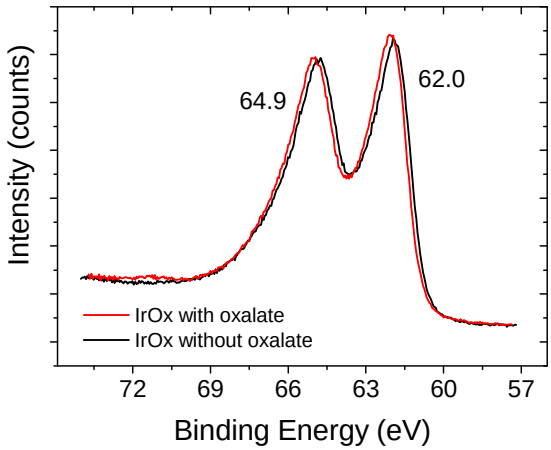

Figure 3.19. Ir4f XPS spectrum for IrOx with and without oxalate samples.

C1s and O1s deconvoluted spectra are shown in Figure 3.20 and the quantification of the deconvoluted peaks respect the total sample, in Table 3.2.

O1s deconvoluted spectrum shows a well defined peak centered on 531.5±0.2 eV, corresponding with the signal obtained for the groups: OH^-, C=O and COO^-. This contribution is the larger, corroborating the oxo-hydroxide structure of the coatings, as previously reported in literature [6]. The other peaks correspond for the signal of

O^{2-} in the oxide and the adsorbed water, at binding energies of 530.0±0.2 eV and 533.2±0.2 eV, respectively.

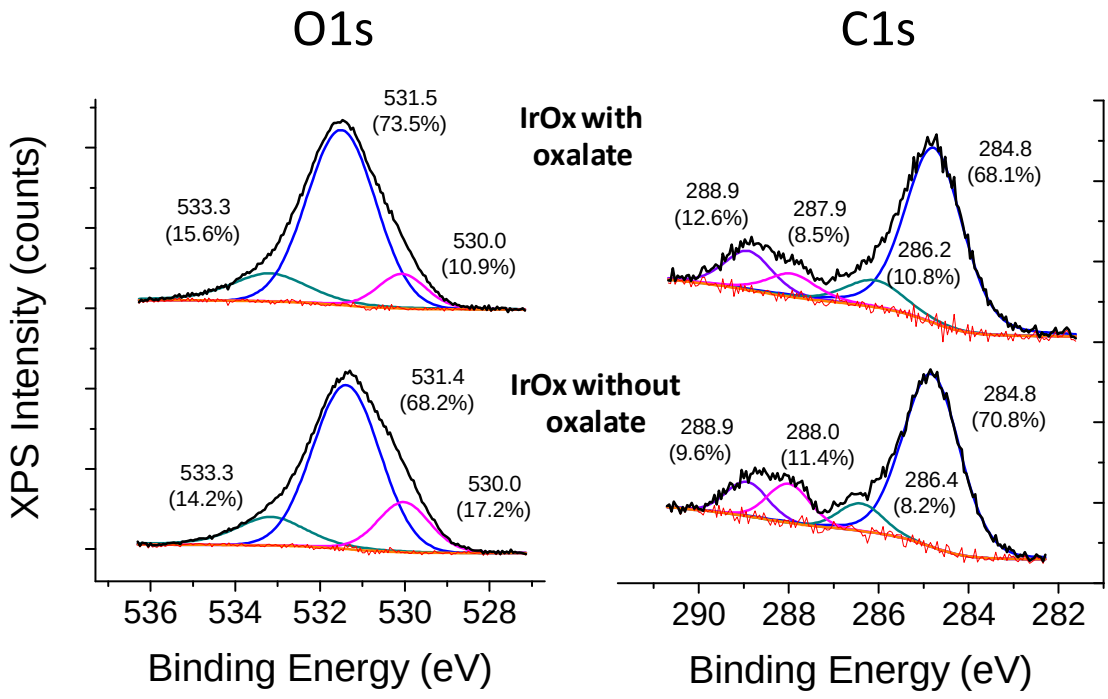

Figure 3.20. Deconvolution of O1s and C1s peaks from the high resolution XPS spectra for IrOx with and without oxalate samples, prepared in the same electrochemical conditions. The contribution of the different peaks to the total peak is expressed in brackets.

C1s spectrum is dominated by a strong hydrocarbon (C-C, C-H) signal, which was used as spectral calibration and corrected to be 284.8±0.2 eV, as usual [77]. Other important contributions of the deconvoluted peak are seen at binding energies of 286.2±0.2 eV (C-OH, C-O-C), 287.9±0.2 eV (C=O) and 288.9±0.2 eV (COO^-).

The absence of peaks corresponding to carbonate, with a typical BE of 286.6±0.2 eV [78,79], being the buffer used during the synthesis, corroborates no retention in the IrOx coatings. Also, no presence of chloride is detected, whereas is commonly retained in other synthesis methods [15].

	Peak assignation/ Position (eV)	IrOx with oxalate (atomic %)	IrOx without oxalate (atomic %)
O1s	O^{2-} /530.0	5.2	8.1
	OH^-,C=O, COO^-/531.5	35.0	32.0
	H_2O/533.3	7.4	6.9
C1s	C-C, C-H/284.8	10.7	10.5
	C-OH, C-O-C/286.2	1.7	1.2
	C=O/287.9	1.3	1.7
	COO^-/288.9	2.0	1.4

Table 3.2. Total quantification of the O1s and C1s peaks components (atomic %) in the studied coatings. Percentages add up to the total quantity of each element from the survey: carbon: 15.7% and 14.8%, and oxygen 47.6% and 47.0%, for IrOx with and without oxalate coatings, respectively.

The results obtained show a very similar chemical surface composition for both coatings. The total amount of aliphatic carbon is also very similar, as expected for samples exposed to air the same time after preparation, and subject to equal treatment before XPS measurements. Also in both cases, the C1s data for C-OH (~1.5%) is considerably lower than the correspondent OH^- percentage for O1s, (33.5%), which suggests that the majority of the OH^- are not bound with carbon, but to iridium. Other observation is that the non-oxalate film presents more lattice oxygen (O^{2-}) and less OH^-. As observed in previous EQCM and TEM experiments, the stabilization of iridium precursors by oxalate, slows down the IrOx synthesis in some way, so the condensation when no oxalate is present in the media is more effective, giving rise to more O-Ir-O bonds.

As mentioned above, the carbon observed in these samples can be considered mostly as adventitious carbon, common in this type of oxides [74]. But for these samples, in a reproducible manner, the measured carbon levels (around 15%) are higher than might be expected on the basis of adventitious carbon (generally 10%) [80], indicating

a large affinity of iridium oxide for carbonaceous species. Adventitious carbon is a thin film of carbonaceous species, generally formed by a variety of (relatively short chain, perhaps polymeric) hydrocarbons species with small amounts of both singly and doubly bound oxygen functionalities. Hence, not all the oxygen determined by XPS will correspond to the oxide; a small amount belongs to carbon impurities. To estimate the organic contribution to the O1s spectra pertaining to adventitious carbon, the formula proposed by Payne et al. [78] was used (Equation 3.1). The first step is to calculate the atomic percentage corresponding to C1s normalized intensity (obtained in Table 3.1). From these intensities, the corresponding normalized O1s concentrations were obtained using the expected O/C relations for the individual functional groups, as indicated in Table 3.3. Finally, the normalized O concentrations were then converted to the respective O1s peak areas. The summary and the final resulting equation is shown in Equation 3.1.

$$O_{ad} = \frac{C_T}{100}\left(1 + C + D + \frac{D}{2} + 3E + 2\frac{(B - D/2)}{3}\right) \qquad \text{(Equation 3.1)}$$

where O_{ad} is the percentage of organic oxygen contribution, C_T the total carbon concentration and the letters B-D correspond with the different C-O* groups described in Table 3.3.

In addition, to quantify a random adventitious carbon sample the next assumptions have to be done:

1) It is assumed that the amounts of the two components of D will be equally split between the two species, so has to be greater than 1/2 D - if not then this assumption cannot be valid.

2) It is assumed that the amounts of the two components B(1) and B(2) will be equally split between the two species. Thus the Carbon/Oxygen ratio for these combined peaks will be 3 Carbon: 2 Oxygen.

Peak and Species Breakdown	Carbon : Oxygen
A) Main Peak (284.8 eV)	
C-C, C-H	No Oxygen
B) Peak at A + 1.4 eV to 1.6 eV	
R_3C-OH (B1)	1 Carbon : 1 Oxygen
R_3C-O-CR_3 (B2)	2 Carbon : 1 Oxygen
R-(C=O)-O-C*R_3 (B3)	1 Carbon : 1 Oxygen
C) Peak at A + 2.8 eV to 3.0 eV	
R_2C=O	1 Carbon : 1 Oxygen
D) Peak at A + 3.7 eV to 4.3 eV	
R-(C*=O)-O-CR_2	1 Carbon : 1 Oxygen
R-(C*=O)-OH	1 Carbon : 1 Oxygen
E) Peak at A + ~4.0 eV to ~5.5 eV*	
Carbonate -(CO_3)	1 Carbon : 3 Oxygen

Table 3.3. Different oxygenated groups present in adventitious carbon, the binding energy shift respect to the main peak at 284.8 eV and the relation expected of carbon:oxygen.

With these premises, after applying the formula, the total oxygen atomic percentage without adventitious oxygen (O_{ad}) contribution is 42.8% and 42.8% for IrOx with and without oxalate, which gives an O/Ir value of 3.24 and 3.19, respectively. In order to calculate the charge balance, the water oxygen contribution can also be removed from the calculus to adjust the result, and the new values obtained are: 2.68 and 2.67 for oxalate and non-oxalate coatings respectively. This new O/Ir relation gives an idea of the oxidation state of the metal. For example, considering IrO_2 and Ir_2O_3 oxides, the relation expected would be 2 and 1.5. However, for the corresponding hydroxides $Ir(OH)_4$ and $Ir(OH)_3$, the O/Ir relation is 4 and 3, respectively. The experimental results obtained do not coincide with any of these expected relations, suggesting the formation of an iridium oxohydroxide with mixed valence (III)/(IV). These non stoichiometric values obtained for O/Ir ratios have been previously reported for this type of materials [71].

The importance of the adventitious carbon consideration and the influence in XPS results is noticed in Figure 3.21, which shows the XPS C1s spectrum of two IrOx samples (with oxalate and same electrochemical preparation) measured 1 and 6 months after preparation. Spectra have not been normalized to better appreciate the difference, which is notable. Moreover, the survey quantification gives a carbon percentage value for the older sample of 60.2%, almost 4 times larger than the value obtained for the recent one (15.7%).

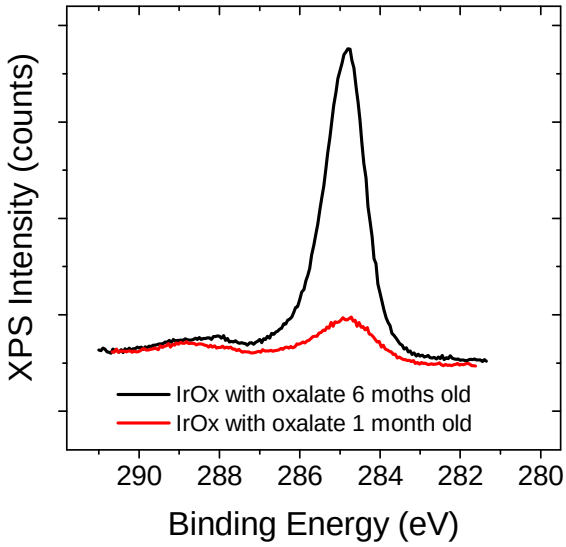

Figure 3.21. XPS spectra for C1s of two IrOx with oxalate coatings, one measured after one month of preparation and the other one after six months.

Different synthesis conditions have been performed in order to study the mechanism synthesis of the coatings. In the EQCM section, synthesis of IrOx (with and without oxalate) with Na_2CO_3 instead K_2CO_3 was presented. The macroscopic aspect was very similar, but to study the chemical surface composition also these samples have been subject to XPS experiments. In addition, IrOx coatings synthesized with another type of base, KOH, have been obtained and compared with previously shown IrOx coatings. In the Table 3.4 the chemical atomic composition for coatings without oxalate prepared in different alkaline media are presented.

Samples	C1s (at.%)	O1s (at.%)	Ir4f (at.%)	K2p (at.%)	Na1s (at.%)	O/Ir	K/Ir
IrOx without oxalate (K_2CO_3)	14.8	47.0	13.4	24.8	0	3.5	1.85
IrOx without oxalate (Na_2CO_3)	55.5	33.9	8.1	0	2.5	4.2	0.3
IrOx without oxalate (KOH)	49.1	32.3	7.6	11.0	0	4.25	1.4

Table 3.4. Quantification (atomic %) for IrOx without oxalate coatings prepared in different alkaline media, obtained from the data of the XPS survey spectra.

The results obtained in the quantification show a very high percentage of carbon for the samples prepared using Na_2CO_3 and KOH however, this is related with the time of preparation of the coatings when the measurement was done, as demonstrated in the IrOx-KOH sample, for which no source of carbon is introduced during the synthesis, therefore all C content can be assumed to come from atmospheric carbon. Considering this feature, the high values obtained for O/Ir relations can be consequence to the increase produced in the O-content due to the C_{adv} presence. This oxygen coming from the impurities, can be calculated with the Equation 3.1 and after the subtraction the recalculated O/Ir relation is around 3.3 for both coatings, very close to that value obtained for IrOx without oxalate coatings when the O_{adv} is removed, 3.19.

Also, the concentration of cations in the coatings is relevant. When KOH is used for the synthesis, the relation K/Ir is close to that obtained in conventional IrOx coatings. However, when Na_2CO_3 is used, the concentration of Na^+ in the films is very low and the relation Na/Ir decreases until 0.3. This low content of sodium in the coatings after the synthesis agrees with the results obtained in EQCM experiments, suggesting higher sodium release during the formation of the films (and possibly exchange with protons) in compassion with potassium, obtaining therefore, lower sodium final content, which can influence the final mass of the coating.

The study of the deconvoluted peaks O1s and C1s do not provide any relevant information. C1s spectra coincide with the typical obtained for adventitious carbon, and O1s spectra is very similar to those obtained in Figure 3.20, with comparable percentages obtained for O^{2-}, -OH and H_2O components.

These results indicate not only the macroscopic similarity of the coatings (semi-transparent blue ones), but the surface chemical composition, which consists in an iridium oxohydroxyde with a large non stoichiometric range. Only small differences in terms of cationic concentration are observed, indicating the valid synthesis of IrOx films independently of the base added to the media (K_2CO_3, Na_2CO_3 or KOH).

In conclusion, iridium oxide coatings with and without oxalate produced by dynamic deposition yield a very similar surface chemical composition, with most of the coordinate oxygen species being terminal (OH^- or H_2O), rather than bridging, as previously observed for other hydrated oxides [81]. High concentration of atmospherical carbon is adsorbed in the surface, and the porous structure allows the retention of large quantity of potassium cations that can be easily exchanged with other charged species in solution after soaking. However, when the synthesis is done using smaller cations, as sodium, the release during the synthesis is more pronounced, and the final concentration in the coating is lower. Also, the only requirement to successfully synthesize IrOx coatings has been demonstrated to be an aged iridium salt in alkaline media, as the obtaining of IrOx films in different conditions has shown. The iridium oxidation state cannot be clearly resolved, but it is supposed to be between III and IV, as the stoichiometric ratios demonstrate. The mixed valence of IrOx in the coatings presents an advantage and it is the basis of these new materials.

3.4.3 Infrared Spectroscopy

The high hydration of the IrOx samples has been studied by infrared spectroscopy measurements. In Figure 3.22 ATR-spectra are shown for samples of IrOx with

oxalate, as prepared and heated during two hours at 100°C. In this case, no measurements of IrOx without oxalate were done, after considering that no relevant differences would be observed.

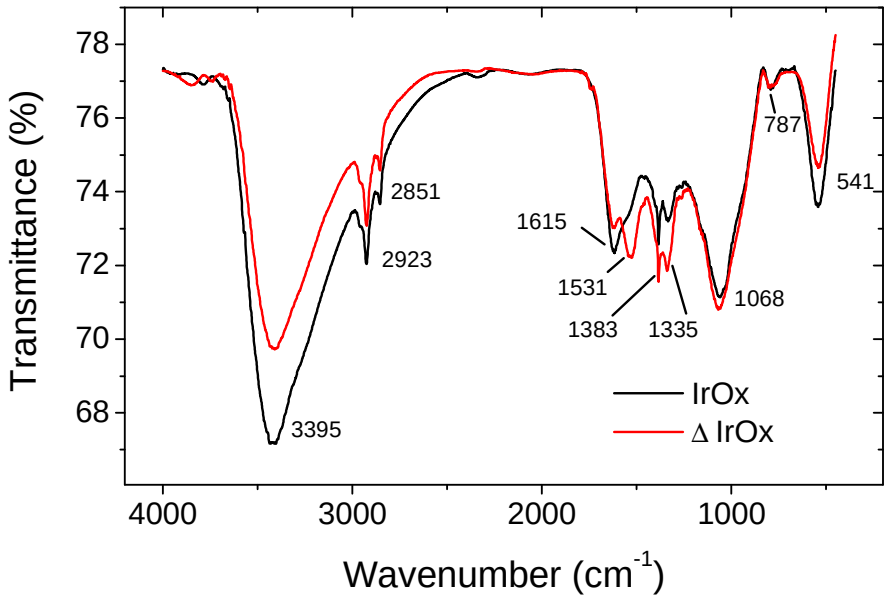

Figure 3.22. ATR spectrum of IrOx with oxalate coatings, as prepared and heated at 100°C during 2 hours.

The presence of water and hydroxyl groups in the oxide structure is demonstrated by the broad band around 3400 cm^{-1} and the peak at 1615 cm^{-1}, attributed to stretching vibrations and bending vibrations of adsorbed water, respectively [82]. In addition, these peaks decrease after heating the sample, showing that a percentage of adsorbed water can be removed with heat, but not all of it at 100°C. The change in the other peaks can be attributed to a mild crystallization due to the temperature. The IR bands at 541 and 787 cm^{-1} are typical for v(Ir-O) vibrations [73], and are very visible in the same spectra. Also, the peak at 1068 cm^{-1} corresponds with the bending vibration of hydroxyl groups in the Ir-OH bond (δ_{OH}) as some authors have pointed out [82]. This peak does not decrease after the temperature treatment, indicating that the hydroxyl groups are forming part of the structure, not only adhered to the surface.

The absence of oxalate or carbonate is also confirmed by IR, as indicated by the lack of the typical sharp line at 1700-1730 cm^{-1} due to the C=O stretch, according with XPS previous results.

The bands 1383 and 1531 cm^{-1} can be assigned to stretching C-C or C-O due to adsorbed impurities, as well as 1335 cm^{-1}, related with the bending of CH_3 (δ_{CH3}).

A more detailed analysis of the hydrated coatings was attempted by TGA measurements in our lab [83], in order to calculate the water content. However, the results obtained showed a complex curve due to a gradual and continued water loss, with non-clear steps.

3.4.4 Micro-Raman Spectroscopy

Raman scattering depends on electron-phonon interactions, which are very sensitive to local environments, and is one of the most useful methods for studying lattice vibrations and their interaction with other excitations. Micro-raman measurements of IrOx samples were made in back-scattering geometry at room temperature, as detailed in Chapter 2, and the results obtained are shown in Figure 3.23.

Raman spectra show the similarities between the two oxides, as shown in previous characterization techniques. The peaks are not well resolved, indicating that the oxide is amorphous. However there is a particular coincidence with the peaks obtained for iridium oxide single crystal at 561 cm^{-1}, 728 cm^{-1} and 752 cm^{-1}, corresponding with the vibration modes E_g, B_{2g} and A_{1g} respectively [84-86]. A little shift (~60 cm^{-1}) to smaller wave numbers is observed, comparing the maximum of the peaks with the reference for single crystal. This red shift and the increased width respect the crystalline IrO_2 can be related with the mixed valence state for iridium, as reported by Mo et al. [61], which observed, for a similar electrodeposited IrOx, an overall shift of the peaks toward lower energies as the Ir^{4+} films were reduced and toward higher energies as the films were oxidized. Also, this shift can be as consequence of size or stress effects between the coating and the substrate [87], and it has been observed that it is minimized as the IrOx coating becomes more

crystalline [85]. Moreover, a little shoulder seems to be appreciated at wave numbers near 350 cm^{-1}. This peak has been described by some authors in terms of poor crystallinity and/or the presence of very fine particles which tend to periodic aggregation [73] or as a stretching mode [85].

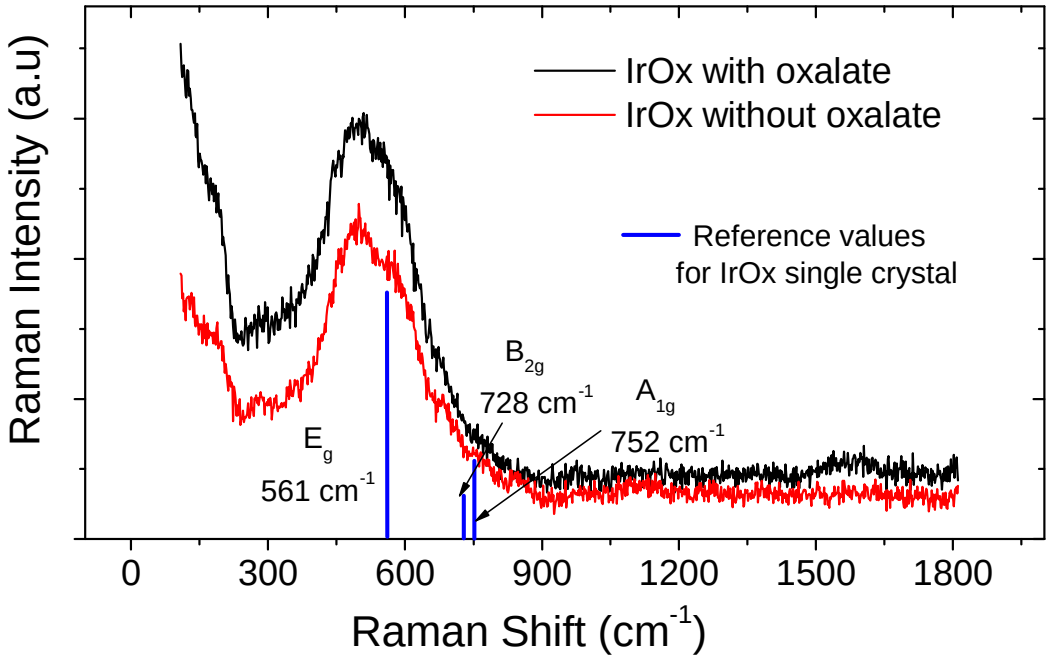

Figure 3.23. Micro-Raman spectra of IrOx with and without oxalate samples, recorded at room temperature.

3.4.5 Scanning Electron Microscopy

Typical SEM images of the surface of IrOx are very similar for samples with and without oxalate. A representative one for an IrOx with oxalate sample is shown in Figure 3.24. It is possible to perceive a cauliflower-type surface, granulated, with medium particle size around 50-150 nm, but homogeneous at large scale.

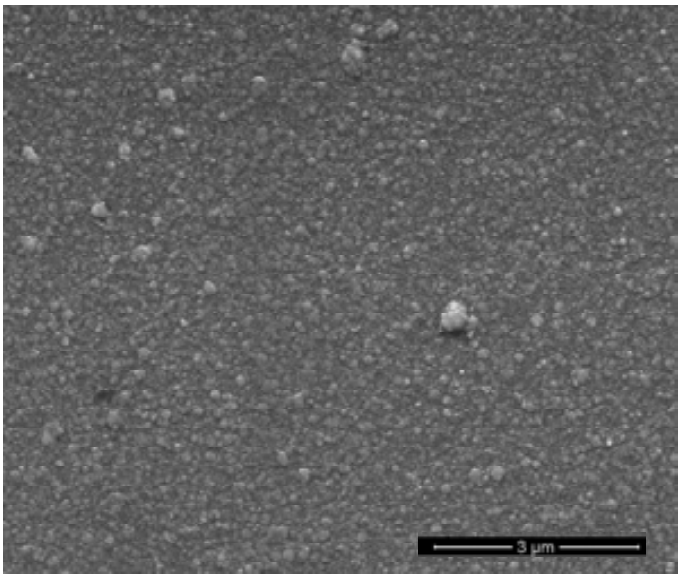

Figure 3.24. SEM image of the IrOx with oxalate sample. Image was taken at 10 kV.

SEM measurements also yield the thickness of the films. The images shown in Figure 3.25 are not very defined due to the poor conductivity resulting from the glass substrate and the small thickness of the coatings. The thickness values are ~30 nm and ~45 nm for 50-cycle IrOx with and without oxalate, respectively. The non-oxalate coating is about 1.5 times than the oxalate one, which corresponds with the values obtained for the charge reached during the synthesis and EQCM measurements. These results suggest that the mass is related with the thickness, or in other words, that both coatings have very similar density.

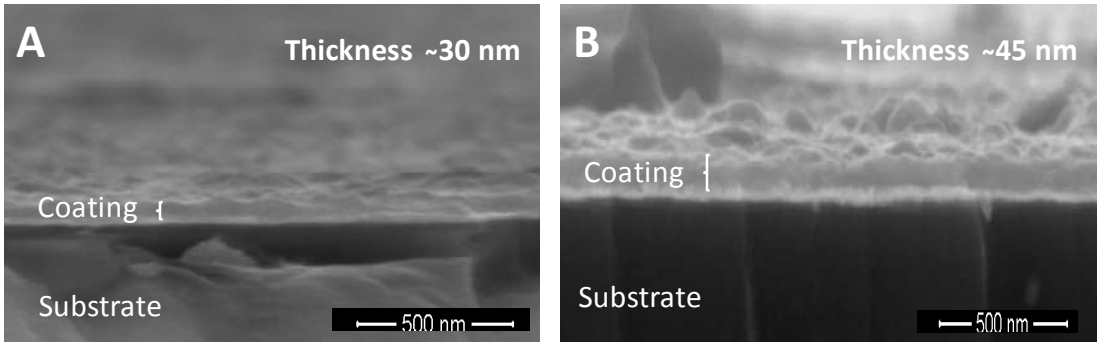

Figure 3.25. SEM images of the border of the samples in order to calculate the thickness. A) IrOx-with oxalate sample and B) IrOx without. Images were taken at 10 kV.

3.4.6 Roughness

The study of the samples roughness is essential for further correlation with the cell culture behavior, as it has been shown to be sensitive to it [88,89]. Morphology of IrOx surface has been evaluated by AFM and by 3D Confocal Microscopy. The latter technique yields more global values, as the working area is bigger and the problems with the AFM tip are avoided. However, for smooth surfaces like IrOx ones, a good concordance in roughness results is obtained with both techniques. The results obtained are useful for subsequent comparison with the roughness obtained for the hybrids.

Figure 3.26 shows the 2D surface, a selected profile after filtering and the three dimensal surface image obtained after the analysis of a sample of IrOx with oxalate by confocal microscopy. The profile shows a very flat surface, and although the surface is not totally homogeneous, the general grain size is very small. Using surface texture analysis software (MountainsMap) is possible to give a value for the roughness, usually the root mean square height, S_q, or RMS surface roughness. For IrOx with oxalate is about **S_q= 3.0 ± 0.5 nm.**

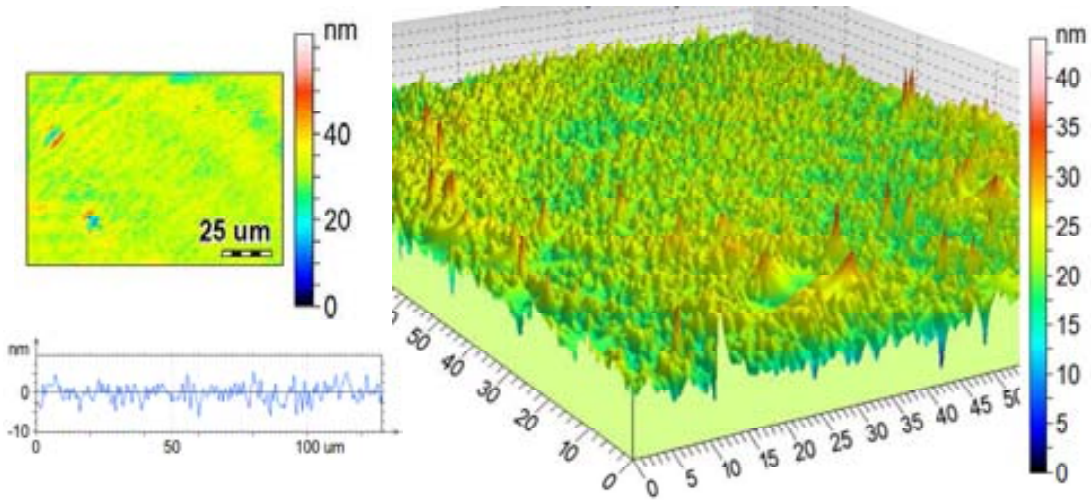

Figure 3.26. Confocal 3D microscopy images showing the 2D map after the scan, a selected characteristic profile and the 3D surface, for IrOx with oxalate sample.

The roughness results obtained by AFM are shown in Figure 3.27, being very similar to the one obtained by confocal 3D microscopy, **S_q=4.6 ± 0.8 nm**. 3D images are also very similar, but in the case of AFM it is possible to observe the characteristic line marks resulting from the tip dragging on the surface of the material, which can entail some error in the roughness parameter.

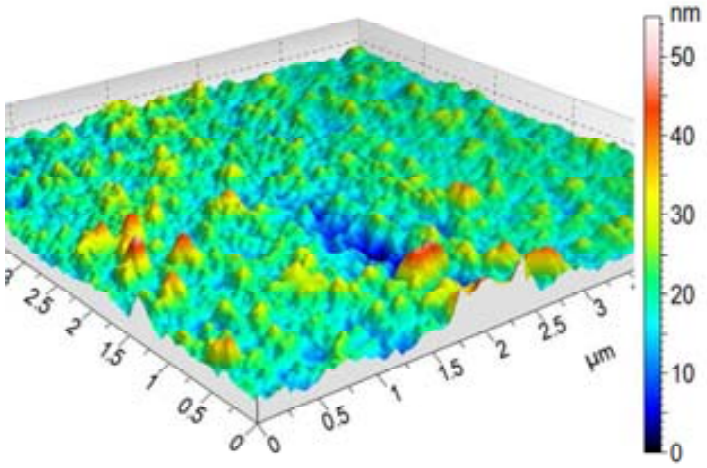

Figure 3.27. AFM microscopy images showing the 3D surface for IrOx with oxalate sample.

The low roughness found in these IrOx coatings, agrees with the electro-flocculation or "electrochemical radical-induced deposition", because the original size of the particles from the precursor solution (about 3-5 nm) is maintained in the solid (coinciding with roughness), whereas, supposing an aggregation, the expected roughness will be larger.

3.4.7 Electrochemical Characterization of the Coatings

The electrochemical behavior of the IrOx coatings was evaluated by cyclic voltammetries in different conditions. These measurements can provide information about the redox composition of the iridium oxide layer. Figure 3.28A shows the corresponding CV curves (cycle 10) for IrOx samples as prepared with and without oxalate. The electrolyte used was phosphate buffered solution (PBS), which has

neutral pH (7.4) and high content of ionic species, similar to biological media, to enhance the migration to the electrode during an electrochemical reaction. The positive and negative limits of the potential waveform have been described in literature for similar IrOx electrodes: -0.6 V and 0.8 V versus Ag/AgCl [8]. For our system, with reference electrode of platinum, the potential window agrees with these values. The use of potentials more negative than -0.6 V or more positive than 0.8 V can be accompanied by significant pH changes, H_2 or O_2 evolution or radical formation, that could be harmful for the tissues and even for the electrode integrity.

The curves obtained for both samples have a semi-rectangular shape suggestive of capacitive behavior, but the charge is substantially faradaic, involving the reversible Ir^{3+}/Ir^{4+} couple, which is fast and reversible and entails the exchange of counterions with the electrolyte for charge balance. Unlike platinum, this redox reaction is confined to the oxide film, not involving the generation of soluble species required for charge transfer at the interface (see Figure 1.1). However, curves are not very well defined due mainly to the size of the working electrode (around 1 cm^2), the geometry and diffusion effects through the coating. Thus, to analyze the different peaks a further study is shown later in different conditions.

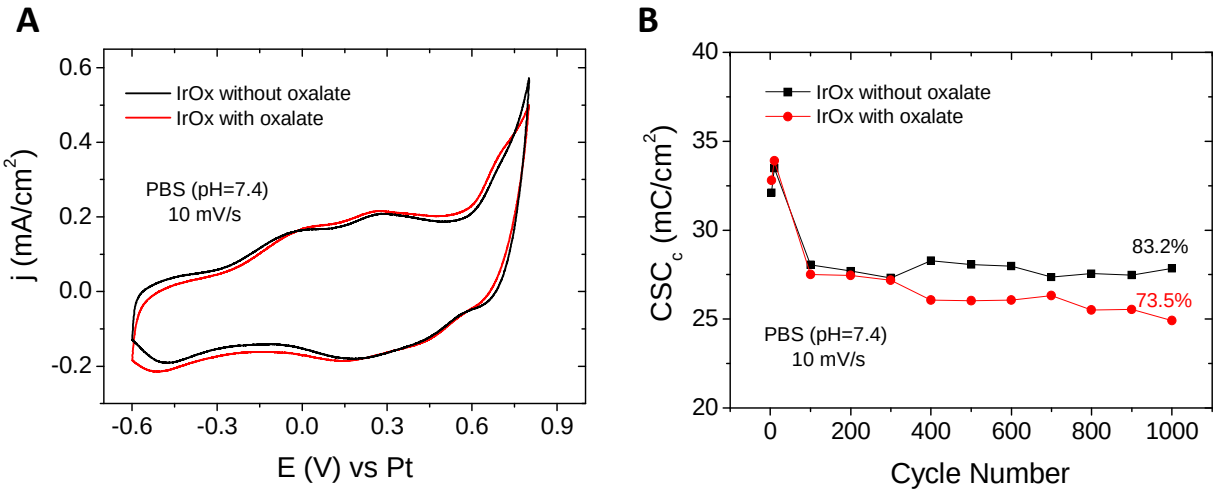

Figure 3.28. A) Cycle 10 of a complete CV for IrOx with and without oxalate as electrodes and B) CSC evolution during 1000 consecutive cycles for samples of IrOx with and without oxalate. Measurements in PBS (pH=7.4), at 10 mV/s and among potential limits from -0.6 V to 0.8 V.

To characterize stimulation electrodes it has become common practice to use the cathodal Charge Storage Capacity (CSC_c) [8], which is proportional to the time integral of the cathodic current during a potential sweep, at low sweep rates. The CSCc value is essentially a relative measure of the total amount of charge available for a stimulation pulse, and an ideal stimulation electrode is supposed to have a high charge capacity storage value. The use of cathodal instead of anodal currents is mainly for physiological reasons, as the leading phase in stimulation is usually cathodal (with the direction of electron flow being from the electrode to the tissue). CSC_C values obtained for both IrOx coatings are very similar, with maximum values of 34.6 mC/cm^2 and 33.8 mC/cm^2 for samples with and without oxalate respectively. These results are very similar to those reported in literature for similar iridium hydrated oxides, with values between 3-30 mC/cm^2 [2,90].

In order to measure the stability of the materials as possible stimulation electrodes, the response of IrOx samples were evaluated during 1000 consecutive cyclic voltammetries in PBS (pH=7.4). Figure 3.28B shows the CSC_c values obtained versus the cycle number. It seems that some type of activation of the coating is necessary, as the CSC_c initially increases until reaching the maximum value around cycle 10. After that, the CSC_c value decreases in an abrupt step, corresponding presumably with cracks formation in the electrode. The total decrease in the CSC_c value after the 1000 cycles is about 16.8%, for the non oxalate coating and slightly higher, 26.5% for the with-oxalate one. However, around 15% of the charge capacity is lost in the first 100 cycles, and remains almost unaltered in the next cycles. This observation is probably related with the partial degradation of the coating during cycling: the formation of bubbles in the surface can delaminate and detach the coating. This degradation has been previously reported in literature, being one of the most important problems observed in practical uses of this type of electrodes [91,92].

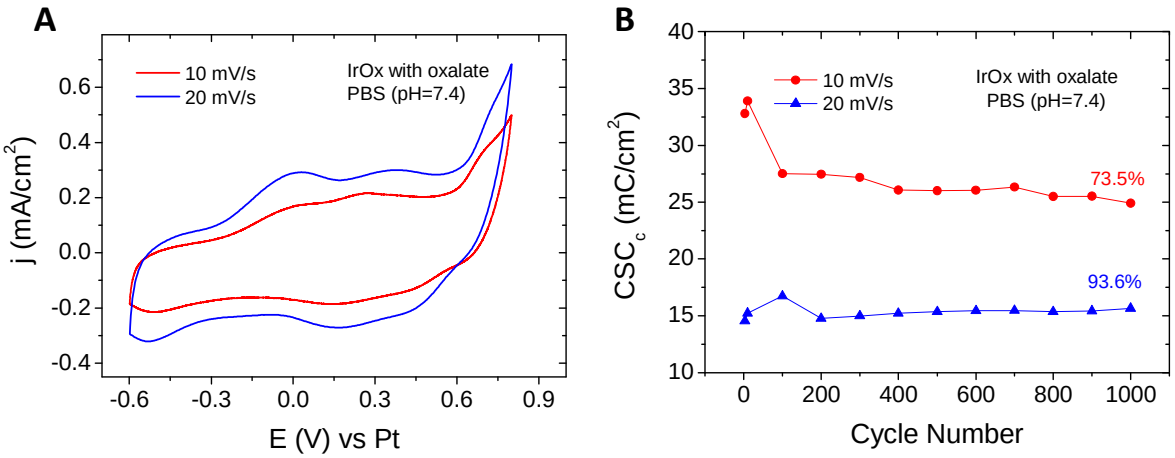

Figure 3.29. A) Cycle number 10 of a complete CV for IrOx with oxalate at 10 mV/s and 20 mV/s in PBS (pH=7.4) and potential limits from -0.6 V to 0.8 V. B) CSC evolution during 1000 consecutive cycles for samples of IrOx with oxalate, in PBS (pH=7.4), at 10 mV/s and 20 mV/s, among potential limits from -0.6 V to 0.8 V.

The influence of the scan rate used in the material response is presented in the Figure 3.29 for the IrOx sample with oxalate (the non oxalate one is very similar). In Figure 3.29A intensity current vs potential curves are presented. The curve recorded at 20 mV/s is broader than the one at 10 mV/s indicating that the fast scan rate enhances the capacitance of the coating, in contrast to the observed for faradaic processes. However CSC_c at 20 mV/s is lower, due to the fact that this value is inversely proportional to the scan rate, as in mainly double-layer capacitors (Figure 3.29B). But even being the CSC_c value considerably lower at high scan rate, the stability of the electrode after 1000 cycling voltammetries is much better, obtaining only a loss in charge storage capacity of 6.4%, which implies that the faradaic processes (with the corresponding intercalation, extended at lower rates) are the responsible of the coating deterioration.

In order to study the shape of the curves to identify the peaks, a deposition of IrOx with and without oxalate was done on a Pt electrode tip, consisting in a polished surface electrode disk diameter of 3 mm. With this electrode, no border effects or other shape alterations are influencing the measurement. CV curves (Figure 3.30A) show how, as the surface of the electrode is smaller and symmetrical, the difference

in the width of the curves is more relevant in the case of IrOx without oxalate. The curves for both coatings present a cathodic peak at -0.22 V and an anodic peak at -0.065 V, which are completely reversible, and coincide with the redox couple Ir^{3+}/Ir^{4+}, as previously reported in literature [6,25,63].

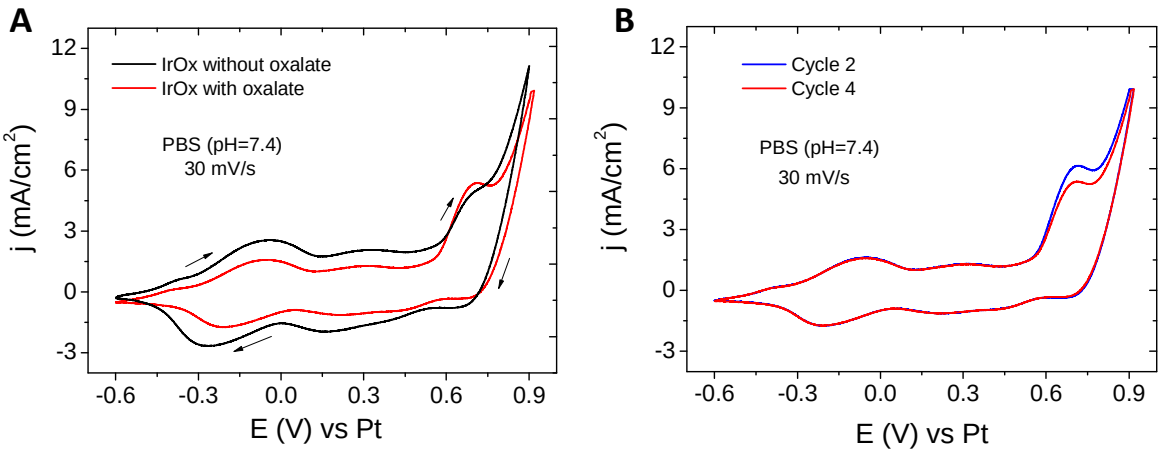

Figure 3.30. A) Cyclic Voltammetry of IrOx with and without oxalate (Cycle 4). B) Cycles 2 and 4 for IrOx with oxalate sample. Both measurements has been done at 30 mV/s in PBS (pH=7.4) among potential limits from -0.6 V to 0.9 V, on a Pt disk of 3 mm of diameter.

The peak shown at 0.7 V can be related with the peak responsible of IrOx electrodeposition during the synthesis (Figure 3.10B), and as mentioned in the section 3.3.1, is presumably the first step of the water oxidation. During the synthesis, successive cycles make this peak to increase, however, once the electrode is formed and placed in PBS as electrolyte, the resulting CV shows how this peak decreases as the number of cycles increase (Figure 3.30B). Considering the radicalary oxidation of hydroxyl groups near an iridium atom to form bridges or, in major extension to produce oxygen, it is expected that in successive cycles fewer OH^- groups will be available to react (as the pH is neutral), and the intensity of this peak will decrease in consequence. On the other hand, at high potentials, oxygen bubbles can be formed in the surface, decreasing the total electrochemical area of the electrode, with the corresponding decrease in intensity.

Also, the couple of peaks at 0.32 V (anionic) and 0.09 V (cationic) is observed, but not as pronounced as in the synthesis. This fact can be related with the pH-dependence of this peak, which entails the presence of hydroxyl groups (Reaction 3.1).

Miniaturization of the system yields higher CSC_c values. With the electrode used in these cases, with circular geometry and with an area of 0.077 cm^2 instead of the normal size of 1 cm^2, is possible to increase the charge storage capacity considerably, obtaining values of 92.5 mC/cm^2 and 69.0 mC/cm^2 for IrOx without and with oxalate, respectively. This is an indication of how much better values for charge storage capacity can be obtained by using microelectrodes in this particular system. In general, for microelectrodes, the transport of counterions is facilitated by the small electrode size and reaction rates are less transport limited, with significantly higher charge-injection densities [8]. However, in this work, larger electrodes have been used for better performance in future cell tests, to make possible the monitoring of cell cultures and the neural response during field application.

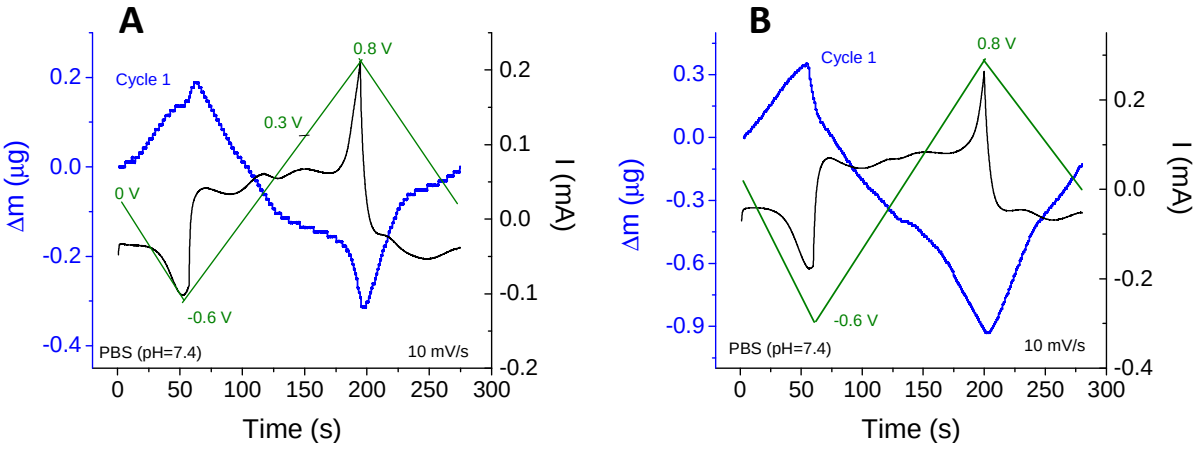

Figure 3.31. EQCM results for the first cycle of a CV performed in PBS (pH=7.4), at scan rate of 10 mV/s and in a potential range from –0.6 V to 0.8 V. A) IrOx with oxalate coating. B) IrOx without oxalate coating. The green line represents the potential (V) vs Pt.

Coatings behavior during cyclic voltammetry has been studied by EQCM, to study the intercalation processes during the electrochemical performance. Mass, intensity and potential changes versus time have been recorded for the first cycle of the CV for IrOx with and without oxalate coatings, and are shown in Figure 3.31. For both coatings, the aspect of the curves is very similar. The mass changes follow an opposite tendency compared with the potential: as the potential becomes more negative, the mass increases, and vice versa.

At the beginning of the CV, as the potential becomes more negative, the mass increase, according with a cationic intercalation. When the potential is reverted and becomes to increase, the tendency is the opposite, the mass decreases as the cationic ions tend to deintercalated, as the charge in the electrode is more positive. However, it is clearly observed how the slope of the mass curve is less pronounced when the potential is near to 0.3 V. As suggested during the synthesis (Reaction 3.1), the oxidation of Ir(IV) to Ir(V) yield to the incorporation of hydroxyls, thus the cationic deintercalation is in part counteracted by hydroxyls, which in addition, are attracted to the electrode as it becomes more positive. However, in this case, as the media used is neutral, the concentration of OH^- is not enough to completely compensate the intercalation (as occurred during the synthesis). When the potential is near 0.8 V, mass decreases abruptly, according with a very sharp peak of intensity. This phenomenon agrees with the proposed water/OH^- oxidation, as hydroxyls belonging to the coating are consumed, so the total mass in the electrode decreases.

When the potential is again reversed and tending to less positive, mass again increases, corresponding to a cationic intercalation to compensate the charge. Again, a change in the slope is observed around 0.18 V, corresponding with the reduction reaction of Ir(V), as commented in the synthesis chapter (Reaction 3.1) where hydroxyl groups are released and the total mass is slightly compensated with the cationic intercalation.

For the sample without oxalate, the mass changes are greater, being the mass loss registered at 0.8 V almost 3 times larger. This can be related with the thicker nature

of the coating and the larger porosity, which enhances the intercalation processes. After the entire cycle, however, the total mass change is near zero, indicating that the intercalation processes are reversible. The final mass loss for non-oxalate coating can be due to the exchange of potassium cations and protons, which present higher mobility.

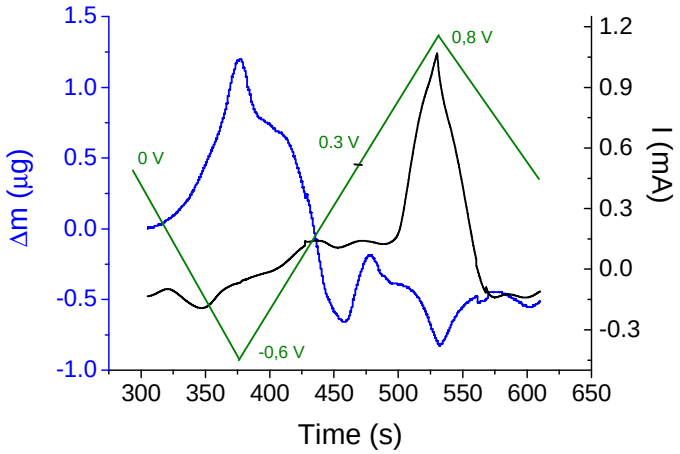

Figure 3.32. EQCM results for the first cycle of a CV performed in PBS (pH=7.4), at scan rate of 10 mV/s and in a potential range from –0.6 V to 0.8 V for an IrOx without oxalate coating, synthesized with Na_2CO_3 instead K_2CO_3. The green line represents the potential (V) vs Pt.

Figure 3.32 shows the CV curve performed in the same conditions for an IrOx without oxalate coating synthesized with Na_2CO_3 instead of K_2CO_3. The tendency observed for mass changes is very similar to those observed for IrOx coatings synthesized in potassium media. However, mass variations are larger, and for example, the first mass increase is almost four times higher than that obtained for IrOx without oxalate synthesized with K. This larger increase can be consequence of the higher mobility of the sodium ions in the coating when compared with potassium. In addition, the mass increase produced around 0.3 V, as consequence of OH intercalation, is very clear, corroborating previous hypothesis.

When the entire cycle is completed, the final mass has decreased around 0.5 μg, which can be an indicative of Na^+/H^+ exchange or resulting by a deterioration of the coating as consequence of the rough mass changes.

As electrodes, these intercalation processes are beneficial, being the responsible to prevent side reactions in biological media, which could yield to dangerous products or changes in the pH, which in turn, can be very harmful for living cells in contact with the material.

All this information obtained from CV measurements is required for the pre-selection of the most appropriate electrode material for stimulation. However, for *in vivo* mainly functional stimulation applications, current pulses are usually much faster than the scan rates used in cyclic voltammetries (for example, for Parkinson disease, the stimulation frequency is around 160 Hz). Therefore, in those cases, during a real stimulation only part of the available electroactive material is accessed. For this reason, these types of materials are considered useful electrodes for dc stimulation using lower scan rates, as those attempted in neural repair or modulation applications, instead of those in functional stimulation.

In order to test the suitability of the electrode material for functional stimulation purposes, the next step would be to determine the material voltage transients as response to a biphasic, cathodic first current pulse and the charge injection limit (Q_{inj}) obtained under the stimulation protocol. These parameters are out of our scope of this work as consequence to the lack of the required equipment, but for similar IrOx coatings, the normal values presented in the literature are between 1-5 mC/cm^2 [8].

3.5 Conclusions

- Pre-deposition solutions with and without oxalate (or any other complexing agents, as shown in literature) used in the IrOx synthesis, yield blue colored solutions, very stable in time, and with no appreciable differences between them. The UV-vis spectroscopy study during the preparation and aging of the solutions does not show large differences between the two preparations. After the dissolution of iridium salts ($IrCl_3$ or $IrCl_4$), the typical bands from Ir-Cl bonds

are observed at 424 nm and 492 nm. This set of bands disappears after the addition of potassium carbonate, indicating the total hydrolysis of Ir-Cl bonds to Ir-OH, as the appearance 312 nm band indicates. After four days of aging, a new band around 575 nm appears which is related with the formation of O-bridged mixed-valence iridium clusters forming oligomers and/or colloidal nanoparticles, as has been demonstrated by DLS and TEM images of the solution. Evidences of the iridium-oxalate complex formation have not been observed, indicating that any complexing agent is necessary to mediate into the posterior electrochemical synthesis of the coatings. However, in some way oxalate can interact with the iridium precursor nanoparticles, dispersing them.

- Analyzing the results obtained in EQCM measurements, a complex synthesis mechanism has been proposed, consisting in an electro-flocculation of the polynuclear iridium precursors onto the electrode as consequence of a pH decrease produced by the hydroxyl/water oxidation to form O_2 or more probable (as no bubbles have been observed during the synthesis) oxygen-radicals. These oxygen radicals, in turn, can participate in the condensation of the IrOx deposited, which entails the exchange of large quantity of ions with the electrolyte as the potential is swept back and forth. This ion mobility is the main responsible for the final porosity and open structure of the IrOx coatings. No evidences of side-reactions during the synthesis have been observed, turning down the oxalate oxidation as main responsible for the IrOx deposition.

- Although in the pre-deposition solutions the presence of oxalate seems not to be important or relevant, during the synthesis it has been observed how for non-oxalate solutions the electrodeposition yields thicker coatings in comparison with solutions prepared with oxalate. Presumably, oxalate anion acts as stabilizer (although not directly bonded) of iridium polynuclear precursors, making them less reactive or more dispersed, and with final result of lower mass deposited, as shown in EQCM results.

- The coatings with and without oxalate, have very similar characteristics, both are highly hydrated and amorphous, as demonstrated by XRD and Raman measurements. The water content has been also shown by ATR experiments. However, after a 4h-thermal treatment at 500ºC IrOx coatings crystallize in a hollandite-type structure with formula K_xIrO_2, in which the presence of potassium has been shown very relevant. This thermal treatment is highly dependent of the final structure, and little changes induce the formation of rutile-type IrO_2, presumably by the sublimation of the KO_2 superoxide.

- Both types of coatings present very similar surface composition (as shown in XPS results), with no notable differences, and no presence of chloride or carbonates. A high content of adventitious carbon, coming from atmospherical impurities, has been observed, as well as a reproducible high amount of potassium, retained in the structure of the coating during the formation. However, when for the pre-deposition solution instead of K_2CO_3 is used Na_2CO_3, the final concentration of Na in the coatings is considerably lower, suggesting a major release of this cation during the synthesis process.

- Electrochemical properties also present similarities between the two coatings, yielding high charge capacities compared with other common neural electrodes as platinum. However, the stability after successive cycling is poor, showing crack formation and final delamination after 1000 cycles. Also, it has been demonstrated how the CSC_c value can be enhanced by miniaturization, which it will be important for future practical applications. Finally, the intercalation processes occurring during CV have been demonstrated, monitoring the mass changes with the EQCM during the electrochemical measurements.

- Being both IrOx coatings (with and without oxalate) very similar in composition and properties, further comparisons with hybrids will be done with coatings prepared with oxalate, as it has been used more commonly in literature.

3.6 References

-[1] Göbbels K., Kuenzel T., Bräunig P., et al. Neuronal cell growth on iridium oxide. *Biomaterials*. **31**, 1055–1067. 2010.

-[2] Meyer R.D., Cogan S.F., Rauh R.D., et al. Electrodeposited iridium oxide for neural stimulation and recording electrodes. *IEEE Trans. Neural. Syst. Rehabil. Eng*. **9**, No.1, 2-11. 2001.

-[3] Cogan S.F., Plante T.D. and Ehrlich J. Sputtered iridium oxide films (SIROFs) for low-impedance neural stimulation and recording electrodes. *Proceedings on the 26th Annual International Conference of the IEEE EMBS*, SF, USA, 2004.

-[4] Gawad S., Giugliano M., Morgan H., et al. Substrate arrays of iridium oxide microelectrodes for in vitro neuronal interfacing. *Front. Neuroeng*. **2**, No.1, 1-7. 2009.

-[5] Mailley S.C., Hyland M., McAdams E.T., et al. Electrochemical and structural characterizations of electrodeposited iridium oxide thin-film electrodes applied to neurostimulating electrical signal. *Mater. Sci. Eng*. **21**, 167–175. 2002.

-[6] Cruz A. M., Abad LL., Casañ-Pastor N. et al. Iridium oxohydroxide, a significant member in the family of iridium oxides. Stoichiometry, characterization, and implications in bioelectrodes. *J. Phys. Chem. C*. **116**, 5155−5168. 2012.

-[7] Weiland J.D., Anderson D.J. and Humayun M.S. In vitro electrical properties for iridium oxide versus titanium nitride stimulating electrodes. *IEEE Trans. Biomed. Eng*. **49**, No.12, 1574-1579. 2002.

-[8] Cogan S.F. Neural stimulation and recording electrodes. *Annu. Rev. Biomed. Eng*. **10**, 275-309. 2008.

-[9] Chen Y., Rasmussen M. and Scherson D. Oxygen reduction on supported iridium oxide films in neutral phosphate buffer: implications for neural stimulation. *Electrochem. Solid-State Lett*. **13**, No.6, F3-F6. 2010.

-[10] Yao S., Wang M. and Madou M. A pH electrode based on melt-oxidized iridium oxide. *J. Electrochem. Soc*. **148**, No.4 H29-H36. 2001.

-[11] Ardizzone A., Carugati A. and Trasatti S. Properties of thermally prepared iridium dioxide electrodes. *J. Electroanal. Chem*. **126**, 287-292. 1981.

-[12] Lodi G., De-Battisti A., Benedetti A., et al. Microstructure and electrical properties of IrO_2, prepared by thermal decomposition of $IrCl_3 \cdot xH_2O$. Role played by the conditions of thermal treatment. *J. Electroanal. Chem*. **277**, 139-150. 1990.

-[13] Bestaoui N., Deniard P. and Bree R. Structural study of a hollandite-type K_xIrO_2. *J. Solid State Chem*. **118**, 372-377. 1995.

-[14] Zhao Y., Hernandez-Pagan E.A., Mallouk T.E., et al. A high yield synthesis of ligand-free iridium oxide nanoparticles with high electrocatalytic activity. *J. Phys. Chem. Lett*. **2**, 402–406. 2011.

-[15] Bestaoui N. and Prouzet E. A chimie douce route to pure iridium oxide. *Chem. Mater.* **9**, 1036-1041. 1997.

-[16] Petit M. A. and Plichon V. Anodic electrodeposition of iridium oxide films. *J. Electroanal. Chem*. **444**, 247-252. 1998.

-[17] Yamanaka K. Anodically electrodeposited iridium oxide films (AEIROF) from alkaline solutions for electrochromic display devices. *Jpn. J. Appl. Phys*. **28**, No.4, 632-637. 1989.

-[18] Yagi M., Tomita E. and Kuwabara T. Remarkably high activity of electrodeposited IrO2 film for electrocatalytic water oxidation. *J. Electroanal. Chem*. **579**, 83–88. 2005.

-[19] Jung Y., Lee J. and Tak Y. Electrochromic mechanism of IrO_2 prepared by pulsed anodic electrodeposition. *Electrochem. Solid-State Lett*. **7**, No.2, H5-H8. 2004.

-[20] Gottesfeld S. and Srinivasan S. Electrochemical and optical studies of thick oxide layers on iridium and their electrocatalytic activities for the oxygen evolution reaction. *J. Electroanal. Chem*. **86**, 89-104. 1978.

-[21] Kang K.S. and Shay J.L. Blue sputtered iridium oxide films (Blue SIROF's). *J. Electrochem. Soc.* **130**, No.4, 766-769. 1983.

-[22] Cogan S.F., Ehrlich J., Rizzo J.F., et al. Sputtered iridium oxide for neural stimulation electrodes. *J. Biomed. Mater. Res. B Appl. Biomater*. **89**, No.2, 353-61. 2009.

-[23] Liu D.Q., Yu S.H., Joo S.K., et al. Electrochemical performance of iridium oxide thin film for supercapacitor prepared by radio frequency magnetron sputtering method. *ECS Trans*. **16**, No.1, 103-109. 2008.

-[24] Burke L.D. and Scannell R.A. Electrochromic iridium oxides. Preparation and properties of hydrous films. *Platinum Metals Rev*. **28**, No.2, 56-61. 1984.

-[25] Baur J.E. and Spaine T.W. Electrochemical deposition of iridium(IV) oxide from alkaline solutions of iridium(III) oxide*. J. Electroanal. Chem*. **443**, 208-216. 1998.

-[26] Yoshino T., Baba N. and Arai K. Electrochromic IrOx thin films formed in sulfatoiridato (III, IV) complex solution by periodic reverse current electrolysis (PRIROF*). Jpn. J. Appl. Phys*. **26**, No.9, 1547-1549. 1987.

-[27] Kruszyna H.G., Bodek I., Milburn R.M., et al. Preparation and reactivity of Tris(oxalate)iridiato(IV) ion in aqueous acidic solution. *Inorg. Chem*. **13**, No.2, 434-438. 1974.

-[28] Van Loon G. and Page J.A. The chemistry of iridium in basic aqueous solution. A polarographic study. *Can. J. Chem*. **44**, 515-520. 1966.

-[29] Castillo-Blum S.E., Richens D.T. and Skyes A.G. Oxidation of hexaaquairidium(III) and related studies: preparation and properties of iridium(III), iridium(IV), and iridium(V) dimers as aqua ions. *Inorg. Chem*. **28**, 954-960. 1989.

-[30] Castillo-Blum S. E., Richens D. T. and Skyes A. G. New Aqua Ions of Iridium in Oxidation States (III), (IV), and (V). *J. Chem Soc., Chem. Commun*. 1120-1121. 1986.

-[31] Hintermair U., Hashmi S.M., Crabtree R.H., et al. Particle formation during oxidation catalysis with Cp* iridium complexes. *J. Am. Chem. Soc*. **134**, 9785-9795. 2012.

-[32] Sánchez-Ortiz V. A., Martínez-Jardines L. G., Skyes A. G., et al. New heterometallic di-μ-hydroxo chromium(III)–iridium(III) and rhodium(III)–iridium(III) dinuclear aqua ions. *J. Chem. Soc., Dalton Trans.* **4**, 663–665. 1998.

-[33] Nakagawa T., Beasley C.A. and Murray R.W. Efficient electro-oxidation of water near its reversible potential by a mesoporous IrOx nanoparticle film. *J. Phys. Chem. C*. **113**, No.30, 12958-12961. 2009.

-[34] Krishnamurty K. and Harris G.M. The chemistry of the metal oxalato complexes. *Chem. Rev*. **61**, No.3, 213-246. 1961.

-[35] Livinstone S.E The chemistry of ruthenium, rhodium, palladium, osmium, iridium and platinum. Vol. **25**. Pergamon Texts in Inorganic Chemistry. Ed. Elsevier. 1973.

-[36] Belova I.D., Varlamova T.V., Sevostyanov M.A., et al. The composition, structure and electronic properties of thermally prepared iridium dioxide films. *Mater. Chem. Phys*. **20**, 39-64. 1988.

-[37] Levitin G. and Schmuckler G. Solvent extraction of rhodium chloride from aqueous solutions and its separation from palladium and platinum. *React. Funct. Polym*. **54**, 149-154. 2003.

-[38] Earnshaw A. and Greenwood N. Chemistry of the elements. Ed. Elsevier. (2^{nd} edition). 1997.

-[39] Pattel A., Leitch P. and Richens D.T. Kinetic studies of the complexation of oxalate to the t_{2g}^{6} hexaaqua ions of ruthenium(II) and rhodium(III). *J. Chem. Soc. Dalton Trans*. **4**, 1029-1036. 1991.

-[40] Carrera F., Torrico F., Sánchez-Marcos E., et al. Combined experimental and theoretical approach to the study of structure and dynamics of the most inert aqua ion $[Ir(H2O)_6]^{3+}$ in aqueous solution. *J. Phys. Chem*. **111**, 8223-8233. 2007.

-[41] Nahor G. S., Hapiot P., Harriman A., et al. Changes in the redox state of iridium oxide clusters and their relation to catalytic water oxidation. Radiolytic and electrochemical studies. *J. Phys. Chem*. **95**, No.2, 616-621. 1991.

-[42] Van Loon G. and Page J. A. The chemistry of iridium in basic aqueous solution. A polarographic study. *Can. J. Chem*. **44**, 515-520. 1966.

-[43] Harriman A., Thomas J.M. and Milward G.R. Catalytic and structural properties of iridium-iridium dioxide colloids. *New J. Chem*. **11**, 757-762. 1987.

-[44] King R.B. Encyclopedia of inorganic chemistry. Vol. **3**. Ed. Wiley. (2^{nd} edition). 2005.

-[45] Fine D.A. Studies of the iridium (III) and (IV)-chloride system in acid solution. *J. Inorg. Nucl. Chem*. **32**, 2731-2742. 1970.

-[46] Harriman A., Nahor G.S., Neta P., et al. Iridium oxide hydrosols as catalysts for the decay of zinc porphyrin radical cations in water. *J. Chem. Soc., Faraday Trans*. *1*. **84**, No.8, 2821-2829. 1988.

-[47] Gottesfeld S., Mcintyre J.D.E., Shay J.L., et al. Electrochromism in anodic iridium oxide films. *Appl. Phys. Lett*. **33**, 208-210. 1978.

-[48] Pankratov D.A., Komozing P.N. and Miselev Y.M. EPR spectroscopy of transformations of iridium(III) and iridium(IV) hydroxo complexes in alkaline media. *Russ. J. Inorg. Chem*. **56**, No.11, 1794-1799. 2011.

-[49] Castillo-Blum S.E., Skyes A.G. and Gamsjäger H. Substitution inertness of $Ir(H_2O)_6]^{3+}$. *Polyhedron*. **6**, No.1, 101-103. 1987.

-[50] Mevin R. and Day P. Mixed valence chemistry-A survey and classification. *Adv. Inorg. Chem. Radiochem.* **10**, 247-422. 1968.

-[51] Slavcheva E., Vitushinsky R., Schnakenberg U., et al. Sputtered iridium oxide films as charge injection material for functional electrostimulation. *J. Electrochem. Soc.* **151**, E226-E237. 2004.

-[52] Gilbert J. A., Eggleston D. S., Meyer T. J. et al. Structure and redox properties of the water-oxidation catalyst $[(bpy)_2(OH_2)RuORu(OH_2)(bpy)_2]^{4+}$. *J. Am. Chem. Soc*. **107**, No.13, 3855-3864. 1985

-[53] Ammam M. Polyoxometalates: formation, structures, principal properties, main deposition methods and application in sensing. *J. Mater. Chem. A*. **1**, 6291–6312. 2013.

-[54] Rüttinger W. and Dismukes G. C. Synthetic Water-Oxidation Catalysts for Artificial Photosynthetic Water Oxidation. *Chem. Rev*. **97**, No.1, 1-24. 1997.

-[55] Dismukes G. C. and van Willigen R. T. Manganese: the oxygen-evolving complex & models. *Encycl. Inorg. Chem*. Ed. Wiley. (2^{nd} Edition). 2006.

-[56] Elsen H. A. Thermodynamic and dynamic investigations of hydrated iridium oxide potentiometric pH micro-sensors. Ph.D. Thesis, University of California, Berkeley. 2002.

-[57] Lori J.A. and Hanawa T. Characterization of adsorption of glycine on gold and titanium electrodes using electrochemical quartz crystal microbalance. *Corros. Sci*. **43**, 2111-2120. 2001.

-[58] Birss V.I. and Elzanowska H. Quartz crystal microbalance measurements during oxidation/reduction of hydrous Ir oxide electrodes. *J. Electroanal. Chem.* **318**, 327-333. 1991.

-[59] Beni G., Rice C.E. and Shay J.L. Electrochromism of anodic iridium oxide films. III. Anion mechanism. *J. Electrochem. Soc.* **127**, No.6, 1342-1348. 1980.

-[60] Hüppauff M. and Lengeler B. Valency and structure of iridium in anodic iridium oxide films. *J. Electrochem. Soc*. **140**, No.3, 598-602. 1993.

-[61] Mo. Y., Stefan I.C., Scherson D.A., et al. In situ iridium L_{III}-edge X-ray absorption and surface enhanced Raman spectroscopy of electrodeposited iridium oxide films in aqueous electrolytes. *J. Phys. Chem. B*. **106**, 3681-3686. 2002.

-[62] Yagi M., Tomita E., Nagai K., et al. Self-assembly of active IrO_2 colloid catalyst on an ITO electrode for efficient electrochemical water oxidation. *J. Phys. Chem. B*. **109**, No.46, 21489-21491. 2005.

-[63] Kuwabara T., Tomita E., Yagi M., et al. Characterization and analysis of self-assembly of a highly active coloidal catalyst for water oxidation onto transparent conducting oxide substrates. *J. Phys. Chem. C*. **112**, 3774-3779. 2008.

-[64] Chuang M.C. and Ho J.A. Efficient electrocatalytic oxidation of water: minimization of catalyst loading by an electrostatic assembly of hydrous iridium oxide colloids. *RSC Adv*. **2**, 4092-4096. 2012.

-[65] Nakagawa T., Bjorge N.S. and Murray R.W. Electrogenerated IrOx nanoparticles as dissolved redox catalysts for water oxidation. *J. Am. Chem. Soc*. **131**, 15578-15579. 2009.

-[66] Chen Y., Taylor P.L. and Scherson D. Electrochemical and in situ optical studies of supported iridium oxide films in aqueous solutions. *J. Electrochem. Soc*. **156**, No.1, F14-F21. 2009.

-[67] Chen Y., Shi P. and Scherson D. Supported iridium oxide films in Aqueous electrolytes: Charge injection dynamics as monitored by time-resolved differential reflectance spectroscopy. Electrochem. *Solid State Lett*. **11**, No.6, F5-F8. 2008.

-[68] Beni G., Shiavone L.M., Scheneider B.S., et al. Electrocatalytic oxygen evolution on reactively sputtered electrochromic iridium oxide films. *Nature*. **282**, 281-283. 1979.

-[69] Kötz R., Barbero C. and Haas O. Probe beam deflection investigation of the charge storage reaction in anodic iridium and tungsten oxide films. *J. Electroanal. Chem*. **296**, 37-49. 1990.

-[70] Steegstra P. Hydrous iridium oxide for in situ pH sensing. Electrodeposition, properties and applications. Ph.D Thesis, University of Gothenburg, Sweden. 2013.

-[71] Augustynsky J., Koudelka M., Conway B.E., et al. ESCA study of the state of iridium and oxygen in electrochemically and thermally formed iridium oxide films. *J. Electroanal. Chem*. **160**, 233-248. 1984.

-[72] Méndez M.E., Márquez J. and Briceño R. Electrochemical growth of hydrous iridium (III) and (IV) oxide on platinum substrate. *Rev. Téc. Ing. Univ. Zulia*. **31**, No.1, 71-78. 2008.

-[73] Music S., Popovic S., Gajovic A., et al. Thermochemical formation of IrO_2 and Ir. *Mater. Lett*. **57**, 4509-4514. 2003.

-[74] Atanasoska L., Gupta P., Thomson J., et al. XPS, AES, and electrochemical study of iridium oxide coating materials for cardiovascular stent application. *ECS Trans*. **16**. No.38, 37-48. 2009.

-[75] Chalamala B.R., Wei Y., Golden D.E., et al. Effect of growth conditions on surface morphology and photoelectric work function characteristics of iridium oxide thin films. *App. Phys. Lett.* **74**, No.10, 1394-1396. 1999.

-[76] Surface Analysis by Auger and X-Ray Photoelectron Spectroscopy. Briggs D. and Grant J.G. Ed: IM Publications. (1^{st} edition). 2003.

-[77] Swift P. Adventitious carbon-the panacea for energy referencing?. *Surf. Interface Anal.* **42**, No.2, 47-51. 1982.

-[78] Payne B.P., Biesinger M.C. and McIntyre N.S.. *J. Electron Spectrosc. Relat. Phenom*. **184**, 29-37. 2011.

-[79] Owe L.E., Tsypkin M. and Sunde S. The effect of phosphate on iridium oxide electrochemistry. *Electrochim. Acta*. **58**, 231-237. 2011.

-[80] Hughes A. E., Taylor R. J., Wilson L., et al. XPS and SEM characterization of hydrated cerium oxide conversion coatings. *Surf. Interface Anal*. **23**, 540-550. 1995.

-[81] Burke L.D. and Whelan D.P. A voltammetric investigation of the charge storage reactions of hydrous iridium oxide layers. *J. Electroanal. Chem*. **162**, 121-141. 1984.

-[82] Kristof J., Mink J., Liszi J., et al. Emission FTIR studies on the formation mechanism of IrO_2/TiO_2 based coatings. *Electrochim. Acta*. **39**, No.11, 1531-1535. 1994.

-[83] Cruz A.M. Obtención y caracterización de materiales electroactivos para soporte de crecimiento neuronal. Ph.D Thesis, Universidad Autónoma de Barcelona, Spain. 2010.

-[84] Thanawala S., Georgiev D.G., Auner G., et al. Characterization of iridium oxide thin films deposited by pulsed-direct-current reactive sputtering. *Thin Solid Films*. **515**, 7059-7065. 2007.

-[85] Liao P.C., Chen C.S., Tiong K.K., et al. Characterization of IrO_2 thin films by Raman spectroscopy. *Thin Solid Films*. **301**, 7-11. 1997.

-[86] Huang Y.S., Lin S.S., Chien F.Z., et al. Raman Spectrum of IrO_2. *Solid State Commun.* **70**, 517-522. 1989.

-[87] Korotcov A.V., Huang Y.S., Tsai D.S., et al. Raman scattering characterization of well-aligned RuO_2 and IrO_2 nanocrystals. *J. Raman Spectrosc*. **38**, 737-749. 2007.

-[88] Lamping M., Warocquier-Clerout R., Sigot-Luizard., et al. Correlation between substratum roughness and wettability, cell adhesion, and cell migration. *J. Biomed. Mater. Res*. **36**, No.1, 99-108. 1997.

-[89] Hallab N.J., Bundy K.J., Jacobs J.J., et al. Evaluation of metallic and polymeric biomaterial surface energy and surface roughness characteristics for directed cell adhesion. *Tissue Eng*. **7**, No.1, 55-71. 2001.

-[90] Cogan S.F, Troyk P.R., Detlefsen D.E., et al. Potential-biased, asymmetric waveforms for charge-injection with activated iridium oxide (AIROF) neural stimulation electrodes. *IEEE Trans. Biomed. Eng*. **53**, No.2, 327-332. 2006.

-[91] Cogan S.F., Guzelian A.A., McCreery D.B., et al. Over-pulsing degrades activated iridium oxide films used for intracortical neural stimulation. *J. Neurosci. Met*. **137**, 141-150. 2004.

-[92] Negi S., Bhandari R., Solzbacher F., et al. Neural electrode degradation from continuous electrical stimulation: Comparison of sputtered and activated iridium oxide. *J. Neurosci. Met*. **186**, 8–17. 2010.

Chapter 4

IrOx-CNTs Hybrid Coatings

This chapter introduces the new IrOx-CNTs hybrid material synthesized as coatings in this thesis. A little introduction is done, remarking the importance of these and other types of hybrids or nanocomposites in the development of new materials to achieve improved properties for a particular use. In this case, for neural cell biocompatibility and electric field applications.

Also, the complete process of synthesis and characterization of the coatings obtained is exposed, comparing the differences found between the hybrids and the previously studied IrOx samples, in Chapter 3.

Finally, the electrochemical properties of the hybrid coatings are tested by cyclic voltammetries in different conditions, in order to determine the feasibility as neural stimulation electrodes and the stability in electrochemical conditions.

4.1 IrOx-CNTs Hybrids

Being IrOx one of the most promising materials to date, used as stimulation electrodes [1-7], recent technological breakthroughs have generated an enormous demand of novel materials, with new and enhanced properties but also, capable to prevent or minimize typical drawbacks found in the actual ones.

Many of the well-established materials as ceramics, polymers and metals cannot fulfill all the technical requirements, and in this sense, mixtures of materials can show superior properties compared with the pure counterparts. In fact, the most successful examples, in order to improve mechanical and physical properties, are hybrids or nanocomposites, which are formed by the incorporation of a basic structural material (usually nanoparticles or fibers) into the matrix of a second material [8].

A hybrid material is defined as a material that includes two moieties blended on the molecular scale [8]. Although this term is used for a wide area of materials, usually one of these counterpart is inorganic and the other one organic in nature. In this work, we have defined the new material IrOx-CNTs as a hybrid but in fact, there is no clear borderline between hybrid or nanocomposite definitions. Commonly, nanocomposite is used for discrete structural units in the respective size regime, and low interactions between the two parts are observed. On the other hand, hybrid materials are often formed in situ by molecular precursors and the result usually is not only a combination of the separate components, as synergy is observed; the resulting material has improved properties compared with the mixture of precursors themselves. Hence, in this work, the term “hybrid” is justified by the synthesis method of the new IrOx-CNTs electroactive material and the final structure observed, as well as the final properties achieved, which show this type of synergetic effect.

The synthetic processes for common hybrids materials are usually based on techniques of copolymerization of functional organosilanes, macromonomers and metal alkoxides, encapsulation of organic components within sol-gel derived silica or metallic oxides, or the organic functionalization of nanofillers or other compounds with lamellar structures [9]. The hybrid material detailed in this work is not only innovative because of the fact that both of the components have inorganic nature,

but also because of the synthesis mechanism, in which the very porous hydrated iridium oxide is electrodeposited *in situ* from a solution onto the substrate and the carbon nanotubes. This IrOx encapsulation of the CNTs induces in turn, the nanotubes acting as a scaffold to support the oxide structure, obtaining a nanostructured hybrid material.

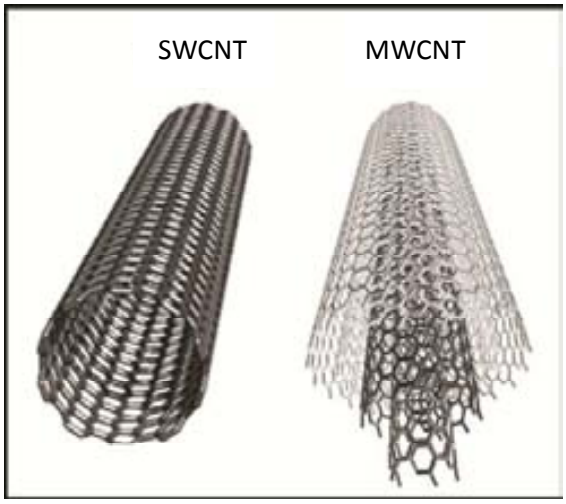

Figure 4.1 Representation of a single (SWCNT) and multiple walled carbon nanotubes (MWCNT).

Carbon nanotubes (CNTs) are allotropes of carbon with a cylindrical nanostructure, which present unique one dimensional geometric and electronic nature, large surface area, good chemical and thermal stability and excellent mechanical properties (Figure 4.1). All these characteristics are very demanded in materials science, and a very large number of applications have been described for CNTs. In this thesis, the preparation of the hybrid material has been based on the combination of iridium oxide and CNTs, with the main objective to combine the properties of each component, even achieving a synergistic effect. In addition, the biocompatibility shown for carbon nanotubes, when no released in the media [10-12], allows the new hybrid to be used as implantable electrode, with expected high conductivity, low resistivity and reinforced stability in biological conditions of chronic stimulation.

In literature, some other functional hybrid materials based on metal oxides and carbon nanotubes have been reported with multiple applications as energy storage, electroanalysis or photocatalysis, with improved properties [13] but none of them oriented for biological purposes. In addition, only physical or mechanical methods of synthesis have been described for these materials, which do not achieve a uniform dispersion of the CNTs into the oxide matrix, limiting the potential properties of the nanocomposite.

4.2 IrOx-CNTs Hybrids Synthesis

The synthesis of IrOx-CNTs hybrid materials has been initially envisaged starting from the hypothesis of great affinity of iridium to form complexes with carboxylate groups, in particular with oxalate, as presented by Petit et al. for the electrochemical synthesis of IrOx [14]. Following this idea, a similar methodology but using oxidized carbon nanotubes was proposed, as shown in Figure 4.2. Carboxylate groups in the surface of carbon nanotubes were proposed to act as ligands for iridium cations in the pre-deposition solution, and later oxidation at the electrode surface would yield to the oxidative decomposition of COO^- groups to CO_2 and the final deposition of the hybrid, being CNTs part of the oxide microstructure.

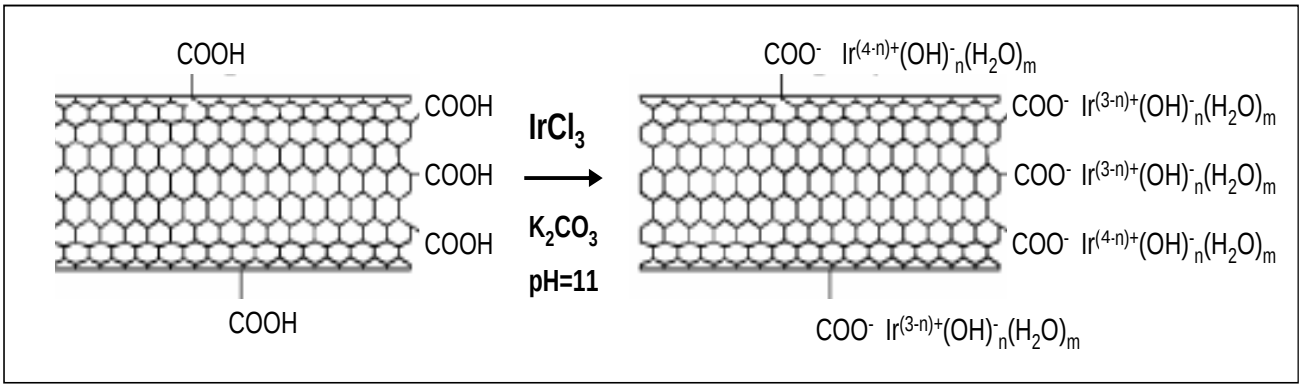

Figure 4.2 Schematic representation of the proposed mechanism for iridium stabilization in the pre-deposition solution with $IrCl_3$ in alkaline media.

However, parallel experiments using IrOx with and without oxalate solutions (Chapter 3), demonstrated that oxalate (or any other complexing agent) is not required to obtain IrOx coatings. Thus, instead of the synthesis from Ir-oxalate complexes, the condensation of iridium precursors into polynuclear species (oligomers or nanoparticles) was proposed. In any case, the presence of oxalate in the media was shown to stabilize these particles/oligomers, inducing a smaller size distribution of iridium precursors aggregates and facilitating the dispersion, as seen in DLS and TEM results. During IrOx electrodeposition, flocculation of the iridium precursors occurs as consequence to the pH decrease produced by hydroxyl/water oxidation.

In IrOx-CNTs synthesis an identical mechanism is expected. The pre-deposition solution would consist of a mixture or polynuclear iridium precursors, which presumably are stabilized by the carboxylate groups in the surface of the nanotubes. Also, the electrochemical deposition has been proposed as an electro-flocculation.

Oxidized carbon nanotubes (CNTs-COOH) are negatively charged in alkaline aqueous solutions, improving the solubility and the stability of the dispersion. Also, migration to the anode during the synthesis may be enhanced because of this negative charge in the CNTs surface. The importance of carboxylated CNTs has been confirmed, because the same synthesis with non functionalized CNTs does not yield any self-standing coating.

After 7-day-aging, the pre-deposition solution seems black due to the dispersed CNTs, although a deep blue color was clearly observed, typically of iridium (III)/(IV) alkaline solutions. This blue color, as mentioned in the previous chapter is related with the charge transfer band present in mixed valence species, and indicates the formation of condensed species with O-bridged idirium atoms (O-Ir-O) [15]. UV-visible spectrum of the pre-deposition solution after 3 days of aging, shows bands at 312 nm and 574 nm, corresponding with the Ir–OH bonds and the formation of IrOx nanoparticles respectively, indicating very similar composition to pure IrOx pre-deposition solutions (Figure 4.3).

Small influence of the dispersed CNTs is appreciated in Uv-Vis, without any band indicating a possible interaction between the nanotubes and the IrOx nanoparticles, although the dispersed carbon species increase the baseline considerably.

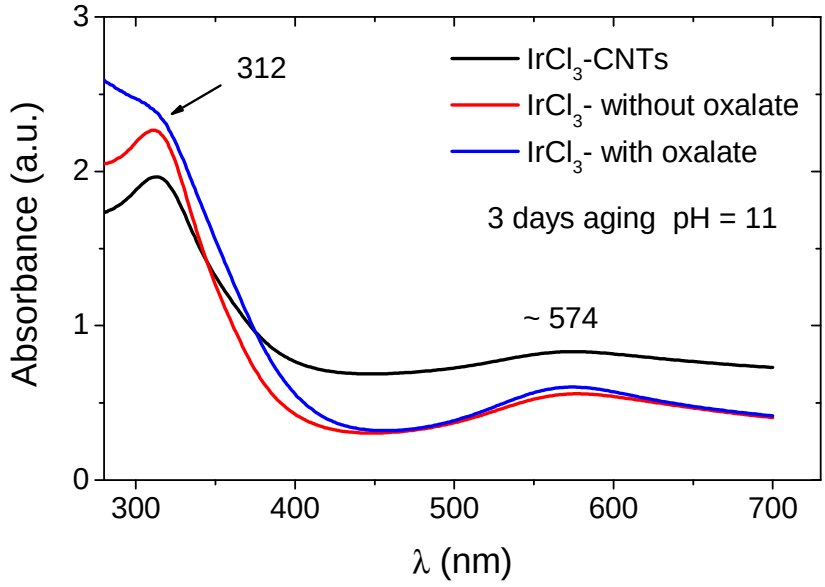

Figure 4.3. UV-visible spectra of the studied pre-deposition solutions after 3 days of aging.

Following the same protocol used in pure IrOx coatings synthesis, potentiodynamic methods were used instead of constant potential methods. For IrOx-CNTs hybrid coatings, the electrochemical method was empirically optimized to obtain good adherence, high CNTs concentration and minimum crack formation, by modifying the initial concentration of CNTs, the potential limits and the sweep rate. The resulting conditions involve a reverse potential of 0.70 V and a scan rate of 5 mV/s. The scan rate is a significant and decisive parameter, to ensure the diffusion of reactive molecules towards the electrode, as the solution in the cell is not stirred. The difference observed with the optimal scan rate used for IrOx synthesis (10 mV/s) is presumably due to the larger dimensions and lower mobility of CNTs through the solution, which may be enhanced with larger changing fields in time.

In addition, the modulation of films thickness and roughness is easily achieved by modifying the number of cycles (usually among 20-50), which is proportional to the

total charge. An example of the voltammetry obtained during a normal synthesis is shown in Figure 4.4.

The shape of the CV curves during the synthesis is similar to those obtained for IrOx, although the current density reached is considerably higher, which suggest an increased conductivity during the electrochemical synthesis, due to the addition of CNTs. Nevertheless, this charge increase may be related with the potential reached in the hybrid synthesis (0.7 V), which is larger than that used in IrOx coatings (0.55 V), and as consequence, more mass can be deposited. In this sense, EQCM experiments will yield more information.

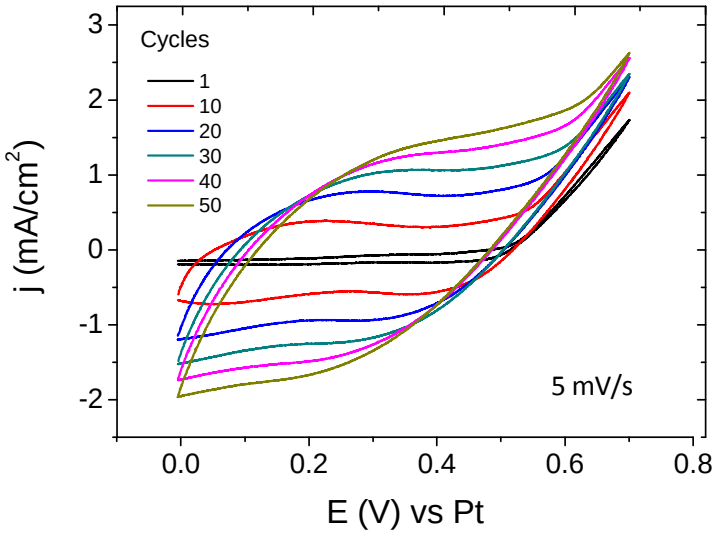

Figure 4.4. Voltammetries obtained during the potentiodynamic synthesis of the IrOx-CNTs hybrid coating at 5 mV/s. For clarity, only one in ten cycles is shown.

The total charge provided to the system for coatings synthesized during 50 cycles was 3.5-4.2 C/cm^2, two orders of magnitude larger than the obtained during IrOx synthesis, although in this case it has also to be considered the higher reverse potential.

IrOx-CNTs synthesis mechanism has been studied by electrochemical quartz crystal microbalance (EQCM) in order to compare results with IrOx synthesis. The mass increase and intensity curves versus time for the first six cycles are plotted in Figure

4.5A. The mass curves are very similar to those obtained in IrOx synthesis at 5 mV/s (Figure 3.11B), a sequential but non-lineal mass increase. However, the intensity corresponding to the reverse potential reached in each cycle, is considerably higher when compared with the value obtained in the IrOx synthesis (for example, in cycle 4, for IrOx I=0.04 mA, whereas for IrOx-CNTs is 0.7 mA), which can be consequence of the higher potential used, but also, a contribution of CNTs. This increase observed in the intensity, however, is not coincident with the mass increase registered. That is, the current is increased around one order of magnitude (~1.5 mA in IrOx-CNTs vs ~0.5 mA in IrOx), but the mass deposited in each cycle is not proportional to this increase (~0.3 µg in IrOx-CNTs vs~0.6 µg in IrOx), an evidence demonstrating again that the IrOx deposition is induced by another redox reaction, as the proposed water/hydroxyls oxidation in Chapter 3.

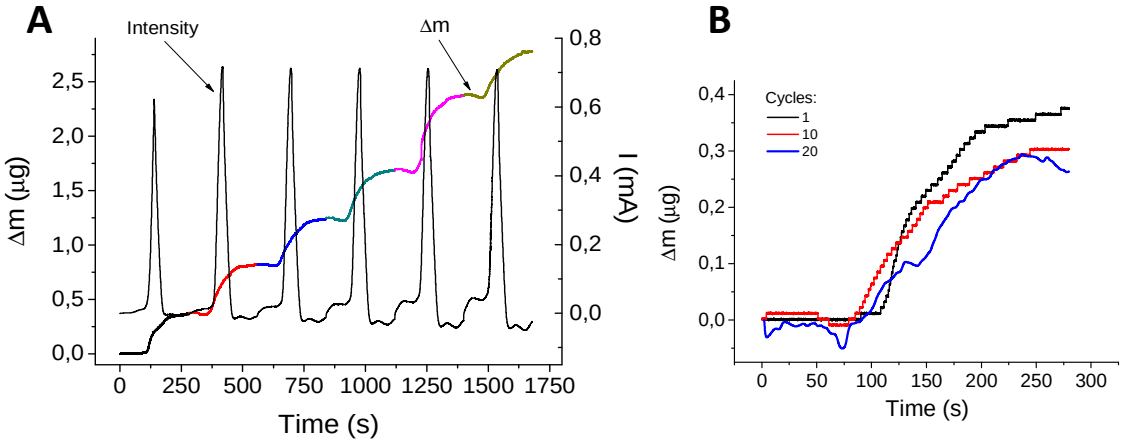

Figure 4.5. EQCM results obtained for IrOx-CNTs hybrid synthesis (scan rate of 5 mV/s and reverse potential of 0.7 V). A) Intensity and mass changes in the first 6 cycles versus time. Different colours in the mass increase curve indicate successive cycles. B) Mass increase registered for the 1st, the 10th and the 20th cycles.

The results obtained for the mass increase pattern during deposition are very similar to those obtained for pure IrOx, which suggest that IrOx deposition occurs in the same manner, in the first cycles. However, Figure 4.6B shows how during cycle 20 the corresponding mass change is very irregular, which indicates an abrupt quartz crystal

resonation. These “discrete” alterations of the resonation can be related with the start of CNTs deposition. Although is not shown, successive cycles, present the same profile.

The evolution of the intensity peak with the successive cycles is shown in Figure 4.6A and is very similar to that obtained for IrOx synthesis (Figure 3.13A). The intensity corresponding with the peaks assigned to the suggested Ir (IV)/(V) redox processes increase with the number of cycles, according with a larger mass deposited, whereas the peak at 0.7 V is maintained almost constant, indicating a possible saturation in the reaction responsible for the electrodeposition.

Figure 4.6B shows the total mass increase obtained for IrOx-CNTs synthesis in comparison with IrOx with and without oxalate coatings. For IrOx-CNTs the curve is not as linear as for IrOx samples, and although the mass deposited in the first cycles is larger for the hybrid, deposition slows down from cycle 15. This fact can be related with the beginning of the CNTs incorporation, as shown by the large alterations undergone in the resonating crystal (Figure 4.5B).

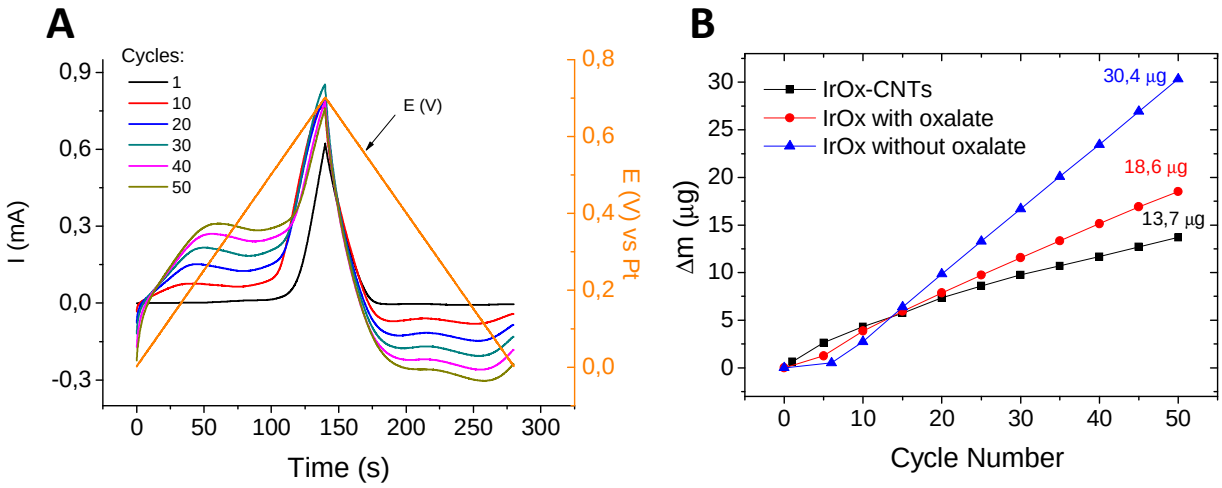

Figure 4.6. EQCM results for the IrOx-CNTs coating. A) Evolution of intensity curve during a complete 50-cycle synthesis (scan rate of 5 mV/s and reverse potential of 0.7 V) and B) Mass increase registered for IrOx-CNTs coatings compared with those for IrOx with and without oxalate.

The resulting IrOx-CNTs coatings present a quasi-transparent blue-black appearance, darker than IrOx ones (Figure 4.7B), due to the presence of carbon nanotubes. However, color can be modulated with the thickness, which in turn, depends on the total amount of charge used during preparation, by varying the number of voltage sweeps. Consequently, the final color can be used as indicative of the thickness of a particular coating (Figure 4.7A).

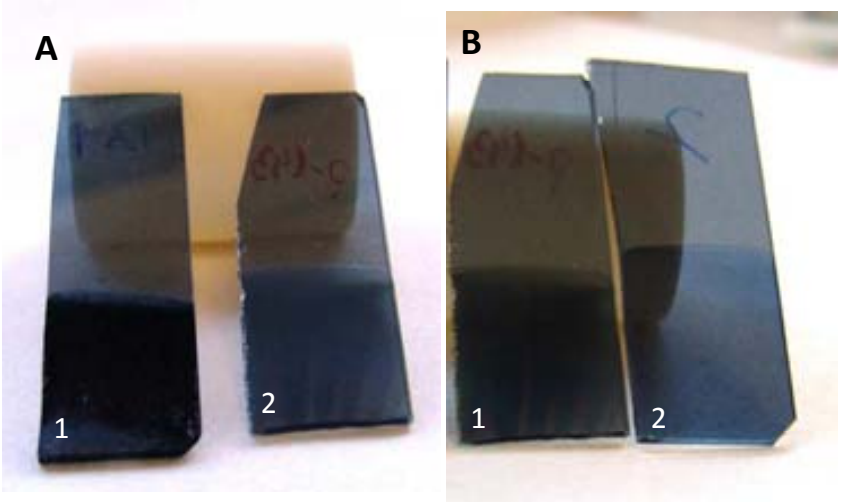

Figure 4.7. Electrodeposited coatings in different conditions. A) Coating of IrOx-CNTs: (1) 50 cycles and (2) 25 cycles. B) (1) IrOx-CNTs 25 cycles and (2) IrOx 50 cycles.

4.3 Characterization of the Samples

The characterization of the samples was carried out with a broad number of techniques in order to elucidate the microstructure, thickness, roughness and chemical composition, as well as the electrochemical properties of the IrOx-CNTs hybrid coatings.

4.3.1 Transmission Electron Microscopy of the Coatings

Figure 4.8 shows TEM images of the solid residue obtained after hybrid coating removal from the substrate and redispersion in EtOH. Bundles of carbon nanotubes are observed in Figure 4.8A with big solid particles covering part of them. In the inset it is possible to observe how these IrOx particles are formed in turn, by IrOx nanoparticles 2-3 nm in size, similar to those obtained for bare IrOx pre-deposition solutions (Figure 3.7), showing that the nature of the solution is maintained, which corroborates the hypothesis of electro-flocculation.

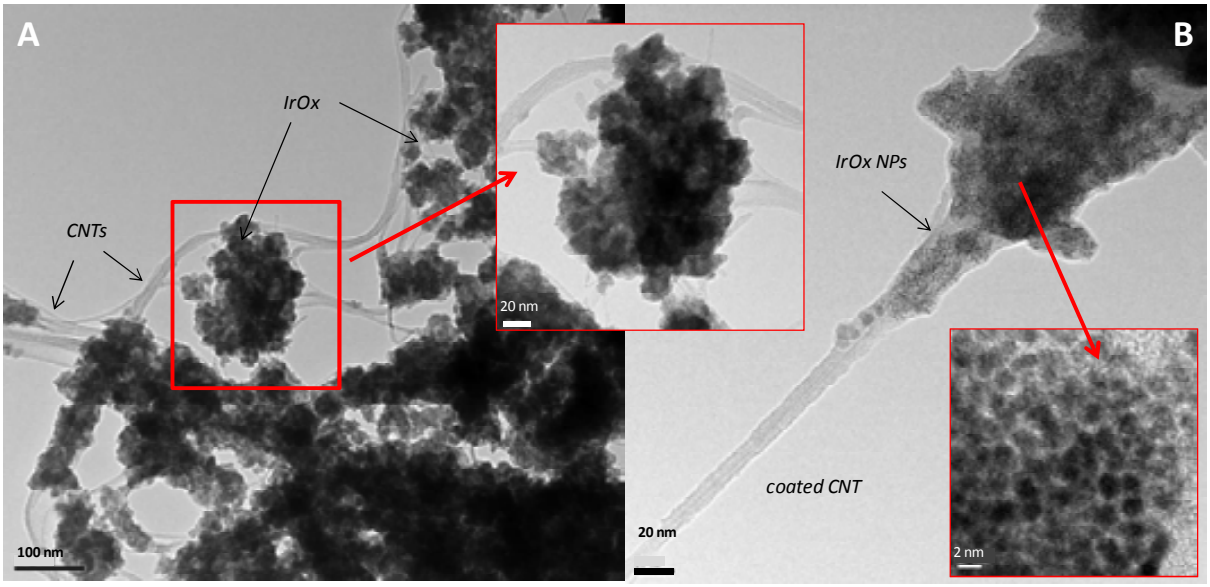

Figure 4.8. TEM images of the solid residue obtained from IrOx-CNTs hybrid coating removed from the soda-lime substrate and redispersed in ethanol. A) CNT bundles with IrOx deposited onto them (in the inset is possible perceive the IrOx nanoparticles) and B) coated CNT with IrOx nanoparticles in the bulk oxide (in the inset zoom of the nanoparticles is shown).

In Figure 4.8B, a single coated nanotube (or maybe few but well aligned) is shown. The rough nanotube surface observed (sharper than in case of bare CNTs-COOH) and the increased diameter when compared with bare carbon nanotubes suggest an efficient coating. This IrOx encapsulation of CNTs may occur when the nanotubes reach the electrode during the hybrid synthesis, becoming an extension of it, and

yielding the carbon nanotube encapsulation. Although also, some chemically interaction can occur between the charged CNTs and the iridium precursors in solution.

4.3.2 Scanning Electron Microscopy

SEM was used to study the surface microstructure and the thickness of the hybrid coatings. Images of the general surface of IrOx-CNTs coatings are shown in Figure 4.9. Hybrid coatings are generally uniform, presenting a granulated texture, with the surface becoming rougher and more porous as the film thickness increases. The grain size seems to be the same for both images, but in the thicker sample more grains are condensed to form bigger particles, a 3D-like structure. In this work, different thicknesses have been tested, but for coatings synthesized at more than 50 cycles, big cracks have been detected in the surface. Thus, in order to obtain a good stability of the electrodes, films thicker than 50 cycles were dismissed, and usually 25-cycle coatings have been considered.

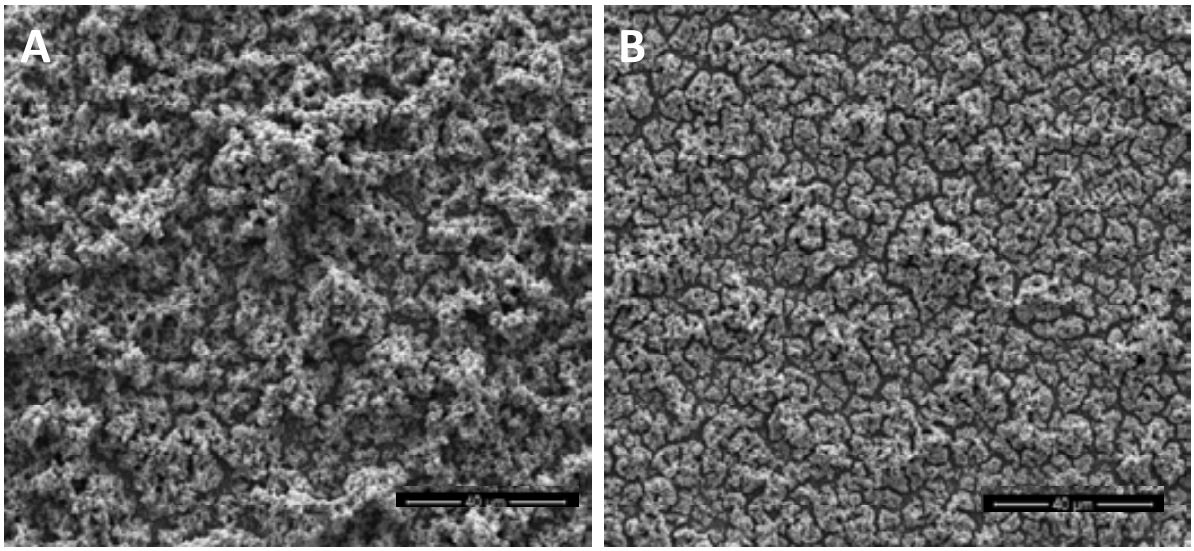

Figure 4.9. SEM images of the surface of IrOx-CNTs samples. A) 50 cycles and B) 25 cycles. Images were taken at 10 kV and with a spot of 2.5.

The mechanism suggested for IrOx-CNTS coating formation is that, when charged carbon nanotubes contact the electrode surface, are conductive themselves and so, IrOx can be deposited onto them. Such model raises from the nanotubes bundles shapes observed in the surface (Figure 4.10E), which are the responsible of the three-dimensional microstructure, confirming the oxide formation around the nanotubes.

The diameter of these observed fibrils are in the range of 30 nm to 60 nm. This change in diameter in comparison with bare CNTs (1-2 nm) can be explained by a thick and uniform oxide coating around the nanotubes. Furthermore, even an individual nanotube coated by IrOx can be observed in the cracks (Figure 4.10F). CNTs acting as nucleation sites have been reported in other oxide-CNTs synthesis, even when no electrochemical methods are involved [16]. In our case, no evidences of chemical reaction have been detected between iridium precursors and carbon nanotubes in solution, although in case of interaction, this may be reinforced by the posterior electrochemical method used for the synthesis of the hybrid coatings.

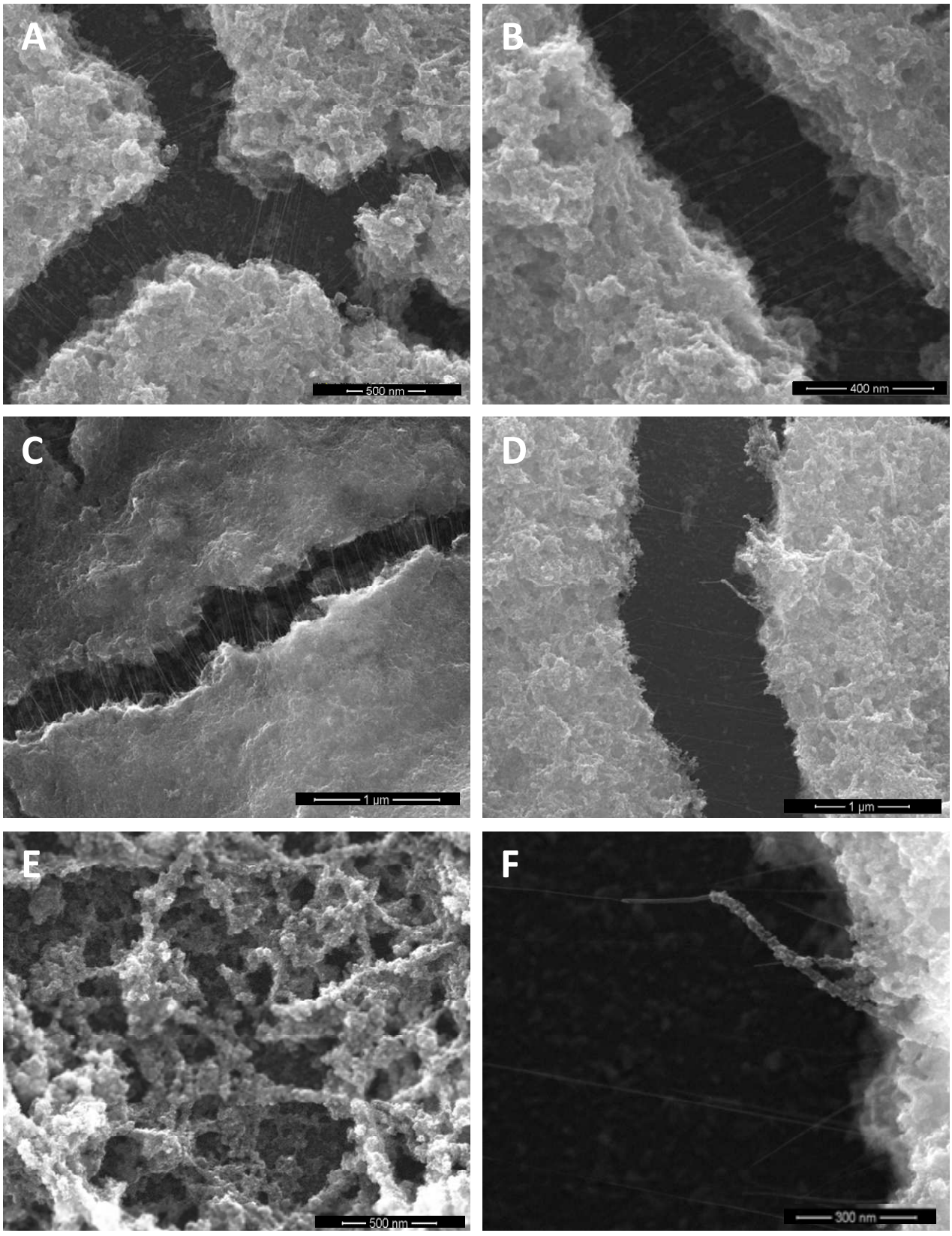

Figure 4.10. SEM images of the surface of IrOx-CNTs coatings (50 cycles). A-D) cracks to appreciate the CNTs, E) surface of the bulk part and F) detail of a covered CNT in a crack. Images were taken at 30 kV.

Although the surface shows evidences of the presence of CNTs, carbon nanotubes are more clearly observed in the inner parts of cracks formed in the borders of the thickest coatings, as presented in Figure 4.10 A-D.

Crack formation has been described in literature [8] as a problem of shrinkage after preparation. For thin films, this aspect can change drastically the surface characteristics and it has to be controlled. In our case, reducing the thickness of the coatings the homogeneity improves, but crack formation cannot be totally avoided. The shrinkage of the material contract the oxide, but the CNTs due to the exceptional hardness, do not break and the result is a crack which looks like “sewed” by the carbon nanotubes. Thus, the nanotubes act scaffolding the global structure.

Thickness of the coatings can be measured using SEM. For this purpose a clean cut was done and the sample was located in parallel with the electron beam, in order to see clearly the border. The results are shown in Figure 4.11.

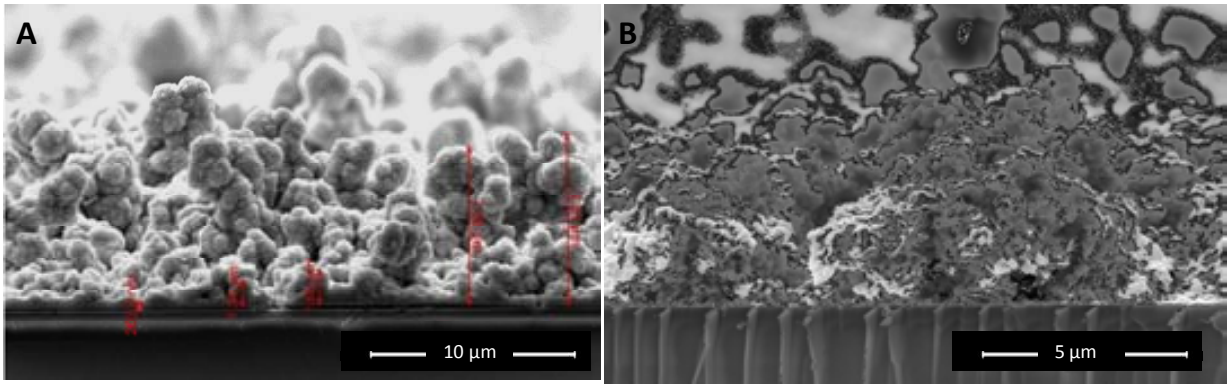

Figure 4.11. SEM images of the border of the samples in order to calculate the thickness of the IrOx-CNTs samples. A) 50 cycles and B) 25 cycles. Images were taken at 10 kV.

IrOx-CNTs hybrid coatings have an average thickness around 4-5 µm for 50-cycle preparation, and 2-3 µm for 25-cycle coatings. Therefore, the thickness has increased considerably in comparison with IrOx coatings (30-50 nm). However, the final mass deposited calculated by EQCM is lower, which indicates also lower density for hybrid coatings compared with bare IrOx.

The structure of IrOx-CNTs surface, as observed in the general SEM (Figure 4.9), has granulated texture, forming like columns of solid, which become bigger as the number of cycles increases.

In bare IrOx coatings, thickness is limited by the obtaining of worse adhered coatings, which undergo delamination under electrochemical conditions [17]. However, thick coatings are very desirable, because are able to supply a elevate charge injection capacity. In this sense, we have obtained a hybrid material, much thicker than the IrOx, with very stable mechanical properties.

4.3.3 Roughness by 3D Confocal Microscopy

The roughness of the material surface was determined by confocal 3D microscopy. AFM was used in some cases, but did not achieve coherent results in rougher cases. Figure 4.12 shows the 2D surface, a selected profile after filtering and the three-dimensional surface image obtained after the analysis of an IrOx-CNTs sample.

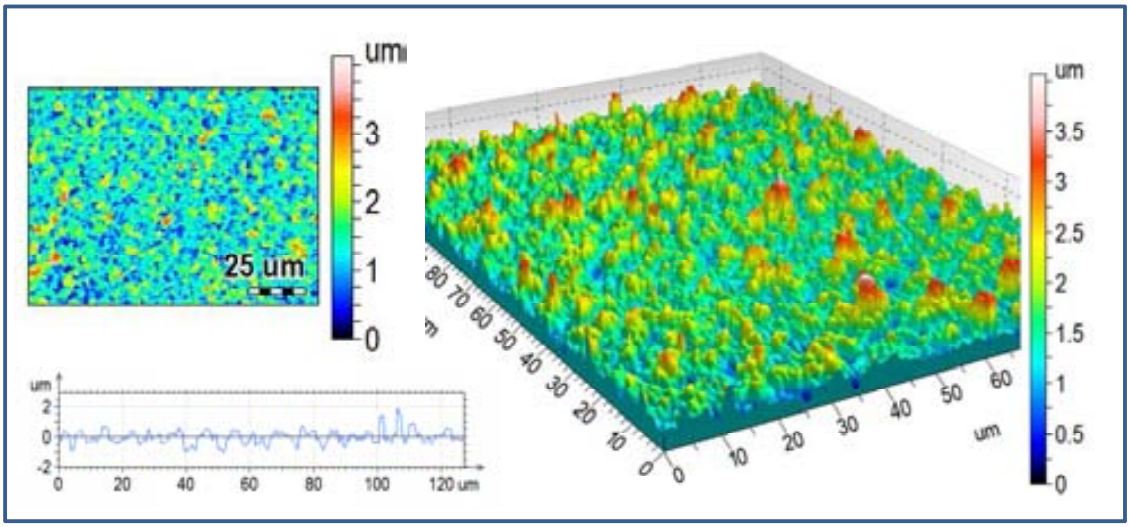

Figure 4.12. Confocal 3D microscopy images showing the 2D map after the scan, a selected characteristic profile and the 3D surface, for a 25-cycle IrOx-CNTs sample.

The profile shows a very rough surface, also seen in previous images of SEM. Using surface texture analysis software (MountainsMap) is possible to give a value for the roughness (S_q or RMS). For 25-cycle IrOx-CNTs hybrid coating is around **S_q= 0.550 µm**. Comparing this value with the S_q= 3.0 nm obtained for IrOx (Figure 3.26), we can conclude that the hybrid is significantly rougher, due to the incorporation of the carbon nanotubes (and CNTs bundles) to the oxide structure. For 50-cycle IrOx-CNTs hybrid coating, values obtained were even larger, yielding S_q= 1.0 µm.

Rougher surfaces increase substantially the effective surface area, improving the charge transfer efficiency and hence, enhancing the electrode electrochemical properties.

4.3.4 Grazing Incidence X-Ray Diffraction

X-Ray Diffraction was used to analyze the crystalline composition of the coatings. In particular, and due to the low thickness of the coatings obtained by electrochemical synthesis, grazing incidence X-ray diffraction measurements were done, using an angle of 0.5º, optimal for the study of thin film composition. The results for the IrOx-CNTs hybrid as prepared, and the hybrid and bare IrOx after 4h-thermal treatment at 500ºC in air are shown in Figure 4.13. The main conclusion obtained with these results is that IrOx-CNTs coating as prepared is amorphous, as well as the corresponding as prepared IrOx (Chapter 3).

The obtained patterns for thermally annealed coatings are almost coincident for both samples, IrOx and IrOx-CNTs, and correspond with the hollandite-type structure presented for K_xIrO_2 [18] described in detail in Chapter 3. The minor differences can be related with different potassium concentration. But in general terms, it can be concluded that the incorporation of CNTs in the iridium oxide matrix, does not alter the final crystalline structure of the oxide.

The non crystalline structure of the electrochemically synthesized IrOx coatings and the high content of water, have been previously reported by some authors [7,19-21] and by us, and could be the origin of optimal performance as neural electrodes: the

open structure allows faster and more efficient ion exchange during redox processes, increasing the charge capacity of the electrode.

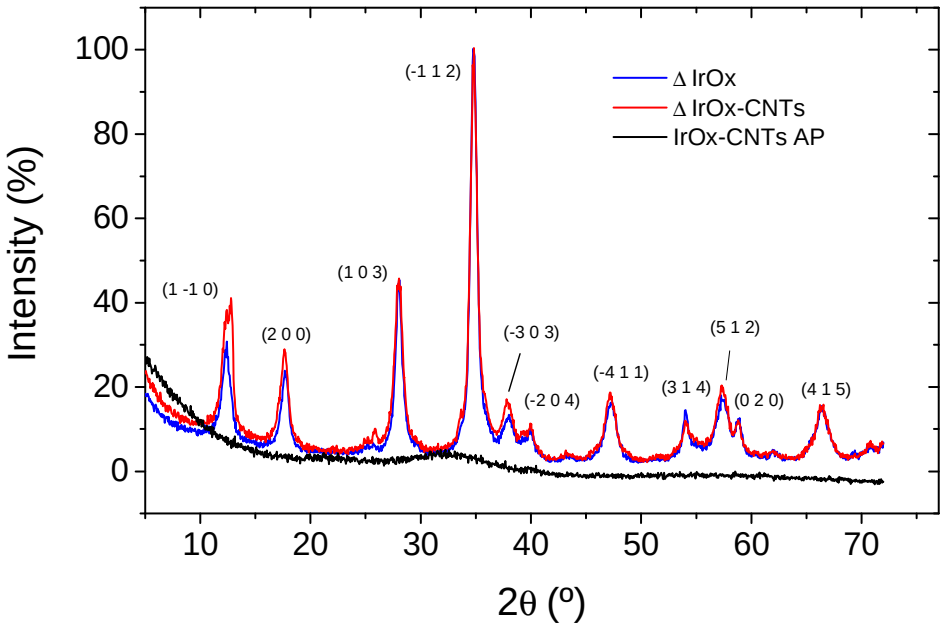

Figure 4.13. GIXRD pattern obtained for as prepared (AP) IrOx-CNTs coatings, and IrOx and IrOx-CNTs coatings after 4h-thermal treatment at 500ºC in air. The crystalline structure corresponds with K_xIrO_2 hollandite-type [18]. The most intense peaks are indexed.

4.3.5 Micro-RAMAN Analysis

Single walled carbon nanotubes are one-dimensional systems, which have specific electronic and vibrational energy states quantified, and hence, the optical transitions are discrete and well defined, being Raman spectroscopy the most powerful tool to elucidate the presence of carbon nanotubes in the prepared hybrid coating.

The main spectral lines observed for SWCNTs are: radial breathing modes (RBM) around 200-300 cm^{-1}, which provide information about the diameter and the quirality of CNTs; the tangential G-band around 1600 cm^{-1}, which indicates the metallic or semiconductor character; and the D (Disorder induced) and G' (overtone D) bands at 1300 and 2650 cm^{-1} respectively, which provide information about the fine structure

of the valence conduction bands of CNTs [22-24]. The vibrations responsible for the RBM and the G-band modes are shown in Figure 4.15.

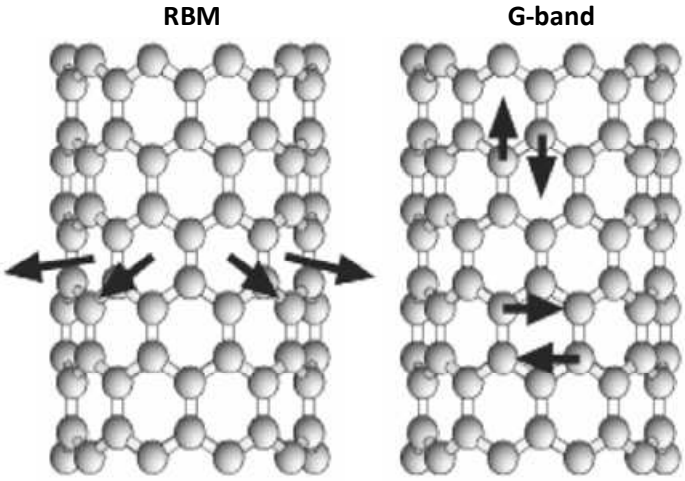

Figure 4.15. Atomic displacement associated with RBM and G-band normal-mode vibrations. [25]

The presence of CNTs in the synthesized coatings was elucidated by RAMAN analysis, taking as reference the well defined signal observed for G-line around 1600 cm^{-1}. The measurements were done for large number of samples (obtaining similar results), and Figure 4.16 shows some representative Raman spectra. The laser was focused in different areas of the sample (marked as zone 1, 2 and 3), observing in all of them the characteristic broad band of amorphous IrOx (see Chapter 3). However, the representative G-line of CNTs, originated from sp^2-hybridized carbon at 1589 cm^{-1} [26] is only observed in zone 1. The sharp and narrow line shape indicates low level of other carbonaceous impurities in the films [27]. In the inset, the high frequency measurement of zone 1 is done to corroborate the presence of CNTs, showing the characteristic G'-line at 2660 cm^{-1}. The D line (usually around 1340 cm^{-1}) is not observed in the spectra, probably due to the low laser excitation energy used during the measurement. The RBM band is not clearly observed, probably by the overlap with IrOx spectral lines or because the radial vibration of carbon nanotubes is minimized due to the iridium oxide coating.

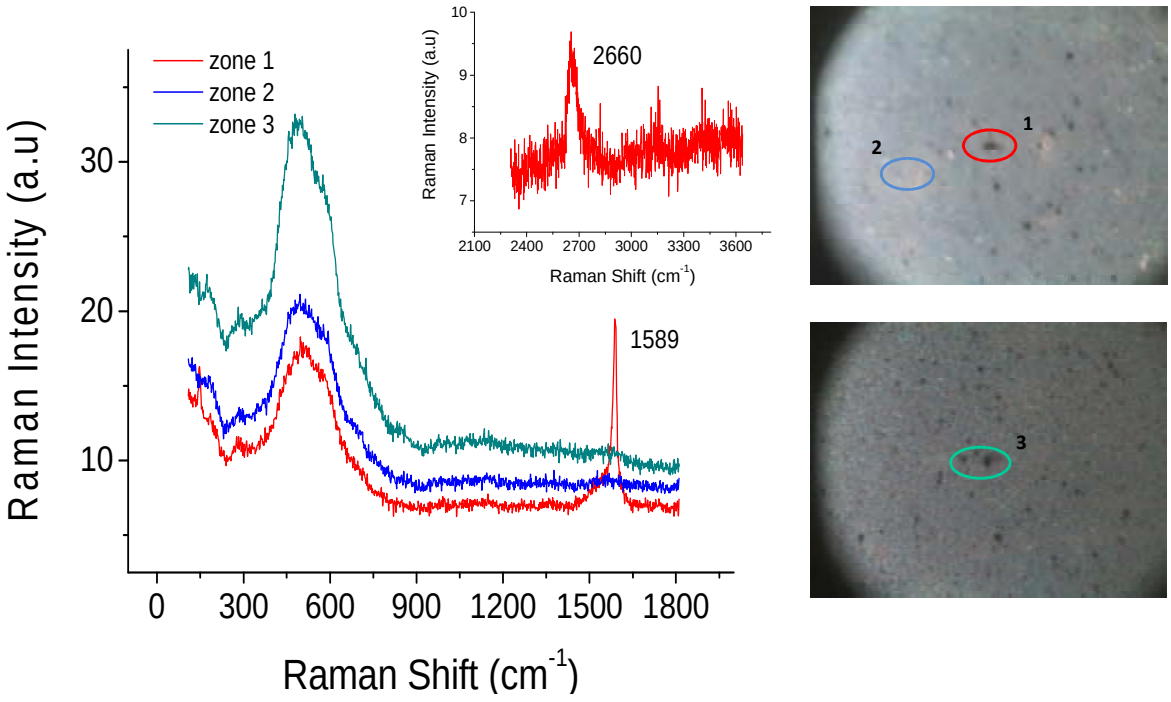

Figure 4.16. Raman spectra of IrOx-CNTs coating in different areas. The inset above is the spectra obtain for zone 1 at higher frequency, showing the second characteristic Raman signal for CNTs.

During the performance of Raman experiments, if the laser was focused on the surface of the IrOx-CNTs coating and the power density was increased, crystallization of iridium oxide occurs. Therefore, peaks corresponding to Raman-active modes (E_g, B_{2g} and A_{1g}) get narrow, and close to those for single crystal IrO_2 [28] as shown in Figure 4.17. The comparison of maximum peak energies for amorphous (0.7 mW) and crystallized (1.4 mW) coatings, shows a little red shift, attributed mainly to stress or size effects [29]. However, this partial crystallization is not observed in IrOx samples analyzed in Chapter 3, which instead, get deteriorated when the laser power is increased. Thus, CNTs presumably prevent the process, dispersing the energy and avoiding the IrOx damage, but allowing the oxide crystallization.

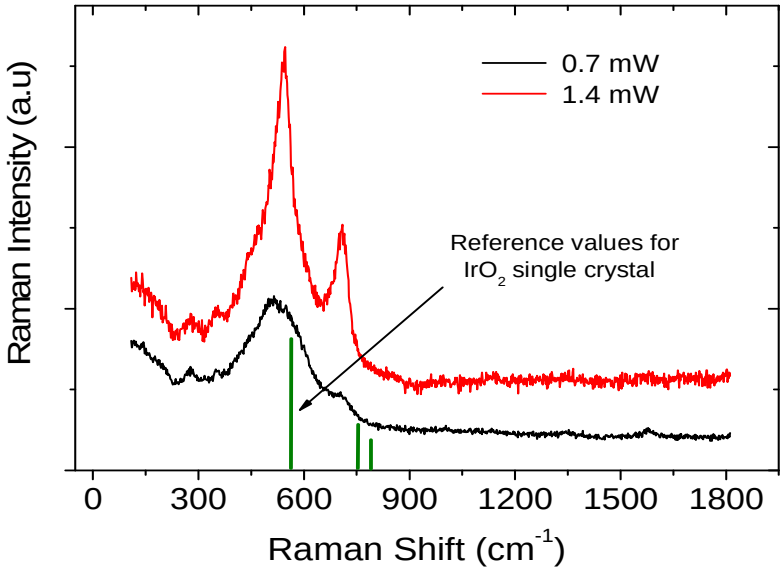

Figure 4.17. Raman spectra of IrOx-CNTs sample with different laser power.

Conventional micro-Raman experiments show the presence of carbon nanotubes in the hybrid coating, but not homogeneously distributed in the sample or, at least not with the enough concentration to be detected in micro-RAMAN experiments of this type. Thus, in order to study the CNTs dispersion within the coatings, Raman-Confocal experiments were performed. First, a single spectrum was taken (Figure 4.18A), showing the main peaks for IrOx (broad due to the amorphous-character) and the characteristic ones for single-walled CNTs [23]. These results agree with the obtained in micro-Raman experiments, but in this case, the D-line at 1480 cm^{-1} is observed.

Considering the Raman spectral line corresponding with the G-line for SWCNTs (1589 cm^{-1}), a Raman scan was done on a 9.5 μm^2 surface and a representative result is shown in Figure 4.18B. Lighter color areas correspond to high intensity of the SWCNTS Raman G-line signal, which indicates high concentration of carbon nanotubes. It is possible to observe how the CNTs form dispersed aggregates in the entire coating, which is expected due to the synthesis method, starting with CNTs bundles in suspension. The presence of amorphous iridium oxide is also confirmed.

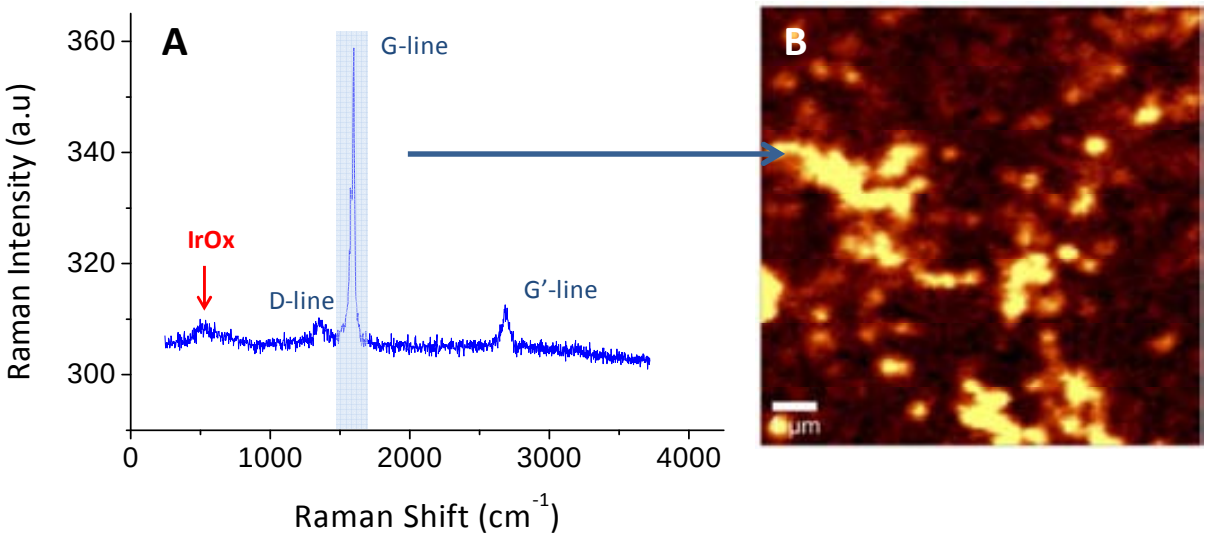

Figure 4.18. A) Single Raman spectra for the sample IrOx-CNTs and B) Confocal Raman scanning image of the distribution of carbon nanotubes in the same sample. The surface scanned was 9.5 µm^2. The yellow areas correspond with nanotubes' clusters.

4.3.6 X-Ray Photoelectron Spectroscopy

XPS technique was used to determine the surface composition and concentration of the different elements present in IrOx-CNTs coatings. Results obtained for IrOx-CNTs and bare IrOx coatings, as comparison, are shown in Figure 4.19. The survey spectra for both coatings are very similar and with all the expected elements: iridium, carbon, oxygen and potassium, a counterion previously reported in IrOx synthesis (Chapter 3).

The quantification of the elements found in IrOx and IrOx-CNTs coatings as prepared, and thermally treated hybrid samples, are shown in Table 4.1. The thermal treatment was 4h-heating at 500ºC in air (Δ IrOx-CNTs), and allows to study the superficial chemical changes produced by the crystallization of the hybrid coating.

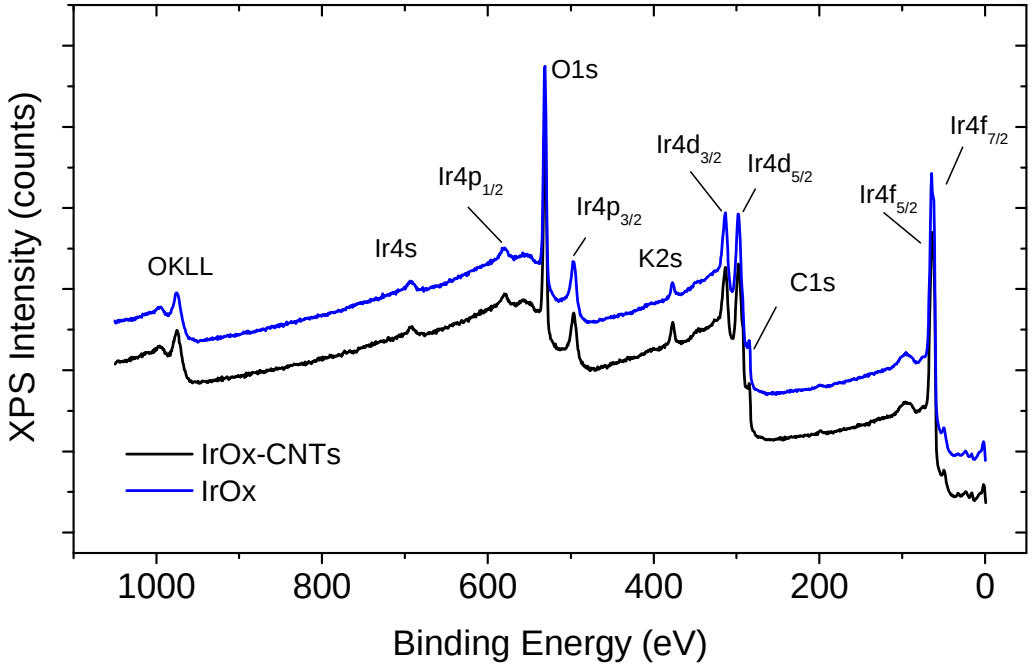

Figure 4.19. XPS survey spectra for IrOx-CNTs hybrid coatings and IrOx synthesized in normal conditions.

Samples	C1s (at.%)	O1s (at.%)	Ir4f (at.%)	K2p (at.%)	Si2p (at.%)	K/Ir	C/Ir	O/Ir
IrOx	15.7	47.6	13.2	23.5	---	**1.78**	**1.18**	**3.60**
IrOx-CNTs	14.2	49.8	12.5	23.5	---	**1.88**	**1.13**	**3.98**
IrOx-CNTs Δ	10.4	55.3	7.7	14.9	11.7	**1.93**	**1.35**	**7.18**

Table 4.1. Quantification (atomic %) for coatings of IrOx and IrOx-CNTs as prepared and IrOx-CNTs after 4-hour thermal treatment at 500ºC, obtained from the data of the XPS survey spectra.

As prepared IrOx and IrOx-CNTs coatings show similar chemical composition, indicating comparable IrOx surfaces in both coatings, with little variations (Table 4.1).

IrOx chapter shows how samples subject to atmospheric conditions (storage time or humidity, among others) can modify the content of C or O in the surface. However,

the quantity of iridium and potassium present in the coatings come only from the synthesis process and would not vary by external conditions. For this reason, the relation K/Ir gives an idea of the reproducibility of the samples. As it is seen in Table 4.1, similar values of K/Ir are obtained for samples of IrOx and IrOx-CNTs, being 1.78 and 1.88 respectively, confirming the statement of similar IrOx surface in both samples. Even for the heated sample, the K/Ir relation is very close (1.93) suggesting that these elements are not altered by the temperature, and the chemical composition of the hollandite-phase is similar to the amorphous phase IrOx.

The O/Ir relation is also an important parameter because it gives information of the metal oxidation state, and is observed in the range of 3.5 to 4 in as prepared coatings. These values are larger than the theoretical expected for IrO_2 (O/Ir=2), and a little smaller than $Ir(OH)_4$, (O/Ir=4), indicating the existence of an oxohydroxyde, as suggested in Chapter 3. However, the high content of water and the impurities present in the surface interfere in this value and contribute to increase this relation.

When IrOx-CNTs coating is heated, a considerably increase of the oxygen is observed, and the relation O/Ir increases up to 7.18. This increase can be related to the formation of potassium superoxide (KO_2) at those temperatures in presence of atmospheric oxygen. This potassium superoxide formation has been previously reported [30], and modifying the heating parameters can yield to KO_2 sublimation, as observed in our laboratory [31]. Considering the formation of KO_2 and subtracting the corresponding oxygen to the O1s total, the new O/Ir relation is 3.3, close to those obtained for as prepared coatings.

As shown in Chapter 3, large percentages of carbon in the surface are obtained, due mainly to adhered adventitious carbon (C_{adv}) from the atmosphere [32,33]. The high affinity of the iridium oxides for this type of carbon has been proven in our experiments in a reproducible manner. However, it is possible as described by Biesinger [34], to calculate the amount of oxygen related with adventitious carbon and hence, have the real percentage of oxygen by difference. For IrOx-CNTs hybrid coatings, the formula may not be as precise as in the case of IrOx, because of the presence of carbon nanotubes. The total carbon, however, is even smaller for the

hybrids, indicating that carbon nanotubes contribution to the total C1s value is negligible. It can be because CNTs are well dispersed, very thin and/or as seen in SEM Figure 4.10F, are coated by thick layer of iridium oxide. For these reasons, the low penetration of the XPS technique (in the range of 3-10 nm), and the large amount of adventitious carbon in the surface complicate the CNTs determination. In any case, using the Biesinger approximation previously utilized for IrOx samples, it is possible to calculate the quantity of oxygen associated with adventitious carbon, which is shown in Table 4.2.

Samples	O1s (at.%)	Total Oxygen from C_{adv} (at.%)	Remaining Oxygen (at.%)	Remaining Oxygen/Ir (at.%)
IrOx	47.6	4.8	42.8	3.24
IrOx-CNTs	49.8	5.1	44.7	3.57

Table 4.2. O1s quantification (atomic %) for the different coatings, showing the percentage of oxygen obtained from the survey, the percentage obtained after using the Biesinger formula indicating the total amount of oxygen coming from the adventitious carbon (C_{adv}), the remaining oxygen after the difference and the relation between the remaining oxygen and the Ir.

The new O/Ir values obtained removing the oxygen contribution due to the adventitious carbon are lower than the previous ones, but still high for pure IrO_2, confirming the oxohydroxyde structure. The ratio “Remaining Oxygen”/Ir is larger in the hybrid than in bare IrOx, presumably due to the contribution of the oxygenated-groups from the surface of functionalized CNTs.

C1s and O1s deconvoluted peaks are shown in Figure 4.20 for IrOx-CNTs and IrOx coatings as prepared, and the hybrid coatings thermally treated. The deconvolution was performed using Gaussian-Lorentzian line shapes for fitting, while the background was adjusted with basic linear Shirley correction.

For all samples, deconvolution of O1s peak gives rise to three defined peaks. The first peak at 530.1±0.2 eV is attributed to the lattice oxygen in the oxide (O^{2-}). The second peak at 531.5±0.2 eV corresponds mainly to oxygen present in hydroxyl groups (OH^-) and other C-O (C=O, COO^-) species. The last one, at 533.4±0.2 eV is assigned to water (H_2O), as shown in other oxide examples in literature [35-38]. This peak decreases significantly when the sample is heated, as can be seen in the thermally treated IrOx-CNTs sample, evidencing dehydration.

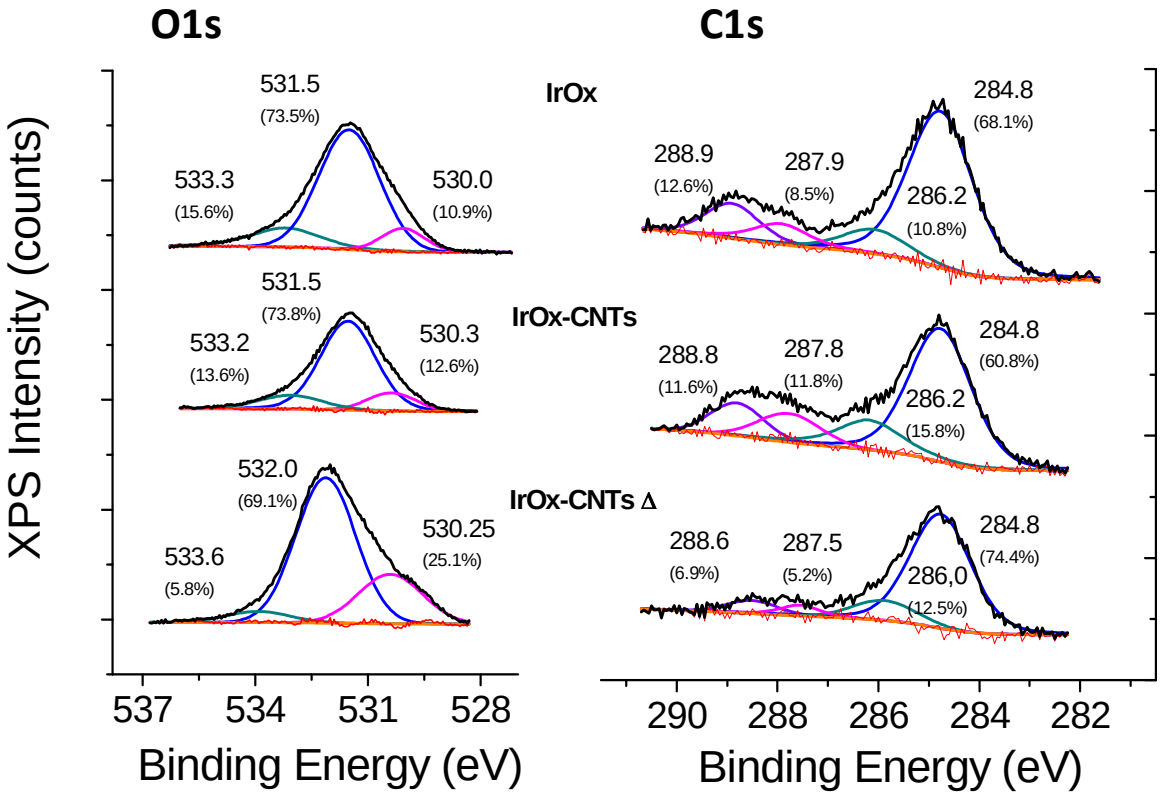

Figure 4.20. Deconvolution of O1s and C1s peaks from the high resolution XPS spectra for IrOx, IrOx-CNTs and IrOx-CNTs after a 4h-thermal treatment at 500ºC (IrOx-CNTs Δ) samples. The contribution of the different peaks to the total peak is expressed in brackets.

C1s deconvolution fits well with four defined peaks. The first of them, at binding energy of 284.8±0.2 eV is typical for aliphatic carbon (C-C, C-H), the second peak, at 286.2±0.2 eV corresponds to the signal associated with a carbon bonded to an ether or hydroxyl group (C-O-C and C-OH), the third one at 287.9±0.2 eV is for C=O, and the

last peak at 288.9±0.2 eV is assigned to the carboxylate group (COO^-) [39]. The non existence of carbonates (CO_2^{3-}) in the samples is confirmed, because the characteristic peak C1s at 290 eV is not observed [36].

Combining the percentage obtained in the deconvolution of the peaks, with the amount of oxygen and carbon from the survey, the total atomic percentage of each species in the sample can be resolved, and it is shown in Table 4.3.

	Peak assignation/ Position (eV)	IrOx (atomic %)	IrOx-CNTs (atomic %)	IrOx-CNTs Δ (atomic %)
O1s	O^{2-}/530.1	5.2 (0.39)	6.3 (0.50)	13.9 (1.8)
	OH^-,C=O, COO^-/531.5	35.0 (2.65)	36.7 (2.94)	38.2 (5.0)
	H_2O/533.4	7.4 (0.56)	6.8 (0.54)	3.2 (0.4)
C1s	C-C, C-H/284.8	10.7 (0.81)	8.7 (0.68)	7.9 (1.02)
	C-OH, C-O-C/286.2	1.7 (0.13)	2.2 (0.18)	1.3 (0.17)
	C=O/287.9	1.3 (0.10)	1.7 (0.14)	0.5 (0.07)
	COO^-/288.9	2.0 (0.15)	1.6 (0.13)	0.7 (0.09)

Table 4.3. Total quantification of the O1s and C1s peaks components (atomic %) in the studied coatings. Percentages add up to the total quantity of each element from the survey: carbon 15.7%, 14.2% and 10.4%, and oxygen 47.6%, 49.8% and 55.3%, for IrOx, IrOx-CNTs and IrOx-CNTs Δ, respectively. (Number in parenthesis express ratios respect to the Iridium).

For the as prepared IrOx and IrOx-CNTs samples, not relevant differences are observed. For both coatings, O1s percentage for OH^- is greater than the one obtained in C1s for C-OH, even including the C=O and COO^- contributions, indicating that OH^- groups mostly are linked to iridium atoms, confirming the oxohydroxyde structure. The atomic percentage of the hydration water can be subtracted to obtain the O/Ir ratio for valence calculation, resulting in 2.68 and 3.03 once the water contribution has been subtracted. These numbers express the (O^{2-} + OH)/Ir, without the C_{adv} contribution.

C1s results are not very relevant. Data are very similar for all the coatings, and as it has been mentioned before, the fact that samples with no carbon nanotubes present higher carbon content in the surface, it is due to the adventitious carbon. Thus, we can conclude that it is not possible to differentiate between samples with and without carbon nanotubes by this technique.

For IrOx-CNTs thermally treated the oxygen component related with the latticed oxygen in IrOx, O^{2-}, has increased considerably and the percentage of water has decreased but remains a small percentage, suggesting that a little amount can be retained as structural water in the oxide matrix. These both changes are possibly related to dehydration and condensation processes. The quantity of adventitious carbon is higher when compared with as prepared films, but can be result of a longer exposition to atmospheric conditions, which has been demonstrated to be significant (Chapter 3).

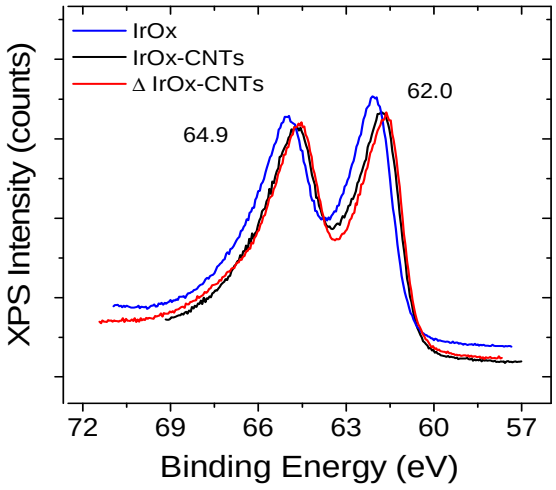

Figure 4.21. . Ir4f XPS spectrum for the studied as prepared and thermally treated IrOx-CNTs coatings, compared with the Ir4f peak obtained for bare IrOx coatings.

Ir4f peak analysis for IrOx-CNTs hybrid, shows an asymmetric peak-shape at BE locations of major and minor Ir $4f_{7/2}$ and $4f_{5/2}$ peaks around 62.0±0.2 eV and 64.9±0.2 eV respectively (Figure 4.21). The distance between the main peaks, 2.9 coincides with those values in literature [39]. Also, these results coincide with those for the

thermally treated hybrid and IrOx coatings, although for the latter, this Ir4f peak is slightly shifted through higher values of BE.

With the aim of calculating the total quantity of CNTs in the hybrid coatings, and after the impossibility of determination of total amount of carbon coming from CNTs by XPS, another experiment was envisaged. IrOx-CNTs and bare IrOx coatings were measured by RBS (Rutherford backscattering spectrometry) in the "*Centro Nacional de Aceleradores*" however, the results are also not concluding. First, spectra are highly distorted, probably by the insulating character of the glass substrate or by high porosity of the coatings, that can considerably alter the measurement. In addition, the high quantity of oxygen in the soda-lime glass used as substrate, do not allow differentiate the oxygen belonging to the coatings. For these reasons, this technique was not useful either for the CNTs quantification in the samples. Some alternatives as deposition of the hybrid films onto silicon slides have been proposed in order to improve the results, but these modifications are out of the scope of this thesis.

4.3.7 Electrochemical Characterization of the Coatings

The electrochemical behavior of IrOx-CNTs coatings was evaluated by cyclic voltammetries (CVs) in different electrolytes and electrochemical conditions, to evaluate the potential use of these materials as neural electrodes. As observed previously in IrOx coatings, reduction and oxidation peaks in CV curves demonstrate that IrOx-CNTs hybrid material undergoes reversible redox reactions due to the mixed valence state of the iridium cation and favored by the porosity of the material.

In most neural stimulation applications, a biphasic, cathodic-first current pulse is used to stimulate nervous tissues [40]. A similar protocol has been used in this work to evaluate the viability of the materials as potential electrodes. The experimental three-electrode cell system used, as described in Chapter 2, has been the same as the one used to electrodeposit the coatings, and the area of the working electrode has been $1cm^2$. Figure 4.22 shows the CV curves at 20 mV/s in pH=7.4 phosphate buffered solution (PBS), for 25-cycle IrOx-CNTs and 50-cycle IrOx coatings. The lack of definition of the peaks obtained suggests that redox processes correspond to a lower

ion transport rates within the film, presumably because of the thickness of the coatings [41].

The values obtained under these conditions for cathodal charge storage capacity (CSC_c), calculated in a potential range of -0.6V to 0.8V vs Pt, are 34.6 mC/cm^2 for IrOx and a considerably higher value, 101.2 mC/cm^2 for the IrOx-CNTs hybrid (Figure 4.22). The presence of CNTs in the structure, which provides higher electrical conductivity, can enhance this parameter. But also the thickness can be an important factor, as thicker films have more electro-active sites, and as consequence, CSC_c values are highly dependent on the effective surface of the electrode. The hybrid with larger roughness and thickness, shows therefore, an enhanced value of charge storage capacity. Rougher surfaces make that electrochemical surface areas greatly exceed geometrical surface areas (however, electrochemical surface areas are difficult to define for porous electroactive electrodes and have not been evaluated in this work).

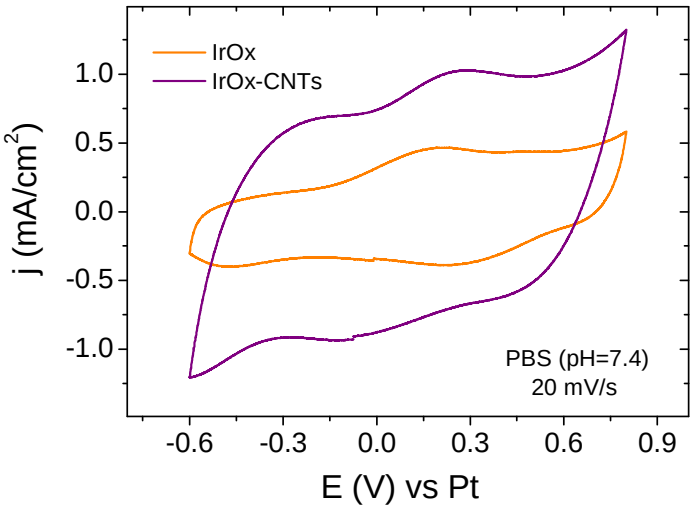

Figure 4.22. Comparison of cyclic voltammetries of IrOx (50 cycles) and IrOx-CNTs (25 cycles) samples in PBS (PH=7.4) electrolyte, at scan rate of 20 mV/s.

These values obtained are among the largest ones obtained in literature for similar hydrated iridium oxides (see Table 4.4). Despite the electrode geometry or size, which highly influences the CSC_C value, other factors related to IrOx can contribute: for example, in AIROF the electrochemical activation time is highly dependent, for

SIROF the film thickness is a decisive factor. CSC_C limits of 80 mC/cm^2 have been reported for AIROF (8h activation time), beyond which continued activation of iridium to higher levels results in delamination of the film, presumably due to large volume changes associated with the exchange of counterions during the activation [42]. For SIROF microelectrodes maximum values of 194 mC/cm^2 have been achieved for coatings 770 nm thick, and linear behavior of CSC_s versus thickness has been observed under this range [5].

Sample and technique	**CSC_c / mC·cm^{-2}**	**Conditions**	**Potential limits**	**REF**
IrOx-CNT electrosynthesized	101.2	PBS, 20 mV/s	-0.6 - 0.8 V vs Pt	-
IrOx electrosynthesized	34.6	PBS, 20 mV/s	-0.6 - 0.8 V vs Pt	-
SIROF	78-194	PBS, 50 mV/s	-0.6 - 0.8 V vs Ag/AgCl	5
AIROF	3-85	Bicarbonate BS, 100 mV/s	-0.6 - 0.8 V vs SCE	42
AIROF	25.0	PBS, 50 mV/s	-0.6 - 0.8 V vs Ag/AgCl	44
AIROF, SIROF	23.0	PBS, 50 mV/s	-0.6 - 0.8 V vs Ag/AgCl	41
EIROF	25.0	PBS, 50 mV/s	-0.6 - 0.8 V vs Ag/AgCl	1
SIROF	2.8	PBS, 20 mV/s	-0.6 - 0.8 V vs Ag/AgCl	44

Table 4.4. Results of CSC_c values obtained in our lab and some values presented in the bibliography.

Therefore, the enhancement of CSC_c values in this type of materials is proportional to the thickness, but the difficulty of obtaining thick and stable coatings has been the limiting issue. In this sense, hybrids obtained in this thesis, can be synthesized with

variable thickness, even some microns, with still high stability, giving a very good result of charge storage capacity.

It is important to remark that values presented in this work have not been optimized yet, and they are only an indication of the promising properties of these materials to act as neural electrodes. A study of the optimal morphology of the electrode, the decrease in the area (microelectrodes arrays) or a low scan rate, may produce higher values and electrochemical performance.

To measure the stability of the materials as stimulation electrodes, IrOx-CNTs coatings were tested during 1000 cyclic voltammetries in PBS (pH=7.4) within a safe potential range, at scan rates of 10 mV/s. During each scan, the hybrid undergoes oxidation and reduction accompanied by ion migration and water diffusion in and out of the material. For this reason, it is important to evaluate how these redox processes affect the stability of the coatings and if the morphology of the films is modified, for example by crack formation. To compare the results, the same measurements have been done with IrOx.

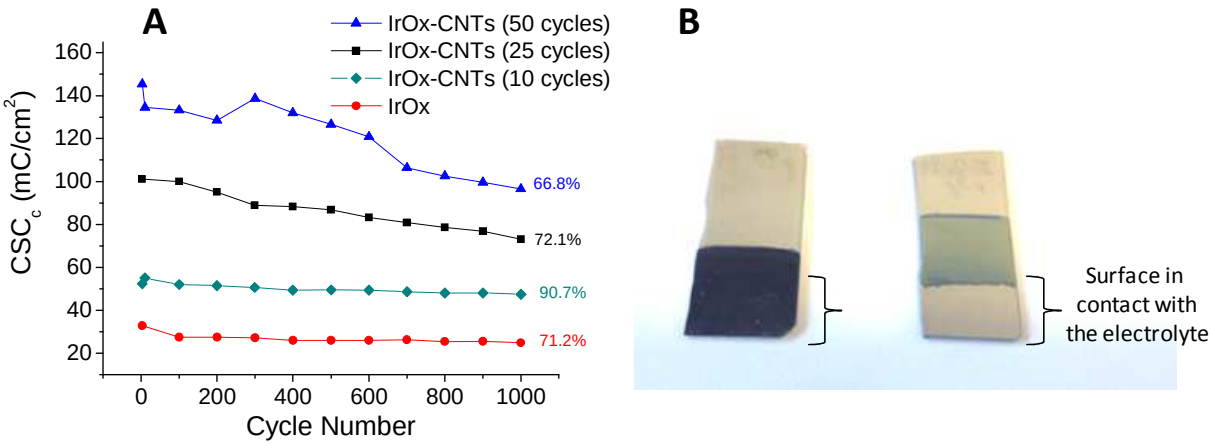

Figure 4.23. A) 1000 cycling performance of the IrOx-CNTs hybrid (synthesized at different cycles) and IrOx (50 cycles) film electrodes, in PBS (pH=7.4) at 10 mV/s. B) Image of the electrodes after the stimulation (IrOx is detached after cleaning with water the surface).

After successive CVs it can be observed how, while for the IrOx electrode the coating is detached from the substrate due to the formation of cracks, IrOx-CNTs one remains unaltered, not presenting cracking or delamination (Figure 4.23B).

CSC_c values for hybrids coatings are highly dependent of the thickness (Figure 4.23A). Samples synthesized at higher number of cycles achieve an increased value of CSC_c however, the stability decreases. Thus, for 50-cycle coatings, after 1000 consecutive cycles, only a 66.8% of the maximum CSC_c is maintained, while this value is 90.7% for the 10-cycle IrOx-CNTs coating. In any case, CSC_c value drops constantly and with a relatively soft slope for IrOx-CNTs as compared to the IrOx sample. On the other hand, a well defined step after the first 100 cycles is observed for IrOx, corresponding presumably with cracks formation in the electrode. The change in the intensity curve (which provokes the CSC_C decrease) is gradual, as shown in Figure 4.24, indicating a progressive degradation, due probably to the intercalation related with redox processes. The total decrease of CSC_c for IrOx coatings is about 24.3% but, 17% of the charge capacity is lost during the first 100 cycles, presenting a quasi-constant value in the next cycles.

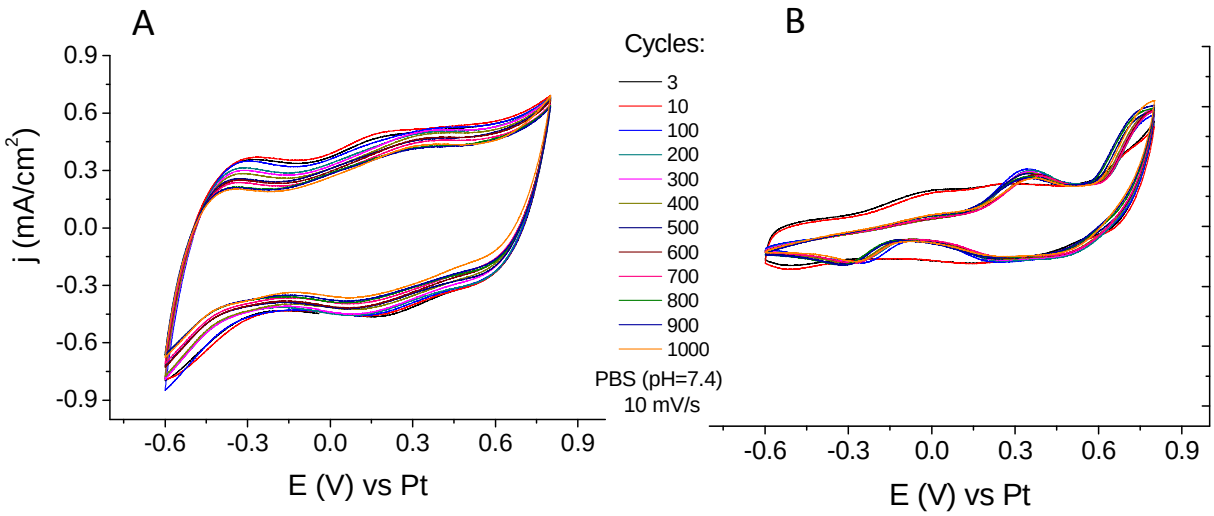

Figure 4.24. Comparison of 1000 cyclic voltammetries (cathodal first) for coatings in PBS (pH=7.4) electrolyte, at scan rate of 10 mV/s. A) 25-cycle IrOx-CNTs and B) 50-cycle IrOx.

The study of the curves obtained in the stability test (Figure 4.24) shows how for the IrOx-CNTs hybrid the area under the curve is decreasing, but the shape is unaltered. However, for bare IrOx, between the cycle 10 and 100 the electrode surface is altered, resulting in an abrupt change of the curve form and in consequence, in an important decrease of the charge storage capacity. This feature is presumably due to be formation of cracks, which allows the contact of the platinum underneath the IrOx film with the solution, and due to the minor resistance, the electrochemical interactions take place onto it, as the peak at -0.3 V indicates (which is related with the reduction of PtO). Although, some IrOx is still in contact, as the CSC_c for bare Pt is considerably lower than the obtained (~5.5 mC/cm^2). For IrOx-CNTs the constant shape of the curve is an indicative of no polarization [45] or physical alteration of the electrode subject to electrochemical tests.

For a complete study of functional stimulation electrode applications, and once the stability and the significant values of charge storage have been demonstrated, materials should be tested by constant current pulses, to determinate the charge injection capacity (Q_{inj}) which is defined as the amount of charge per unit of area delivered in the leading phase of a stimulation pulse [42,44,46]. A high value of Q_{inj} is desirable for stimulation electrodes, because this implies that for a given pulse of current, the voltage generated is lower, and hence, safer for neural tissue [47]. Also, the voltage transient produced during this fast current pulse can be evaluated, and a low level is expected, to avoid surpass the safe potential limits. However, as commented in Chapter 3, these experiments are out of our scope in this thesis, and would be tested in further work. Nevertheless, the good results obtained in the performed electrochemical measurements for the hybrid coatings, show promising expectations for neural electrode uses, not only in stimulation but in neural modulation and growth.

The good results of CSC_c obtained in biological conditions, yield us to test the coatings also as possible cathode in a supercapacitor system. KOH electrolyte was used to evaluate the charge capacity of the material, and the results were compared with usual values for this type of materials reported in literature. Figure 4.25A- shows the CVs for IrOx and IrOx-CNTs coatings, plotted as current versus potential, at sweep rates from 2 to 100 mV/s, in 0.1M KOH solution. As expected, current increases with increasing sweep rate. Also, comparison between the two materials at the same sweep rate (50 and 100 mV/s) is presented in Figure 4.25C-D.

Curves obtained are very similar to those found in literature, taking into account that the CV response can appear very different depending on the sweep rate, the electrode geometric area or the surface roughness. In a general view, it is appreciated how current response of hybrids is considerably higher than for IrOx, mainly at high sweep rates, suggesting a higher capacitance. The enhancement of the capacitance can be attributed to the presence of the carbon nanotubes in the bulk of the iridium oxide (which improves the electric conductivity thanks to the directional conductor behavior of CNTs), or as consequence to a larger surface, as shown in the previous section. IrOx itself presents a pseudo capacitive behavior, due in part to the multiple oxidation state of the iridium ion, which allows internal redox reactions and the intercalation process that these reactions involve (as explained in the Introduction Chapter).

The observed capacitance increase for the hybrid, agrees with a simultaneous work presented by Chen and coworkers for composites of IrO_2 and MWCNTs synthesized by sputtering or CVD [48,49]. However, IrOx-CNTs hybrid coatings presented in this thesis have an open structure, a larger content of water and the structure obtained is highly porous. Also, the carbon nanotubes, even forming aggregates, are dispersed homogeneously through the entire solid, contributing to reduce the bulk density. These properties, which are not achieved by the physical methods of synthesis used by Chen et al., induce an improvement in the specific capacitance value under the same electrochemical conditions.

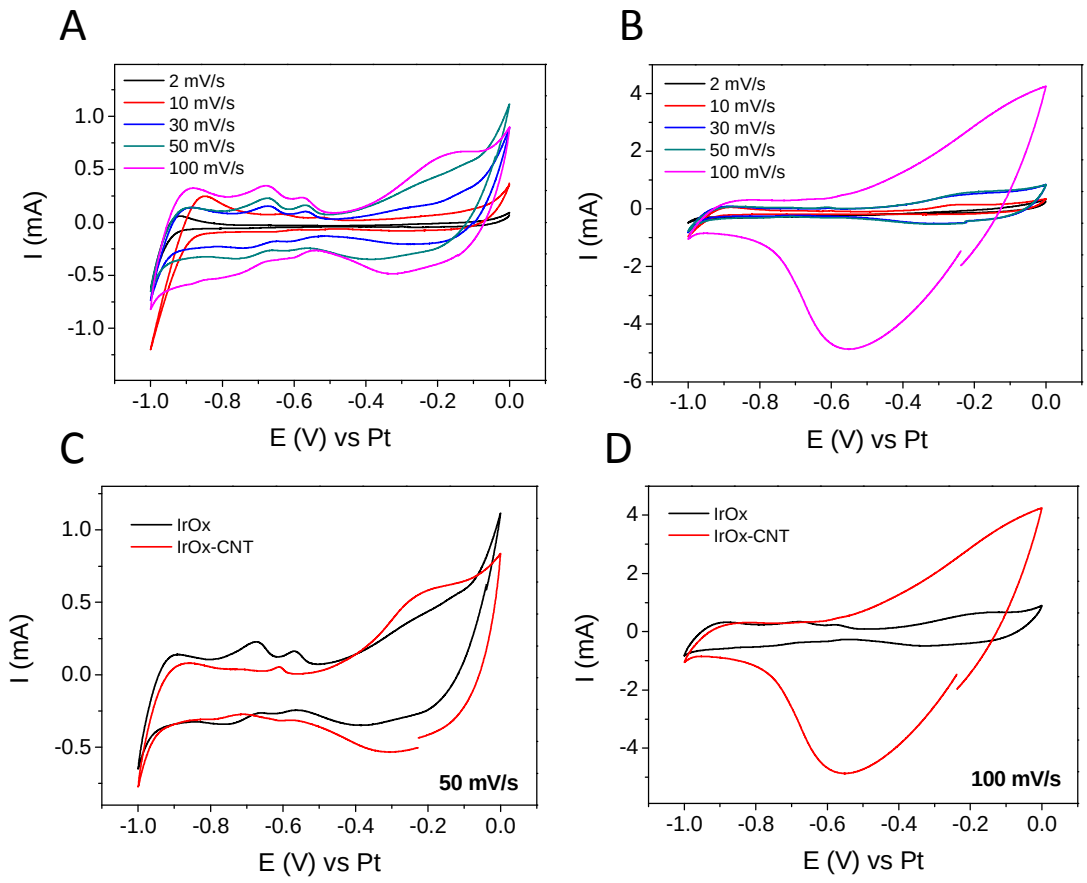

Figure 4.24. Cyclic voltammetries of IrOx and IrOx-CNTs samples in KOH 0.1M electrolyte. A) IrOx at 2-100 mV/s sweep rate, B) IrOx-CNTs at 2-100 mV/s sweep rate, C) Comparison between IrOx and IrOx-CNTs at 50 mV/s and D) Comparison between IrOx and IrOx-CNTs at 100 mV/s.

The specific capacitance can be estimated using the CV curves, according to the formula:

$$C_g = \frac{\int I\, dV}{m\Delta V S}$$

Where C_g is the specific capacitance, $\int I\, dV$ the integrated area enclosed in the CV curve (in this case, the cathodic part), m the mass of the active material, ΔV the scanned potential range and S the scan rate.

Using the mass value obtained in EQCM experiment for IrOx-CNTs coatings (8.6 µg for 25-cycle samples), specific capacitance obtained is around 329.2, 155.3, 101.7 and 230.6 F/g for 10, 30, 50 and 100 mV/s respectively. These values are larger than those obtained for bare IrOx: 102.2, 35.5, 29.4 and 21.0 F/g for scan rates of 10, 30, 50 and 100 mV/s respectively, and also compared with the value of pristine multi-walled carbon nanotubes given for some authors, around 10-15 F/g [50] (although functionalized CNTs can reach higher values, around 50 F/g [51]).

C_g obtained for the scan rate of 50 mV/s (101.7 F/g) is considerably higher that the previously 69 F/g reported for similar IrOx-CNTs coatings by Chen et al. [48]. This electrochemical enhancement can be attributed to the more porous structure obtained in this work, in contrast with the crystalline structure presented by Chen et al. synthesized by CVD.

With this initial experiment it has been demonstrated the potential use of this type of IrOx-CNTs hybrid materials for supercapacitor uses, although the specific capacity values would be contrasted with galvanostatic charge/discharge experiments and a more detailed study is necessary.

4.4 Conclusions

- Hybrid coatings of IrOx-CNTs have been prepared and fully characterized. The synthesis conditions have been optimized to obtain good adherence, thickness and stability (decreasing the superficial cracks). The large surface area and excellent conductivity of CNTs, confers a network-like structure to the oxide, obtaining a hybrid with rougher surface and hence, increasing the conductivity and the CSC_c of the material as electrode.

- A complete structural characterization has been done. SEM images reveal the rough surface morphology and the presence of CNTs, clearly visible in the cracks and guessed in the bulk, as bundles coated by IrOx. Also, thickness has

been determined, obtaining for the same number of cycles, thicker coatings than for bare IrOx. In addition, hybrid surface is much rougher in comparison with IrOx, as corroborated by 3D-confocal measure of the roughness.

- XRD experiments have determined that as prepared IrOx-CNTs hybrids are not crystalline, although crystallization is possible by 4-hour thermal treatment at 500ºC in air, observing crystallites with hollandite-type structure (K_xIrO_2). However, crystalline structure is not optimal for uses as stimulation electrode, because involves the loss of electroactive area and difficulties ionic intercalation/ deintercalation from the solution during redox cycles.

- Raman results also have demonstrated the non-crystalline structure of the IrOx in hybrid IrOx-CNTs coatings, and the presence of CNTs. With a scanning 3D Confocal Raman microscope was possible to obtain a map of CNTs dispersion showing that, even forming agglomerates, CNTs are dispersed all over the sample and in high concentration.

- XPS results have shown, in addition to the expected elements, a big quantity of adventitious carbon in the surface of the samples, and as consequence, the impossibility of quantifying CNTs, presumably due to the coating of CNTs by IrOx and the low penetration of the XPS technique. Also, similar chemical composition has been observed for IrOx and IrOx-CNTs coatings, a highly hydrated iridium oxohydroxyde. The presence of high and reproducible quantities of potassium has been observed, retained in the coating during the electrochemical synthesis. This potassium can form a superoxide when the sample is heated in air, and at higher temperatures can sublime.

- Finally, the viability of the new hybrid materials as neural electrodes has been tested. Good performance during CVs and very high values for CSC_C, in comparison with bare IrOx, have been achieved, supporting the suitability as materials for stimulation electrodes. In addition, good stability has been

obtained for chronic stimulation and the formation of cracks or delamination is minimized during electrochemical measurements. This outstanding stability is presumably due to the CNTs incorporation, which creates a nanostructured and porous IrOx matrix, with CNTs reinforcing the coating against deformation or cracking during ionic intercalation in faradaic processes.

4.5 References

-[1] Meyer R.D., Cogan S.F., Rauh R.D., et al. Electrodeposited iridium oxide for neural stimulation and recording electrodes. *IEEE Trans. Neural. Syst. Rehabil. Eng*. **9**, No.1, 2-11. 2001.

-[2] Göbbels K., Kuenzel T., Bräunig P., et al. Neuronal cell growth on iridium oxide. *Biomaterials*. **31**, 1055–1067. 2010.

-[3] Weiland J.D. and Anderson D.J. Chronic neural stimulation with thin-film, iridium oxide electrodes. *IEEE Trans. Biomed. Eng.* **47**, No.7, 911-918. 2000.

-[4] Mailley S.C., Hyland M., McAdams E.T., et al. Electrochemical and structural characterizations of electrodeposited iridium oxide thin-film electrodes applied to neurostimulating electrical signal. *Mat. Sci. Eng*. **21**, 167–175. 2002.

-[5] Cogan S.F., Ehrlich J., Rizzo J.F., et al. Sputtered iridium oxide for neural stimulation electrodes. *J. Biomed. Mater. Res. B Appl. Biomater*. **89**, No.2, 353-61. 2009.

-[6] Weiland J.D., Anderson D.J. and Humayun M.S. In vitro electrical properties for iridium oxide versus titanium nitride stimulating electrodes. *IEEE Trans. Biomed. Eng*. **49**, No.12, 1574-1579. 2002

-[7] Cruz A. M., Abad LL., Casañ-Pastor N. et al. Iridium oxohydroxide, a significant member in the family of iridium oxides. Stoichiometry, characterization, and implications in bioelectrodes. *J. Phys. Chem. C*. **116**, 5155−5168. 2012.

-[8] Kickelbick G. Hybrid Materials: Synthesis, characterization, and applications. Wiley-VCH. (1st Edition). 2006.

-[9] Sanchez C., Julián B., Popall M., et al. Applications of hybrid organic-inorganic nanocomposites. *J. Mater. Chem*. **15**, 3559-3592. 2005.

-[10] Wang K., Fishman H.A., Harris J.S., et al. Neural stimulation with a carbon nantotube microelectrode array. *Nano Lett.* **6**, No.9, 2043-2048. 2006.

-[11] Liopo A.V., Stewart M.P., Pappas T.C., et al. Biocompatibility of native and functionalized single-walled carbon nanotubes for neuronal interface. *J. Nanosci. Nanotechnol*. **6**, 1365-1374. 2006.

-[12] Smart S.K., Cassady A.I., Martin D.J., et al. The biocompatibility of carbon nanotubes. *Carbon*. **44**, 10-34-1047. 2006.

-[13] Zhang W-D., Xu B. and Jiang L-C. Functional hybrid material based on carbon nanotubes and metal oxides. *J. Mater. Chem*. **20**, 6383-6391. 2010.

-[14] Petit M. A. and Plichon V. Anodic electrodeposition of iridium oxide films. *J. Electroanal. Chem*. **444**, 247-252. 1998.

-[15] Robin M.B. and Day P. Mixed valence chemistry – A survey and classification. *Adv. Inorg. Chem. Radiochem.* **10**, 247-422. 1968.

-[16] Lupo F., Kamalakaran R., Rühle M., et al. Microstructural investigations on zirconium oxide–carbon nanotube composites synthesized by hydrothermal crystallization. *Carbon*. **42**, 1995–1999. 2004.

-[17] Slavcheva E., Vitushinsky R., Schnakenberg U., et al. Sputtered iridium oxide films as charge injection material for functional electrostimulation. *J. Electrochem. Soc.* **151**, E226-E237. 2004.

-[18] Bestaoui N., Deniard P. and Bree R. Structural study of a hollandite-type K_xIrO_2. *J. Solid State Chem*. **118**, 372-377. 1995.

-[19] Bestaoui N. and Prouzet E. A chimie douce route to pure iridium oxide. *Chem. Mater.* **9**, 1036-1041. 1997.

-[20] Yagi M., Tomita E., Nagai K., et al. Self-assembly of active IrO_2 colloid catalyst on an ITO electrode for efficient electrochemical water oxidation. *J. Phys. Chem. B*. **109**, No.46, 21489-21491. 2005.

-[21] Kuwabara T., Tomita E., Yagi M., et al. Characterization and analysis of self-assembly of a highly active colloidal catalyst for water oxidation onto transparent conducting oxide substrates. *J. Phys. Chem. C*. **112**, 3774-3779. 2008.

-[22] Harris P.J.F. Carbon nanotube science: synthesis, properties and applications. Cambridge University Press. 2009.

-[23] Ferrari A.C. Raman spectroscopy of graphene and graphite: Disorder, electron–phonon coupling, doping and nonadiabatic effects. *Solid State Communs.* **147**, 47-57. 2007.

-[24] Dresselhaus, M.S., Jorio A., Saito R., et al. Perspectives on carbon nanotubes and graphene Raman spectroscopy. *Nano Lett*. **10**, 751-758. 2010.

-[25] Jorio A., Pimenta M.A., Dresselhaus M.S., et al. Characterizing carbon nanotube samples with resonance Raman scattering. *New J. Phys*. **5**, 139.1-139.17. 2003.

-[26] Domingo C. and Santoro G. Raman spectroscopy of carbon nanotubes. *Opt. Pura Apl*. **40**, No.2, 175-186. 2007.

-[27] Mamedov A.A., Kotov N.A., Hirsh A., et al. Molecular design of strong single-wall carbon nanotube/polyelectrolyte multilayer composites. *Nat. Mater*. **1**, 190-194. 2002.

-[28] Huang Y.S., Lin S.S., Chien F.Z., et al. Raman spectrum of IrO_2. *Solid State Commun*. **70**, No.5, 517-522. 1989.

-[29] Korotcov A.V., Huang Y-S., Tsai D-S., et al. Raman scattering characterization of well- aligned RuO_2 and IrO_2 nanocrystals. *J. Raman Spectrosc*. **38**, 737-749. 2007.

-[30] Carabetta R. and Kaskan W.E. The oxidation of sodium, potassium, and cesium in flames. *J. Phys. Chem*. **72**, No.7, 2483–2489. 1968.

-[31] A.M. Cruz. Degree Thesis. Universidad Autónoma de Barcelona, Spain. 2010.

-[32] Payne B.P., Biesinger M.C. and McIntyre N.S. The study of polycrystalline nickel metal oxidation by water vapour. *J. Electron Spectrosc. Relat. Phenom*. **157**, 55-65. 2009

-[33] Payne B.P., Biesinger M.C. and McIntyre N.S. X-ray photoelectron spectroscopy studies of reactions on chromium metal and chromium oxide surfaces. *J. Electron Spectrosc. Relat. Phenom*. **184**, 29-37. 2011.

-[34] Payne B.P., Biesinger M.C. and McIntyre N.S.. *J. Electron Spectrosc. Relat. Phenom*. **184**, 29-37. 2011.

-[35] Yao S., Wang M. and Madou M. A pH electrode based on melt-oxidized iridium oxide. *J. Electrochem. Soc*. **148**, No.4, H29-H36. 2001.

-[36] Hughes A. E., Taylor R.J., Wilson L., et al. XPS and SEM characterization of hydrated cerium oxide conversion coatings. *Surf. Interface Anal*. **23**, 540-550. 1995.

-[37] Henderson M. A. and Chambers S. A. HREELS, TPD and XPS study of the interaction of water with the a-Cr_2O_3(001) surface. *Surf. Sci*. **449**, 135–150. 2000.

-[38] Perron H., Vandenborre J., Catalette H., et al. Combined investigation of water sorption on TiO_2 rutile (110) single crystal face: XPS vs. periodic DFT. *Surf. Sci*. **601**, 518–527. 2007.

-[39] Atanasoska L., Gupta P., Thomson J., et al. XPS, AES, and electrochemical study of iridium oxide coating materials for cardiovascular stent application. *ECS Trans*. **16**. No.38, 37-48. 2009.

-[40] Merrill D.R, Bikson M. and Jefferys J.G.R. Electrical stimulation of excitable tissue: design of efficacious and safe protocols. *J. Neurosci. Methods*. **141**, 171-198. 2005.

-[41] Cogan S.F., Plante T.D. and Ehrlich J. Sputtered iridium oxide films (SIROFs) for low-impedance neural stimulation and recording electrodes. *Conf. Proc. IEEE Eng. Med. Biol. Soc*. **6**, 4153-4156. 2004.

-[42] Beebe X. and Rose T. L. Charge injection limits of activated iridium oxide electrodes with 0.2 ms pulses in bicarbonate buffered saline. *IEEE Trans. Biomed. Eng*. **35**, No.6, 494-498. 1988.

-[43] Cogan S.F., Troyk P.R., Detlefsen D.E., et al. Potential-biased, asymmetric waveforms for charge-injection with activated iridium oxide (AIROF) Neural Stimulation Electrodes. *IEEE Trans. Biomed. Eng.* **53**, No.2, 327-332. 2006.

-[44] Cogan S.F. Neural stimulation and recording electrodes. *Annu. Rev. Biomed. Eng*. **10**, 275-309. 2008.

-[45] Toupin M., Brousse T. and Bélanger D. Influence of microstucture on the charge storage properties of chemically synthesized manganese dioxide. *Chem. Mater*. **14**, 3946-3952. 2002.

-[46] Kelliher E.M. and Rose T.L. Evaluation of charge injection properties of thin film redox materials for use as neural stimulation electrodes. *Mat. Res. Soc. Symp. Proc*. **110**, 23-27. 1989.

-[47] Luo X., Weaver C.L., Cui X.T, et al. Highly stable carbon nanotube doped poly(3,4-ethylenedioxythiophene) for chronic neural stimulation. *Biomaterials*. **32**, 5551-5557. 2011.

-[48] Chen Y-M., Cai J-H., Tsai D.S., et al. Preparation and characterization of iridium dioxide-carbon nanotube nanocomposite for supercapacitors. *Nanotechnol*. **22**, 115706-115712. 2011.

-[49] Chen Y-M., Cai J-H., Tiong K-K., et al. A nanostructured electrode of IrOx foil on the carbon nanotubes for supercapacitors. *Nanotechnol*. **22**, 355708-355714. 2011.

-[50] Chen Y-M. The study of iridium oxide/CNT nanocomposites. Ph.D Thesis, National Taiwan University of Science and Technology, Taiwan, 2011.

-[51] Peng C., Jin J. and Chen G.Z. A comparative study on electrochemical co-deposition and capacitance of composite films of conducting polymers and carbon nanotubes. *Electrochim. Acta*. **526**, 525-537. 2007.

Chapter 5

IrOx-PEDOT-CNTs Hybrid Coatings

This chapter introduces the synthesis and characterization of IrOx-PEDOT-CNTs (IPC) hybrids. First, the necessity to synthesize these new materials is explained, in order to emphasize the importance of new hybrids to fulfill nowadays technological breakthroughs in the biolectrodes area.

In second place, the complete protocol followed in the synthesis of the IPC hybrids is shown. Also, the synthesis of a PEDOT-Reference coating is presented, with the same procedure but without IrOx or CNTs, useful as a blank to compare compositional differences.

Chemical and structural characterization of the prepared coatings is shown in the next sections with special emphasis in the dopant determination and the physical properties that will be significant as neural electrode.

Finally, the electrochemical performance of the coatings is studied, together with the stability after successive cycling.

5.1 IrOx-PEDOT-CNTs (IPC) Hybrids

Iridium oxide has been presented in previous chapters as a good candidate for bioelectrodes, due mainly to the optimal biocompatibility, high storage capacity and high stability. However, some drawbacks can be found when used in neural tissue interfaces. One important in this aspect can be the rigidity of the oxide structure, which is not compatible with soft tissues as brain. Also, the expensive cost of iridium derivatives represents a challenge to find cheaper materials for the same purpose. In this sense, conducting polymers have attracted attention due to its versatility, its usual low cost and its flexible structure, which makes a goal for future soft tissue electrodes, in contrast with oxides. The excellent electronic and ionic conductivity, which provide low impedance and high capacitance, is a required property. Also, rougher surfaces of polymers, in comparison with oxides or metals, induce a smaller inflammatory response and hence, a superior implant integration in tissues. Finally, the feasibility of incorporation of different counterions and/or the immobilization of active molecules (peptides, proteins…) in the surface can modify largely the electrical properties, the biocompatibility or the stability, and is a wide field of study for these types of materials. In that sense, possible hybrids of biocompatible electroactive materials (as IrOx and CNTs) and conducting polymers seems a good alternative for bioelectrodes.

Conducting polymers are polymers with high electronic conductivity in its oxidized (or less frequently, reduced) state, and were discovered in the 1970's, after several precursor studies and even theoretical predictions [1]. Nowadays, the most studied ones in terms of bio-applications are polypyrrole (Ppy), polyaniline (PANi), polythiophene (PT) and derivatives of the latter as poly(3,4-ethylenedioxythiophene) as well known as PEDOT. Figure 5.1 shows the dimer structures in neutral state of the polymers commented above. The simple synthesis process, usually by chemical oxidation or electropolimerization, and the versatility to modulate the properties by the counterion/dopant used in the preparation, makes possible a large number of applications in different fields for this type of materials. Also, the apparently excellent

biocompatibility suggests conducting polymers as useful electrode materials in biological research.

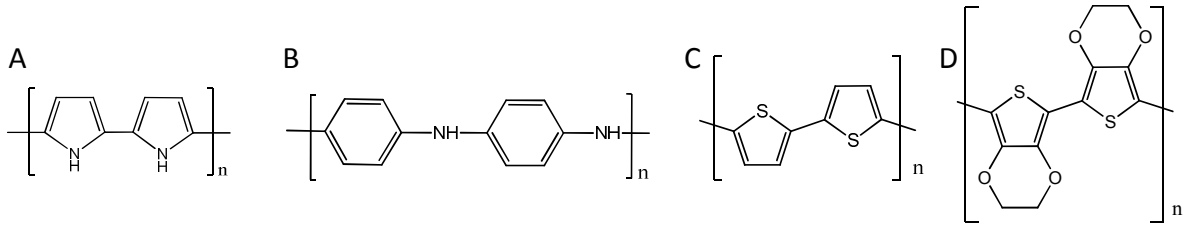

Figure 5.1. Schematic representation of the chemical structure of dimers: A) PPy, B) PANi, C) PT and D) PEDOT, in neutral state.

In our laboratory, we had based our investigations in mainly two types of polymers, PPy and PEDOT, because of the biocompatibility shown for neural tissue, especially when biomolecules instead of surfactants are used as counterions [2-5]. PEDOT is an evolved polymer from PT, where a dioxyethylene bridging group across the 3- and 4-positions of the hetero-ring, blocks the possibility of a α-β' coupling and renders superior electrochemical stability against oxidation, temperature and pH changes. In addition, the conductivity is higher and the impedance lower. For all this factors, PEDOT has been the polymer used to initially synthesize hybrids with carbon nanotubes and IrOx.

Despite the promising chemical properties of PEDOT, biocompatibility has not been thoroughly studied and some data is unclear. Some *in vitro* and *in vivo* data suggest that it is compatible with cultured cells and brain tissue, and does not release to the media toxic substances [6]. Nevertheless, as commented above, depending of the nature of the doping molecules used to synthesize the polymer, the properties of the resulting material can be altered considerably. In this sense, several investigations have tried the intercalation during the synthesis of bioactive molecules: aminoacids, ECM proteins, cell adhesion molecules or even DNA. The final objective is to increase the biocompatibility of the coatings, enhancing the cellular survival and development [7-9] and even the final aim of releasing these active molecules in the biological

environment during the electrostimulation. The release of these molecules is possible due to the redox properties of these polymers, which permit processes of intercalation of molecules from the solution and/or deintercalation of molecules from the coating, during oxidation and/or reduction processes, and also by adsorption-desorption at the surface.

PEDOT-CNTs nanocomposites have been previously reported in literature, [10-15] as well as PPy-CNTs ones [16], all of them with the aim of improving the stability, which has been one of the drawbacks observed in the practical use of these types of materials [10,17]. Moreover, in the majority of the cases, lower impedance and high charge capacities have been also obtained, confirming the success of the combination.

In the work presented in this thesis, the challenge is to obtain a reinforced polymer coating with enhanced conductive properties and stability, using negatively charged CNTs-COO^- and hydrated colloidal nanoparticles of IrOx as dopants for PEDOT, to balance the positive charge in the backbone of the polymer during oxidative electrodeposition. The incorporation of IrOx nanoparticles can improve the properties of the final coating, respecting another published CNTs-polymer hybrids, as it has been demonstrated that the negatively CNTs can only partially dope the polymer [18].

The coatings obtained by this method, show that CNTs and IrOx particles are actually inserted in the polymeric structure, showing good adhesion of the hybrid-polymer to the metallic substrate, crucial for the future stability of the electrode. Usually, thicker coatings of polymer display lower impedance and higher charge capacity however they are subject to a greater delamination. This adhesion is suggested to improve with the addition of CNTs, which can act as a type of template for the polymer formation. Also, an improvement of electric conductivity is expected due to the good conductive properties of the carbon nanotubes and the IrOx, which minimizes the conducting-insulating switch during charge-discharge cycles for these types of polymers [19].

5.2. Electrochemical Synthesis of IrOx-PEDOT-CNTs Coatings

The electropolymerization of PEDOT entails monomer (EDOT) oxidation as starting point of the polymerization. The positive charge created has to be compensated with an anion present in the solution (counterion or dopant). This anion will form part of the final polymer structure and will contribute to the final properties of the material. However, not only the dopant but other factors as the solvent, the pH, the monomer concentration or the synthesis parameters (potential or current) have influence in the final properties of the synthesized polymer.

The mechanism of oxidation involves the formation of radical cations which react with each other or with the starting monomer, developing the polymeric structure (in figure 5.2 is represented the PEDOT polymerization). Subsequent polymer oxidation creates positive charges (holes), which are mainly compensated with anions from the solution. Those charges are delocalized in the π-conjugated hetero-aromatic backbone, and are responsible for the electronic conduction of this type of polymers [20].

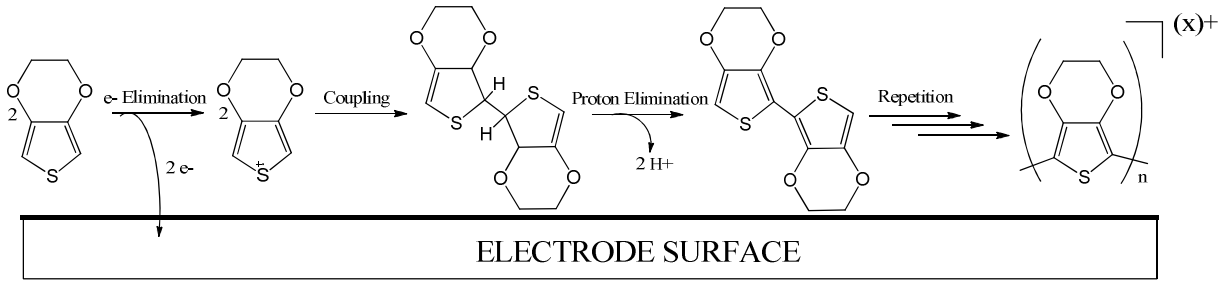

Figure 5.2. Electro-polymerization of EDOT to produce PEDOT.

During the electrochemical co-deposition, CNTs could serve as charge carriers allowing the polymer synthesis onto them but also, acting as backbone for a three-dimensional nanoporous structure, as observed in the Chapter 4. In addition, negatively charged carbon nanotubes can act as charge-balancing dopants, together with the IrOx nanoparticles.

Pre-deposition solutions are described in the Chapter 2. As in the case or IrOx-CNTs hybrids, solutions contain dispersed functionalized CNTs (CNTs-COOH) to ensure a homogeneous CNTs suspension, which have been demonstrated as a requirement for reproducible deposition [11], but also EDOT and iridium precursors.

The electro-polymerization has been performed with a conventional three-electrode system, with the Pt-covered soda lime glass acting as working electrode, a Pt foil as the counter electrode and a Pt wire as reference electrode. Two different protocols have been tested: constant potential and dynamic potential sweeps. EDOT monomer oxidation begins near 0.9 V vs Pt under these conditions. Thus, potential cycles up to 0.9 V vs Pt or constant potentials of 1 V vs Pt were used for polymerization, to prevent over-oxidation of the coatings.

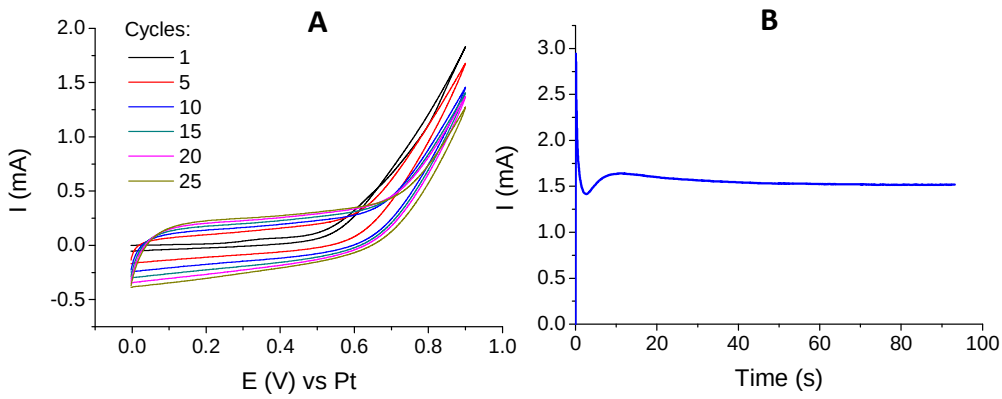

Figure 5.3. A) Potentiodynamic deposition of an IrOx-CNT-PEDOT coating (5 mV/s, 25 cycles). B) Constant potential deposition of an IrOx-CNT-PEDOT coating.

Representative synthesis curves for both processes are shown in Figure 5.3. In the potentiodynamic method, successive cycles increase the capacity of the coating, as more mass is deposited (Figure 5.3A). The final charge used during the synthesis has been around 0.45 C/cm^2 (25-cycle samples) or 0.75 C/cm^2 (50-cycle samples). The curve shape is very different that the obtained for IrOx synthesis (Figure 3.8), suggesting that mainly PEDOT is deposited in the surface of the electrode. The lack of 0.19 V (anodic) and 0.09 V (cathodic) typical IrOx peaks, indicates that IrOx is

presumably in small proportion in the coating. The presence of EDOT, an oxidable precursor at high potentials, can prevent the water oxidation and hence, IrOx deposition. Therefore, the incorporation of IrOx in the IPC coating can be suggested as nanoparticles negatively charged to compensate the positive polymer.

In constant potential methods, an initial sharp decrease in the intensity is observed, which represents the dramatic impedance difference between the Pt/electrolyte interface and the PEDOT/electrolyte interface. Once the electrode is fully covered by PEDOT, the current intensity decreases gradually due to the increased effective surface area of the thicker film. The slight intensity increase is related to the actual co-deposition before depleting precursors from solution or over-oxidation of the deposited phase, which can cause a loss in conductivity. By this synthesis method, variable final charge was obtained, in the range from 0.07 to 0.8 C/cm^2.

Other polymeric phases have been synthesized to compare chemical and electrochemical properties with the novel IPC phases. For instance, a PEDOT coating used as a blank (PEDOT-Ref), synthesized starting from EDOT in an oxalic acid/K_2CO_3 buffer (same conditions of IPC but without CNTs or IrOx) or the previously reported PEDOT-PSS [9]. During the electrodeposition, the final charge obtained during 400 seconds is significantly higher for IPC when compared with PEDOT-Ref or PEDOT-PSS. CNTs possess a huge surface area and excellent conductivity, their network-like structure distribution within the PEDOT film can effectively enlarge the electrode/electrolyte interface, increasing in that way the conductivity and the number of active sites, making the deposited polymer a very conductive substrate for subsequent layers.

Both processes yield very similar coatings macroscopically, with color depending on the amount of material deposited: thicker coatings are completely black, whereas thinner ones are blue-green colored. The final thickness can be controlled by the total charge applied during deposition, which usually is lineal [11]. The final aspect of the coatings is shown in the Figure 5.4.

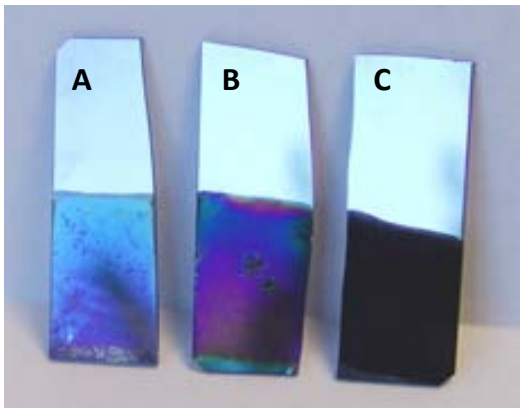

Figure 5.4. Images of the as prepared coatings of IrOx-PEDOT-CNTs. A) 15 cycles, B) 25 cycles and C) 50 cycles.

5.3 Characterization of the Samples

The characterization of the samples was carried out with a broad number of techniques in order to elucidate the chemical composition, the microstructure, the thickness and other characteristics, as well as the electrochemical properties.

5.3.1 Scanning Electron Microscopy

SEM images of the IrOx-PEDOT-CNTs coatings are shown in Figure 5.5. As in the IrOx-CNTs samples (Chapter 4), the existence of carbon nanotubes in the surface, is perceived by the network-like microstructure composed by interconnected fibrils with similar diameters (Figure 5.4.A), but is clearly visible in the cracks (Figure 5.4B-F). Generally, the aspect of the coatings is uniform, with the surface becoming slightly rougher as the film thickness increase. The fibrils responsible of the three-dimensional microstructure have an average diameter of 15-30 nm, corroborating the polymer coating of the CNTs, and the increase in roughness provoked by the nanotubes incorporation. The obtained scaffolded-structure is similar to those proposed for IrOx-CNTs coatings (Chapter 4).

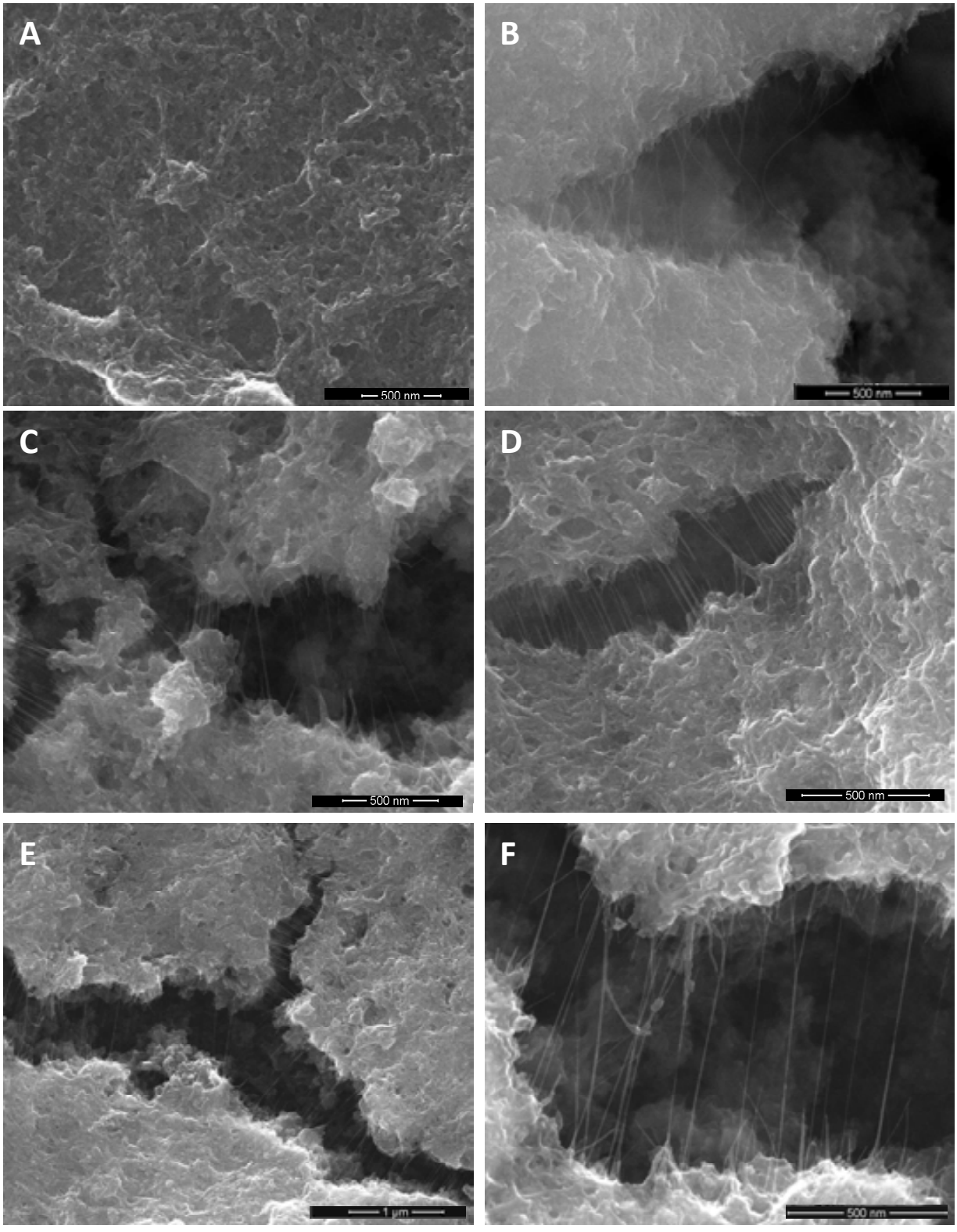

Figure 5.5. SEM images of the IrOx-PEDOT-CNTs coatings. A) Detail of the surface and B-F) cracks of different samples prepared in the same conditions (25 cycles). Images were taken at 10 kV (A) and 30 kV (B-F).

The texture is slightly different in comparison with the IrOx-CNTs sample, which presents a more granulated structure. The presence of all the elements expected has been initially corroborated by EDX experiments, which shows an atomic proportion of monomer/IrOx in the range 3-4 (based in the relation S/Ir). The presence of carbon nanotubes cannot be quantified by this technique and it will test in next sections.

The thickness of the coatings has been measured using SEM. A clean cut was done and the sample was placed in parallel with the electron beam, in order to see clearly the border. The results obtained for 50 and 25-cycle samples are shown in Figure 5.6. As expected, the sample subject to more charge during the synthesis is thicker (~2 µm vs 1 µm), but despite this, both are very similar in texture.

Thicker coatings present more disadvantages in macroscopic terms: the number of cracks increases, delamination during electrochemical performance is more relevant and the deep black color do not permit the *in-vitro* monitoring of cell cultures (which have to be stained to control the development in biological studies). For these reasons, we are focused our studies to 25-cycle samples, which are optimal for future tests as bioelectrodes.

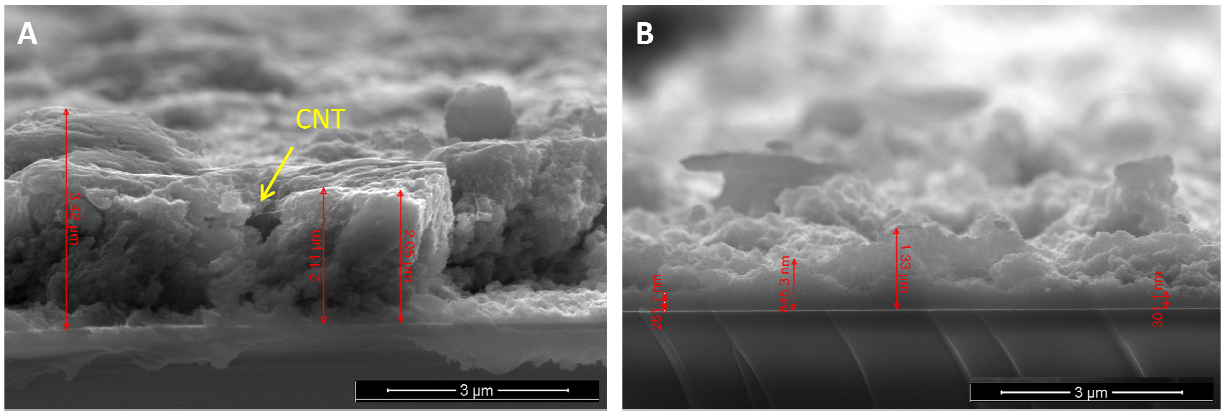

Figure 5.6. SEM images of the border of cut samples, to calculate the thickness of IrOx-PEDOT-CNTs prepared at A) 50 and B) 25 cycles respectively. Images were taken at 10 kV.

5.3.2 Roughness by 3D Confocal Microscopy

The roughness of the surface was determined by 3D confocal microscopy. The Figure 5.7 present the 2D surface, a selected profile after filtering and the 3 dimensions surface image obtained after the analysis of a 25-cycle IPC sample.

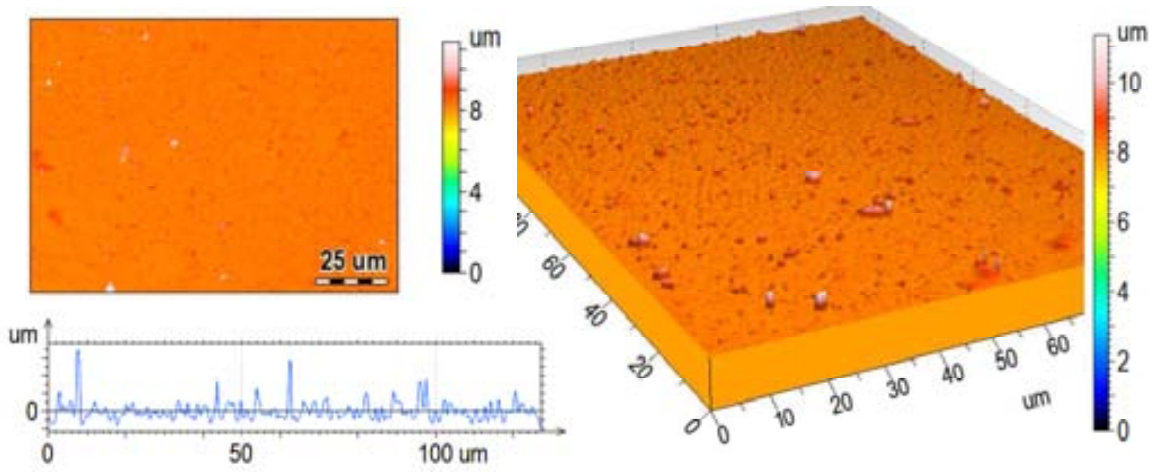

Figure 5.7. Confocal 3D microscopy images showing the 2D map after the scan, a selected characteristic profile and the 3D surface of a 25-cycle IPC coating.

The profile shows a relatively smooth surface, as shown in SEM images, as compared with IrOx-CNTs samples. Using surface texture analysis software (MountainsMap) the RMS surface roughness can be calculated. In the case of IrOx-PEDOT-CNTs coating is about **S_q= 0.16 µm**, 3 time smoother than the 25-cycle IrOx-CNTs hybrid (S_q=0.55 µm), but one order or magnitude rougher than 25-cycle PEDOT-PSS surfaces, which S_q=0.02 µm. This confirms that CNTs and IrOx incorporation in the polymer structure produces an increase of the roughness and hence, higher effective surface areas

Permeation through the polymer surface will significantly enlarges the electrode-electrolyte interface, facilitating ion exchange within the bulk film, which is expected to yield better electrochemical performance in comparison with smoother polymers.

5.3.3 Grazing Incidence X-Ray Diffraction

The IPC polymer coating does not give any signal in XRD measurements, due to the amorphous character of the polymer and the IrOx, and the low concentration of carbon nanotubes. However, to confirm the presence of IrOx in the coating, a sample heated at 500ºC during 4 hours was analyzed and the results obtained by grazing incidence XRD at different angles are shown in Figure 5.8. At this temperature the polymer is decomposed and the obtained pattern is for iridium oxide. The diffractogram obtained is not well resolved, but the IrO_2 rutile-type diffraction peaks are observed, mainly at the grazing angle 0.4°, the optimal for intermediate layers. In Chapters 3 and 4, a hollandite-type structure was obtained for IrOx under the same thermal treatment. The discrepancy can result from small differences in the heating ramps or even can depend on the used oven, as previously observed in our laboratory [21].

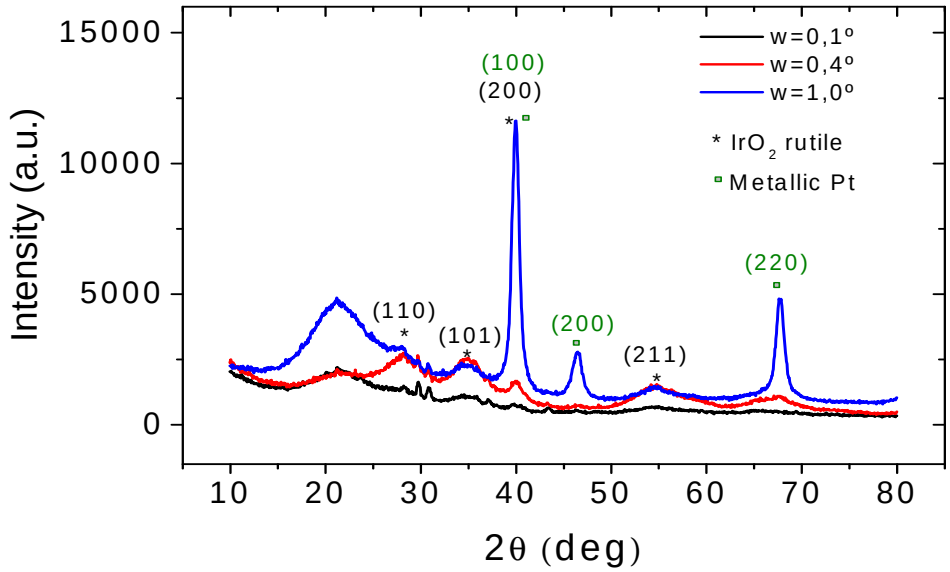

Figure 5.8. GIXRD diffractogram for IrOx-PEDOT-CNTs sample previously heated at 500ºC during 4 hours, at different grazing angles of 0.1°, 0.4° and 1.0°.

The broad peak around 20° is due to the quartz substrate, as deduced from the fact that it is more intense at the grazing angle of 1° (which implies larger penetration). At

this angle is also observed the peaks for crystalline platinum. CNTs could have a peak near 25°, but in this case is improbable assign this peak to nanotubes [22].

Near 30° two small peaks are observed. Presumably, from an impurity which has not been identified.

5.3.4 Micro-RAMAN Analysis

Micro-Raman spectra for IrOx-PEDOT-CNTs and PEDOT-Ref coatings are shown in Figure 5.9. The resulting spectra are very similar for both coatings, indicating the presence of PEDOT, which has very strong peaks. Also, the same peaks have been reported in literature for PEDOT-PSS [23,24], indicating that in general, counterions do not contribute to Raman spectra, due to the strong signals of the polymer itself.

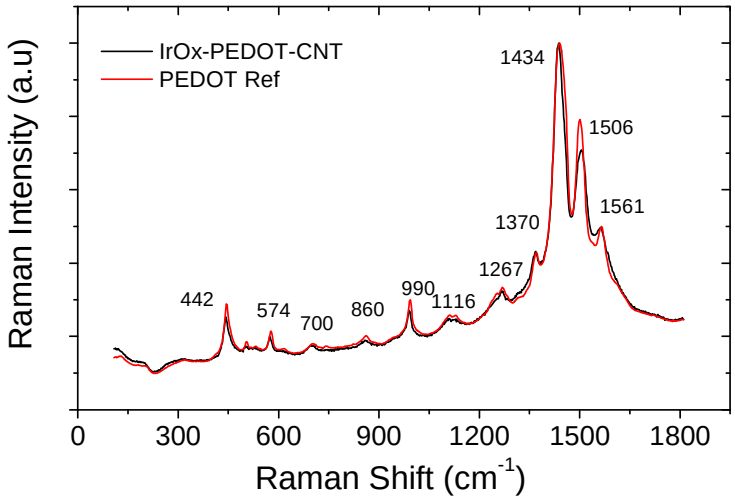

Figure 5.9. Micro-Raman spectra of IrOx-PEDOT-CNTs sample compared with a PEDOT coating used as reference, synthesized with the same conditions but not IrOx or CNTs in the structure.

These strong signals do not permit to verify the existence of IrOx or CNTs in the structure, since the high intensity of the polymer signals hides the less intense ones. For analytical purposes the IPC sample was heated up to 500ºC during 4 hours in air.

After the thermal treatment, the entire polymer is decomposed while the IrOx and the CNTs remains in the surface and can be detected by Raman. Figure 5.10 shows the results obtained using Raman-confocal microscopy to these samples.

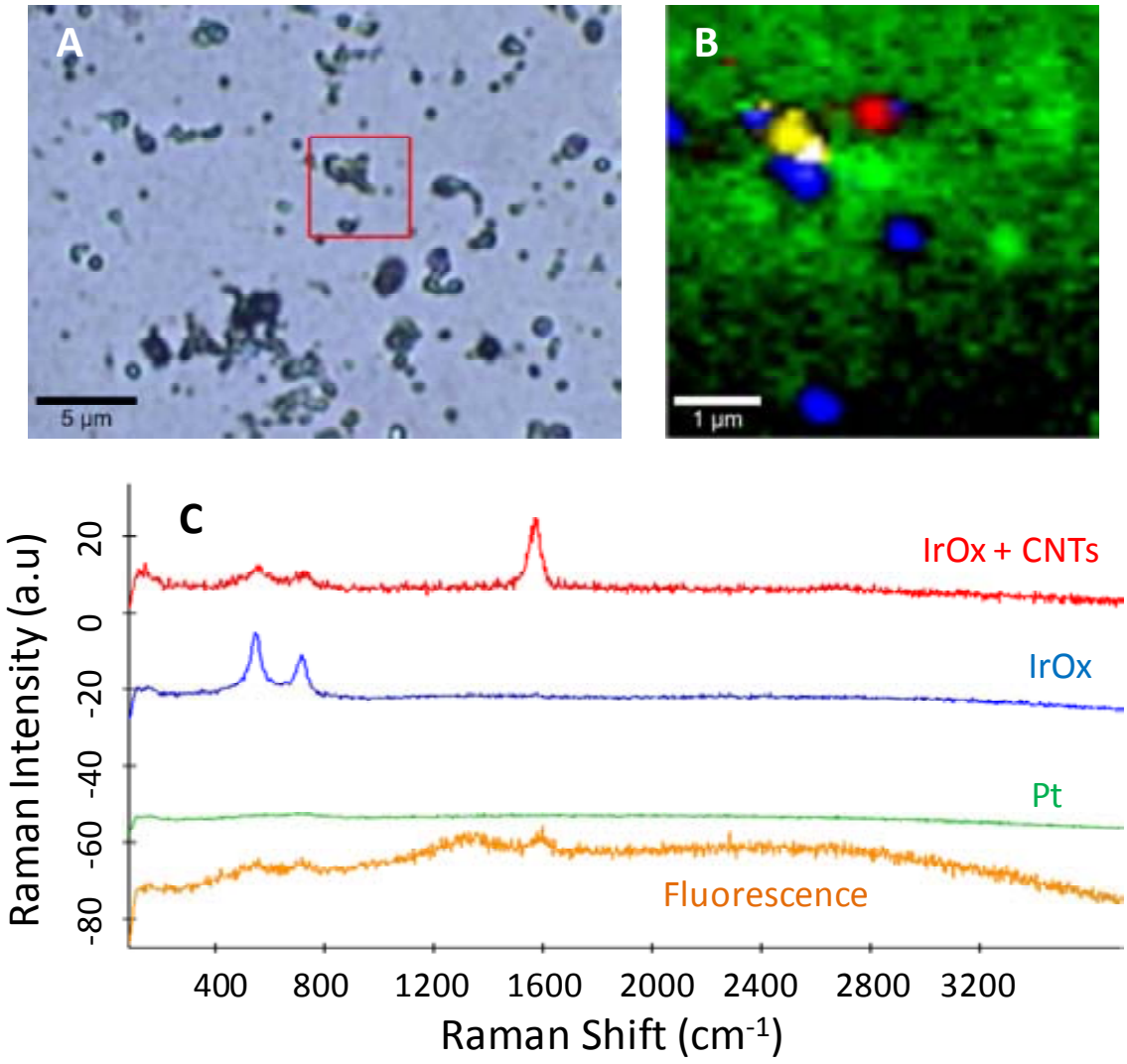

Figure 5.10. Results obtained after the measurements by Raman-Confocal Microscope to a sample of IrOx-PEDOT-CNTs heated at 500ºC during 4 hours. A) Image taken of the surface of analysis by optical microscope, B) Digital image resulting from the Raman scanning of the sample, showing the different contributions: each color represent a different component of the surface, red: mainly CNTs, blue: IrOx, green: Platinum, the substrate and in yellow is the fluorescence observed. C) Decomposition of the spectra obtained during the scanning analysis, showing the correspondence.

The optical image (Figure 5.10A) shows the surface of the sample, which has been removed almost completely, and just some particles remain. Focusing in a group of particles, a Raman scanning was made in a surface of 5 μm^2. The resulting complex Raman spectra can be then deconvoluted in simple ones, which are presented in Figure 5.10C, separating the different contributions (for the CNTs determination, the characteristic peak between 1544.2-1614.6 cm^{-1} was taken and for IrOx at 527.1-565.59 cm^{-1}).

Figure 5.10B shows the mapping image created after successive Raman scans for all the components of the coating. The vast majority of the surface is platinum (green), the substrate used to deposit the sample. However, the colored particles, coinciding with those observed in the optical image, corroborate the presence of IrOx and CNTs. These results do not indicate that IrOx and/or CNTs are confined in the colored areas, but the presence in the coating before the thermal treatment, as some aggregation can occur during heating.

5.3.5 X-Ray Photoelectron Spectroscopy

Representative XPS general spectra obtained for IPC and PEDOT-Ref are shown in Figure 5.11. The expected elements are present in both coatings: C, O, Ir, S and also counterions as K or Cl. The two spectra are quite similar, only differing in the amount of counterions and the presence of iridium in the IPC coating. A detailed quantification is shown in Table 5.1.

The IPC hybrid may be considered mostly PEDOT with some counterions inside the structure. CNTs quantification is not clear in this case, due to the intrinsic carbon of the polymer. However, the presence of iridium in the general survey indicates that IrOx nanoparticles has been satisfactory inserted in the structure. The doping degree for IrOx NPs, can be calculated from the S/Ir relation, being 2.1. However chloride and potassium are also counterions present in the structure. K^+ usually is present in

IrOx coatings and can come from the IrOx NP, suggesting that only Cl^- acts as polymer dopant.

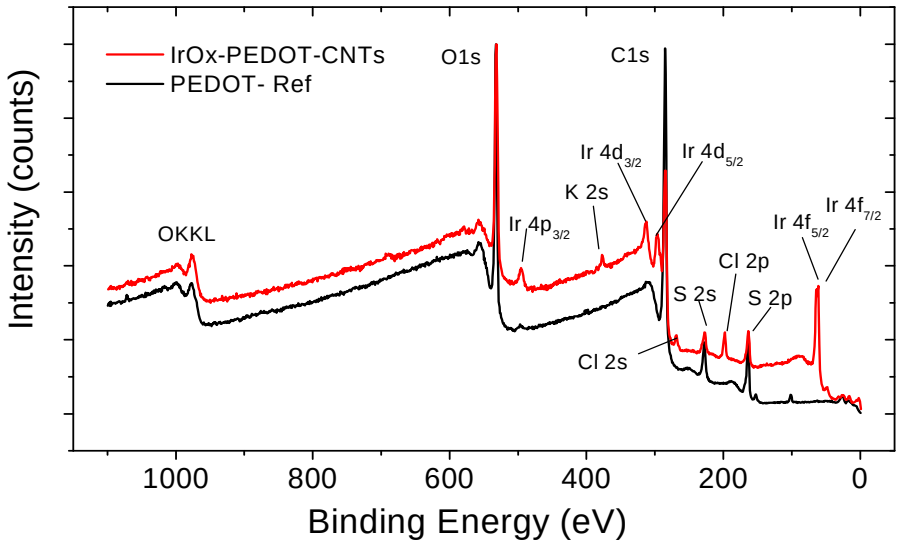

Figure 5.11. XPS survey spectra for IPC and PEDOT-Ref samples.

The PEDOT coating used as reference (PEDOT-Ref), shows only carbon, oxygen and sulfur, indicating that the counterion in this case may be oxalate or carbonate. The ratio O/S is lower than for IPC coating, as expected from the IrOx absence, while the amount of carbon is higher (as shown by C/S ratio). These results correspond with a carbonated counterion. The signal for carbonate, which appears around 290 eV [25], is not observed in C1s deconvolution therefore, the counterion for PEDOT-Ref is oxalate.

Samples	C1s (at.%)	O1s (at.%)	S2p (at.%)	K2p (at.%)	Cl2p (at.%)	Ir4f (at.%)	S/Ir	O/S	C/S
IPC	50.4	33.1	6.6	3.7	3.0	3.2	**2.1**	**5.0**	**7.6**
PEDOT-Ref	69.6	24.0	6.4	--	--	**--**	**--**	**3.8**	**10.8**

Table 5.1. Quantification (atomic %) for IPC and PEDOT-Ref coatings, obtained from the data of XPS survey spectra.

The larger amount of oxygen in the IPC sample is consequence of IrOx presence in the coating. Subtracting to the total O1s percentage, the O-contribution related with IrOx (O/Ir=3.6, Chapter 3), the new O/Ir is 3.3. This relation is now smaller than the obtained for PEDOT-Ref coating (O/Ir=3.8), as expected for a coating with only oxalate anions as dopants.

O1s and C1s signals can be deconvoluted in order to study the composition of the coatings and to differentiate the contributions from different types of chemical bonds (Figure 5.12).

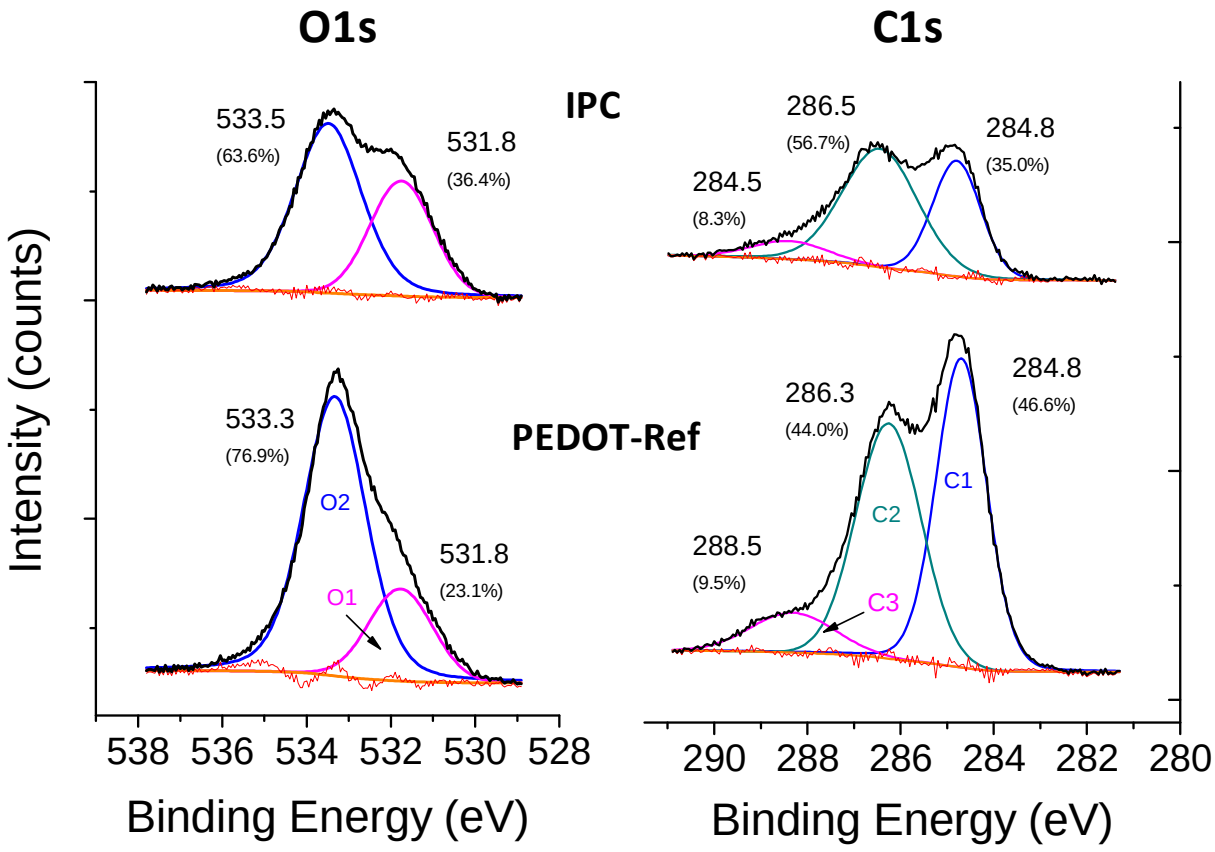

Figure 5.12 Deconvolution of O1s and C1s XPS peaks for IrOx-PEDOT-CNTs hybrid and PEDOT-Ref coatings.

O1s peak may be deconvoluted in two well defined peaks. The first peak at 531.8±0.2 eV is attributed to the oxygen species linked to carbon like carboxylate (COO^-) or C=O and also to the hydroxyl groups which conform the IrOx nanoparticles. The second peak at 533.4±0.2 eV is assigned mainly to C-O-C groups of the dioxyethylene bridge in PEDOT but also physisorbed water can contribute.

C1s peak can be deconvoluted in three peaks. The first one, at 284.8±0.2 eV is related with the aliphatic carbon (C-C, C-H), the second at 286.4±0.2 eV is attributed to the C-OH, C-O-C and C-S-C species and the last at 288.5±0.2 eV is assigned to C=O and COO^- species.

The relative percentage obtained in the deconvolution of each peak, can be combined with the total amount of oxygen and carbon from the survey, and the total atomic percentage of each species can be achieved (Table 5.2).

	Peak assignation/Position (eV)		IrOx-PEDOT-CNTs (atomic %)	PEDOT-Ref (atomic %)
O1s	*O1*:	OH^-,C=O, COO^-/531.8	12.0	5.5
	O2:	C-O-C/533.5	21.1	18.5
C1s	*C1:*	C-C, C-H/284.8	17.6	32.4
	C2:	C-OH, C-O-C, C-S-C/286.5	28.6	30.6
	C3:	C=O, COO^-/288.5	4.2	6.6

Table 5.2. Total quantification of the O1s and C1s peaks components (atomic %) in the studied coatings. Percentages add up to the total quantity of each element from the survey: carbon 50.4% and 69.6% and oxygen 33.1% and 24.0%, for IPC and PEDOT-Ref coatings, respectively.

For the IPC hybrid, atomic percent for O1 (corresponding with OH, C=O and COO^-) is 12.0, however as mentioned above, mostly is due to hydroxyl groups conforming the IrOx nanoparticles. On the other hand, O1 percentage for the blank PEDOT-Ref (O1=5.5), is due to oxalate acting as dopant and is very close to the atomic percentage of C3 (C=O, COO), as expected.

The C2 peak mainly corresponds with C-O-C and C-S-C groups. Subtracting the O2 value, the total C-S-C atomic percentages can be obtained. For IPC samples, C2-O2=7.5, a value which is close to the atomic percentage of S (6.6), indicating the validity of the peak assignation. For PEDOT-Ref samples, C2-O2 is higher than the S atomic percentage, but in this case, the presence of oxalate as dopants can interfere.

5.3.6 Electrochemical Characterization of the Coatings

Figure 5.13 shows the electrochemical response of PEDOT-PSS and IrOx-PEDOT-CNTs in PBS buffer. Also Pt performance is shown as comparison. Both polymeric electrodes present a quasi-rectangular shape of the CV curve from -0.4 V to 0.4 V, indicating a capacitor-like behavior in this potential range. This CV curve can also be used to evaluate the charge storage capacity, which is proportional to the enclosed area, as described in former chapters. The potential limits in this case, were from -0.6 V to 0.6 V (vs Pt) to prevent that polymer films become insulating at very negative potentials or over-oxidized at positive potentials [15,16].

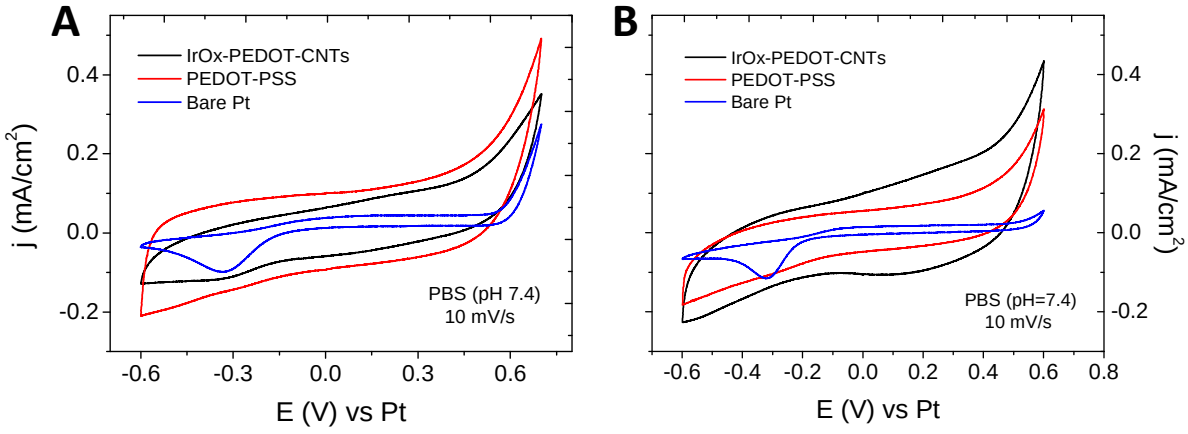

Figure 5.13. Cyclic voltammograms of IPC, PEDOT-PSS and bare Pt electrodes, performed in PBS (pH=7.4) at 10 mV/s (cycle 5). A) Polymeric coatings synthesized at constant potential with the final same charge (70 mC/cm^2) and B) polymeric coatings synthesized at 20 cycles.

A linear relationship has been observed between the charge delivered to the electrode during deposition and the final charge storage capacitance until a certain limit (as thicker films are rougher and present more electro-active species) [10,26]. Therefore, for a precise comparison of CSC_C values, the electrodeposition charge has been maintained constant the preparations at constant potential (70 mC/cm^2). However, also IPC and PEDOT-PSS coatings synthesized by potentiodynamic deposition (20 cycles) have been studied. The reason was the observation that electrochemical deposition of IPC hybrid coating was kinetically favored. Therefore, constant potential deposition can result in thicker and rougher PEDOT-PSS coatings whereas potentiodynamic methods (where the deposition time is the same) yields thicker IPC coatings. The synthesis of polymer coatings with the same thickness has not been achieved yet.

For samples synthesized at constant potential, the calculated CSC_C values are 6.9 and 9.9 mC/cm^2 for IPC and PEDOT-PSS, respectively (Figure 5.13A). The corresponding value for bare Pt is 2.5 mC/cm^2. The value obtained of Pt is significantly lower than those for polymeric phases, suggesting higher performance of polymers for this type of application. IPC and PEDOT-PSS coatings have similar curves, and the presence of IrOx and CNTs in the IPC films do not produce any visible alteration, which may be an indicative of low concentration or totally covering of these species by PEDOT. On the other hand, the larger CSC_C value obtained for PEDOT-PSS coatings can be related with the longer time of synthesis, which can yield thicker coatings.

Figure 5.13B shows the CV curves for IPC and PEDOT-PSS synthesized by potentiodynamic methods. In this case, CSC_C values are 18.1 and 7 mC/cm^2 for IPC and PEDOT-PSS, synthesized during 20 cycles. The charge capacity in this case is higher for the hybrid, indicating enhanced electrochemical performance. However, the difference can be as consequence of the final thickness/roughness of the final coating as previously mentioned.

Electrochemical performance also has been evaluated for hybrid PEDOT-IrOx and PEDOT-CNTs coatings, and the results are shown in Figure 3.14.

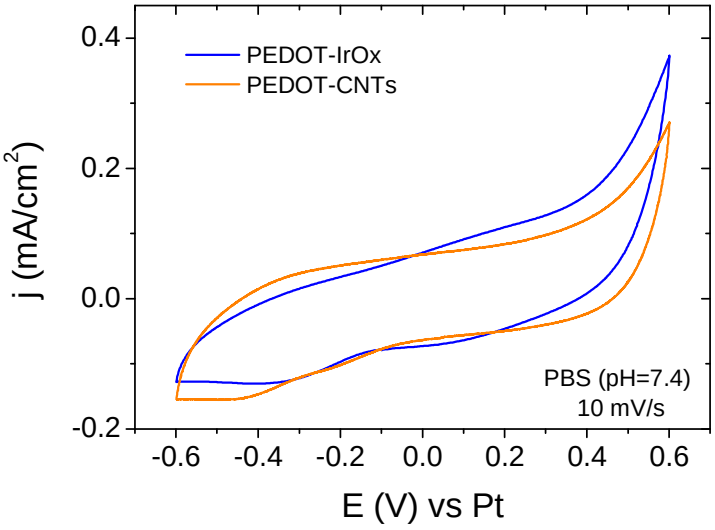

Figure 5.14. Cyclic voltammograms of PEDOT-IrOx and PEDOT-CNTs samples, performed in PBS (pH=7.4) at 10 mV/s. Coatings synthesized at constant potential with a final charge of 90 mC/cm^2.

CSC values obtained for PEDOT-IrOx and PEDOT-CNTs are 8.5 mC/cm^2 and 13.2 mC/cm^2, respectively, similar to those obtained for IPC or PEDOT-PSS synthesized at constant potential. These results indicates that the presumably, the polymer coats this species, minimizing their electrochemical performance. However, the higher value obtained for PEDOT-CNTs hybrid may indicate that coatings with carbon nanotubes are more conductive than those with only IrOx particles as dopants.

The stability of polymer coatings during 1000 successive cycles in PBS has been studied and the results are shown in Figure 5.15. IPC coatings synthesized at 5 and 15 cycles show a similar initial CSC_C value, which decreases at the number of cycles increase. The pronounced drop of CSC_C values indicates a deterioration of the electrochemical reversibility in the electrode, which can be correlated with the formation of cracks or delamination of the conducting polymer films, as also observed for IrOx coatings (Chapter 3). This fact is usually due to mass transport during intercalation/deintercalation with potential pulses or sweeps, and is more

detrimental when smaller counterions are used in the polymeric phase, as bigger dopants cannot be released easily [11,16,18].

For the thinner IPC coating this drop is not as drastic as observed in 15-cycle IPC coating, suggesting a slower deterioration. PEDOT-PSS also shows this behavior, indicating the poor stability of these polymeric phases under electrochemical measurements.

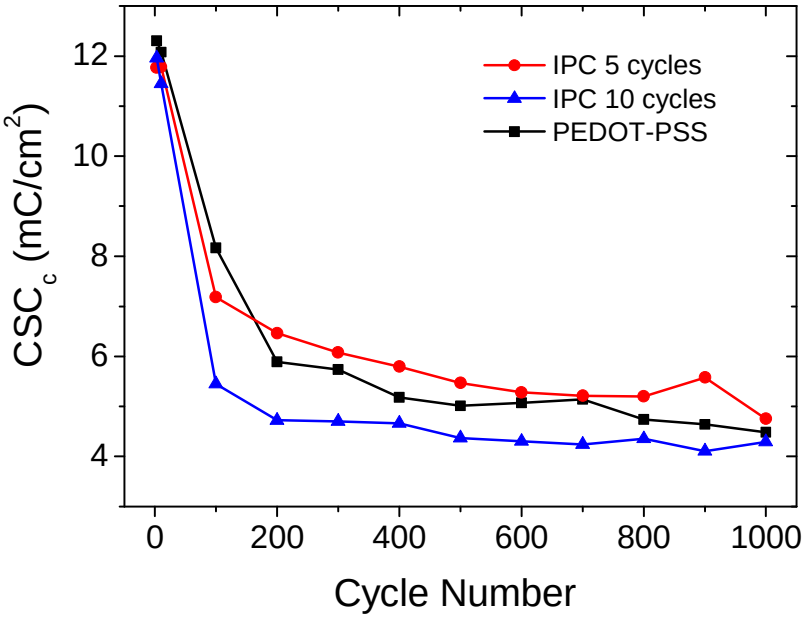

Figure 5.15. A) 1000 cycling performance of IrOx-PEDOT-CNTs hybrid coating synthesized at different cycles and 10-cycle PEDOT-PSS film to compare, in PBS (pH=7.4) at 10 mV/s.

The evolution of the CV curves during the stability test is shown in Figure 5.16 for 10-cycle coatings of IPC and PEDOT-PSS. For both coatings, the curve drastically changes in the first 100 cycles, coinciding with the drastic decrease in CSC_C value observed in Figure 5.15. These changes in CSC_C and curve shape are due to the delamination of the polymer films and the contact of the underneath Pt with the solution, as the shape of the new curve indicates (very similar to those obtained for bare platinum).

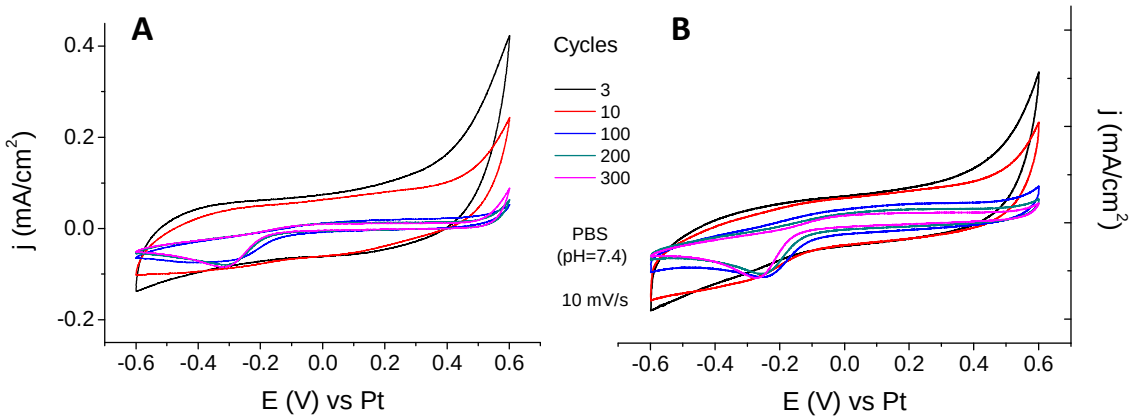

Figure 5.16. Cyclic voltammetry curves of the 300 first cycles of a stability test consisting in 1000 CVs (cathodal first) at 10 mV/s in PBS (pH=7.4). For 10-cycles coating of A) IPC and B) PEDOT-PSS.

The aim of this IrOx-PEDOT-CNTs hybrid synthesis was that mechanically strong CNTs distributed across the film reinforced the structure, preventing the polymer film for undergoing deformation and cracking or even expansion and shrinkage effects produced in redox reactions [10]. Also, CNTs and IrOx nanoparticles, acting as immobile anionic dopants, allowing cation expulsion instead of anion incorporation during the oxidation of the polymer backbone, enhancing the conduction and the stability. However, the results show no relevant increase in stability or electrochemical performance after the CNTs and IrOx addition, which presumably are completely coated, as no electrochemical signals are detected [26]. The differences found in CSC_C values are suggested to be related with the differences in thickness and/or roughness, as Figure 3.13 indicates.

However, although these results are not optimal for long-term stimulation, other electrochemical protocols, as dc current pulses at slow scan rates can be used to induce cellular response, as recently tried in our laboratory.

5.4 Conclusions

- IrOx-PEDOT-CNTs (IPC) hybrid coatings have been synthesized starting from iridium precursors, dispersed CNTs and EDOT. Two synthesis methods have been used, constant potential or potentiodynamic deposition, both yielding similar coatings. The appearance of the films depends on the charge used during depositions but it is from gree-blue to black, as the thickness increases.

- SEM images of the IPC samples show a rough surface, with CNTs forming a network-like microstructure composed of interconnected fibrils with higher diameter values than those for pristine CNTs, suggesting the polymer coating of the carbon nanotubes. However, CNTs are clearly observed in the cracks, providing a scaffold for the polymer formation. SEM images of the borders, allow measure the thickness of the coatings, which results in around 2 μm for 50-cycle films, and 1 μm for 25-cycle ones.

- The roughness of the coatings was S_q=0.16 μm, calculated by 3D confocal microscopy. This value is lower than the previously obtained for IrOx-CNTs hybrid coatings (0.55 μm), but one order of magnitude higher than those obtained for PEDOT-PSS (0.02 μm).

- XRD measurements do not show any characteristic peak for the amorphous polymer, however under a thermal treatment of the coating (4h at 500ºC in air), the obtained diffractrogram shows the corresponding peaks of IrO_2 rutile-structure, confirming the iridium oxide in the film.

- Raman spectrum of the as prepared IPC hybrid coating shows the typical peaks for PEDOT and due to the high intensity of the peaks, is not possible to differentiate the dopants present in the coatings. To determinate the presence

of IrOx and CNTs, a thermally treated sample (4h at 500ºC in air) was measured. Raman scanning image shows, after the PEDOT removal, the expected components dispersed in the surface.

- XPS also demonstrate the presence of iridium in the IPC coatings, with a doping rate S/Ir of 2.1. The sample used as a blank for chemical characterizations (PEDOT-Ref) has been doped by oxalate ions, as XPS results suggest. Once the respective contributions of IrOx and oxalate are removed of the total percentages, the composition of two coatings is very similar. The presence of CNTs by this technique is not possible due to the high carbon content of the polymer itself.

- Electrochemical performance of IPC coatings have been measured by cyclic voltammetries in PBS (pH=7.4) at different conditions. The results show larger CSC_C values for polymers (IPC and PEDOT-PSS) than for platinum, used as reference. However, no relevant changes in electrochemical behavior has been observed in IPC coatings respect to PEDOT-PSS, and charge capacity storage variations can be attributed to differences in the thickness and/or the roughness of the polymeric coatings. The stability during successive cycling under the used conditions is poor, and before the cycle 100 the coatings is delaminated. Therefore, to further applications as stimulation neural electrodes the stability and integrity of the coatings have to be improved. However, other possible used as neural electrodes which implies lower scan rates and dc currents, can be used to modulate neuron development and functionality, as shown in our laboratory.

5.5 References

-[1] Inzelt G. Conducting Polymers: a new era in electrochemistry. Ed Springer (2nd Edition). 2012.

-[2] George P.M., Lyckman A.W., Sur M., et al. Fabrication and biocompatibility of polypyrrole implants suitable for neural prosthetics. *Biomaterials*. **26**, 3511-3519. 2005.

-[3] Wang X., Gu X., Chen G., et al. Evaluation of biocompatibility of polypyrrole *in vitro* and *in vivo*. *J. Biomed. Mat. Res. A*. **68A**, No.3, 411-422. 2004.

-[4] Richardson-Burns S.M., Hendricks J.L., Martin D.C., et al. Polymerization of the conducting polymer poly(3,4-ethylenedioxythiophene) (PEDOT) around living cells. *Biomaterials*. **28**, 1539-1552. 2007.

-[5] Cui X. and Martin D.C. Electrochemical deposition and characterization of poly(3,4-ethylenedioxythiophene) on neural microelectrode arrays. *Sens. Actuators, B*. **89**, 92-102. 2003.

-[6] Baibarac M., Lira-Cantú M., Gomez-Romero P., et al. Electrochemically functionalized carbon nanotubes and their application to rechargeable lithium batteries. *Small*. **2**, No.8-9, 1075-1082. 2006.

-[7] Moral-Vico J., Carretero N.M., Casañ-Pastor N., et al. Dynamic electrodeposition of aminoacid-polypyrrole on aminoacid-PEDOT substrates: Conducting polymer bilayers as electrodes in neural systems. *Electrochim. Acta*. **111**, 250-260. 2013.

-[8] Asplund M., von Holst H. and Inganas O. Composite biomolecules/PEDOT materials for neural electrodes. *Biointerphases*. **3**, No.3, 83-93. 2008.

-[9] Moral-Vico J. Materiales electroactivos poliméricos e híbridos como sustrato de crecimiento neuronal. Ph.D Thesis, Universidad Autónoma de Barcelona, Spain. 2012.

-[10] Luo X., Weaver C.L., Cui T., et al. Highly stable carbon nanotube doped poly(3,4-ethylenedioxythiophene) for chronic neural stimulation. *Biomaterials*. **32**, 5551-5557. 2011.

-[11] Gerwing R., Fuchsberger K., Stelzle M., et al. PEDOT–CNT composite microelectrodes for recording and electrostimulation applications: fabrication, morphology, and electrical properties. *Front. Neuroeng*. **5**, No.8, 1-11. 2012.

-[12] Bhandari S., Deepa M., Kant R., et al. Poly(3,4-ethylenedioxythiophene)-multiwalled carbon nanotube composite films: structure-directed amplified electrochromic response and improved redox activity. *J. Phys. Chem. B*. **113**, 9416-9428. 2009.

-[13] Kim K.S. and Park S.J. Influence of dispersion of multi-walled carbon nanotubes on the electrochemical performance of PEDOT–PSS films. *Mat. Sci. Eng. B*. **176**, 204-209. 2011.

-[14] Zou J., Tran B., Zhai L., et al. Transparent carbon nanotube/poly(3,4-esthylenedioxythiophene) composite electrical conductors. *Soft Mat*. **7**, No.4, 355-365. 2009.

-[15] Peng C., Jin J. and Chen G.Z. A comparative study on electrochemical co-deposition and capacitance of composite films of conducting polymers and carbon nanotubes. *Electrochim. Acta*. **53**, 525-537. 2007.

-[16] Lu Y., Li T., Duan Y.Y., et al. Electrodeposited polypyrrole/carbon nanotubes composite films electrodes for neural interfaces. *Biomaterials*. **31**, 5169-5181. 2010.

-[17] Jan E., Hendricks J.L., Kotov A., et al. Layered carbon nanotube-polyelectrolyte

electrodes outperform traditional neural interface materials. *Nano Lett*. **9**, No.12, 4012-4018. 2009.

-[18] Snook G.A., Chen G.Z., Shaffer M., et al. Studies of deposition of and charge storage in polypyrrole–chloride and polypyrrole–carbon nanotube composites with an electrochemical quartz crystal microbalance. *J. Electroanal. Chem*. **568**, 135-142. 2004.

-[19] Wallace G.G, Spins G.M., Teasdale P.R. and Kane-Maguire L.A.P. Conductive Electroactive polymers. Intelligent materials systems. Ed. CRC Press (2nd Edition). 2003.

-[20] Cruz A.M. Obtención y caracterización de materiales electroactivos para soporte de crecimiento neuronal. Ph.D Thesis, Universidad Autónoma de Barcelona, Spain. 2010.

-[21] Wang J., Wang C.Y., Wallace G.G., et al. Highly-flexible fibre battery incorporating polypyrrole cathode and carbon nanotubes anode. *J. Power Sources*. **161**, 1458-1462. 2006.

-[22] Ouyang J., Xu Q., Shinar J., et al. On the mechanism of conductivity enhancement in poly(3,4-ethylenedioxythiophene):poly(styrene sulfonate) film through solvent treatment. *Polymer*. **45**, 8443-8450. 2004.

-[23] Sakamoto S., Okurura M., Furukawa Y., et al. Raman spectral changes of PEDOT–PSS in polymer light-emitting diodes upon operation. *Chem. Phys. Lett*. **412**, 395-398. 2005.

-[24] Hughes A.E., Taylor R.J., Wilson L., et al. XPS and SEM characterization of hydrated cerium oxide conversion coatings. *Surf. Interf. Anal*. **23**, 540-550. 1995.

-[25] Cui X.T and Zhou D.D. Poly(3,4 ethylenedioxythiophene) for chronic neural stimulation*. IEEE Trans. Neural Syst. Rehab. Eng.* **15**, No.4, 502-508.2007.

-[26] Moral-Vico J., Sánchez-Redondo S., Casañ-Pastor N., et al. Nanocomposites of iridium oxide and conducting polymers as electroactive phase in biological media. *Acta Biomater*. **10**, 2177-2186. 2014.

Chapter 6

Other Carbon-based IrOx Hybrids

This chapter briefly introduces the preparation and basic characterization of new hybrid coatings prepared with IrOx and carbon-based species as graphite and graphene, following the same protocol used in the IrOx-CNTs coatings synthesis.

First, preparation of the oxidized precursors (graphite and graphene oxides) and the synthesis mechanism for the hybrid coatings are summarized.

Also, an initial characterization of the IrOx-graphite and IrOx-graphene hybrid coatings is shown: SEM images to observe the surface microstructure and the thickness, EDX and XPS for surface chemical composition, confocal microscopy to determine the roughness and cyclic voltammetries under different conditions to calculate the charge storage capacity and the stability under successive cycling steps. However, further characterization must be done in order to complete the compositional information.

Finally, the synthesis of an IrOx hybrid with N-doped graphene has been tested, with promising results: chemical evidence of the incorporation of the N-graphene into the oxide structure and considerably enhanced electrochemical properties. These initial results must be completed further in the group.

6.1 Graphite and Graphene- IrOx Hybrids

The good results obtained for IrOx-CNTs hybrids in terms of stability and electrochemical performance, have triggered the attempt of synthesize other carbon-based IrOx hybrids with the aim of obtain enhanced properties in layered materials. Oxidized kish graphite coarse powder and graphene oxide (GO) have been tested, given the promising perspectives that these materials present, in terms of conductivity and stability, derived from the nanocharacter.

Graphene is a 2D material, constituted by a flat monolayer of carbon atoms tightly packed in a honeycomb lattice, and is the building block for all graphitic materials, reason why it is commonly called “mother of all graphitic forms” [1]. It can be wrapped up to OD fullerenes, rolled into 1D nanotubes or stacked into 3D graphite (Figure 6.1). Ideally graphene is a single-layer material, but bi-layer graphene and few-layer graphene are also common species. Graphene, being just one atom thick, has outstanding mechanical, electronic, thermal and chemical properties. It is very robust but stretchable, very good electronic and thermal conductor and it can be easily functionalized. Also is very sensible to adsorbed species, so promising as sensor [2-4].

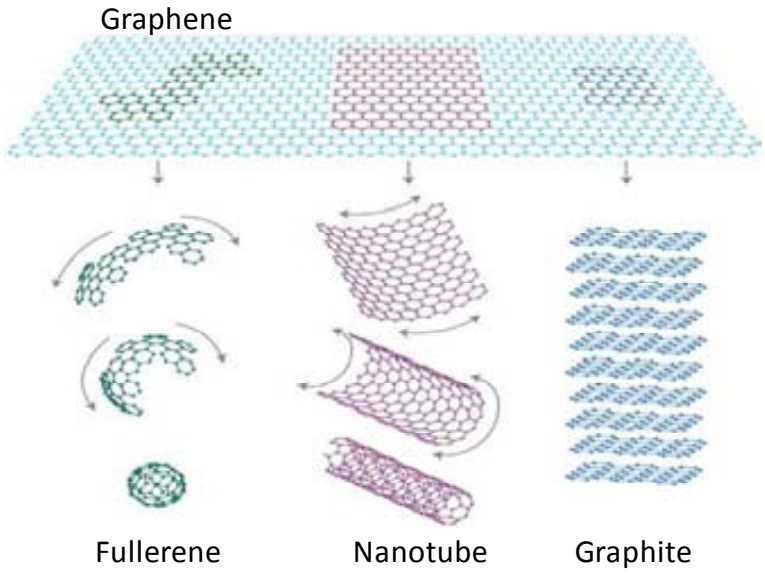

Figure 6.1. Graphene as mother of all graphitic forms. [From reference 1]

On the other hand, graphite is another allotrope of carbon, a stack of several graphene planes. Graphite has some of the exceptional graphene properties, as the electricity conduction within the carbon layers, due to the vast long range delocalized electrons (aromaticity) [5]. However, it does not reach the unusual properties that make graphene so attractive.

These outstanding properties have permitted the use of these carbon materials in a broad number of applications: fuel cells, energy storage devices or supercapacitors, among others [6,7]. Also, applications in bio-medical areas, as bio-sensors or tissue engineering have been recently reported [8] evidencing the suitable biocompatibility observed for these carbonaceous species [9,10].

The use of graphene to synthesize nanocomposites has been suggested in literature since its recent discovery, in order to obtain a synergetic effect of its properties with other different materials [11]. However, most of the attempts to synthesize carbon-based nanocomposites have been performed with polymeric materials [12-14] and not with oxides, as proposed in the present work. Recently, Shim et al. have presented the synthesis of iridium nanoparticles supported on graphene nanosheets to study the electrocatalytic activity in the oxygen reduction reaction [15], being the first attempt, as far as we concern, to combine these two materials in order to join their unique properties.

6.2 Carbon-based IrOx Hybrids Synthesis

6.2.1 Oxidized Carbon-based Precursors

Kish graphite coarse powder was oxidized following a method described in the article of G. Tobias et al. for the oxidation and functionalization of carbon nanotubes [16]. Strong oxidation of graphite yields to graphene/graphitic oxide however, the use of mild conditions allows the obtaining of big graphite-COOH particles. After the oxidation, in comparison with pristine graphite, the concentration of hydroxyl and epoxide functional groups increases on their basal planes, in addition to carbonyl and carboxyl groups located at the sheet edges [17]. The presence of these functional

groups in the surface, increases the hydrophilicity, which allows graphite to readily swell and disperse in water, particularly in alkaline solutions.

To determine the effectiveness of the graphite functionalization (concentration of oxygenated groups in the particles after oxidation treatment) XPS measurements were performed. The general survey, indicating the elements found in the coating and the relative atomic percentage, is shown in Figure 6.2, for graphite pre- and post-oxidized.

All the expected elements have the distinctive signal in the survey spectrum: carbon and oxygen. The O1s peak in the non oxidized graphite can be due to impurities, defects in the graphite or atmospheric oxidation [18]. However it is clearly observed how in the graphite-COOH sample, the oxygen concentration is almost four times higher than for the non-oxidized graphite sample (atomic percentages of 7.6% and 1.9% respectively), indicating the satisfactory graphite oxidation. To better observe these differences, the detailed spectra of oxygen (O1s) and carbon (C1s) are shown in Figure 6.3.

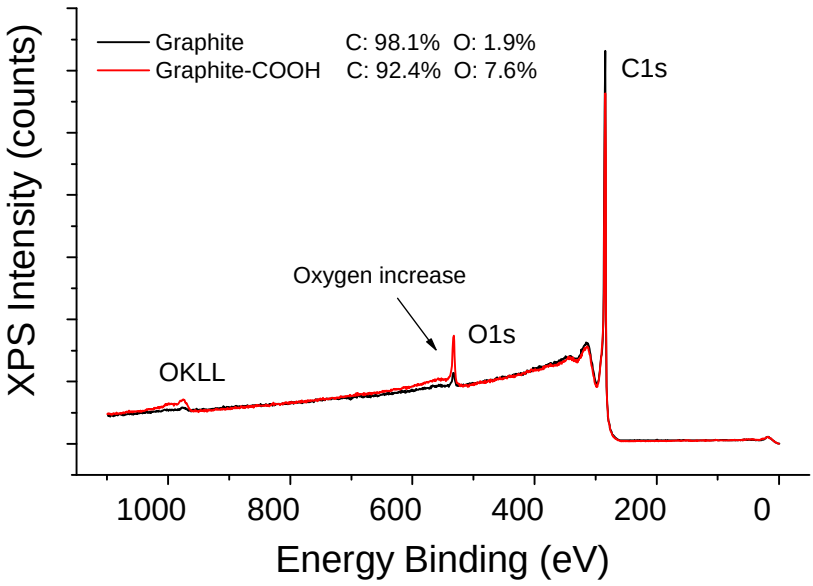

Figure 6.2. XPS survey spectra for graphite, pre and post-functionalization. The atomic quantification percentage of C and O elements is also indicated (atomic%).

The deconvolution of the O1s peak for both graphite samples, gives three well defined peaks at 531.6±0.2 eV, 533.3±0.2 eV and 535.4±0.2 eV, which can be assigned to C=O, COOH and -OH/H_2O respectively (Figure 6.3). Comparing the two samples, COOH and C=O deconvoluted peaks are smaller in the non-treated graphite, confirming the difference with the functionalized graphite, which is oxidized. In order to quantify the oxidation degree, the total percentage of each deconvoluted peak, are gathered in the Table 6.1.

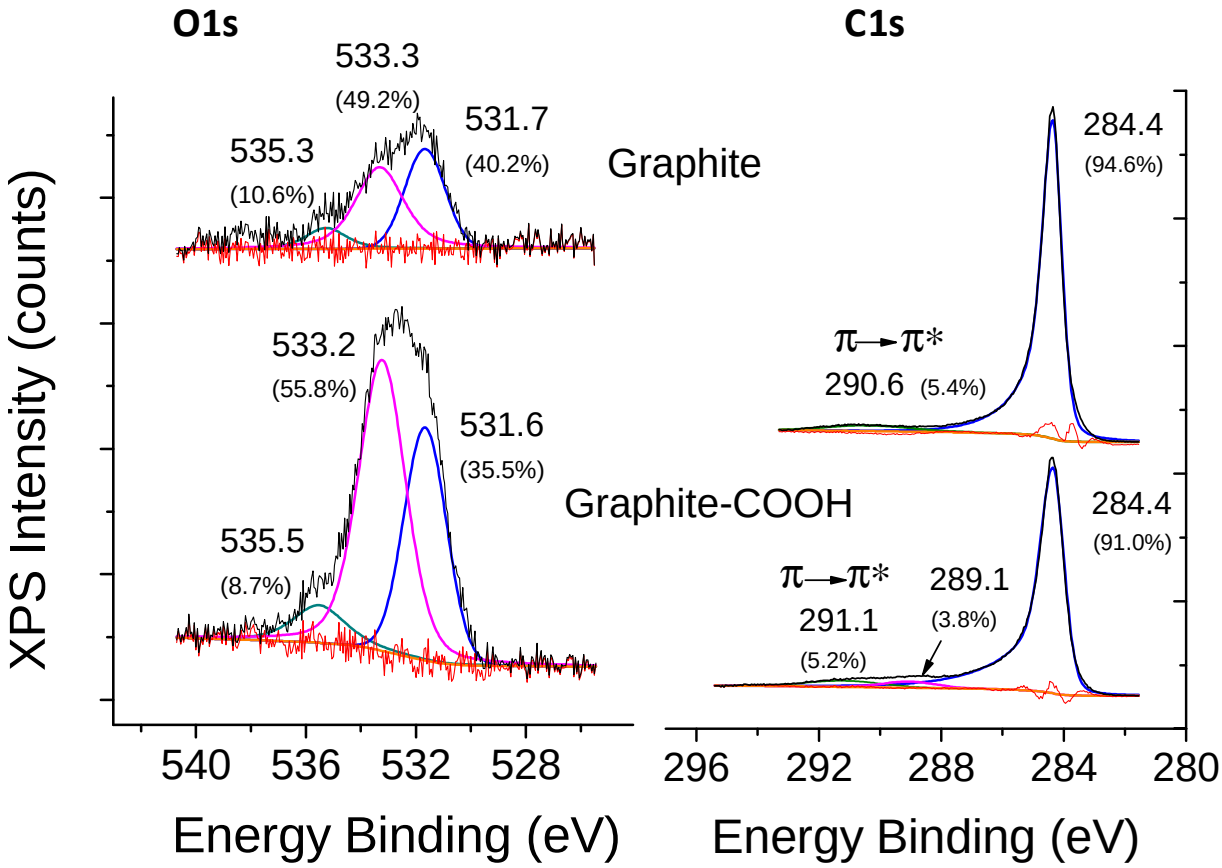

Figure 6.3. Deconvoluted O1s and C1s XPS spectra for graphite and functionalized graphite (graphite-COOH).

In C1s peak deconvolution for both graphite samples, the peak observed at 284.4±0.2 eV is related with the graphitic carbon, described in literature [19]. In the oxidized graphite sample, another peak at 289.1±0.2 eV is observed, which corresponds with

carbonyl and carboxyl groups [20]. However, the main peak is for graphitic carbon, which means that we cannot consider the phase as graphite oxide but rather as graphite oxidized in a small rate. Around 291.0±0.2 eV a plasmon peak appears, characteristic of conductive samples, such as graphite and metals [21]. The corresponding total concentrations are summarized in Table 6.1.

Peak	Peak assignation/ Position (eV)	Graphite (atomic %)	Graphite-COOH (atomic %)
O1s	C=O/ 531.6	0.8	2.7
	COOH/533.2	0.9	4.2
	OH/535.3	0.2	0.7
C1s	C-C/284.4	92.8/100*	84.1/95.9*
	C=O, COOH/289.1	---	3.5/4.1*
	$\pi \rightarrow \pi^*$/291.1	5.3	4.8

*Table 6.1. Total quantification of the O1s and C1s peaks components (atomic %) for graphite and oxidized graphite. Percentages add up to the total quantity of each element from the survey: carbon 98.1% and 92.4%, and oxygen 1.9%, and 7.6%, for graphite and graphite-COOH, respectively. (*atomic percentage after the subtraction of the plasmon contribution).*

Table 6.1 shows how the relation between the plasmon ($\pi \rightarrow \pi^*$) and the C-C contribution is the same for both samples, 0.057, indicating that the compositional differences observed in graphite-COOH are consequence of the treatment oxidation.

XPS results give an idea of the degree of oxidation, and the relation of total carbon and oxygen, gives a functionalization of around 10 wt (%). This value is under the normal efficiency (which is around 20-25%) supporting a mild oxidation. To calculate the total carbon amount for each of the samples is necessary the subtraction of the percentage related with the Plasmon (Table 6.1 with asterisks). For graphite, little contributions of CO and COOH are also observed in the O1s peak, however no significant C1s signal for C=O or COOH is seen, indicating that these contributions are so small that in the C1s peak are negligible.

To have an idea of the size and the shape of the graphite particles, TEM images were obtained (Figure 6.4).

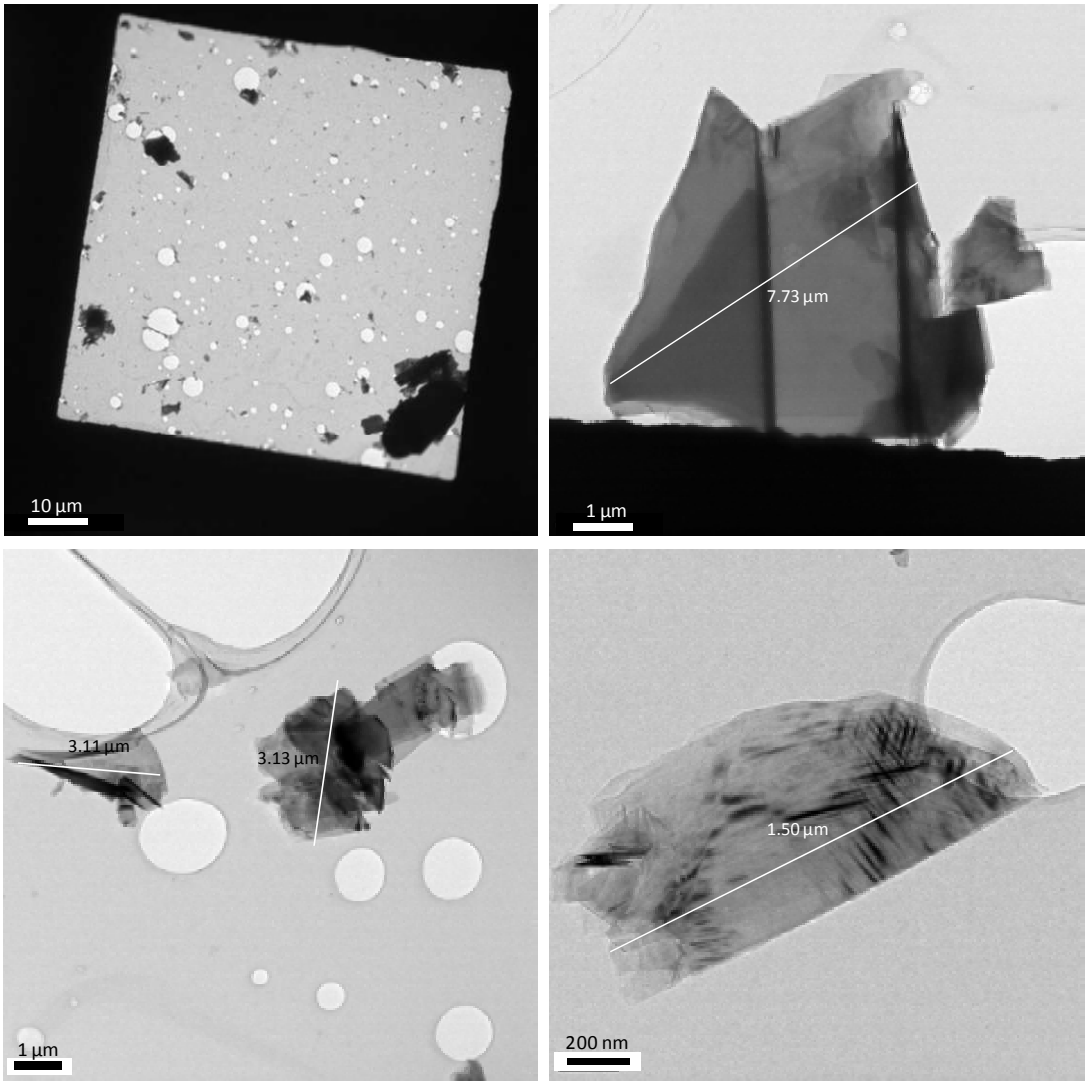

Figure 6.4. TEM images of the graphite-COOH particles.

The graphene oxide (or graphitic oxide as it has not been proved the existence of single graphene sheets) was obtained using the protocol described by Hummers [22] by the Carbon *Nanomaterials and Inorganic Nanostructures* group. In this case, the oxidation degree has been calculated by them, using TGA measurements and is about 20 wt (%). To obtain the graphene sheets (or few-layered sheets) the resulting black powder was extensively sonicated, before the pre-deposition solution preparation.

6.2.2 Pre-Deposition Solutions and Electrochemical Deposition

Pre-deposition solutions for both hybrids have been prepared dispersing by sonication graphite-COOH or graphene/graphitic oxide (GO) in water. Then, $IrCl_3$ was added and finally, K_2CO_3 was added until reach pH 10. These solutions were aged during one week at 37ºC in an incubator, and kept at 4ºC until use. The solutions were dark because of the dispersion of carbonaceous particles, but the characteristic blue color of alkaline iridium (III) chloride solutions is also observed, very similar to the pre-deposition solution for IrOx-CNTs hybrids.

The deposition of the coatings was performed following the steps described in the experimental section, using a potentiodynamic technique with a potential sweep from open circuit potential (~0.0V) to 0.70 V vs Pt (graphite-COOH) or 0.85 V vs Pt (GO) and scan rate of 5 mV/s. The number of cycles was optimized to obtain good adherence and semi-transparent aspect, and was fixed in 20-25 cycles. Typical synthesis curve intensity/potential is shown in Figure 6.5. In these conditions, the total charge provided to the system during the synthesis was around 0.27 C/cm^2 and 0.45 C/cm^2 for 25-cycle IrOx-graphite and 20-cycle IrOx-graphene, respectively.

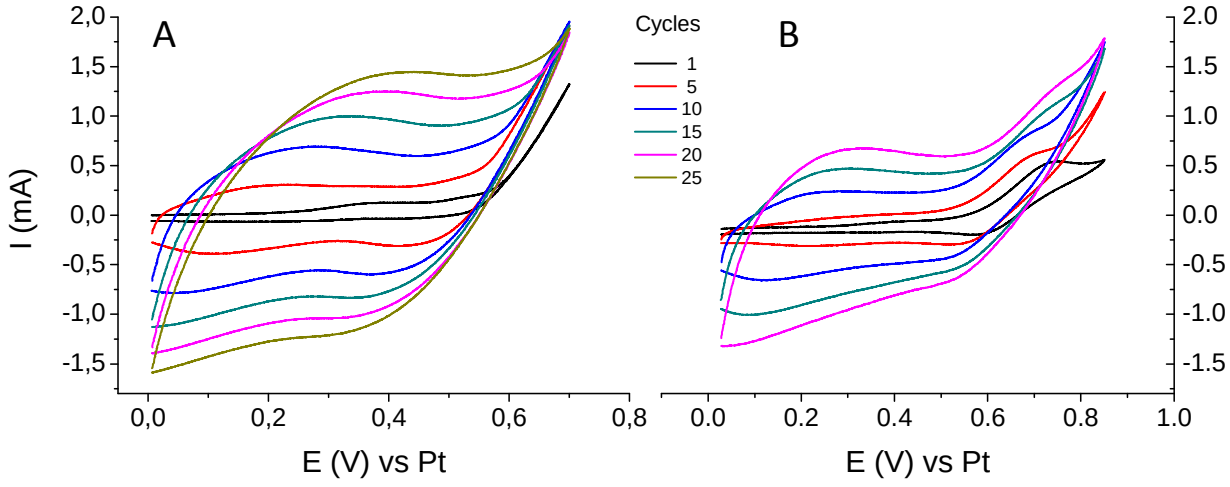

Figure 6.5. Curves obtained during the potentiodynamic synthesis of the hybrids at 5 mV/s. A) IrOx-graphite and B) IrOx-graphene. For clarity, only one in ten cycles is plotted.

Although the carbon precursors are oxidized (graphite-COOH and GO), the hybrid coatings will be named IrOx-graphite and IrOx-graphene for simplicity (even considering the possibility of few-layered graphene).

IrOx-graphite and IrOx-graphene thin film coatings show homogeneous appearance, with blue-grey color, very similar to IrOx-CNTs samples but darker than iridium oxide ones, as can be seen in Figure 6.6. As mentioned in previous chapters, the color can be modulated with the thickness and can be optimized depending on the final purpose.

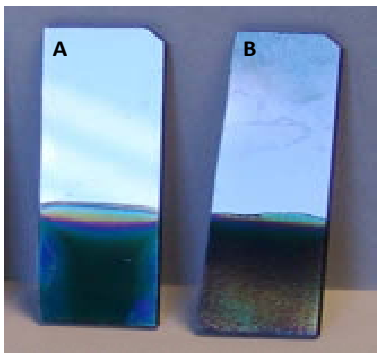

Figure 6.6. Images of the 25-cycle hybrid samples. A) IrOx-graphite and B) IrOx-graphene.

The thinnest coatings (20-25 cycles), presenting blue color, have been observed with optical microscopy and the images obtained are presented in Figure 6.7.

Dark particles in IrOx-graphite sample correspond to graphite. The variety of shapes and sizes (between 4 and 40 μm) was previously observed for graphite-COOH in TEM images (Figure 6.4). The dispersion of graphite in the coating is homogeneous in the entire sample, despite the different morphology of the particles.

IrOx-graphene coating also presents black dispersed particles with diameters between 1 and 4 μm (Figure 6.7C). The size of these particles suggests the presence of few-layered graphene sheets, although the presence of bigger graphite particles is also probable.

The incorporation of carbon in both hybrid materials is obvious when compared with IrOx coatings (Figure 6.7D). In IrOx coating is possible also to observe little black dots, but probably due to pores, as the circular shape indicates.

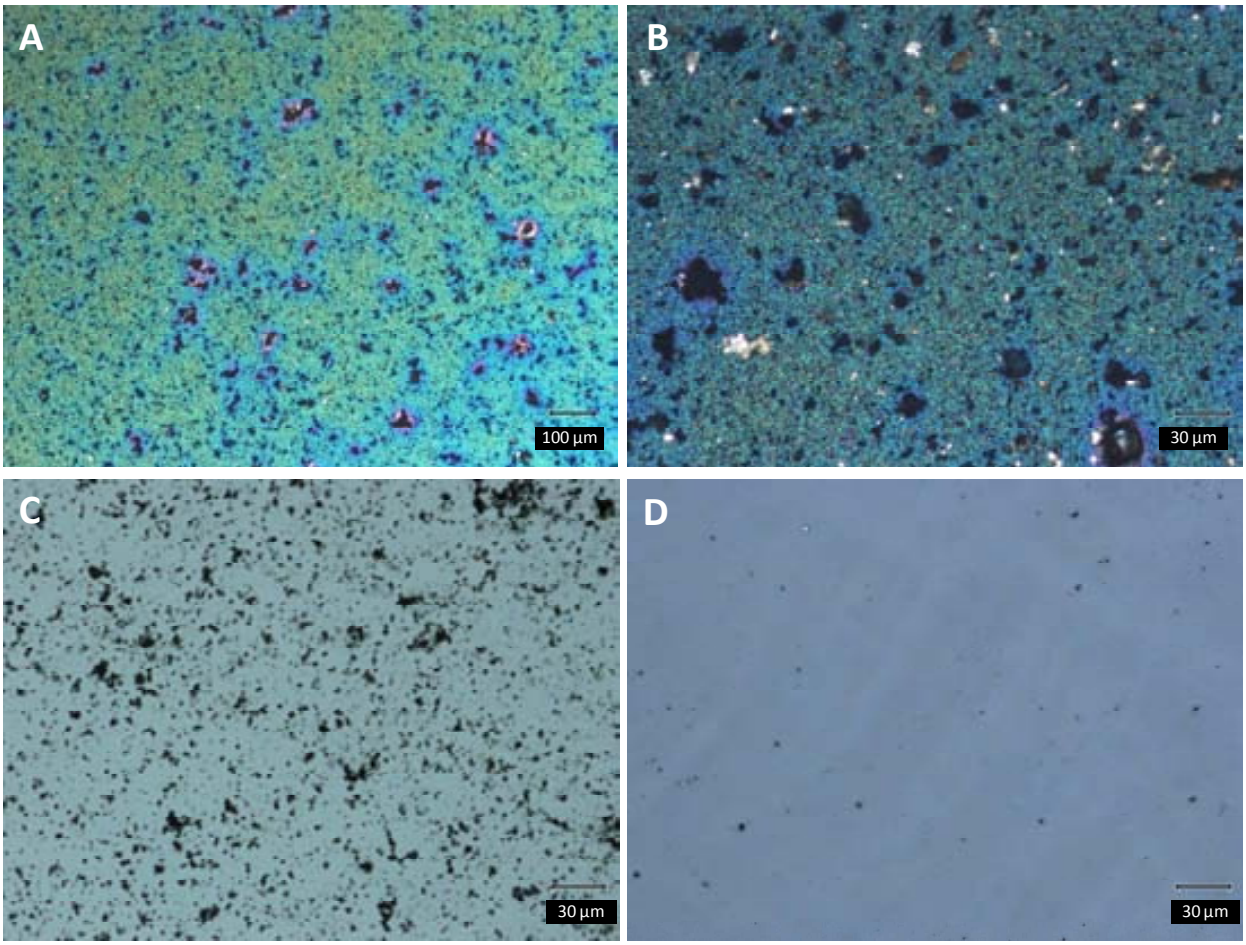

Figure 6.7. Optical microscope image of A-B) IrOx-graphite coatings at different zooms, C) IrOx-graphene and D) IrOx.

6.3 Characterization of the Samples

An initial characterization has been performed to determine the composition and structure of the coatings, although more experiments are necessary to fully characterize these new materials, as the quantification of the total carbon introduced in the samples. Also, the existence of graphene has not been confirmed and needs additional studies.

6.3.1 Scanning Electron Microscopy

SEM was used to study the surface microstructure and the possible alterations induced by the incorporation of carbonaceous particles in the iridium oxide structure. Also the thickness was evaluated with this technique.

IrOx-graphite SEM images show graphite particles in the surface, as previously seen by optical microscopy (Figure 6.8). However, no evidence of graphite in the in the bulk of the coating can be proven. Despite the big size particles, the surface seems very similar compared to IrOx-CNTs coatings, with cracks, that are prevented in thinner samples. Focusing in the particle surface (Figure 6.8B), is possible to observe how the roughness is different from the bare carbon particle observed in TEM images (Figure 6.4), suggesting the formation of iridium oxide on the particle surface. Therefore, carbon particles are coated by IrOx, as previously observed for CNTs (Chapter 4).

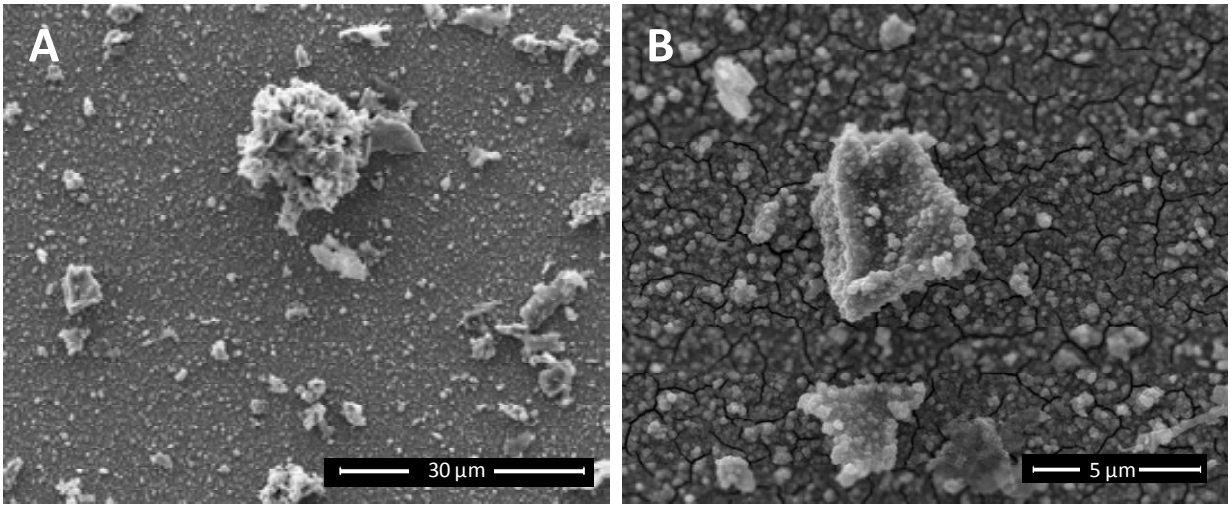

Figure 6.8. SEM images of the surface of IrOx-graphite coatings. Images were taken at 10 kV.

The chemical composition of the samples was evaluated by EDX (Energy Dispersive X-Ray Analysis). The results, in comparison with IrOx coatings are show in Figure 6.9.

A significant difference is observed between IrOx-graphite and IrOx samples, in terms of roughness. For the same magnification, graphite-hybrid coating is considerably

rougher, with bigger particles and grain size than the bare iridium oxide. IrOx coatings are thinner, and the substrate interferes in the measure, for this reason Si appears in the EDX results.

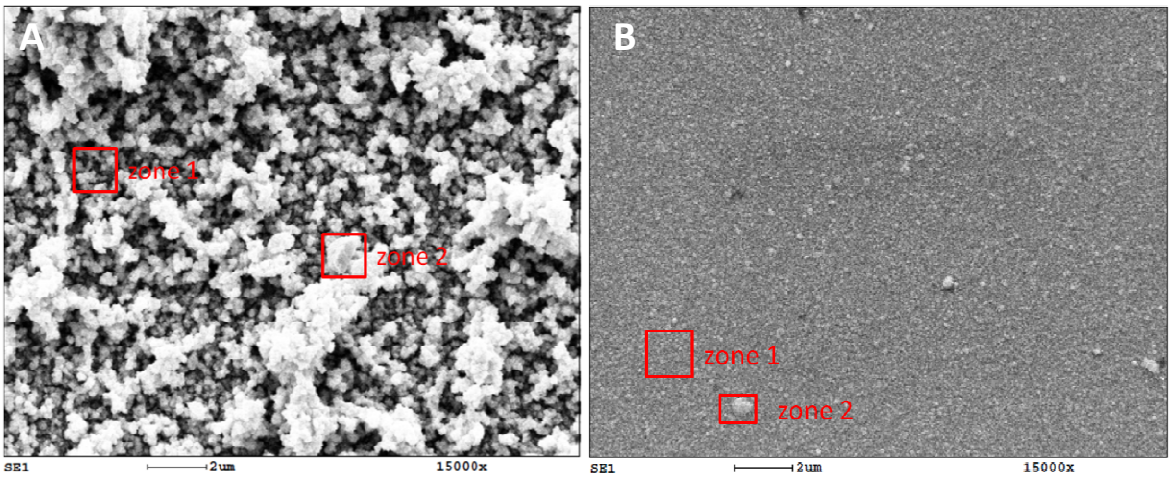

% atomic	C	O	Ir	K
Zone 1	32.6	41.1	16.7	9.6
Zone 2	66.7	23.8	4.2	5.3

% atomic	C	O	Ir	K	Si
Zone 1	34.0	34.3	5.7	2.9	23.1
Zone 2	36.2	37.8	13.1	4.8	8.1

Figure 6.9. SEM images of the surface of A) IrOx-graphite and B) IrOx coatings. The respective EDX analysis is shown in the tables.

When the electron beam is focused on an IrOx-graphite particle (zone 2 in Figure 6.9A), the amount of carbon significantly increases (C/Ir relation from 1.95 to 15.88), whereas the amount of oxygen and iridium (IrOx components) decreases. These facts correspond with the result expected for an IrOx-coated graphite particle. On the other hand, in IrOx samples, carbon also appears in a large amount. As shown in previous chapters, it is due mainly to adventitious carbon, which cannot be avoided. The zone 2 in the IrOx sample (Figure 6.9B) focuses also in superficial particle. However no substantial differences in carbon concentration are appreciated, just the Si is in significantly lower percentage because the beam has been focused in a higher elevation and the substrate does not interfere too much in the measurement. Therefore, we can conclude that IrOx coatings are homogeneous in composition,

whereas for IrOx-graphite coatings the presence of big carbon particles alters this homogeneity.

The thickness of the obtained IrOx-graphite coatings has been determined by SEM measurements with the sample in parallel with the electron beam. The image shows an irregular surface, with a medium thickness of about 400 nm for 25-cycle samples (Figure 6.10).

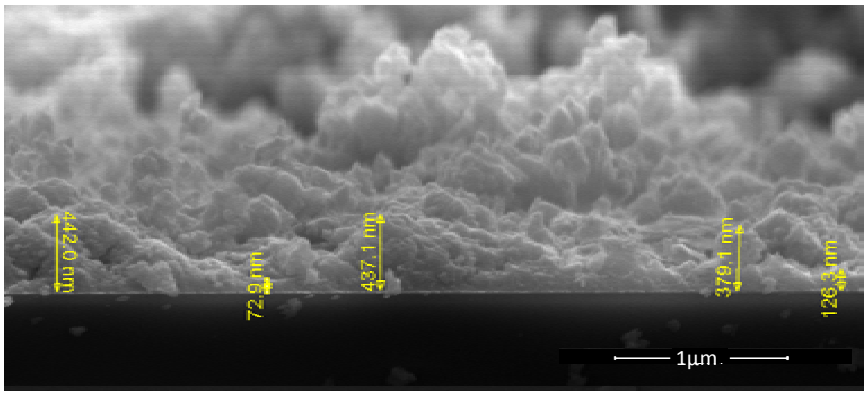

Figure 6.10. SEM image of the border of the 25-cycle IrOx-graphite sample in order to calculate the thickness. Images were taken at 10 kV.

IrOx-graphene coatings also have been characterized by SEM. However, in this samples, the identification of graphene is not as obvious as graphite (Figure 6.11), due mainly to the thinner graphene sheets, which make difficult its direct observation in the oxide matrix. However, a rougher surface when compared with bare IrOx is observed, indicating the alteration in the oxide structure produced by the GO incorporation. The thickness observed by SEM for these coatings was around 1.5 µm, for 20-cycle coatings, similar to those obtained for IrOx-CNTs coatings.

EDX analysis (Figure 6.12) in two different zones of the IrOx-graphene sample does not show important differences in composition, and in zone 1 and 2 the relation C/Ir is almost identical (1.81 and 1.87 respectively). This fact indicates that, few-layered graphene sheets, with smaller size than graphite particles, are homogeneously distributed in the entire sample and completely coated by IrOx.

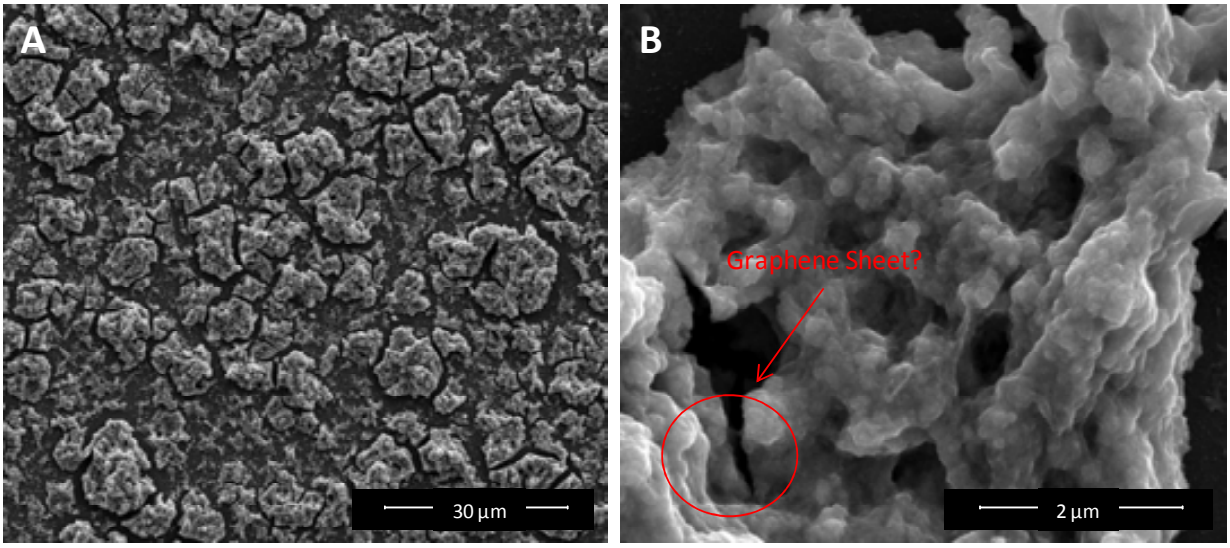

Figure 6.11. SEM images of the IrOx-graphene coatings surface at different magnifications.

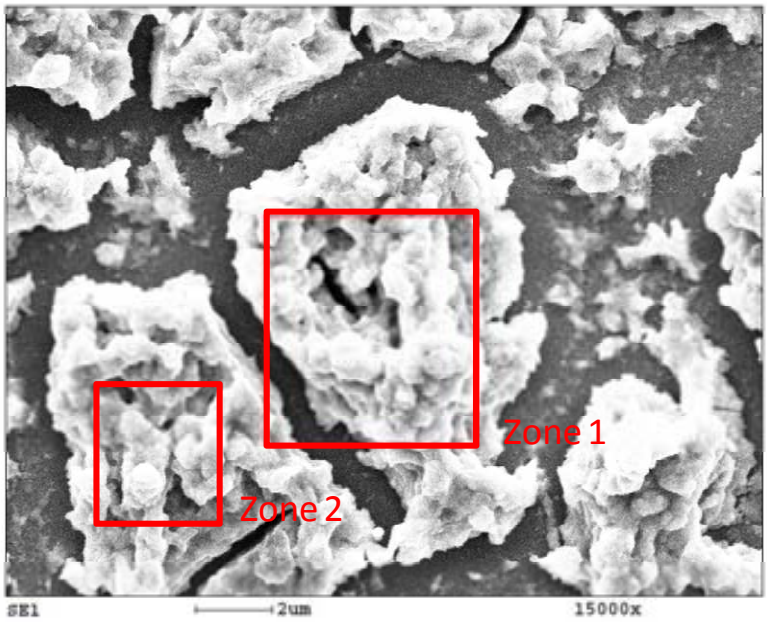

% atomic	C	O	Ir	K	Si
Zone 1	30.6	40.1	16.9	9.6	2.8
Zone 2	32.5	39.8	17.3	9.8	0.6

Figure 6.12. SEM image of the surface of IrOx-graphene coating and the corresponding EDX analysis in two zones.

6.3.2 Roughness by 3D Confocal Microscopy

The roughness of the IrOx-graphite and IrOx-graphene 25-cycle coatings has been evaluated with 3D confocal microscopy (Figure 6.13). The calculated values using height parameters for RMS are approximate **S_q= 2.2 µm** and **S_q=1.15** µm respectively.

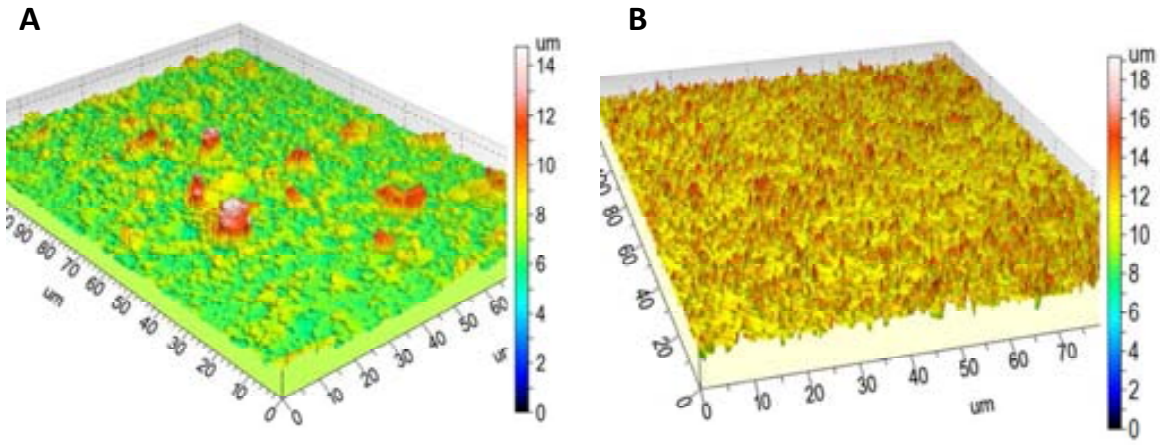

Figure 6.13. Confocal 3D microscopy images showing the 3D surface, for A) IrOx-graphite and B) IrOx-graphene coatings, synthesized at 25 cycles.

The presence of big particles in the surface of IrOx-graphite seems to be the responsible for the larger roughness obtained. In addition, the presence of these carbon particles makes the coating less homogeneous than the corresponding IrOx-graphene which, although significantly rougher than IrOx or IrOx-CNTs samples, is quite homogeneous. This roughness increase in IrOx-graphite and IrOx-graphene coatings, provides a larger real superficial area, which may be significant for high performance in electrochemical measurements.

6.3.3 X-Ray Photoelectron Spectroscopy

XPS measurements were performed to determine the elements present in the surface and their concentration. The resulting XPS survey spectra for both graphite and graphene hybrid coatings are shown in Figure 6.14.

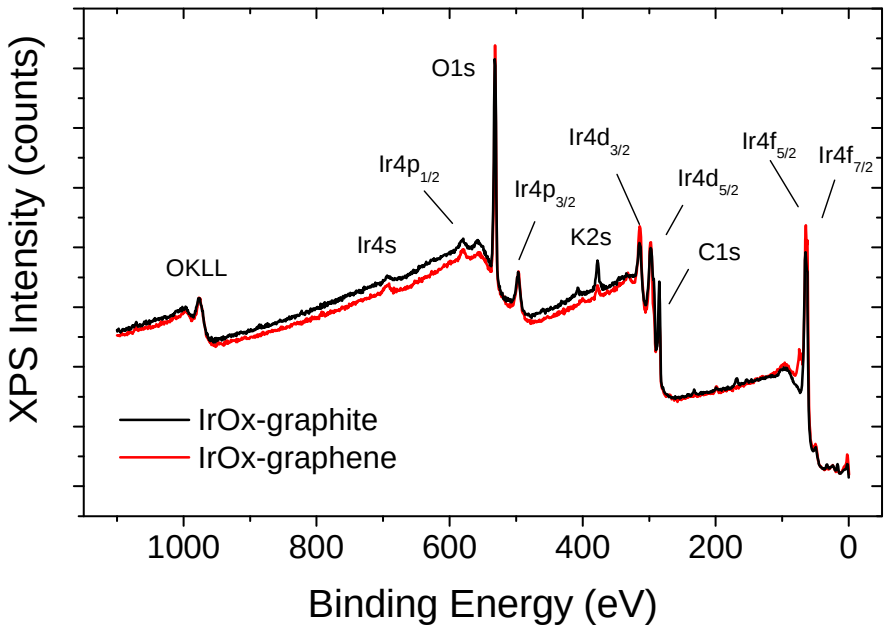

Figure 6.14. XPS survey spectra for IrOx-graphite and IrOx-graphene coatings.

The obtained spectra are very similar for IrOx-graphite and IrOx-graphene samples. The carbon amount is considerably higher than for IrOx and IrOx-CNTs coatings, as can be expected due to the bigger size of the carbonaceous particles, clearly seen in optical microscopy images. The relation O/Ir obtained for the carbon-based hybrids are 4.74 and 5.09 for graphite and graphene respectively, which are high values compared with the respective ones for IrOx-CNTs and IrOx (3.98 and 3.60). These differences are attributed to the relevant contribution of oxidized groups in the surface of the carbonaceous particles to the total amount of oxygen. Deconvolution of the O1s peak allows knowing how of this oxygen is bonded to carbon (Table 6.3), and subtracting this percentage, new O/Ir relations of 3.7 and 3.8 are obtained for IrOx-graphite and IrOx-graphene, respectively. These values are very similar to those obtained for IrOx and IrOx-CNTs coatings, suggesting that the iridium oxide matrix is the same in all the samples.

On the other hand, the presence of potassium is observed in all the coatings, as reported in previous cases. The relation K/Ir is very similar for all the samples, in the

range 1.7-1.9, indicating that despite the carbon allotrope introduction in the structure, the oxide component of the coatings is always an hydrated IrOx with high concentration of potassium absorbed in the structure, as described in Chapter 3.

Sample	C1s (at.%)	O1s (at.%)	Ir4f (at.%)	K2p (at.%)	K/Ir	C/Ir	O/Ir
IrOx-graphite	32.2	41.7	8.8	17.3	1.96	3.66	4.74
IrOx-graphene	27.3	47.4	9.3	16.0	1.72	2.93	5.09
IrOx-CNTs	14.2	49.8	12.5	23.5	1.88	1.13	3.98
IrOx	15.7	47.6	13.2	23.5	1.78	1.18	3.60

Table 6.2. Quantification (atomic %) for different coatings, obtained from the data of the XPS survey spectra.

Using the information obtained in the general survey and the deconvolution of the peaks (Figure 6.15), the absolute quantities of each species can be devised, and is shown in the Table 6.3. The results obtained for these carbon-based hybrids, show the C1s peak shifted for the normal position for adventitious carbon (284.8±0.2 eV), demonstrating the presence of graphitic particles (which C1s BE is 484.4±0.2 eV). Thus, carbon signal cannot be attributed to adventitious carbon as in IrOx-CNTs and IrOx samples, although the presence of some atmospheric impurities is always expected. C1s deconvoluted peaks for IrOx-graphene coincide with the ones obtained in bibliography for GO [23]. The percentage of oxygenated carbon species (CO, COH, COO, COC) is higher in case of IrOx-graphene due to the initial larger functionalization.

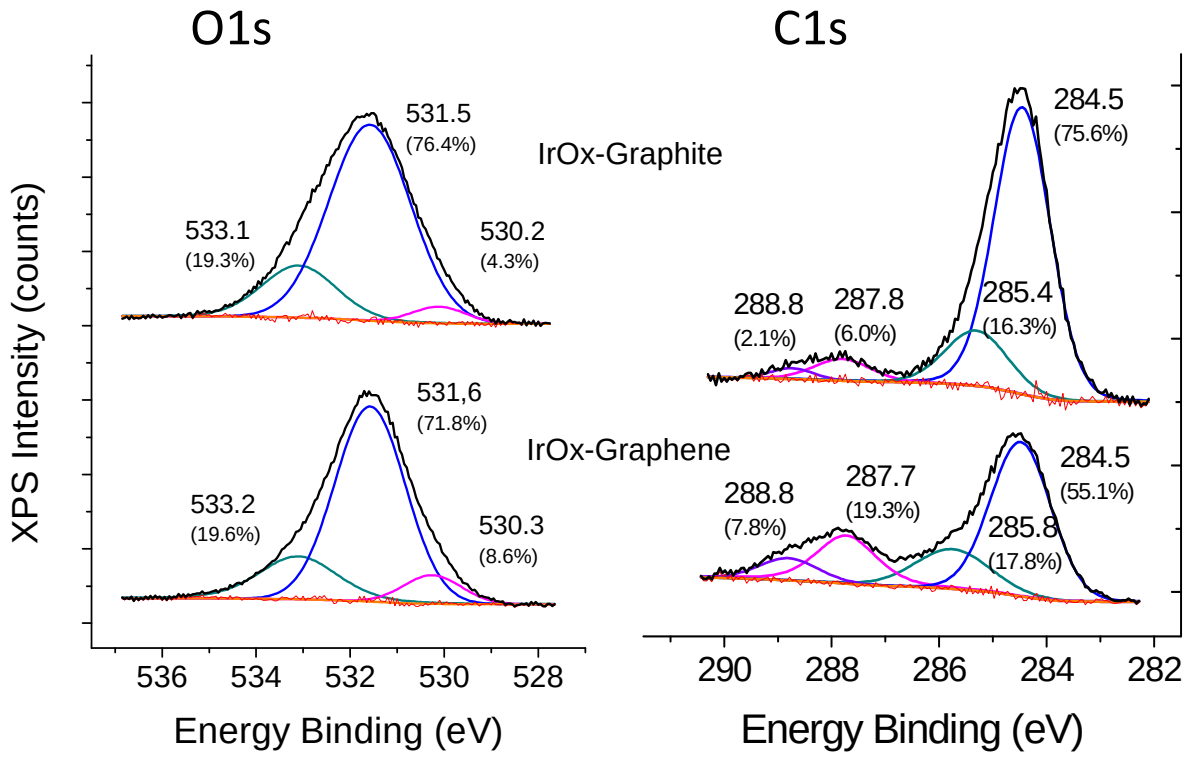

Figure 6.15. Deconvolution of O1s and C1s XPS peaks for IrOx-graphite and IrOx-graphene coatings.

	Peak assignation/ Position (eV)	IrOx-graphite (at.%)	IrOx-graphene (at.%)	IrOx-CNTs (at.%)	IrOx (at.%)
O1s	O^{2-}/530.2	1.8	4.1	6.3	5.2
	OH^-,C=O, COO^- /531.6	31.9	34.0	36.7	35.0
	H_2O/533.1	8.0	9.3	6.8	7.4
C1s	C-C, C-H/584.5	24.3	15.0	8.7	10.7
	C-OH, C-O-C/285.8	5.3	4.9	2.2	1.7
	C=O/287.8	1.9	5.3	1.7	1.3
	COO^-/288.8	0.7	2.1	1.6	2.0

Table 6.3. Total quantification of the O1s and C1s peaks components (atomic %) in IrOx-graphite, IrOx graphene, IrOx-CNTs and IrOx coatings. Percentages add up to the total quantity of each element from the survey.

6.3.4 Electrochemical Characterization of the Coatings

The electrochemical behavior of the coatings was evaluated by cyclic voltammetries, following the same protocol used in previous chapters. The conditions for all materials were maintained, for better comparison. The electrolyte used was PBS (pH=7.4), and the potential window used from -0.6 V to 0.8 V, to avoid side reactions.

Under these conditions, the Figure 6.16 shows the CVs obtained for the different hybrid coatings. CSC_C values, which are proportional to the enclosed area of the curves, are 127.8 mC/cm^2 and 108.2 mC/cm^2 for IrOx-graphite and IrOx-graphene, respectively. These values are slightly larger than those obtained for IrOx-CNTs hybrid (101.2 mC/cm^2) synthesized at 25 cycles, but significantly higher than the values obtained for IrOx (34.6 mC/cm^2) even synthesized at 50 cycles. This increase in the charge storage capacity can be due, as mentioned previously, to the significant increase in roughness provided by the incorporation of the carbonaceous particles in the oxide structure. Rougher surfaces have larger electrochemical surfaces, which enhance the contact of the material with the electrolyte, allowing the exposure of more active centers to the redox interface. Also, the conducting properties of the carbonaceous particles can be the responsible of the improved electrochemical behavior, with lower resistance in the global circuit.

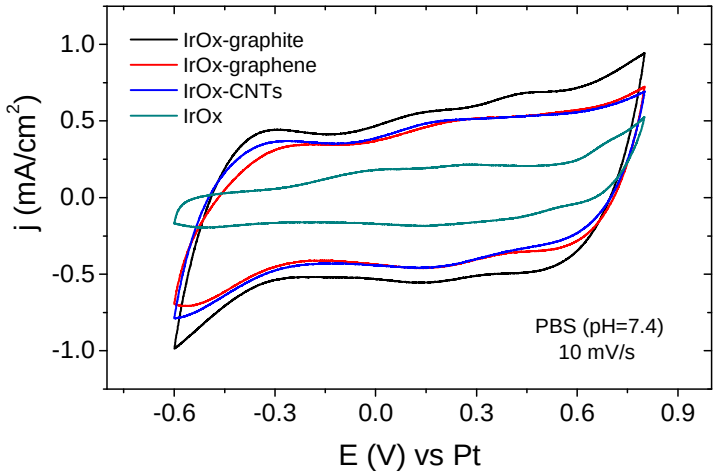

Figure 6.16. Comparison of cyclic voltammetries of IrOx hybrids with graphite, graphene and CNTs and bare IrOx samples (cycle 10) in PBS (PH=7.4) electrolyte, at sweep rate of 10 mV/s. Hybrids coatings synthesized during 25 cycles, IrOx during 50 cycles.

Although no biocompatibility tests has been performed yet for these new materials, the stability of the coatings as possible stimulation electrodes has been studied, performing 1000 cyclic voltammetries and monitoring the changes produced in the charge storage capacity. The results shown in Figure 6.17, demonstrate that although the IrOx-graphite achieves the highest CSC_C value, the stability is not reproducible, and the value drops upon successive cycles, suggesting the possible formation of cracks. The big size of the graphite particles can produce a perturbation in the oxide structure, debilitating the stability of the coating when subject to external stimuli. After de successive cycling, the coating is still adhered but some cracks are clearly perceived macroscopically.

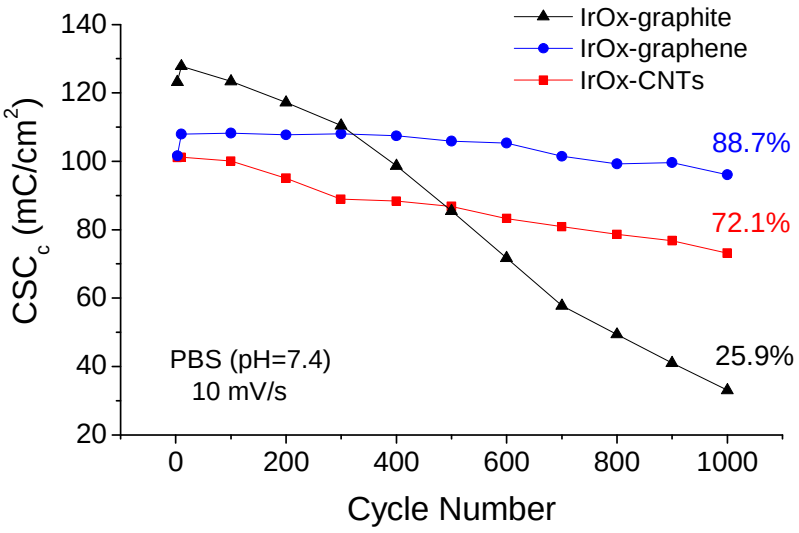

Figure 6.17. 1000 cycling performance of IrOx-carbon hybrids (synthesized at 25 cycles) in PBS (pH=7.4) at 10 mV/s.

On the other hand, the IrOx-graphene coating, in addition to a very high CSC_C value presents a very good stability, with 88.7% of the maximum charge storage capacity remaining after 1000 cycles, an improvement over the value obtained for IrOx-CNTs (72.1%). Also, IrOx-graphene coatings as previously observed in IrOx-CNTs films, remains unaltered after the successive cycling tests, which indicates the good stability of this new hybrid in electrochemical performances.

The good results achieved, mainly in terms of charge storage capacity and stability, indicate the relevance of these hybrids not only in stimulation electrodes but in other energy storage electrochemical devices, as supercapacitors for instance.

Characterization of the surface composition after cycling was performed by XPS for IrOx-graphene coatings. Table 6.4 shows that after 1000 cycles all the potassium has been removed. Since cycling is performed in a high Na^+ concentrated media, sodium is now present in the oxide structure. Thus, an ionic exchange has occurred during cycling, and the most abundant and mobile cation is finally remaining in the structure. The relation C/Ir is 2.96 and 2.93 for IrOx-graphene post cycling and as prepared, respectively, suggesting no degradation of the coatings. However, the relation O/Ir for the sample post cycling is 6.6, higher than the as prepared coating (5.1). When the corresponding O1s deconvolution is done, it is seen that this oxygen increase is mainly due to the OH^- contribution (not shown). Therefore, during the stability test, also an exchange of hydroxyl groups with the electrolyte occurs. Also it is possible to observe how in the post cycling sample, some platinum is detected and, as no mass loss is appreciated in the electrode, this fact may be an indicative that the structure after the electrochemical measurements is more porous as consequence of the ion-exchange so, the substrate is more easily observable by XPS.

Sample	C1s (at.%)	O1s (at.%)	Ir4f (at.%)	K2p (at.%)	Na1s (at.%)	Pt4f (at.%)
IrOx-graphene post cycling	25.0	55.6	8.4	----	8.6	2.4
IrOx-graphene	27.3	47.4	9.3	16.0	----	----

Table 6.4. Quantification (atomic %) for IrOx-graphene coatings, as prepared and after 1000 cyclic voltammetries.

6.4 IrOx-(Graphene-N) Hybrids

The very promising results obtained for IrOx-CNTs and IrOx-graphene hybrids, have opened the route to explore new carbon-based fillers for IrOx coatings. In collaboration with the ICMAB group of *Carbon Nanomaterials and Inorganic Nanostructures* we also tried to synthesize an IrOx hybrid with nitrogen-doped graphene. N-doped graphene (graphene-N) was obtained from graphene oxide and further reaction with ammonia (ammonolysis), yielding a surface with high concentration of active N-species. This increase in polar groups can enhance the dispersion of the graphene sheets in aqueous solutions, improving the efficiency of the co-deposition electrochemical synthesis. On the other hand, the introduction of nitrogenated groups in the graphene structure has been demonstrated to considerably enhance the conducting properties of the material, since nitrogen doping can tune graphene from being a p-type to n-type semiconductor [24,25]. This also confers to graphene-N a high performance in electrochemical applications compared to pristine graphene. For instance, higher capacities as electrode for supercapacitors [26] or greater electrocatalytic activity toward O_2 reduction reaction (ORR), a key reaction in many electrochemical energy devices such as fuel cells and metal-air batteries [27-29]. Even the biocompatibility has been improved in N-doped carbon structures as CNTs, compared with pristine ones [30].

6.4.1 IrOx-(Graphene-N) Synthesis

The electrodeposition of IrOx-(graphene-N) coatings was done starting from an aged solution of $IrCl_3$ and N-doped graphene in alkaline media, as detailed in Chapter 2. The synthesis protocol used was the same of that used for IrOx-graphene coatings: scan rate of 5 mV/s, reverse potential at 0.85 V and 20-50 cycles. Typical CV curves are shown in Figure 6.18. The total charge provided to the system during the IrOx-graphene-N electrodeposition has been around 0.75 C/cm^2 for 25-cycle coatings. This charge increase produced in IrOx-(graphene-N) when compared with IrOx-graphene (0.45 C/cm^2) can be consequence of the presence of nitrogen, which enhances the ability of graphene sheets to donate electrons.

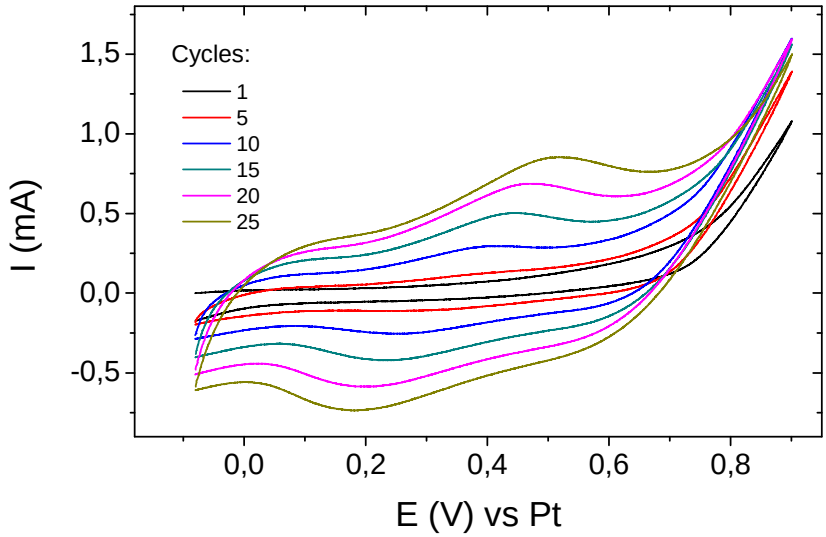

Figure 6.18. Curves obtained during the potentiodynamic synthesis of the IrOx-(graphene-N) hybrid coating. Scan rate of 5 mV/s, 25 cycles. For clarity, only one in ten cycles is shown.

The synthesized coatings are semi-transparent and colored depending on the thickness: the thinnest ones are blue-green with golden shimmer, similar to those obtained with non-doped graphene, as can be seen in Figure 6.19. In contrast, the thickest ones synthesized at 50 cycles are completely black.

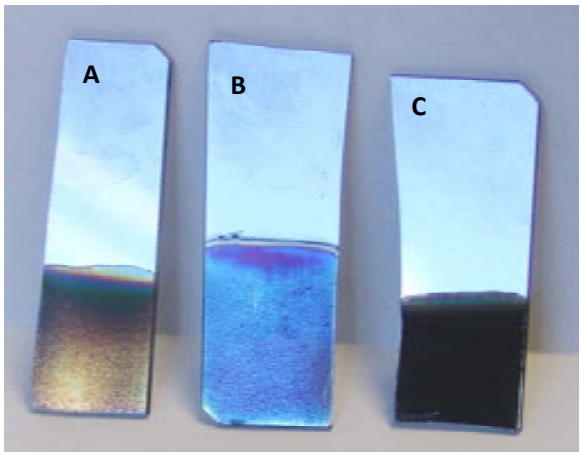

Figure 6.19. Graphene hybrid coatings. A) 20-cycle IrOx-graphene, 25-cycle IrOx-(graphene-N) and C) 50-cycle IrOx-(graphene-N) coatings.

6.4.2 IrOx-(Graphene-N) Surface Characterization

The surface morphology and the thickness were studied by SEM. The surface was very similar to the IrOx-graphene coatings, very rough but homogenous throughout the entire sample. The thickness measured was around 2.5 µm for 25-cycle coatings and 7.5 µm for 50-cycle coatings (Figure 6.20).

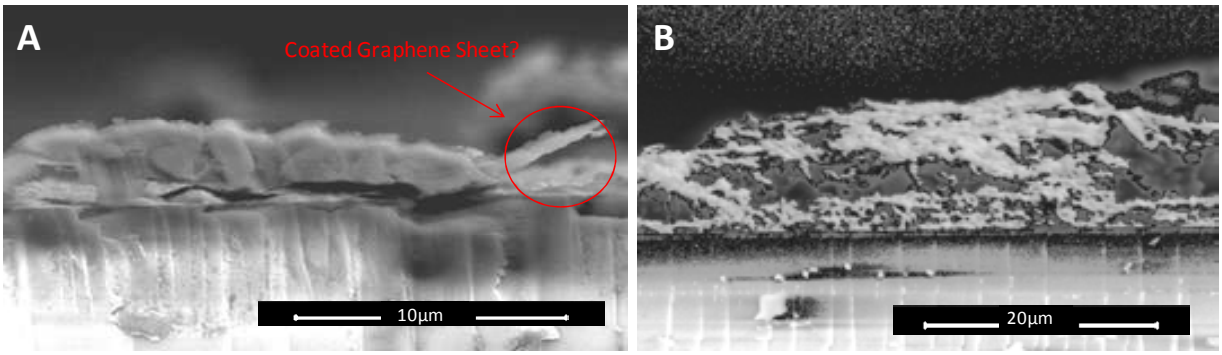

Figure 6.20. SEM image of the border of IrOx-(graphene-N) sample in order to calculate the thickness. A) 25-cycle and B) 50-cycle samples. Images were taken at 10 kV.

The surface compositional characterization of the new coating has been done by XPS. The general survey spectra are shown in Figure 6.21, compared with the IrOx-graphene. The main difference in chemical composition is the presence of the nitrogen peak (N1s), at binding energy around 400 eV, which indicates the effective introduction of N-doped graphene in the structure. The general quantification of all the elements is shown in Table 6.5.

The analysis of the XPS results obtained for IrOx-(graphene-N) hybrid, gives a relation K/Ir=1.87, within the range expected for this counterion inside IrOx coatings. The relation O/Ir is 4.17, higher than for IrOx, but it can be due to the contribution of part of the total oxygen to carbonated-O species or N-O species, as observed previously for the other carbon-based hybrids.

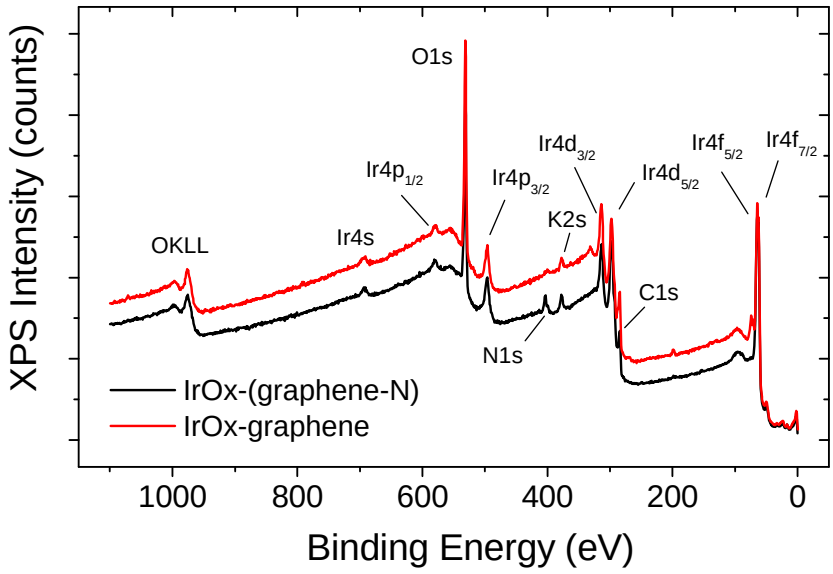

Figure 6.21. XPS survey spectra for IrOx-(graphene-N) and IrOx-graphene coatings.

	C1s (at.%)	O1s (at.%)	Ir4f (at.%)	K2p (at.%)	N1s (at.%)	K/Ir	C/Ir	O/Ir
IrOx-graphene-N	15.7	45.1	10.8	20.2	8.2	1.87	1.45	4.17
IrOx-graphene	27.3	47.4	9.3	16.0	----	1.72	2.93	5.09

Table 6.5. Quantification (atomic %) for IrOx-(graphene-N) and IrOx-graphene coatings, obtained from the data of the XPS survey spectra.

N-doped graphene hybrids present, in comparison with IrOx-graphene films, a considerably lower total carbon concentration. A possible reason can be found in the N-doping process, where high temperatures (around 200°C) are reached and some carbon is lost as CO_2. Also, the N-doping can generate best dispersion of the GO sheets, and hence, graphene sheets coated by IrOx are fewer, which yields lower total carbon determination. Other possible explanation can be that, after the N-doping graphene sheets are more conductive and during the electrodeposition, the IrOx deposition onto the graphene sheets is more effective in this doped graphene, obtaining more efficient iridium oxide coverings.

The deconvolution of the main peaks C1s and O1s are shown in Figure 6.22. The number of peaks and the position coincide with the obtained for IrOx-graphene but the quantities are slightly different. To study these differences, the total percentages of each species contribution are shown in Table 6.6.

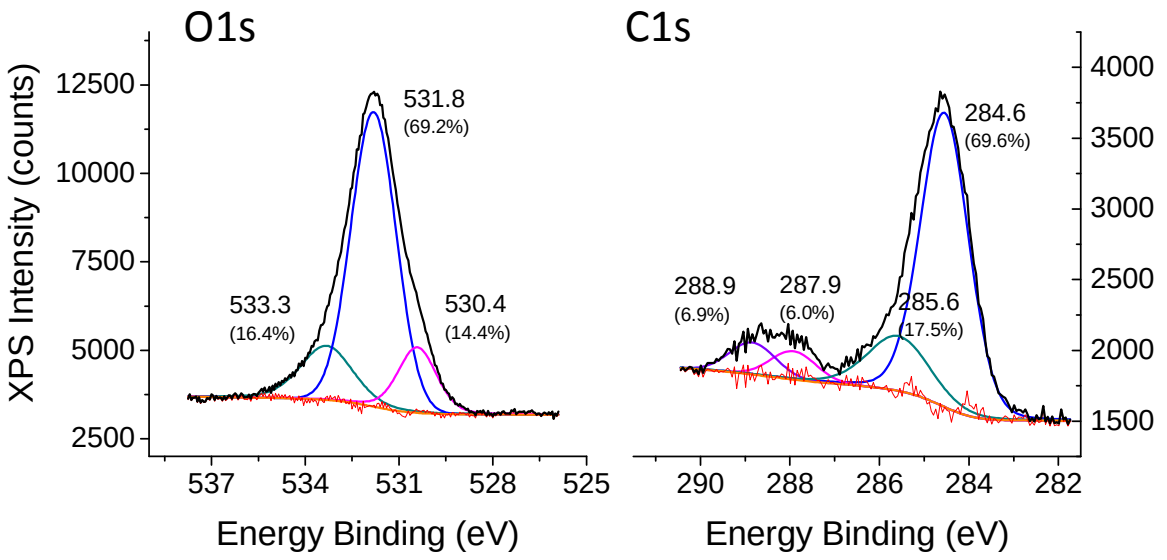

Figure 6.22. Deconvoluted O1s and C1s XPS peaks for IrOx-(graphene-N).

	Peak assignation/ Position (eV)	IrOx-(graphene-N) (atomic %)	IrOx-graphene (atomic%)
O1s	O^{2-}/530.4	6.5	4.1
	OH^-,C=O, COO^-/531.8	31.2	34.0
	H_2O/533.3	7.4	9.3
C1s	C-C, C-H/284.6	10.9	15.0
	C-OH, C-O-C, C-N/285.6	2.7	4.9
	C=O/287.9	1.0	5.3
	COO^-/288.9	1.1	2.1

Table 6.6. Total quantification of the O1s and C1s peaks components (atomic %) in the studied coatings. Percentages add up to the total quantity of each element from the survey, for hybrid IrOx-(graphene-N) and IrOx-graphene to compare.

The results obtained show an increase in O^{2-} oxygen for IrOx-(graphene-N) respecting to IrOx-graphene, that can be consequence of the increase in the number of defects in the graphene sheets provoked by the doping. These defects in the graphene sheets can act as nucleation sites for IrOx particles. Carbon atoms adjacent to N dopants possess a substantially higher positive charge density to counterbalance the strong electronic affinity of the N, which can result in an enhanced interaction with the negatively charged IrOx nanoparticles/olygomers present in the pre-deposition solution. Similar theory is used to explain the higher electrocatalytic activity observed in N-doped graphene, although the role of the real "electro-catalytically active sites" is still controversial [29]. Also, the amount of oxygenated carbon species (CO, COO^- and COC) has been reduced, as result of the elevate temperatures reached in the doping step.

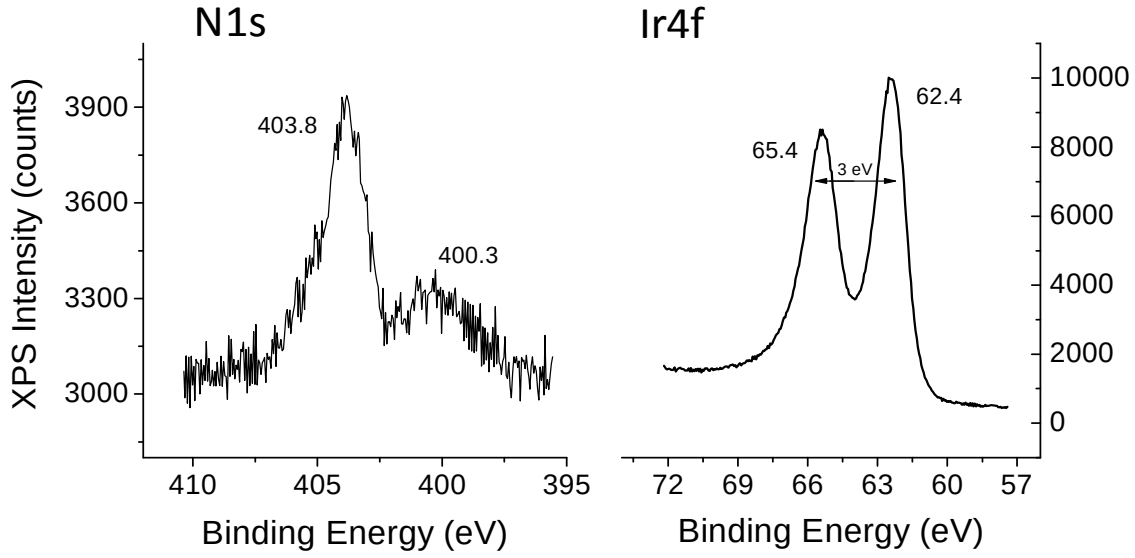

Figure 6.23. N1s and Ir4f XPS spectra for the IrOx-(graphene-N) coating.

The presence of iridium has been demonstrated also with XPS, and Figure 6.23 shows the characteristic peak for Ir4f, a doublet with separation between peaks of ~3 eV. In the same figure, the peak N1s is shown.

Generally, several nitrogen functional groups exist in N-doped carbon species, which characteristic XPS binding energies shown in Figure 6.24. These include pyridinic-N (~398.6 eV) which refers to N atoms at the edge of graphene planes, each of them bonded to two C atoms and donating one p-electron to the aromatic π system, pyrrolic-N (~400.5 eV) which refers to N atoms that are bonded to two C atoms and contribute to the π system with two p-electrons, quaternary-N or graphitic-N (~ 401.3 eV), in which N atoms are incorporated into the graphene layer and replace directly C atoms and N-oxides of pyridinic-N (~402.0-405.0 eV), which are bonded to C and O atoms [31].

The N1s spectrum obtained for the IrOx-(graphene-N) indicates that the nitrogenated species are oxidized. The peak at 400.3±0.2 eV is for pyrrolic-N, but the peak at 403.8±0.2 eV is assigned to nitrite [32]. This result indicates that during the hybrid electrodeposition, when the N-doped graphene sheets reach the electrode, N-groups can be oxidized; remaining in reduced state mostly the pyrrolic ones. This N-oxidation can be beneficial in future applications of this material as neural electrode, since it can enhances the charge capacity properties and since nitric oxide has been reported to be a neurotransmitter and its presence is usual in neural environments which can be an advantage in terms of biocompatibility [33,34].

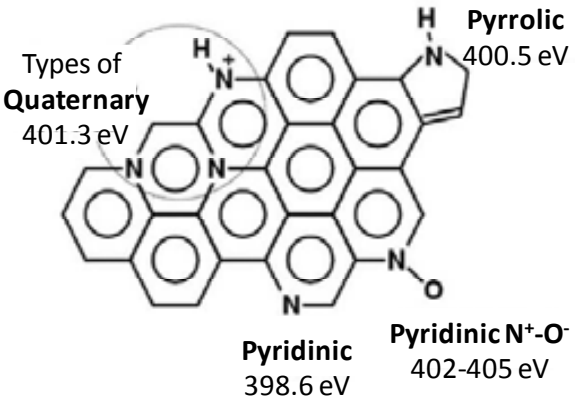

Figure 6.24. Nitrogen species commonly reported in N-doped carbon species. From reference 31.

6.4.3 Electrochemical Characterization of IrOx-(Graphene-N) Coatings

The electrochemical characterization performed by CV measurements has shown very good results of charge storage capacity and stability. Figure 6.25A shows the CV curves along with those for IrOx-graphene and bare IrOx for comparison. CSC_c values obtained are 158.9 and 125.1 mC/cm^2 for IrOx-(graphene-N) electrodes synthesized at 50 and 25 cycles, respectively. These results represent a considerable increase with respect to the value for 25-cycle coatings with non-doped graphene (108.6 mc/cm^2). This increase in capacity can be related with the previously demonstrated enhancement of the electrical conductivity, or as mentioned in the IrOx-CNTs chapter, can be due to the increase in roughness provoked by the incorporation of the carbon species in the iridium oxide structure.

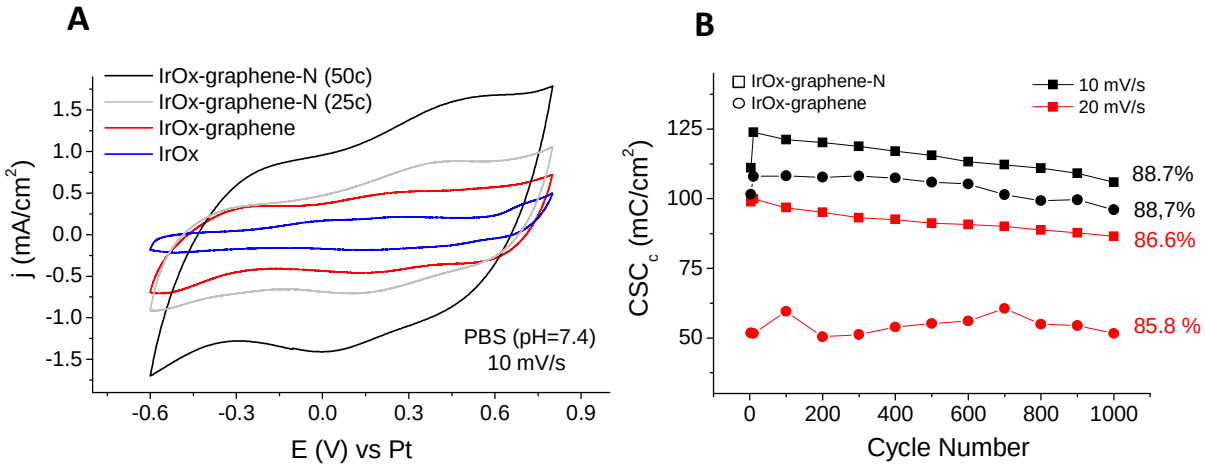

Figure 6.25. A) Comparison of cyclic voltammetries of IrOx-(graphene-N),25- cycle IrOx-graphene and 50-cycle bare IrOx samples (cycle 10) in PBS (PH=7.4) electrolyte, at sweep rate of 10 mv/s. B) 1000 cycling performance of the 25-cycle IrOx-(graphene-N) (squares) and 25-cycle IrOx-graphene (circles) hybrids, in PBS (pH=7.4) at 10 mV/s (in black) and at 20 mV/s (in red).

IrOx-(graphene-N) coatings are very stable when subject to 1000 successive cycles, as shown in Figure 6.25B. At high scan rate, the value of CSC_C drops as previously

observed in Chapter 3 however, the stability is maintained. In IrOx coatings, the stability was enhanced at higher scan rate (Figure 3.29) due to the minor relevance of faradaic processes at high rates. Therefore, the presence of graphene sheets presumably minimizes the deterioration provoked by faradaic reactions.

The higher performance of N-doped graphene has also been reported in electrochemical measurements for ultracapacitors, showing a specific capacitance by about 4 times compared to that for pristine graphene. This improved capacitance is likely attributed to the N-doped sites at basal planes [35].

6.5 Conclusions

- Hybrids with IrOx and different carbon-based fillers have been successfully synthesized and characterized, presenting very good stability and electrochemical performance in most of the cases.

- In first place, IrOx-graphite hybrid has been described, starting from the oxidized graphite precursor and synthesized following the protocol used in the IrOx-CNTs electrodeposition. The obtained hybrid coatings present an irregular surface as SEM images demonstrates, with big particles in the surface but not evidence of particles inside the coating. However, images taken by optical microscope indicate that the particles are spread in the entire sample, defining a very rough surface with a RMS of around 2.2 μm. By XPS, an increase in the percentage of carbon in the surface is evident, in comparison with the bare IrOx samples shown in previous chapters. However the relation K/Ir is almost maintained, confirming the similar composition of the IrOx matrix: an oxohydroxide with high content of potassium embedded in the structure during the electrodeposition. Finally, the electrochemical properties have been tested, showing a very high charge storage capacity (127.8 mC/cm^2) but very low stability under successive cycles, probably due the low cohesion between grains in the oxide structure provoked by the big graphite particles insertion, which make the coatings subjected to delamination.

- Secondly, graphene oxide provided by the ICMAB group *Carbon Nanomaterials and Inorganic Nanostructures* has been the precursor to successfully preparation of IrOx-graphene hybrids. The coatings present lower roughness than IrOx-graphite ones (RMS=1.5 μm), with no clear visible graphene sheets in the surface by SEM, but presence of homogeneously dispersed particles in the entire coating, as shown in optical microscope images. XPS results in this case, show also high concentration of C in comparison with bare IrOx, indicating the high possibility of having few-layered sheets of graphene instead individual sheets conforming the coating. However, the IrOx matrix also seems to be very similar to the bare IrOx. For this hybrid, the electrochemical measurements are very promising, with high values or CSC_c reached (108.2 mC/cm^2) and high stability to successive cycling, with only the 11.3% of the maximum CSC_c lost after 1000 cycles in PBS.

- Finally, N-doped graphene supplied by the ICMAB group *Carbon Nanomaterials and Inorganic Nanostructures* was incorporated in the iridium oxide matrix to synthesize IrOx-(graphene-N) coatings. The same protocol used in the electrochemical deposition of previous hybrids was performed, and the result was a self-standing coating. XPS results show the incorporation of the N-doped graphene, as the signal N1s is clearly observed. However, similar percentages of C are obtained in comparison with the bare IrOx or the IrOx-CNTs hybrids, which can indicate a very effective coating of the graphene-N sheets as observed in the CNTs and hence, not possible differentiation between C from graphene or from adventitious carbon (very easily absorbed in this kind of iridium oxides) is possible. As in the previous hybrids described, the IrOx matrix seems to be very similar to bare IrOx. Also, XPS has shown that most of the nitrogen introduced in the doping has been oxidized, and in the coatings is mainly as pyridinic N^+-O^-. The outstanding electrochemical properties obtained, with CSC_c values of 158.9 mC/cm^2 and 125.1 mC/cm for 50 and 25-cycle IrOx-(graphene-N) coatings respectively, and high stabilities

(around the 87-% of the maximum charge capacity is maintained after 1000 cycles) make this new material the objective of further investigations in order to complete the characterization and the possible applications of the unique properties.

6.6 References

-[1] Geim A.K. and Novoselov K.S. The rise of graphene. *Nat. Mat*. **6**, 183-191. 2007.

-[2] Castro-Neto A.H., Guinea F., Geim A.K., et al. The electronic properties of graphene. *Rev. Mod. Phys*. **8**1, No.1, 109-162. 2009.

-[3] Yuang W. and Shi G. Graphene-based gas sensors. *J. Mater. Chem. A*. **1**, 10078-10091. 2013.

-[4] Robinson J.T., Perkins F.K., Sheehan P.E., et al. Reduced graphene oxide molecular sensors. *Nano Lett*. **8**, No.10, 3137-3140. 2008.

-[5] Primak W. and Fuchs L.H. Electrical conductivities of natural graphite crystals. *Phys. Rev.* **95**, No.1, 22-30. 1954.

-[6] Yu A., Roes I., Chen Z., et al. Ultrathin, transparent, and flexible graphene films for supercapacitor application. *Appl. Phys. Lett*. **96**, 253105. 2010.

-[7] Mahmood N., Zhang C., Hou Y., et al. Graphene-based nanocomposites for energy storage and conversion in lithium batteries, supercapacitors and fuel cells. *J. Mater. Chem. A.* **2**, 15-32. 2014.

-[8] Chung C., Kim Y.K., Min D.H., et al. Biomedical applications of graphene and graphene oxide. *Acc. Chem. Res.* **46**, No.10, 2211-2224. 2013.

-[9] kenner G.H., Williams W.S., Lovell J.E., et al. Two-year biocompatibility of ORNL graphite. *J. Biomed. Mater. Res. Symposium*. **6**, 67-72. 1975.

-[10] Pinto A.M., Gonçalves I.C. and Magalhaes F.D. Graphene-based materials biocompatibility: A review. *Colloids Surf. B*. **111**, 188– 202. 2013.

-[11] Stankovich S., Dikin D.A., Ruoff R., et al. Graphene-based composite materials. *Nature*. **442**, 282-286. 2006.

-[12] Goyal R.K., Samant S.D., Kadam A., et al. Electrical properties of polymer/expanded graphite nanocomposites with low percolation. *J. Phys. D: Appl. Phys*. **43**, 365404 (7pp). 2010.

-[13] Kovtyukhova N,I., Ollivier P.J., Gorchinskiy A.D., et al. Layer-by-layer assembly of ultrathin composite films from micron-sized graphite oxide sheets and polycations. *Chem. Mater.* **11**, 771-778. 1999.

-[14] Luo X., Weaver C.L., Cui X.T., et al. Pure graphene oxide doped conducting polymer nanocomposite for bio-interfacing. *J. Mater. Chem. B*. **1**, 1340-1348. 2013.

-[15] Shim J.H., Kim J.E., Lee Y., et al. Oxidation-state dependent electrocatalytic activity of iridium nanoparticles supported on graphene nanosheets. *Phys.Chem. Chem. Phys.* **15**, 15365-15370. 2013.

-[16] Tobias G., Shao L., Green M.L.H., et al. Enhanced sidewall functionalization of single-wall carbon nanotubes using nitric acid. *J. Nanosci. Nanotechnol*. **9**, 6072-6077. 2009.

-[17] He H., Klinowski J., Lerf A., et al. A new structural model for graphite oxide. *Chem. Phys. Lett.* **287**, 53–56. 1998.

-[18] Szabó T., Berkesi O., Dékány I., et al. Evolution of surface functional groups in a series of progressively oxidized graphite oxides. *Chem. Mater*. **18**, 2740-2749.2006.

-[19] Davis D.W. and Shirley D.A. The prediction of core-level binding-energy shifts from CNDO molecular orbitals. *J. Electron. Spectrosc. Relat. Phenom*. **3**, No.2, 137-163. 1974.

-[20] Yumitori S. Correlation of C1s chemical state intensities with the O1s intensity in the XPS analysis of anodically oxidized glass-like carbon samples. *J. Mat. Sci.* **35**, 139-146. 2000.

-[21] Jeong H.K., Colakerol L., Lee Y.H., et al. Unoccupied electronic states in graphite oxides. *Chem. Phys. Lett*. **460**, 499-502. 2008.

-[22] Hummers W.S. and Offeman R.E. Preparation of graphitic oxide. *J. Am. Chem. Soc.* **80**, No.6, 1339–1339. 1958.

-[23] Dreyer D.R., Park S., Ruoff R.S., et al. The chemistry of graphene oxide. *Chem. Soc. Rev.* **39**, 228–240. 2010.

-[24] Wei D., Liu Y., Yu G., et al. Synthesis of N-doped graphene by chemical vapor deposition and its electrical properties. *Nano Lett.* **9**, No.5, 1752-1758. 2009.

-[25] Wang X., Li X., Dai H., et al. N-doping of graphene through electrothermal reactions with ammonia. *Science*. **324**, 768-771. 2009.

-[26] Qiu Y., Zhang X. and Yang S. High performance supercapacitors based on highly conductive nitrogen-doped graphene sheets. *Phys. Chem. Chem. Phys*. **13**, 12554–12558. 2011.

-[27] Qu L., Liu Y., Dai L., et al. Nitrogen-doped graphene as efficient metal-free electrocatalyst for oxygen reduction in fuel cells. *ACS Nano*. **4**, No.3, 1321-1326. 2010.

-[28] Shao Y., Zhang S., Lin Y., et al. Nitrogen-doped graphene and its electrochemical applications. *J. Mater. Chem*. **20**, 7491–7496. 2010.

-[29] Shao Y., Sui J., Gao Y., et al. Nitrogen-doped carbon nanostructures and their composites as catalytic materials for proton exchange membrane fuel cell. *Appl. Catal. B*. **79**, 89-99. 2008.

-[30] Carrero-Sánchez J.C., Elías A.L., Terrones M., et al. Biocompatibility and toxicological studies of carbon nanotubes doped with nitrogen. *Nano Lett*. **6**, No.8, 1609-1616. 2006.

-[31] Matter P.H., Zhang L. and Ozkan U.S. The role of nanostructure in nitrogen-containing carbon catalysts for the oxygen reduction reaction. *J. Catal*. **239**, 83–96. 2006.

-[32] Vovk E.I., Turksoy A., Ozensoy E., et al. Interactive surface chemistry of CO_2 and NO_2 on metal oxide surfaces: competition for catalytic adsorption sites and reactivity. *J. Phys. Chem. C.* **117**, 7713−7720. 2013.

-[33] Rand M.J. and Li C.G. Nitric oxide as neurotransmitter in peripheral nerves: Nature of transmitter and mechanism of transmission. *Annu. Rev. Physiol*. **57**, 659-682. 1995.

-[34] Bult H., Boeckxstaens G.E., Herman A.G., et al. Nitric oxide as an inhibitory non-adrenergic non-cholinergic neurotransmitter. *Nature*. **345**, 346-347. 1990.

-[35] Jeong H.M., Lee J.W., Choi J.W., et al. Nitrogen-doped graphene for high-performance ultracapacitors and the importance of nitrogen-doped sites at basal planes. *Nano Lett*. **11**, 2472-2477. 2011.

Chapter 7

Biocompatibility and Cell Behavior

In this chapter, evaluation of the biocompatibility of some of the materials synthesized is done. A brief study of the wettability and the changes produced in the coating surface after poly-L-Lysine (PLL) adhesion is performed, in order to correlate the subsequent cell behavior.

Then, the results obtained for neural cultures grown on IrOx, IrOx-CNTs and IPC coatings as substrates are exposed, showing good development and functional response to a depolarizing stimulus. Thus, indicating that neurons grown on IrOx-CNTs as well as IrOx, can effectively survive and differentiate into synaptic competent glutamatergic and GABAergic neurons. Also, co-cultures of astrocytes-neurons on IPC coatings are introduced, as a new surface functionalization method to increase biocompatibility in electrodes, without decrease electrochemical responses. All these biological studies have been done in the *Instituto de Investigaciones Biomédicas de Barcelona* (IibB), by the group of Neurochemistry and Neuropharmacology.

Also, the stability of the materials after the culture conditions is demonstrated, not observing delamination or detachment of the material.

Finally, the most recent experiments are mentioned: first attempts to apply electric fields to neural cells *in vivo*.

7.1 Neural Interfaces and Biocompatibility

The main objective for the new material synthesis is the development of new electrodes, with high biocompatibility, suitable for neural system. For this purpose, the biocompatibility of IrOx-CNTs and IPC hybrid materials has been tested, using the coatings as support to seed and grow neural cells onto them, with the final aim of studying cell behavior and development.

Biocompatibility depends on the material's toxicity but mainly, on the interface between the material surface and cells [1,2]. The chemical and topographical characteristics of surfaces have important effects on the response observed for cells and tissues to synthetic materials. For this reason it is important to consider surface properties of the materials under study. In this sense, modulation of chemical surface and roughness of biomaterials has been proposed in order to improve the performance in biotechnological applications [3,4].

An usual method to enhance the biocompatibility of cellular substrates is the surface chemical modification or the adsorption of particular molecules, which act as adhesive phase between the material and the cells. For neurons, these molecules are usually proteins as laminin, fibronectin and collagen, or simpler polypeptides as polylysine [5-9]. Cell-matrix adhesive interactions provide tissue structure and generate anchorage forces that mediate cell spreading and migration, neurite extension, muscle-cell contraction or cytokinesis among other processes. Therefore, the development of biointerfaces that elicit specific cell-adhesive responses is central to numerous biomedical applications.

Poly-L-Lysine (PLL) is a synthetic polypeptide usually utilized in neural cultures, and it has been observed that cells attach firmly and spread in surfaces coated with this adhesion phase [7,10]. PLL is formed by lysine residues, which at physiological pH are positively charged (Figure 7.1A). The polycationic polylysine molecules can strongly absorb to solid surfaces, being the cationic sites the responsible to interact with the negatively charged cell membranes (Figure 7.1B).

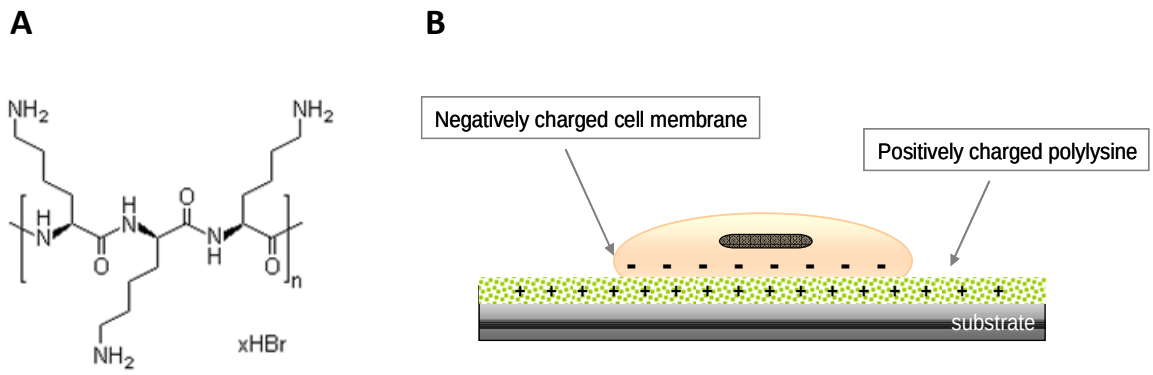

Figure 7.1. A) Poly-L-Lysine (PLL) structure. B) Schematic representation of the interaction between the positively charged PLL coating and the negatively charged cell membrane.

Previous experiments done in our laboratory demonstrated how PLL can be adsorbed in different amount depending on the material substrate. It was found that larger quantities of poly-L-lysine were adsorbed in IrOx than in polymeric coatings (PEDOT-PSS in this case). The complex process of cell/protein adhesion in surfaces is still under study, but it is known as the result of one or more of the following interactions: Van der Waals, electrostatic, hydrogen bonding or hydrophobic effects [11]. Thus, the experimentally high affinity of IrOx for PLL, can be related with different aspects as chemical affinity, hydrophobic effects (carbon chains in the polypeptide have high affinity with IrOx hydrophobic surfaces [12]) and/or electrostatic effects. In this sense, the high content of hydroxyls in IrOx, makes the surface more electronegative in aqueous solutions, increasing the attraction with the positively charged polypeptide.

In conclusion, surface properties as chemical composition, roughness or hydrophilicity can modify the adhesion phase between the material and cells, having an effect on the resulting cellular survival. Therefore, a study of these surface properties is important for further correlation with cell response.

7.2 Hydrophilicity and Roughness Changes with PLL Adhesion

Surface wettability has been measured by contact angle, to study and compare different materials [13]. Contact angle results obtained for the coatings under study (IrOx, IrOx-CNTs and IPC) are shown in Figure 7.2. For 50-cycle IrOx samples, the angle obtained is around 90º, which corresponds with the limit hydrophobicity observed in our samples. Also this behavior is observed for thinner hybrid IrOx-CNTs coatings (10 cycles) however, as the thickness increases, this angle drops: the coating becomes totally hydrophilic. The same tendency is observed in IPC coatings, samples synthesized at 10 cycles present a value near those obtained for PEDOT-PSS coatings [14] however, 25-cycle samples shown a completely hydrophilic behavior, which presumably is related with microstructure changes (porosity and roughness) observed in thicker films. Hence, considering the possible influence of PLL adsorption with the hydrophilicity of the coatings and the tendency observed in previous works, the adsorption of PLL will be different in thicker hybrid coatings (IrOx-CNTs and IPC) in comparison with thinner ones, which would influence cell cultures.

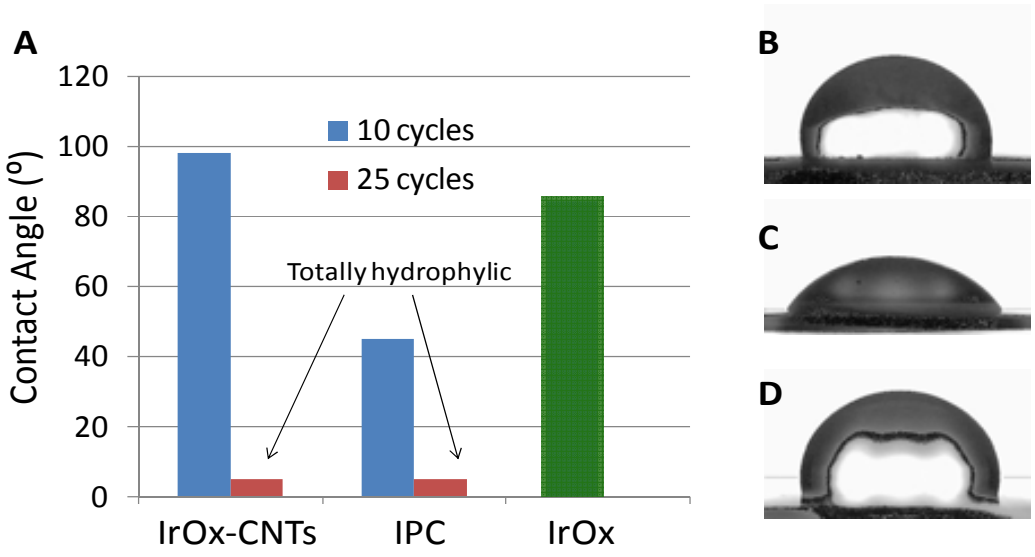

Figure 7.2. Contact angle of the samples under study. A) IrOx-CNTs and IPC synthesized at different cycles and 50-cycles IrOx. B) 10-cycle IrOx-CNTs, C) 10-cycle IPC and D) 50-cycle IrOx.

Once the PLL is adsorbed on the surface, the influence of this polypeptide layer in the roughness has also been studied in order to correlate it with cellular response. Figure 7.3 shows the modulation in coatings roughness when a PLL (45 µg/mL) is adsorbed on the surface. For IrOx coatings, with initial smooth surface (3-5 nm), the adsorption of PLL considerably increases the roughness. However, for IrOx-CNTs coatings, which are very rough (~0.55 µm), the addition of poly-L-lysine decreases the roughness, presumably because the polypeptide is filling the porous structure of the hybrid, leveling the surface. For IrOx-PEDOT-CNTs coatings, the adsorption of PLL also increases considerably the roughness, but in this case, also the tendency of polymers to swell in solution has to be considered.

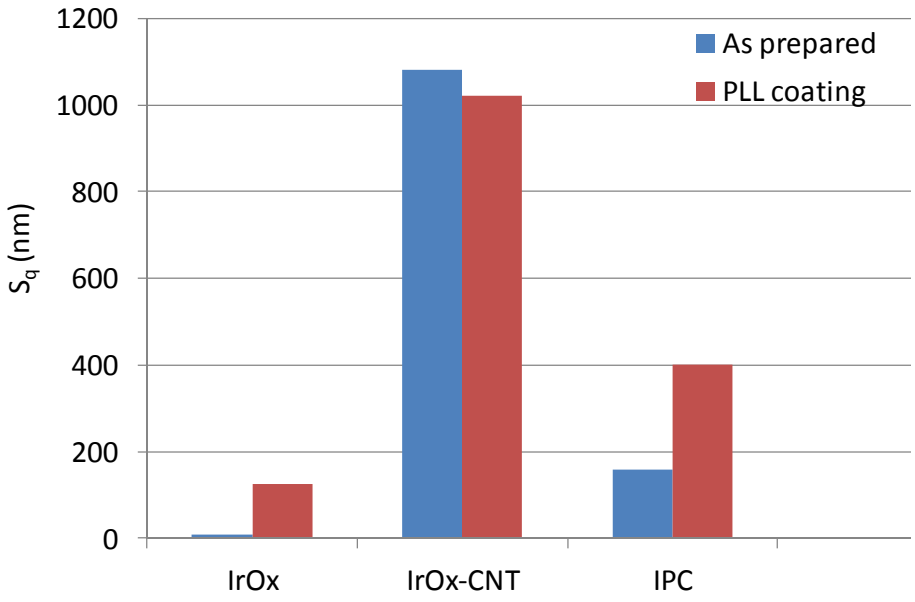

Figure 7.3. Effect of the PLL adhesion in the roughness of different surfaces. 50-cycle IrOx, 25-cycle IrOx-CNTs and 25-cycle IPC samples have been evaluated by Confocal 3D microscopy.

7.3 Neural Cultures

Primary cultures of cortical neurons were prepared following the indications shown in Chapter 2. Cell suspension from the cerebral cortex of mice embryos were seeded onto the materials (115000 cells/cm^2) and under this work conditions, 99% of the

cells grown were neurons. After 5 days in vitro (DIV), neurons were fixed with paraformaldehyde (PFA) and stained by immunocytochemistry, using tau antibody to stain the cytoskeleton and Bis-benzimide for nuclear staining. Cell viability was assessed by counting the number of cells effectively stained with tau antibody with normal appearance nuclei (non-apoptotic). The quantification obtained for IrOx-CNTs, IPC and IrOx samples, is shown in Figure 7.4, together with the obtained for borosilicate, the usual reference in this kind of cultures.

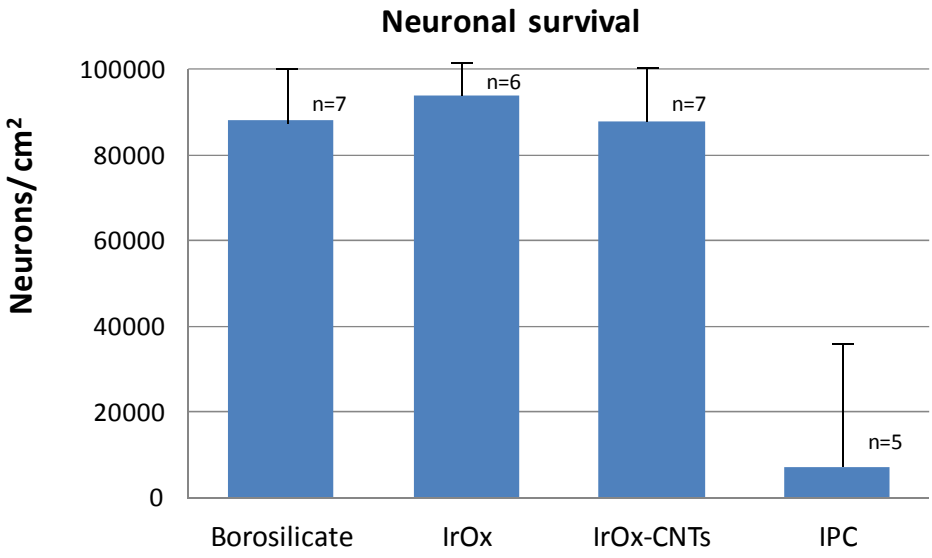

Figure 7.4. Neuronal survival after 5 DIV on borosilicate as control surface and on IrOx, IrOx-CNTs and IPC films. Bars represent the mean +/- standard error of cell counts of n independent cortical neuronal cultures. Data obtained in the IibB by M. Lichtenstein.

After 5 DIV the number of neurons grown on the IrOx-CNTs coatings was very similar to that in IrOx and borosilicate substrates, used as reference. However, for IPC samples the cell survival and reproducibility (observed in the error bar length) is considerably lower. The minor reproducibility associated to this type of polymeric PEDOT materials, has been observed before [14,15].

The chemical factors influencing the neural response are no trivial. IrOx and IrOx-CNTs have a very similar surface composition as shown in XPS results (Chapter 4), but very different roughness being the hybrid almost 2 orders of magnitude rougher as compared with bare IrOx (Figure 4.12). Also, the hydrophilicity of 25-cycle IrOx-CNTs hybrids is considerably larger than that for bare IrOx. However, the similar values for neuronal survival obtained for both materials, indicate that in this case, mainly the chemical aspects are playing a decisive role in the cellular development, and neither the roughness nor the hydrophilicity are crucial.

Figure 7.5 shows images of stained neural cells grown in different substrates. In IrOx and IrOx-CNTs films, the survival is high, cells are well adhered and the neuronal networks are well established, indicating healthy growth in those substrates and no differences with borosilicate used as reference. The morphology of neurons was indistinguishable on the IrOx and IrOx-CNTs substrates, demonstrating full compatibility of the IrOx-CNTs hybrid substrates for the growing and differentiation of neuronal cells. In addition, even in high density cultures, it has been observed how cells are highly spread and no tendency to form aggregates is appreciated, which is indicative of the "comfort" of neurons on the tested materials.

The morphology of the cells grown in IPC substrates is similar, but the total number of cells is considerably lower. Also, neurons are not homogenously spread in the entire coating, suggesting the existence of different areas in the same sample, where cells "feel" better. However, when it is compared with PEDOT-PSS (another polymeric material highly studied by its electrochemical properties as neural electrode [16,17]), it is observed how cell survival in IPC is slightly enhanced under the same conditions, although the irreproducibility of the measurements does not allow to have a specific quantification [14]. The low cell survival in PEDOT-PSS films were presumably attributed to the PSS surfactant used as dopant, which may interact with the cell membrane in some way and decrease the biocompatibility. In this sense, previously in our laboratory, and some others authors, have demonstrated that in terms of biocompatibility, polymers doped with "biological molecules" as aminoacids or peptides have worked much better than those doped with PSS or other surfactants

[15,18]. These results indicate that biocompatibility in PEDOT polymeric coatings seems to be highly dependent on the dopant. On the other hand, CNTs or IrOx nanoparticles have not show any toxicity in coatings (as demonstrated in previous chapters), suggesting that the low neural survival in IPC coatings has to be related with the resulting material properties after the mixture of the counterparts.

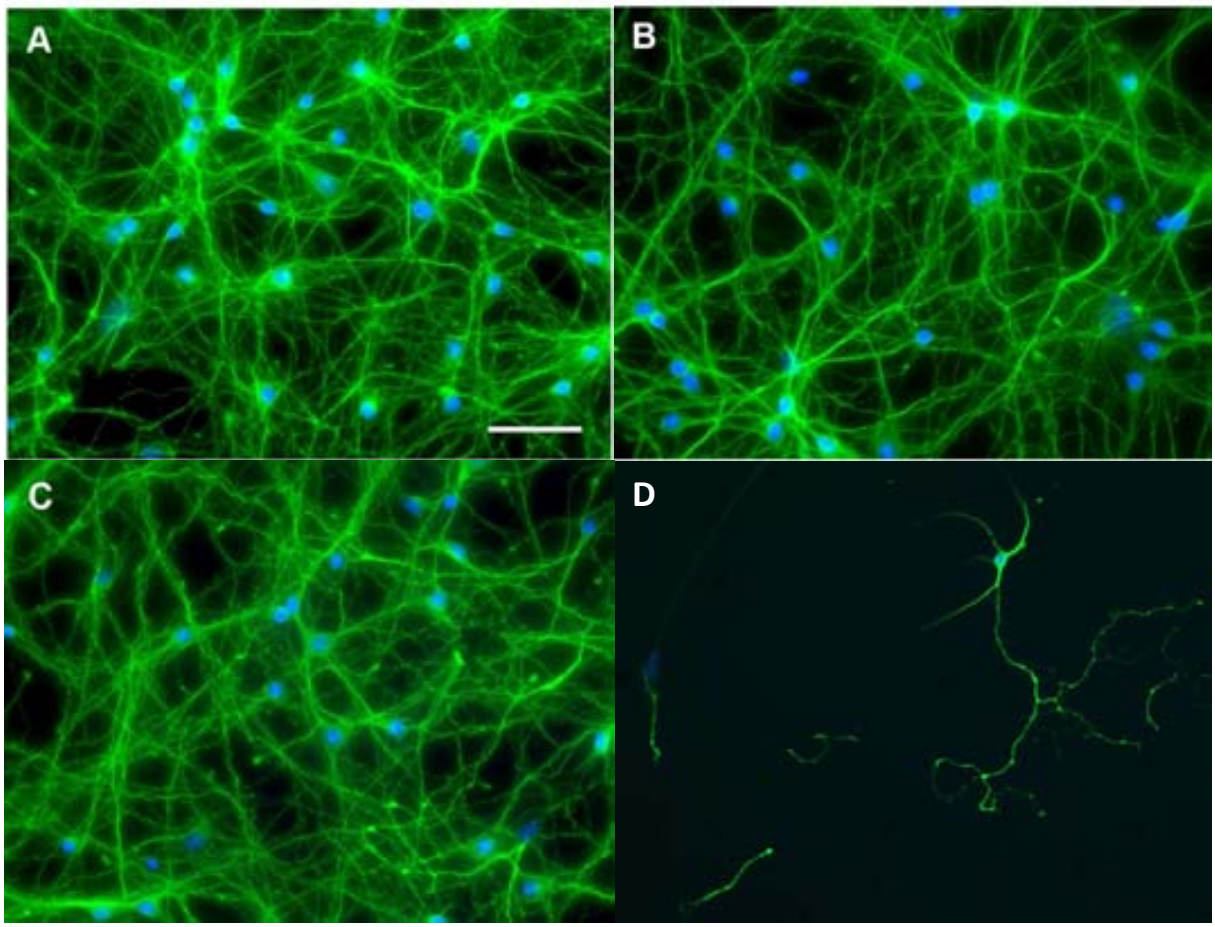

Figure 7.5. Representative fluorescent microphotographs of cortical neurons (115000 cells/cm^2) on different materials cultured 5 DIV. A) Borosilicate, B) IrOx, C) IrOx-CNTs and D) IPC. Cells membranes were stained with Tau (green) and nuclei with Hoescht (Bis-benzimide) (blue). Scale bar = 50 µm. Images were taken in the IibB by M. Lichtenstein.

These results suggest that IrOx-CNTs hybrid coatings as substrate materials are not citotoxic and support healthy cell attachment and neurite outgrowth, as previously

shown for IrOx [12]. The immobilization of CNTs in the hybrid electrode by oxide encapsulation avoids the diffusion into the ECM or the contact with the tissues, enhancing the biocompatibility and preventing the toxicity found in respiratory exposure or tissue accumulation in large doses [19-22]. For IPC coatings, although no toxicity has been observed for PEDOT itself, the biocompatibility is highly dependent on the dopant. Also, the heterogeneous surface of the polymeric films may decrease the reproducibility of cell cultures. However, despite these observations, the actual reason for the low cell survival on IPC coatings is not still known.

7.4 Viability and Functional Response of Neurons Supported on the Materials

The communication between neurons is carried out by action potentials. After the arrival of an action potential at the synapse, neurons undergo depolarization resulting in the release of neurotransmitters and the eventual activation of receptors that will trigger a physiological response. In vitro, neuronal depolarization can be achieved by increasing the extracellular K^+ concentration in the media, and subsequently the cellular membrane potential is changed. As a consequence of this external action, neurons release neurotransmitters to the extracellular media, which can be quantified by HPLC. In this case, these main excitatory and inhibitory neurotransmitters detected are glutamate and GABA, respectively.

Primary cortical neurons were grown on borosilicate (as reference), IrOx and IrOx-CNTs substrates for 6 DIV and consecutively exposed to basal conditions, that consists in Hank's solution containing 5 mM K^+, and to a depolarizing stimulus, with the same solution but higher potassium concentration (90 mM K^+). The resulting concentration of glutamate and GABA in both conditions was determined in the culture media and quantified (Figure 7.6).

The K90/K5 ratio of glutamate and GABA, which indicates changes in neurotransmitters concentration, in the culture media after and before the depolarizing stimulus was 2.4±0.4 and 2.3±0.4 respectively, for IrOx-CNTs material. It

was similar to that obtained for IrOx films (2.6±0.6 and 2.3±0.3, respectively) and for borosilicate coverslips (2.8±0.4 and 2.8±0.3, respectively), corroborating that neurons grown on IrOx-CNTs and IrOx substrates are functional and able to release glutamate and GABA in response to depolarization, as the concentration of these neurotransmitters is considerably increased.

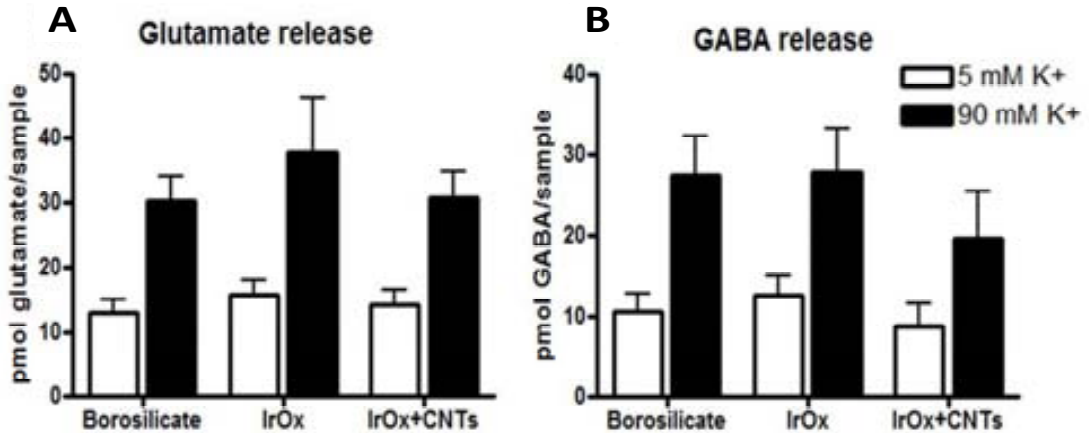

Figure 7.6. Glutamate (A) and GABA (B) release from cortical neurons. Cells were exposed to a basal solution (containing 5 mM K^+) or to a depolarizing solution (containing 90 mM K^+) to induce the release of neurotransmitters. Glutamate and GABA content in both solutions was determined by HPLC. Graphs show the mean +/- Standard Error of 6 independent experiments done in duplicate. Data obtained in the IibB by M. Lichtenstein.

Once glutamate and GABA neurotransmitters are released to the media, fast neuronal response is mediated by the activation of the postsynaptic membrane receptors NMDA-glutamate and $GABA_A$ (NMDAR and $GABA_AR$). Therefore, we examined whether the cultured neurons express these receptors. After performing immunocytochemistry to analyze the pattern of expression of both receptors, we show that neurons cultured on IrOx-CNTs expressed NMDAR and $GABA_AR$ (Figure 7.7 C and F) in the same way that cells cultured on IrOx (Figure 7.7 B and E) or on borosilicate (Figures 7.7 A and C). NMDAR (green, Figure 7.7 A–C) and $GABA_AR$ (green,

Figure 7.7 D–F) were expressed on the soma and neurites, giving the appearance of a ring around the neuronal nuclei (blue).

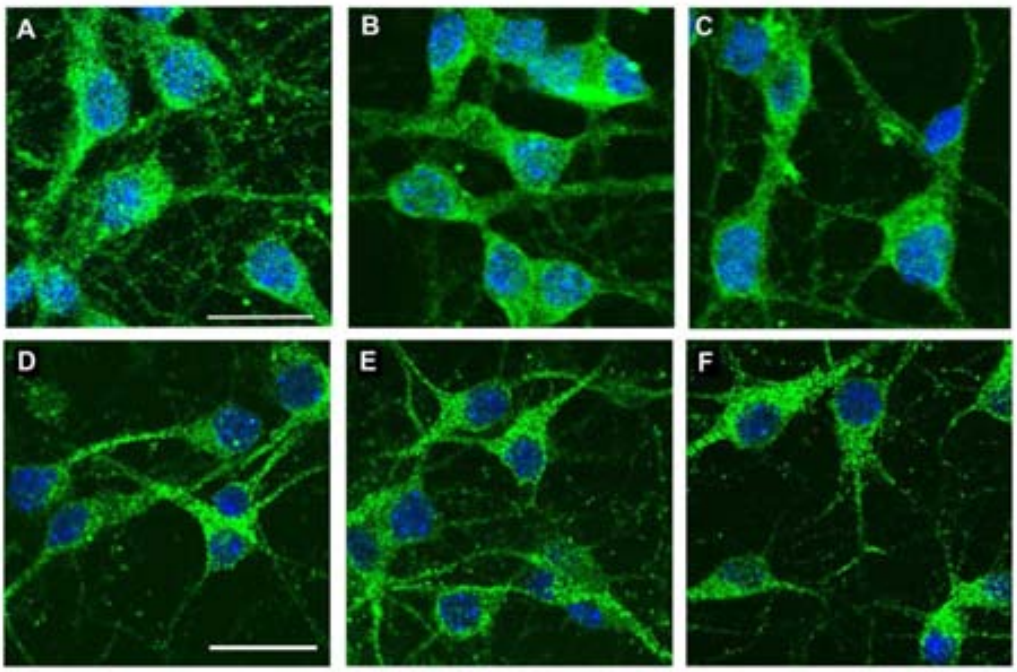

Figure 7.7. Glutamatergic and GABAergic phenotype of cultured cortical neurons. A–C) Expression of NMDA/glutamate and D-F) $GABA_A$ receptors. Confocal microphotographs of a representative cortical culture growing on Borosilicate (A,D), IrOx (B,E) and IrOx+CNT (C,F). Scale bar = 20 µm. NMDA and $GABA_A$ receptors are visualized in green and nuclei in blue. Images were taken in the IibB by M. Lichtenstein.

As mentioned before, neuronal communication in the brain is driven by the secretion of chemical messengers, namely neurotransmitters, and their reception in specific proteins (receptors). In these experiments, it has been demonstrated that neurons grown on IrOx or IrOx-CNTs have the complete machinery for these neuronal processes, so neurons keep functional. Furthermore this is the first time that the characterized IrOx films show their full biocompatibility, regarding brain excitatory (glutamatergic) and inhibitory (GABAergic) neurotransmission.

7.5 Co-Cultures of Astrocytes-Neurons

The low reproducibility and cell survival observed for IPC coatings when used as cell culture substrate induced the idea that the response may be cell dependent. Thus, we analyze the possibility of using a new cell culture model, consisting of astrocytes-neurons co-cultures. Astrocytes represent the 90% of the total cells in the central nervous system and, as mentioned in the Introduction Chapter, can play different roles as supporting neurons, providing the brain cyto-arquitecture. Thus, an initial astrocytes layer using the material as substrate can provide a more biologically compatible support for subsequent neurons development, in a culture model that is closer to *in vivo* and that is able to recapitulate neuron-astrocyte interactions.

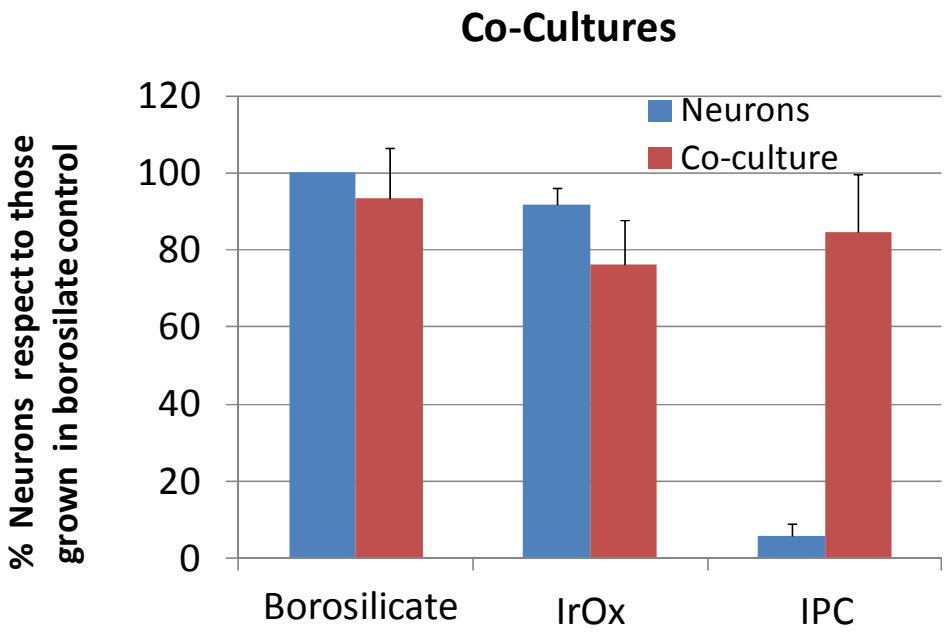

Figure 7.8. Neuronal survival after 5 DIV on borosilicate as control surface, IrOx and IPC films. Neurons: grown directly in the PLL-coated surface of the samples. Co-culture: neurons grown onto a previous astrocytes culture (2 weeks in vitro). Bars represent the mean +/- standard error of cell counts of 5 independent cortical neuronal cultures. Data obtained in the IibB by M. Lichtenstein.

Once astrocytes were seeded, grown and spread in the entire coating (usually it takes about 2 week *in vitro*), neurons were seeded onto this intial astrocytes monolayer. Figure 7.8 shows results of neurons survival seeded on PLL-coated IPC substrates, or when co-cultures are performed. IPC coatings, when PLL is used as adhesion layer, are not optimal for neuron survival; however, this survival can be increased considerably when a previous astrocyte layer acts as adhesion phase. The cell survival on IPC coatings is even higher than those obtained in co-cultures on IrOx, indicating that neurons prefer PLL-coated IrOx substrates to develop than astrocytes.

These results show the preference of neural cells to develop onto the astrocytes than onto the as prepared IPC material, even when PLL is adsorbed. Astrocytes are the natural environment where cells are grown, so the survival increase is expected. This outstanding increase in neural survival produced in co-cultures, yields to consider this method as surface “bio-functionalization” for biocompatibility enhancement.

In order to study if these astrocyte layer modify the IPC electrochemical behavior as electrode, CVs have been performed within the safe potential range for this kind of materials, -0.6 V to 0.6 V [23], at scan rate of 10 mV/s and in PBS (pH=7.4). Results are shown in Figure 7.9.

The curves obtained for bare IPC and astrocytes-coated IPC electrodes do not present significant differences. The shape of the curves is similar and only a minor increase in the capacitance is observed when comparing bare IPC with IPC + astrocytes (2 or 3 weeks) and slightly larger in the co-culture, as a consequence of the thickness change. The identical curve obtained for IPC as electrode, coated with astrocytes grown during 2 and 3 weeks, must be due to the fact that both astrocytes coatings are the same, suggesting that two weeks is enough for a total coating of the surface and cells cannot continue proliferating.

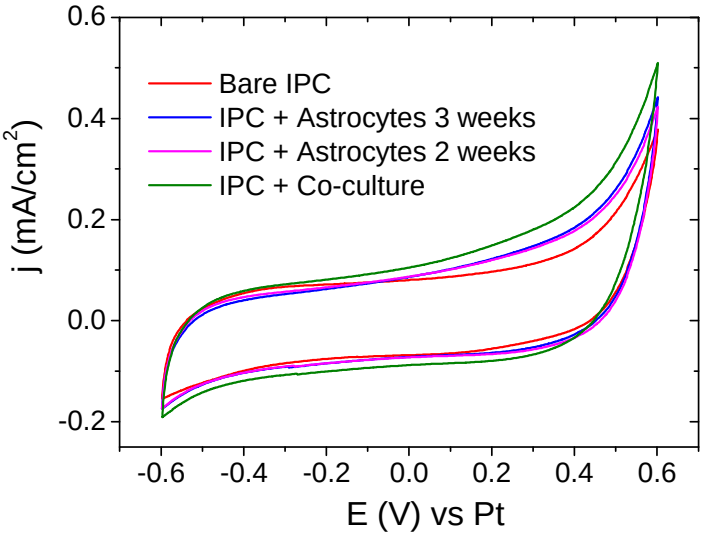

Figure 7.9. Cyclic voltammetries performed at 10 mV/s in PBS (pH=7.4). Different coatings were used as working electrode: bare IPC, IPC coated with astrocytes grown during 2 and 3 weeks in vitro and IPC coated by astrocytes (2 weeks in vitro) + cortical neurons (5 DIV) grown onto them.

7.6 Stability of the Coatings After Cell Cultures

In order to evaluate the changes produced in the material surface under the conditions of cleaning, sterilizing and cell growth during 5 DIV, substrates used for cell growth, were evaluated by SEM (Figure 7.10). The images were taken in high vacuum conditions, without observing any damage due to the low pressure. Low voltage (5 kV) was used for high detail of the surface components, without damaging the cells.

The images confirm the stability of the material, since the surface is not modified by sterilizing processes or cell attachment itself. The appearance and the granulated surface are very similar to those obtained for bare, as prepared materials; neither new cracks nor surface alterations are observed. Cell spread is observed for all the materials, although in some cases can be influenced by the substrate roughness.

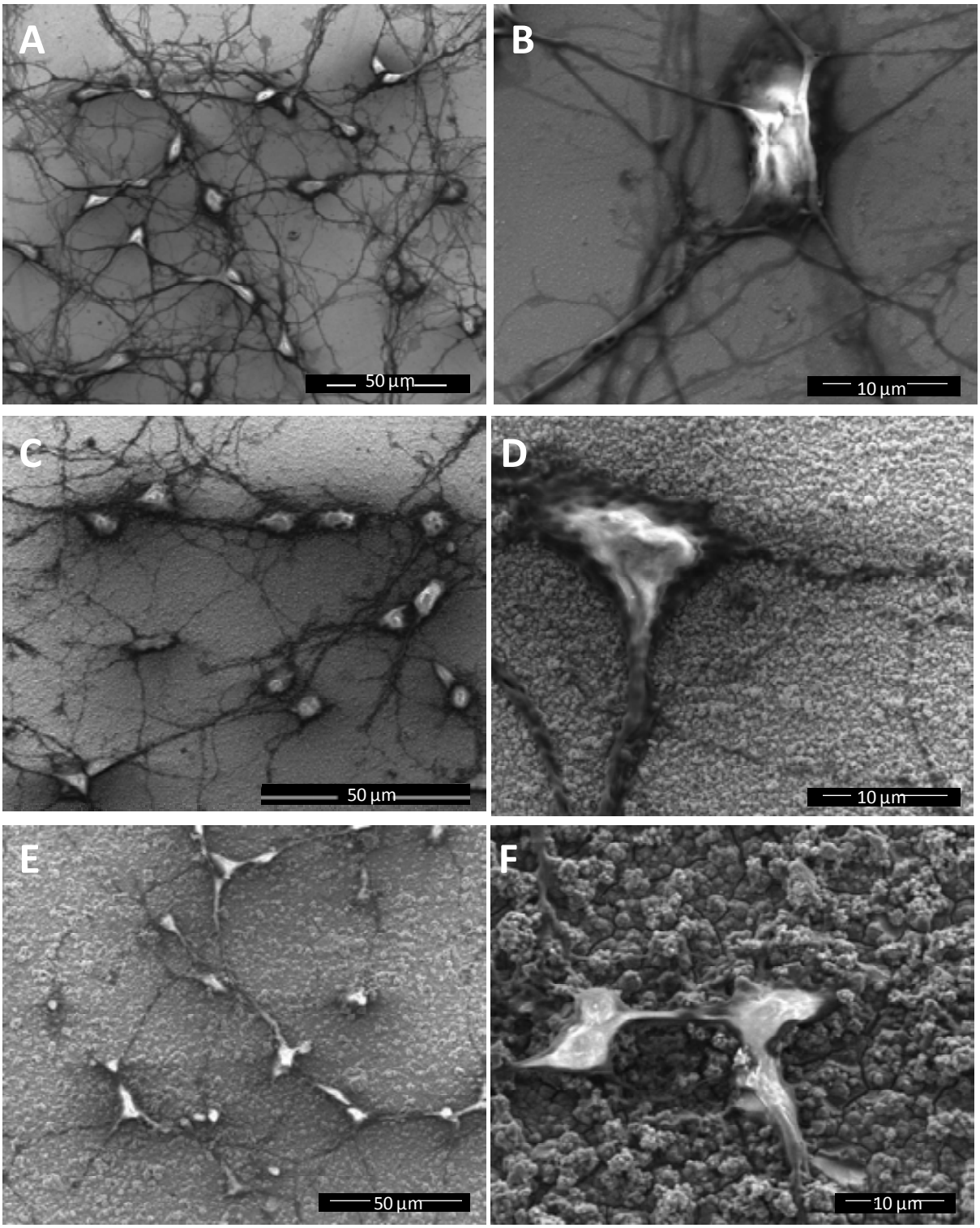

Figure 7.10. SEM images of the cells fixed with glutaraldehyde supported on A-B) bare IrOx, C-D) IrOx-CNTs and E-F) IPC coatings. Images were taken at 5 kV.

7.7 Application of Electric Fields to Neural Cells

The final aim of the preparation of electroactive coatings is their use as electrodes for neural stimulation or modulation. In particular, the objective is to create electrodes which apply slow dc electric currents to neurons, to achieve the best faradaic behavior of the materials. Also, this type of electrostimulation has shown to be optimal for modulation, inducing neurites elongation or polarization, which is desirable in spinal cord lesions [24,25].

Initial electric field (EFs) application experiments have been attempted in order to evaluate cell and electrode response, and to find a safe and reproducible protocol for future applications. The electrochemical cell proposed for these first tests is shown in Figure 7.14. It consists in a soda-lime glass coated with Pt but with a gap in the middle, which remains non conductive. Then, conducting Pt-sides are used to deposit the electroactive material, which would be the cathode and anode of the electrochemical cell. As container of the saline solution and to separate the two electrodes, a plastic cell culture-slide is attached to the substrate with non-toxic silicone. The electric contacts were done with Cu wires, silver paint and conducting silicone to seal the contacts. Finally, a salt bridge made with agar-agar completes the circuit. The system described tolerates high temperatures required for sterilizing.

The electrochemical cell is previously sterilized, and then, primary cortical neurons are seeded and grown into it. After 5 DIV, the electrochemical cell is connected with a potentiostat and neurons are subject to dc current pulses. Some protocols applying dc current are being studied, limiting the total charge based on the CSC of the material, although ac currents at low scan rates have been recently proposed in order to prolong the electrode practical use.

Experimental parameters as buffer solution to maintain the cells, current protocols, stimulation chamber, etc… are still being tested, however, some experiments have been already performed, using as electroactive materials IrOx and a polymeric phase (PEDOT-PPY with lysine [15]).

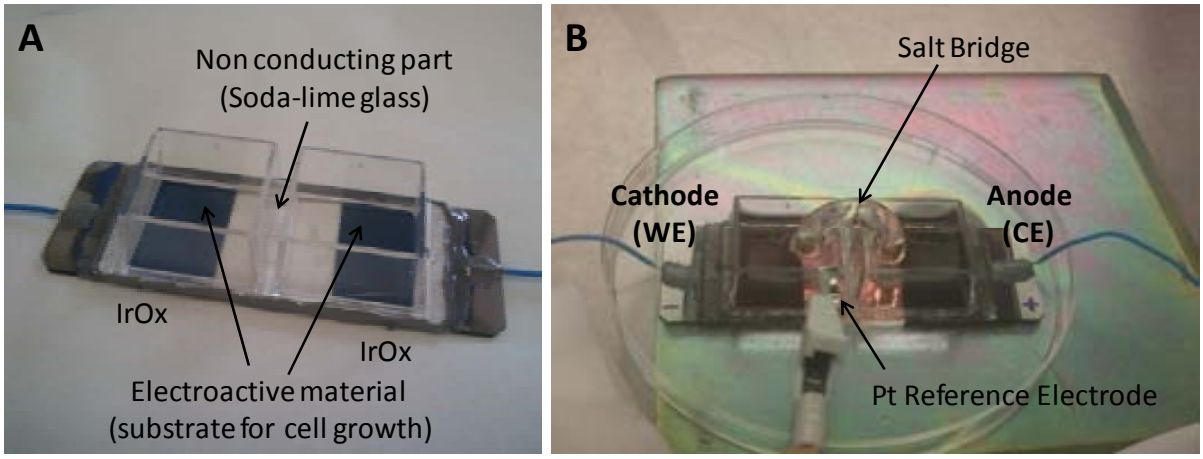

Figure 7.14. A) Electrochemical cell for EFs application to neurons, and B) Complete electrochemical system in which the cathode and anode are seeded with cortical neurons and connected to the potentiostat.

Initial results obtained after the application of cathodic dc currents using IrOx as electrode have yielded some observations. In first place, after electric field application, only cells in the cathode are alive. In particular, only cells seeded on the non-conducting soda-lime glass part have good appearance, which presumably indicates that during the de current pulse, toxic radicals are being formed in the anode, with the consequent cell death. Also, when the total charge produced during the pulse exceeds the inherent material capacity at the cathode, neurons die, indicating that when the material is completely reduced, other side reactions can yield another type of radicals, which can damage the cells. In this particular case, the application of an ac current can minimize the neurons alteration.

Future electric field applications involve the artificial formation of a “scratch” in the cellular culture, as a model to study how the presence of electric fields can induce the migration and closing of the artificial wound produced in the *in vitro* culture.

7.8. Conclusions

- The biocompatibility of hybrid IrOx-CNTs and IPC coatings has been studied in terms of hydrophilicity, roughness and PLL adhesion, in comparison with previously reported IrOx films. The results shown relevant differences among the materials. IrOx has a smooth surface and is highly hydrophobic, however, it has been demonstrated large adhesion of PLL, which considerably increase its roughness. On the other hand, 25-cycle hybrids coatings have rougher surfaces and are hydrophilic.

- Cell cultures performed in the hybrid coatings as substrate, show very good neuronal survival and development for IrOx and IrOx-CNTs coatings, similar to those values obtained for borosilicate, used as reference. These results, indicates that mostly chemical aspects are influencing cell response, as IrOx and IrOx-CNTs have very similar chemical composition but different roughness or wettability. For IPC coatings the cellular survival is poor and irreproducible, as previously reported for PEDOT-PSS coatings.

- After an induced depolarization, consisting in a K^+ concentration increase in the media, cells grown in IrOx and IrOx-CNTs substrates keep functional, releasing glutamate and GABA neurotransmitters, which have been quantified to observe the corresponding increase in comparison to basal conditions.

- To increase the biocompatibility and neural survival of IPC coatings a co-culture method has been proposed. It consists in the initial culture of an astrocytes layer on the ICP substrate and a posterior seeding on neurons onto them. This protocol increases considerably the neurons survival, and can be presented as a novel method to improve biocompatibility in general neural electrodes, as no changes in electrochemical performance are observed.

- The stability of the coatings after sterilization and cell culture steps have been demonstrated by SEM images of the coatings, with no additional cracks or delamination.

- Finally, the first attempt of electric field applications to neurons is reported, using the materials under study as cathode and anode.

7.8. References

-[1] García A.J. Interfaces to control cell-biomaterial adhesive interactions. *Adv. Polymer Sci*. **203**, 171-190. 2006.

-[2] Rao S.S. and Winter J.O. Adhesion molecule-modified biomaterials for neural tissue engineering. *Front. Neuroeng*. **2**, No.6, 1-14. 2009.

-[3] Yeniyol S., Bölükbasi N., Ozdemir T., et al. Relative contributions of surface roughness and crystalline structure to the biocompatibility of titanium nitride and titanium oxide coatings deposited by PVD and TPS coatings. *ISRN Biomaterials*. **2013**, 1-9. 2013.

-[4] Hossain M.M. and Gao W. How is the surface treatments influence on the roughness of biocompatibility? *Trends Biomater. Artif. Organs*. **22**, No.3, 144-157. 2008.

-[5] Santini M.T., Cametti C., Donelli G., et al. Polylysine induces changes in membrane electrical properties of K562 cells. *J. Biomed. Mater. Res*. **35**, 165-174. 1997.

-[6] Richert L., Arntz Y., Picart C., et al. pH dependent growth of poly(L-Lysine)/poly(L-glutamic) acid multilayer films and their cell adhesion properties. *Surf. Sci*. **570**, 13-29. 2004.

-[7] Mazia D., Schatten G. and Sale W. Adhesion of cells to surface coated with polylysine. *J. Cell Biol*. **66**, 198-200. 1975.

-[8] Turner D.C., Flier L.A. and Carbonetto S. Indentification of a cell-surface protein involved in PC12 cell-substratum adhesion and neurite outgrowth on laminin and collagen. *J. Neurosci*. **9**, 3287-3296. 1989.

-[9] Venstrom K. and Reichardt L. β_8 integrins mediate interactions of chick Sensory neurons with laminin-1, collagen IV, and fibronectin. *Mol. Biol.Cell*. **6**, 419-431. 1995.

-[10] Yavin E. and Yavin Z. Attachment and culture of dissociated cells from rat embryo cerebral hemispheres on polylysine-coated surface. *J. Cell Biol*. **62**, 540-546. 1974.

-[11] Malmsten M. Formation of adsorbed protein layers. *J. Colloid Inteface Sci*. **207**, 186-199. 1998.

-[12] Cruz A. M., Abad LL., Casañ-Pastor N. et al. Iridium oxohydroxide, a significant member in the family of iridium oxides. Stoichiometry, characterization, and implications in bioelectrodes. *J. Phys. Chem. C*. **116**, 5155−5168. 2012.

-[13] Lee J.H., Khang G., Lee H.B., et al. Interaction of different types of cells on polymer surfaces with wettability gradient. *J. Colloid Inteface Sci.* **205**, 323-330. 1998.

-[14] Moral-Vico J. Materiales electroactivos poliméricos e híbridos como sustrato de crecimiento neuronal. Ph.D Thesis, Universidad Autónoma de Barcelona, Spain. 2012.

-[15] Moral-Vico J., Carretero N.M., Casañ-Pastor N., et al. Dynamic electrodeposition of aminoacid-polypyrrole on aminoacid-PEDOT substrates: Conducting polymer bilayers as electrodes in neural systems. *Electrochim. Acta*. **111**, 250-260. 2013.

-[16] Collazos-Castro J.E., Polo J.L., García-Rama C., et al. Bioelectrochemical control of neural cell development on conducting polymers. Biomaterials. 31, 9244-9255. 2010.

-[17] Cui X. and Martin D.C. Electrochemical deposition and characterization of poly (3,4-ethylenedioxythiophene) on neural microelectrode arrays. *Sens. Actuators, B.* **89**, 92-102. 2003.

-[18] Asplund M., von Holst H. and Inganas O. Composite biomolecule/PEDOT materials for neural electrodes. *Biointerphases*. **3**, No.3, 83-93. 2008.

-[19] Lam C.W., James J.T., Hunter R.L., et al. A review of carbon nanotube toxicity and assessment of potential occupational and environmental health risks. Crit*. Rev. Toxicol*. **36**, 189-217. 2006.

-[20] Jain A.K., Mehra N.K., Jain N. K., et al. Carbon nanotubes and their toxicity. *Nanotoxicology*. **1**, No.3, 167-197. 2007.

-[21] Lam C.W., James J.T., Hunter R.L., et al. Pulmonary toxicity of single-wall carbon nanotubes in mice 7 and 90 days after intratracheal instillation. *Toxicol. Sci*. **77**, 126-134. 2004.

-[22] Firme C.P. and Bandaru P.R. Tocixity issues in the application of carbon nanotubes to biological systems. *Nanomedicine: NBM*. **6**, 245-256. 2010.

-[23] Cogan S.F. Neural stimulation and recording electrodes. *Annu. Rev. Biomed. Eng*. **10**, 275-309. 2008.

-[24] Borgens R.B. Electrically-mediated regeneration and guidance of adult mammalian spinal axons into polymeric channels. *Neuroscience*. **91**, 251-264. 1999.

-[25] Shapiro S., Borgens R., Nelson, P. et al. Oscillating field stimulation for complete spinal cord injury in humans: a phase 1 trial. *J. Neurosurg. Spine.* **2**, 3-10. 2005.

Chapter 8

Final Conclusions

Considering the experimental results obtained in this thesis and the posterior analysis of the data, some conclusions can be formulated.

- The satisfactory electrochemical synthesis of IrOx-Carbon based hybrids has been achieved with several carbonaceous species, as carbon nanotubes, graphite or graphene (several layered graphene). Even a polymeric tri-hybrid, IrOx-PEDOT-CNTs, has been synthesized. The potentiodynamic synthesis, yield homogeneous and well adhered coatings, with thickness and roughness modulated by the charge used during the synthesis.

- IrOx with and without oxalate pre-deposition solutions and their respective coatings, have been studied as reference material for hybrids. The alkaline solutions show the presence of IrOx nanoparticles (as seen in TEM and DLS results), which agree with the condensation of iridium species during the aging step, to form oligomers/nanoparticles with mixed valence. These nanoparticles are more dispersed when a complexing agent, as oxalate, is present in the media, indicating stabilization.

- The synthesis mechanism for IrOx coatings has been considered as a dynamic deposition which involves a complex mechanism as shown by quartz crystal microbalance studies. It the redox oxidation of OH^-/H_2O, with the consequent pH decrease, and as a consequence, the flocculation of IrOx oligomers/nanoparticles in the surface of the electrode. Subsequent reactions of condensation can occur in the deposited iridium oxide, involving intercalation/deintercalation of cationic and anionic (K^+ and OH^-) species. Also catalytic effects are observed by the large charge used during preparation. This mechanism has been also proposed for hybrid coatings but, in these cases, carbonaceous species can act as an extension of the electrode, being coated by IrOx. SEM and TEM images have demonstrated this effective coating, yielding a nanostructured material, very rough and porous.

- IrOx-CNTs coatings present a semi-transparent blue color, darker than the obtained for bare IrOx coatings. The surface is rough because of the CNTs presence in the entire coating, which confers a 3D network-like structure and a rough surface. The chemical surface analysis by XPS does not allow obtaining the CNTs concentration, given the large amount of adventitious carbon and the low penetration depth of the technique. Also, the presence of high and reproducible quantities of potassium is observed. The highly hydrated structure has been presented as an iridium oxohydroxyde, with mixed valence state (among III and IV), in which the CNTs are embedded. The initial amorphous structure of as prepared IrOx-CNTs hybrids, changes when the sample is heated at 500ºC, and the formation of crystallites with hollandite-type structure has been observed. As electrodes in electrochemical performance, IrOx-CNTs coatings show considerably higher CSC_C values as compared with bare IrOx films, and large stability in successive cycling tests.

- IrOx-PEDOT-CNTs hybrids synthesized show also a semi-transparent blue-black appearance. The presence of CNTs is observed in SEM images of the coatings, but also has been confirmed by Raman experiments, demonstrating the presence of IrOx. The incorporation of CNTs considerably increases the roughness of the coatings. However, in this case the electrochemical properties of the coating do not improve, in comparison with other polymeric films as PEDOT-PSS. The influence expected due to the increased roughness or the presence of electroactive dopants in the coating is not observed, presumably as consequence of the polymer coating of these species, which minimizes the electrochemical properties of IrOx and CNTs.

- IrOx-graphite and IrOx-graphene hybrids have been prepared starting from the oxidized precursors. The coatings obtained present deep blue color, which can be modulated with the charge of synthesis. The introduction of large quantity of carbon particles in the coatings has been shown in optical images, but also

SEM images shows big graphite particles coated by the oxide. However, for IrOx-graphene samples, the presence of graphene sheets has not been demonstrated, and has been supposed to be few-layered graphene. For these samples, XPS results show high concentration of carbon in the surface, which cannot be correlated only with adventitious carbon. Also, large contents of potassium are obtained. The electrochemical performance of both coatings as electrodes, show high values of CSC_C, 127.8 and 108.2 mC/cm^2 for IrOx-graphite and IrOx-graphene, respectively. However, the stability under successive cycling for the graphite hybrid is very poor, and after 1000 cycles only a 25.9% of the total charge storage capacity is maintained, in contrast with values found for IrOx-graphene coatings, around 88.7%.

- The synthesis of IrOx-(graphene-N) coating has been also achieved, starting from N-doped graphene. The hybrid films obtained are well adhered to the substrate and present blue-black color. The chemical surface analysis do not yield any information about the carbon concentration, as level C content has been observed, and the data can be influenced by the presence of adventitious carbon. However, the same IrOx composition is observed when compared with bare IrOx samples, highly hydrated oxohydroxyde. The electrochemical study of these hybrids coatings, yield to very high values of CSC_C (158.9 mc/cm^2), which indicates that the presence of nitrogenated-species enhance the electrode conductivity. Also, good stabilities have been obtained for consecutive cycling.

- IrOx-CNTs and IPC coatings have been tested as support for neural growth. IrOx-CNTs hybrids have not shown toxicity, and the number of cells growing on it after 5 DIV was very high, as those obtained for bare IrOx or borosilicate substrates. These results indicate that surface factors as roughness or hydrophilicity, very different in IrOx and IrOx-CNTs coatings, are not relevant for cell development and only the chemical composition seems to influence. Also, cells growth in these substrates was found to be functional under

external stimulus, confirming the suitability of these materials for neural electrodes. However, the neuron survival shown in IPC samples was considerably low, also showing a heterogeneous spreading of cells and high irreproducibility among different cultures. On the other hand, a co-culture model has been tested with these samples, in which neurons are seeded in the top of a previous astrocyte layer. The results obtained in this cell cultures has been considerably enhanced compared to the neuron-only ones, indicating the preference of astrocytes for this hybrid material. Therefore, co-cultures can be considered as a method to biologically modify surfaces, in order to improve biocompatibility.

In conclusion, different hybrids materials have been synthesized and characterized (Table 8.1), but those obtaining higher electrochemical performance (in terms of CSC_C and stability) are IrOx-CNTs, IrOx-graphene and IrOx-(graphene-N). In addition, large the biocompatibility shown for IrOx-CNTs as substrates for neural growth, make this material as very promising for neural electrode applications (for graphene and graphene-N coatings, biocompatibility has to be tested).

Material	**Cycles of synthesis**	**CSC_C (mC/cm^2)**	**Stability (CSC_{final}/CSC_{max}) after 1000 cycles**
IrOx	50	33.8	71.2%
IrOx-CNTs	25	101.2	72.1%
IrOx-graphite	25	127.8	25.9%
IrOx-graphene	25	108.2	88.7%
IrOx-(graphene-N)	25	125.1	88.7%
IPC	20	18.1	~ 41.6 %

Table 8.1. Different materials and the results obtained during electrochemical measurements in PBS, at 10 mV/s.

APPENDIX A

Acronyms and Abbreviations

AFM	Atomic force microscopy
AIROF	Anodic or Activated iridium oxide films
AraC	Cytosine arabinoside
ATR	Attenuated total reflectance
B27	Serum-free supplement for neural growth
BE	Binding Energy
BS	Buffered solution
BSA	Bovine serum albumin
C_{adv}	Adventitious carbon
CCD	Charge coupled device
C_g	Specific capacitance
CNS	Central neural system
CNTs	Carbon nanotubes
CSC	Charge storage capacity
CSC_C	Cathodal charge storage capacity
CV	Cyclic voltammetry
CVD	Chemical vapor deposition
DBS	Deep brain stimulation
DC	Direct current
DIV	Days *in vitro*
DLS	Dynamic light scattering
DMEM	Dulbecco's modified Eagle's medium
DNA	Deoxyribonucleic acid
ECM	Extracellular matrix
ECQM	Electrochemical quartz crystal microbalance
EDOT	Ethylenedioxythiophene
EDTA	Ethylenediaminetetraacetic acid
EDX	Energy dispersive X-ray analysis
EF	Electric field
EIROF	Electrodeposited iridium oxide films
ESCA	Electron spectroscopy for chemical analysis

EXAFS	X-Ray absorption fine structure
FBS	Fetal bovine serum
FWHM	Full width at half maximum
GABA	γ-aminobutyric acid
GFAP	Glial fibrillary acidic protein
GIXRD	Grazing incidence X-ray diffraction
GO	Graphene/graphitic oxide
HBSS	Hank's balanced solution with HEPES
HEPES	4-(2-hydroxyethyl)-1-piperazineethanesulfonic acid
HPLC	High performance liquid cromatography
ICMAB	Instituto de Ciencia de Materiales de Barcelona
IibB	Instituto Investigaciones Biomédicas de Barcelona
IPC	Hybrid coatings of IrOx, PEDOT and CNTs
IR	Infrared
IrOx	Hydrated iridium oxide
IrOx-(graphene-N)	Hybrid coatings of IrOx and N-doped graphene
IrOx-CNTs	Hybrid coatings of IrOx and CNTs
IrOx-graphene	Hybrid coatings of IrOx and graphene oxide
IrOx-graphite	Hybrid coatings of IrOx and graphite particles
IVCT	Inter-valence charge transfer
MWCNTs	Muti walled carbon nanotubes
NMDA	N-methyl-D-aspartate
NPs	Nanoparticles
O_{ad}	Adventitious oxygen
OPC	Open circuit potential
ORR	O_2 reduction reaction
PaNi	Polyanilina
PBD	Probe beam deflection
PBS	Phosphate buffered solution
PEDOT	Poly(3,4-ethylenedioxythiophene)
PEDOT-Ref	PEDOT synthesized with K_2CO_3 and $H_2C_2O_4$
PFA	Paraformaldehyde

PLL	Poly-L-Lysine
PPy	Polypyrrol
PSS	Poly(styrene sulphonate)
PT	polytiophene
Q-crystal	Quartz crystal
Q_{inj}	Charge injection limit
RBM	Radial breathing modes
RBS	Rutherford backscattering spectrometry
RMS	Root mean square height, roughness parameter
SEM	Scanning electron microscopy
SIROF	Sputtered iridium oxide films
S_q	Root mean square height, roughness parameter
SWCNTs	Single walled carbon Nnanotubes
TEM	Transmission electron microscopy
TGA	Thermogravimetric analysis
TIROF	Thermal iridium oxide films
UHV	Ultra high vacuum
UV	Ultraviolet
UV-vis	Ultraviolet-visible
WOC	Water-oxidizing complex
XAS	X-ray absorption spectroscopy
XPS	X-ray photoelectron spectroscopy
XRD	X-ray diffraction

APPENDIX B

Scientific Divulgation

B1. Conferences, talks and meetings

- M. Lichtenstein*, J. Moral-Vico, **N. M. Carretero**, N. Casañ-Pastor and C. Suñol. "Neural growth and functional development on new biocompatible hybrid materials", 15º Congreso Nacional de la Sociedad Española de Neurociencia (SENC) in Oviedo (Spain). September 2013. Poster presentation.

- **N. M. Carretero**, J. Moral-Vico, A. M. Cruz, N. Casañ-Pastor*. "Electroactive Biomaterials". Invited talk in IBEC, Barcelona (Spain). April 2013.

- **N. M. Carretero**, J. Moral-Vico, A. M. Cruz, N. Casañ-Pastor*. "Electroactive Materias in the Neural System". Invited talk in Georgetown University, Washintong DC. (USA). October 2012.

- **N. M. Carretero**, J. Moral-Vico, N. Casañ-Pastor*. "Iridium Oxide Hybrids with Carbon Nanotubes". Pacific Rim Electrochemical Society Meeting. Hawaii (USA). October 2012. Oral presentation.

- J.Moral*, **N. M. Carretero**, C. Suñol, S. Sánchez-Redondo, N. Casañ-Pastor. "Conducting polymers as electrodes in neural systems. Bilayer composites and aminoacid counterions". QIES 2012, Girona (Spain). July 2012. Oral presentation.

- **N. M. Carretero**, J. Moral-Vico, A. M. Cruz, N. Casañ-Pastor*. "Electroactive Materials as electrodes. Nano and electrochemistry". Invited talk in Dep. Inorganic Chemistry in University of Buenos Aires, Buenos Aires (Argentina). May 2012.

- **N. M. Carretero**, J. Moral-Vico, A. M. Cruz, N. Casañ-Pastor*. "Electroactive Materials as Electrods. Nano and Electrochemistry". XII Encuentro en Superficies y Materiales Nanoestructurados. Cordoba (Argentina). May 2012.

- **N. M. Carretero**, J. Moral, A.M. Cruz and N. Casañ-Pastor*.“Iridium Oxide hybrids as electrodes for the Neural System”. MRS Fall Meeting, Boston (USA), November 2011. Oral presentation.

- **N. M. Carretero**, J. Moral-Vico, A. M. Cruz and N. Casañ-Pastor. “On electrochemical intercalation and materials tunning: New phases, new properties, energy and bio-applications (Analytic Chemistry)” Invited talk in the 25th National Chemistry Congress, Erzurum (Turkey), July 2011.

- **N. M. Carretero**. “Electrodeposition of iridium oxide and carbon nanotubes”, 1st PhD Student Meeting, organized by ICMAB-CSIC. Barcelona (Spain), May 2011. Oral presentation.

- **N. M. Carretero**, J. Moral-Vico, A. M. Cruz, N. Casañ-Pastor*. “Electroactive Materials in Energy and Biological Systems”. Invited talk in EULASUR, Bello Horizonte (Brasil), April 2011.

- **N. M. Carretero***, Javier Moral, Ana M. Cruz and N. Casañ-Pastor. “Study of polypeptide adhesion on biomaterials”. Summer School on Nanoscale Science of Biological Interfaces. Santa Barbara-California (USA). June 2010. Poster presentation.

- **N. M. Carretero***, J. Moral, A. M. Cruz and N. Casañ-Pastor. “Study of polypeptide adhesion on biomaterials”. XI Congreso Nacional de Materiales. Zaragoza (Spain). June 2010. Poster presentation.

- J. Moral*, **N. M. Carretero**, A. M. Cruz and N. Casañ-Pastor. “Modificación y funcionalización superficial de materiales para aplicaciones biomédicas”. XI Congreso Nacional de Materiales. Zaragoza (Spain). June 2010. Poster presentation.

- J. Moral-Vico*, A.M. Cruz, **N. M. Carretero**, J.P. Sordo, F. García, N. Casañ-Pastor. “Conductive polymers containing aminoacids and inorganic IrOx electroactive materials for soft tissue applications”. 2nd China-Europe Symposium on Biomaterials in Regenerative Medicine. Barcelona (Spain) 2009. Oral presentation.

- A.M. Cruz, C. de Haro, J. Moral, **N. M. Carretero**, Ll. Abad, M. Carballo, V. Padial, J. Collazos Castro, N. Casañ-Pastor*. “Electroactive Materials, Electrochemistry, Field Application, Interfaces and Cultures”. 4st PROGRESS MEETING NERBIOS PROJECT. Aberdeen (Great Britain) 2009. Oral presentation.

B.2 Publications

- A. M. Cruz, Ll. Abad, N. M. Carretero, J. Moral-Vico, J. Fraxedas, P. Lozano, G. Subías, V. Padial, M. Carballo, J. E. Collazos-Castro and N. Casañ-Pastor. Iridium Oxohydroxide, a Significant Member in the Family of Iridium Oxides. Stoichiometry, Characterization, and Implications in Bioelectrodes. J. Phys. Chem. C. 116, 5155-5168. 2012.

- J. Moral-Vico, N. M. Carretero, E. Pérez, C. Suñol, M. Lichtenstein, N. Casañ-Pastor. Dynamic Electrodeposition of Aminoacid-Polypyrrole on Aminoacid-PEDOT substrates: Conducting polymer bilayers as electrodes in neural systems. Electrochim. Acta, 111, 250–260. 2013.

- N. M. Carretero, M. Lichtenstein, E. Pérez, L. Cabana, C. Suñol, and N. Casañ-Pastor. IrOx-Carbon Nanotubes Hybrid: A Nanostructured Electrode in Neural Systems. In progress.

- N. M. Carretero, S. Sandoval, E. Pérez, G. Tobías, and N. Casañ-Pastor. Graphene-Iridium Oxide Hybrids Electrodeposition from Various Precursors. A Significant Increase in Charge Capacity. In progress.

- M. Lichtenstein, N. M. Carretero, E. Pérez, C. Suñol, and N. Casañ-Pastor. Astrocyte-Neurons Co-Cultures on PEDOT and PEDOT Hybrids. Surface effects and model for real in vivo tissues. In progress.

- N. M. Carretero, M. Lichtenstein, E. Pérez, C. Suñol, and N. Casañ-Pastor. Trihybrid IrOx-C-PEDOT as Electrode in Biological Systems. In progress.